COLOUR 85

CRANFIELD INSTITUTE OF TECHNOLOGY

School of Mechanical Engineering

PhD Thesis

Academic Year 1987-88

A. HADDAD

SUPERSONIC NOZZLE DESIGN OF ARBITRARY CROSS-SECTION

Supervisor : Professor J. B. MOSS

ABSTRACT

HADDAD, A.; PhD; Cranfield Institute of Technology; 1988
Title: Supersonic nozzle design of arbitrary cross-section.

An investigation, both theoretical and experimental in nature, has been undertaken to develop a simple method for the design of supersonic nozzles and, indeed, inlets of quite complex shapes from known or calculated axisymmetric flowfields.

The axisymmetric flowfield is determined using a computer program based on the method of characteristics. Streamlines are calculated by direct integration of the axisymmetric stream function.

The desired shape is chosen at the exit of the computed axisymmetric nozzle having the desired length and Mach number. Its describing points are then traced along the corresponding streamlines back to the throat. Streamsheets formed by these streamlines define the new shape.

Following this approach, two three-dimensional nozzles were designed : one of elliptical cross-section and a two-dimensional wedge. Flows within the two configurations were further simulated using a general purpose three-dimensional CFD code, "PHOENICS", while the elliptical nozzle was subsequently manufactured and submitted to experimental tests.

Results from the experimental tests and three-dimensional numerical simulation, as well as predictions of the performance of the nonaxisymmetric nozzles and their axisymmetric counterparts were obtained and compared.

Good agreement was achieved between the several components of the study demonstrating that it is possible, using this relatively simple method, to design satisfactory three-dimensional nozzles.

Acknowledgments

Two important requirements are needed for the successful completion of a research project. Hard work is the first requirement, and that is solely dependent on the person doing the research. The second requirement is strong support. I would like to take this opportunity to acknowledge some of the support I received during this study.

My thesis advisor, Prof. J. B. Moss, was a great support. His great ability and speed for grasping new ideas and responding to them has taken the author several times by surprise. He contributed in his own individual way to enhance the quality of this thesis.

Dr. L. H. Townend was an immense source of experience to draw upon. His contribution and his interest are deeply appreciated.

Dr. A. El-Zafrany, a personal friend, has me forever in his debt. He provided me with the mathematical routines and allowed me to incorporate them in the program developed.

My friend, Dr. J. R. Barbosa, has always found the time to switch his attention from his own work in order to discuss my problems and answer my questions. His help is appreciated.

The author express appreciation to personnel at RAE Bedford, in particular Mr. J. P. Sheffield, for their useful suggestions which materially aided this investigation.

British MoD support, from the very beginning to the very end, is likewise acknowledged with appreciation.

LIST OF CONTENTS :

LIST OF FIGURES:

NOTATION :

1. The coordinate system

In the two-dimensional computations (comprised in sections 3 and 4) involving the calculation of the flowfield within the axisymmetric nozzle, the system of coordinate is represented by:

x : axial coordinate direction,
y : radial coordinate direction,
u : axial component of the velocity,
v : radial component of the velocity.

When the three-dimensional computations are involved (section 6 and 7), the system of coordinate is then represented by:

z : axial coordinate direction,
y : radial coordinate direction,
x : azimuthal coordinate direction,
w : axial component of the velocity,
v : radial component of the velocity,
u : azimuthal component of the velocity.

2. If not otherwise stated, the main notation followed are:

a : speed of sound
A : area
A^* : throat area
A_a : Attachment angle
A_e : exit angle
A_w : coefficient of the wall contour parameter

B : coefficient in the law-of-the-wall equation (chapter 2.4.4)
B_w : coefficient of the wall contour polynomial

C_a : parameter related to axisymmetric flow
C_c : throat contraction factor
C_p : specific heat capacity at constant pressure
C_w : coefficient of the wall contour polynomial

d : density ratio, (ρ_e/ρ)

f' : velocity defect profile, ($\rho_e u_e - \rho u)/\rho_e u_e$

g : standard gravitational acceleration
g' : enthalpy defect profile, ($h_{t,e} - h_t)/h_{t,e}$

h : enthalpy

K : molecular kinematic conductivity
K_e : effective kinematic conductivity
K_t : turbulent kinematic conductivity

$\dot{m}$: mass flow per unit time
M : Mach number

P : pressure (except in equation D.12 where it represents the parameter defined in equation D.14).
P_r : molecular Prandtl number
P_{rt} : turbulent Prandtl number

q : local heat flux
Q : parameter in equation D.12 defined in equation D.15

r : radius
R : specific gas constant (except in equation D.12 where it represents the parameter defined in equation D.16).
R_{td} : nozzle throat downstream radius of curvature
R_{tu} : nozzle throat upstream radius of curvature
R_{δ^*} : Reynolds number based on displacement thickness, $\delta^* u_e/\nu$

T : temperature
$T_{(+)}$; $T_{(-)}$: coefficients in finite-difference equations (Appendix A).

u_e : axial velocity at the edge of the boundary layer
$u+$: y/y_τ
u_τ : friction velocity, $(\tau_w/\rho_w)^{1/2}$

x_a : axial coordinate of attachment point
x_e : axial coordinate of exit-lip point

y_a : radial coordinate of attachment point
y_e : radial coordinate of exit-lip point
y_t : throat radius
$y+$: u/u_τ
y_τ : length scale of the wall region, ν/u_τ

Greek notation :

α : molecular diffusivity or angle
α_e : effective heat conductivity

γ : specific heat ratio

δ : coefficient in gas dynamic equation (3.1 and A.12) $\delta = 0$ for planar flow and $\delta = 1$ for axysimmetric flow or flow boundary layer thickness (Appendix E).
δ^* : boundary layer displacement thickness
δ^*_K : kinematic displacement thickness $\int_0^\infty [(\rho_e u_e - \rho u)/(\rho_e u_e (r/r_w))] \, dy$
Δ : temperature boundary layer thickness

$\sigma_1;\sigma_2$: coefficients in the compatibility and characteristic equations (Appendix A).

η : non-dimensional coordinate normal to the wall, y/δ^*

$\lambda_{(+)};\lambda_{(-)}$: slopes of the left-hand and right-hand characteristics respectively.

ν : molecular kinematic viscosity
ν_e : effective kinematic viscosity
ν_t : turbulent kinematic viscosity

ψ : stream function

ρ : density

Θ : flow angle (except in equation D.20 where it represents the boundary layer momentum thickness).

τ : shear stress
T : non-dimensional effective viscosity, $\nu_e/(u_e \delta^*)$
T_g : non-dimensional effective conductivity, $K_e/(u_e \delta^*)$

φ,Φ : inner and outer effective viscosity functions

χ, : wall and defect wall variables for the effective kinematic viscosity function.

Subscript and superscript :

$(\ )_a$: ambient state
$(\ )_{Hg}$: state of mercury
$(\ )_t$: total state
$(\ )_{t,e}$: total state at the edge of the boundary layer
$(\ )_{th}$: state at throat
$(\ )_w$: wall state
$(\ )_1$: known or calculated point
$(\ )_2$: known or calculated point
$(\ )_4$: solution point
$(\ )_{4'}$: predicted value at solution point
$(\ )_{4''}$: corrected value at solution point
$(\ )_+$: along left-hand characteristic
$(\ )_-$: along right-hand characteristic

SECTION 1 : Introduction

1.1. General

A variety of aerospace applications require three-dimensional supersonic internal flow analysis. These include three-dimensional nozzles for propulsion engines having nonsymmetric area constraints and for aircraft where airframe/propulsion integration plays an increasingly important role as the mission requirements for advanced tactical aircrafts become more stringent.

Methods which solve three-dimensional flows are available. Special techniques are usually used for specific cases but the basic tendency has been towards developing a general method, involving the introduction of more and more sophistication into complex numerical programs. This creates substantial difficulty for the user in understanding the program and preparing the inputs. Long operating and turn-around times are necessary and consequently high costs.

One of the most popular methods for the solution of two and three-dimensional flowfields is the finite-difference method (FDM). While its application has now become common place in industry, one of the most important remaining technological deficiencies is in the area of geometric modeling. FDM computer codes are generally tailored to a specific grid topology. Body geometries that fit this topology are analysed accurately by the corresponding FDM computer code. However, severe loss of grid line orthogonality often occurs as a grid is body fitted about a new geometry not suited to the particular topology. The effects of nonorthogonality may be reduced by increasing the number of grid points or by redesigning the grid for each complex geometry. The first approach is very costly while the second is inconvenient at best, possibly requiring a separate computer code for each grid configuration.

1.2. Applications and Scope

1.2.1 Applications

This work involves the investigation of a simple method for determining theoretical wall contours of supersonic nozzles and inlets of arbitrary cross-section shape from known axisymmetric flows. It would also make available a wide range of complicated shapes whose investigation would be quite difficult even with three-dimensional computational approaches. It may also provide a method of solving some other critical aerodynamic problems encountered in hypersonic flows.

In the particular case of a hypersonic wind tunnel, it would be very helpful if a three-dimensional expansion could be used to avoid the usual thin slit which would appear at the throat of such a nozzle if it were two-dimensional. Furthermore, at hypersonic Mach numbers, calculations involving low Reynolds number flows are not perfect and the desired axisymmetric contours (region 'R' in Figure 1.1.a) tend to generate disturbances which seem to focus at a point on the centreline, changing the flow properties (point 'P_1' of Figure 1.1.b). This causes particular problems for aerodynamic models which are mounted on the axis in order to be tested. Such concentration is assumed to be caused by the cross-section constant radius. This symmetry tends to focus any disturbance to a single spot. One simple way of avoiding that happening is to make the radius vary within the cross-section, shifting the foci to points P_2 and P_3 of Figure 1.1.c for example, and resulting in a nonaxisymmetric cross-sectional contour.

Concerning supersonic flows, there seems to be considerable potential for the integration of two-dimensional wedge nozzles into fighter aircraft (Figure 1.2). This, for example, would reduce the cruise drag allowing a lower fuel consumption and therefore greater mission range. This application is examined fairly extensively in the literature reviewed in Section 3.

A better integration of nozzles into propulsion engines having nonsymmetric area constraints would enhance their performance. The integration of three-dimensional propulsion nozzle into a supersonic missile (Figure 1.3) would reduce its drag, resulting in an increase of its thrust.

1.2.2 Scope

The method investigated herein is based on three main features of axisymmetric inviscid flows :

1. Streamlines of such flows lie in planes through the streamwise axis,
2. Flow in any one such plane is the same as that in any other,
3. Streamsheets (formed by the above streamlines) form surfaces across which there is no flow and, hence, may be replaced by solid boundaries.

These characteristics will be exploited in order to calculate comparatively simply the nozzle having the desired shape. First, the axisymmetric nozzle having the desired length and Mach number is computed. Then, choosing the desired cross-section shape at the exit, the streamlines which pass through its periphery are located and traced back to the throat. The streamsheets formed by these streamlines will then constitute the walls of the desired nozzle.

Utilising this approach, two three-dimensional nozzles were designed: one of elliptical cross-section and a two-dimensional wedge. Validation of the performance of the design method was carried out by performing a detailed analysis of the flowfield within the nonaxisymmetric configurations. Furthermore, a nozzle was constructed to the specifications of the elliptical nozzle and tested with air as the flowing medium. While the method of characteristics used to carry out the axisymmetric flowfield computations illustrates the general performance of the initial axisymmetric configurations, the three-dimensional computations performed by'Phoenics' as well as the experimental investigation would demonstrate the behaviour of the flowfield within the nonaxisymmetric nozzles. Comparison between the several components of such investigation, performed in terms of static pressure ditributions, developed thrust and exit velocity would then demonstrate the ability of the approach to design satisfactory three-dimensional nozzles.

This thesis has been divided into nine main sections. While the first briefly introduces the method investigated and its main applications, the second section reviews some of the literature which has been used in the development of the research. This includes analytical detail as with the method of characteristics (for main flow computations) and boundary layer calculation methods, as well as a broader view of the concept of integrating nonaxisymmetric nozzles into fighter aircraft and its applicability.

Section 3 describes the specific implementation of the method of characteristics as well as the computations of the inviscid flows within the two axisymmetric contours. The subsequent section deals with the calculation of the viscous boundary layer, under the assumption that the viscosity is small enough for its influence to be confined in the immediate neighbourhood of the walls. Its implications for the inviscid flowfield are assessed.

Section 5 shows how, using the method investigated, the axisymmetric nozzles are transformed into nonaxisymmetric ones.

Section 6 and 7 introduce the studies undertaken to validate this design procedure. Section 6 will deal with the experimental programme, involving design, manufacture and testing of a supersonic nozzle of elliptical cross-section whilst that which follows investigates the three-dimensional simulation using a grid generation code "I-Deas" and a generalized flow analysis code "Phoenics".

Results, comparisons and conclusions are presented in the last two sections.

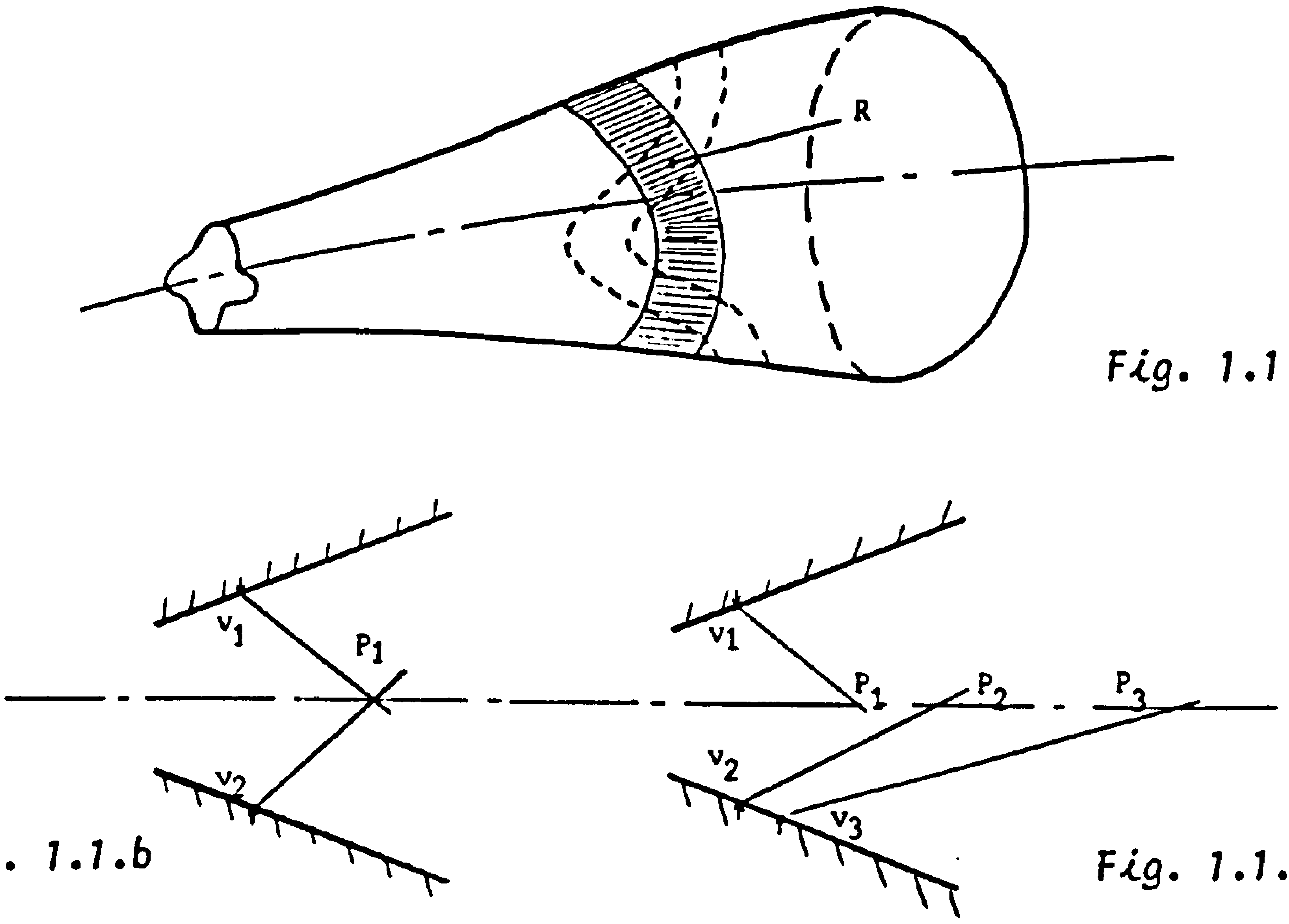

Fig. 1.1.a

Fig. 1.1.b

Fig. 1.1.c

Fig. 1.1: Focusing of disturbances in hypersonic nozzle. (Townend, 1985)

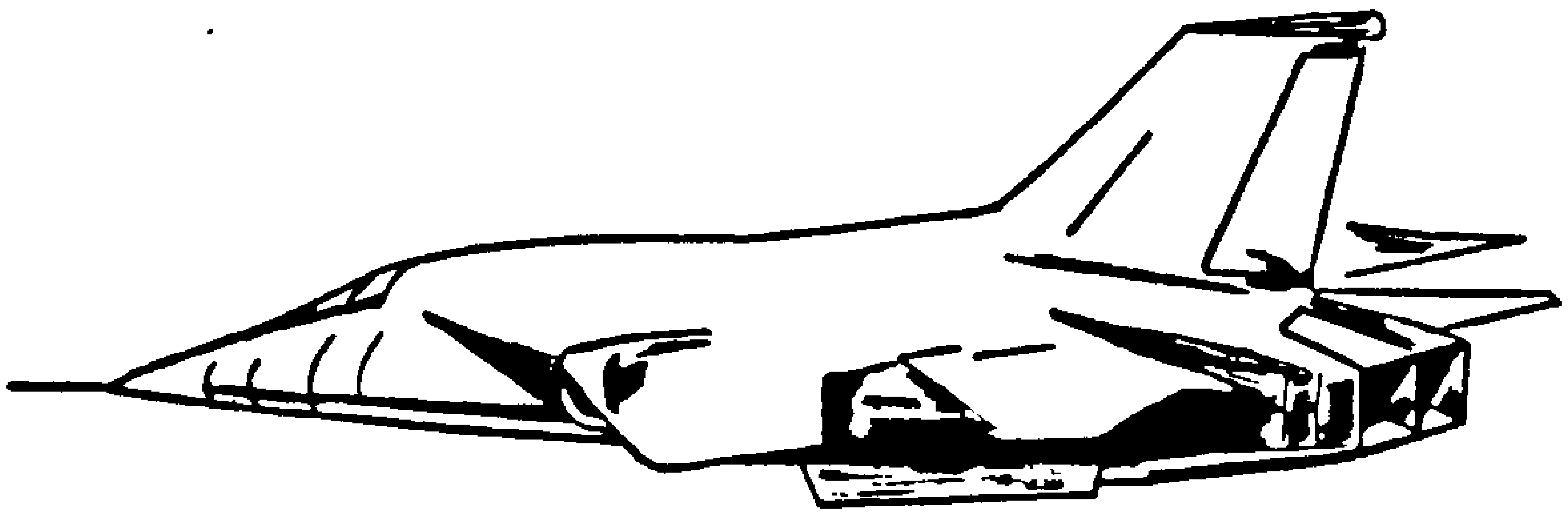

Fig. 1.2: Integration of a two-dimensional wedge nozzle into a supersonic aircraft.

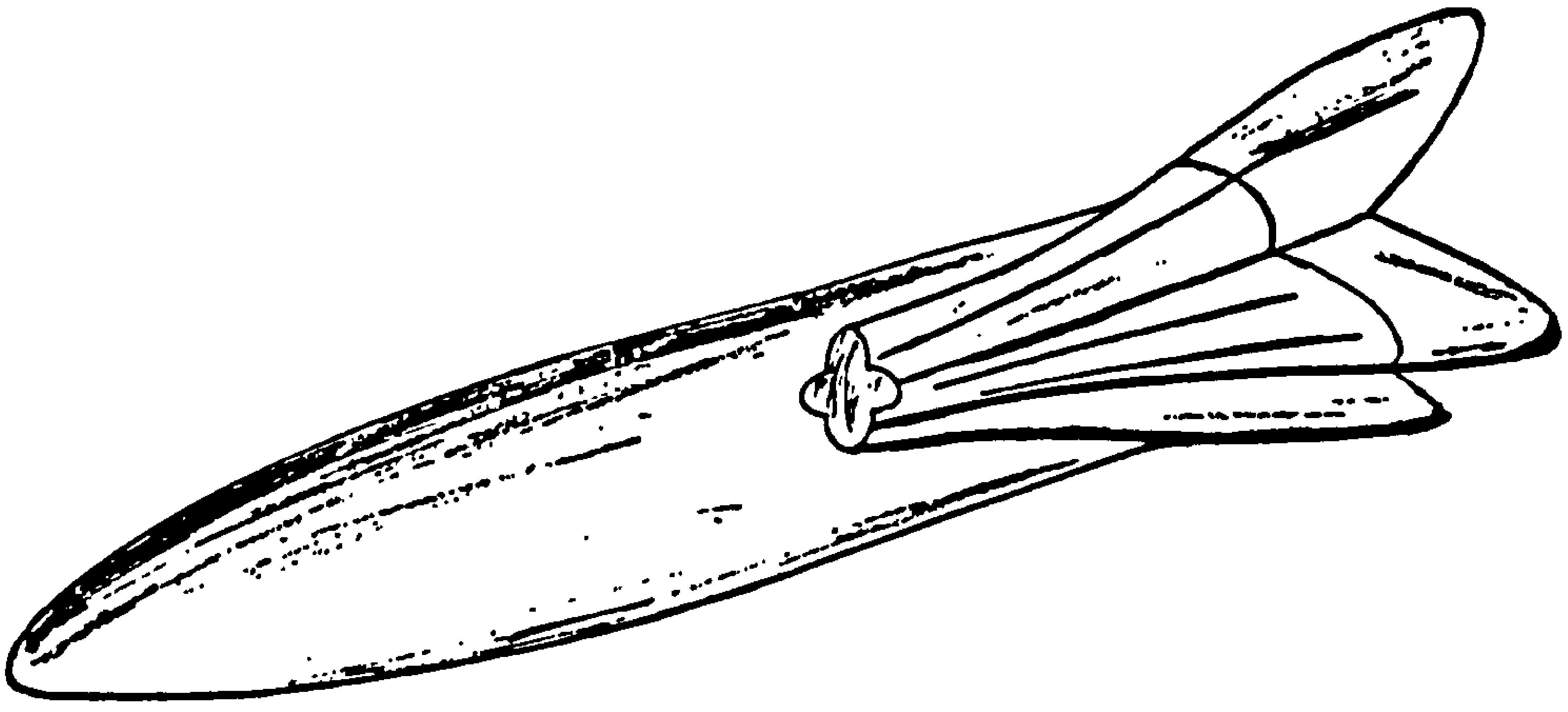

Fig. 1.3: Integration of a three-dimensional nozzle into a supersonic missile.(Townend, 1985)

SECTION 2 : Literature survey

2.1. General

This chapter will deal with a survey of the literature concerning nozzle flows but emphasising three relatively distinct areas. It starts with a review of the early work in design of rocket nozzles followed by the development of the method of characteristics for two-dimensional, irrotational flows.

In order to realistically simulate a fluid flow, viscosity has to be taken into account. However, it is appropriate in many applications to assume its influence is small enough to be confined to the vicinity of the wall. Boundary layer theory is briefly reviewed from early model assumptions to the actual calculation methods.

For the last ten years, considerable interest has turned towards integrating two-dimensional wedge nozzles into supersonic aircraft. This would enhance cruise performance at supersonic speeds and enable them to land and take-off from shorter runways. A summary of recent work and test results is provided.

In the present research programme, experimental tests have been carried out on an elliptical cross-section nozzle and the measurement of static pressure, both in the exit plane and along its centreline, necessitated the design of appropriate probes. A brief survey of the available methods is also presented in this chapter.

2.2. Rocket nozzles

One of the major parameters in the design of rocket motors is the determination of the optimum contour of the exhaust nozzle. This has a great effect upon the determination of the thrust developed by the rocket.

A convergent-divergent De Laval nozzle is typically used to convert the heat liberated in the combustion chamber into kinetic energy for propulsion. Thrust is mainly produced by the momentum imparted to the products of combustion when discharging through the exhaust nozzle. During their passage, the gases are continuously accelerated from low subsonic to high supersonic velocities.

The Con-di nozzle may be divided into three parts :

1. the convergent subsonic section whose design influences the mass flow of the exhaust gases and, to some extent, the combustion efficiency achieved in the chamber,
2. the throat section which determines, with the operating conditions in the combustion chamber, the mass flow rate through the nozzle, and
3. The divergent supersonic section whose wall configuration, together with the exit area, determines the additional velocity imparted by the expansion of gases through this portion of the nozzle.

This division is most appropriate because of the different effects each part has in determining the thrust developed, and because of the different methods of analysis which have to be used for computing the flowfield in each one of the regions.

2.2.1 Parameters describing a Con-di nozzle

Study of the flow in nozzles has led to the definition of a certain number of parameters, characteristic of the propellant-motor combination. They are: the mass flow, the pressure and area ratios, the thrust, the thrust coefficient and the characteristic velocity.

For a given fluid, the ratio of the exit area to the throat area is a function of the pressure ratio only. The thrust coefficient, defined as the ratio of the thrust to the chamber pressure times the throat area, is a parameter characteristic of the gas flow accelerated through the nozzle. The characteristic velocity is a parameter representative of the combustion chamber. These last two parameters, when combined together, will characterise the whole system.

By making use of a one-dimensional simple model, the above parameters may be described in a simple and straightforward way (i.e. Barrere et al, 1960).

2.2.2 Different rocket nozzle configurations

2.2.2.1 Ideal nozzles

The thrust developed by a nozzle reaches a maximum when this latter is discharging the gases in a uniform parallel manner (no flow divergence) at a pressure equal to the ambient pressure. Such a nozzle is known as ideal. For rocket engines operating at high altitudes where the pressure ratio is very small, large area ratios would be required for the ideal nozzle. At sea level, the ratio would be relatively high and small area ratios would be needed.

Because of that dependance upon the ambient pressure, the performance unit of the divergent supersonic nozzle is measured in terms of its vacuum thrust coefficient, defined as :

$$C_{fv} = \frac{\text{thrust when discharching to vacuum}}{P_{cc}\, A_{th}} \qquad \ldots\ (\ 2.1\ )$$

As can be seen from Figure 2.1 which shows the comparative length as a function of the area ratio for various types of nozzles, the ideal nozzle that gives maximum thrust performance is particularly long and consequently heavy.

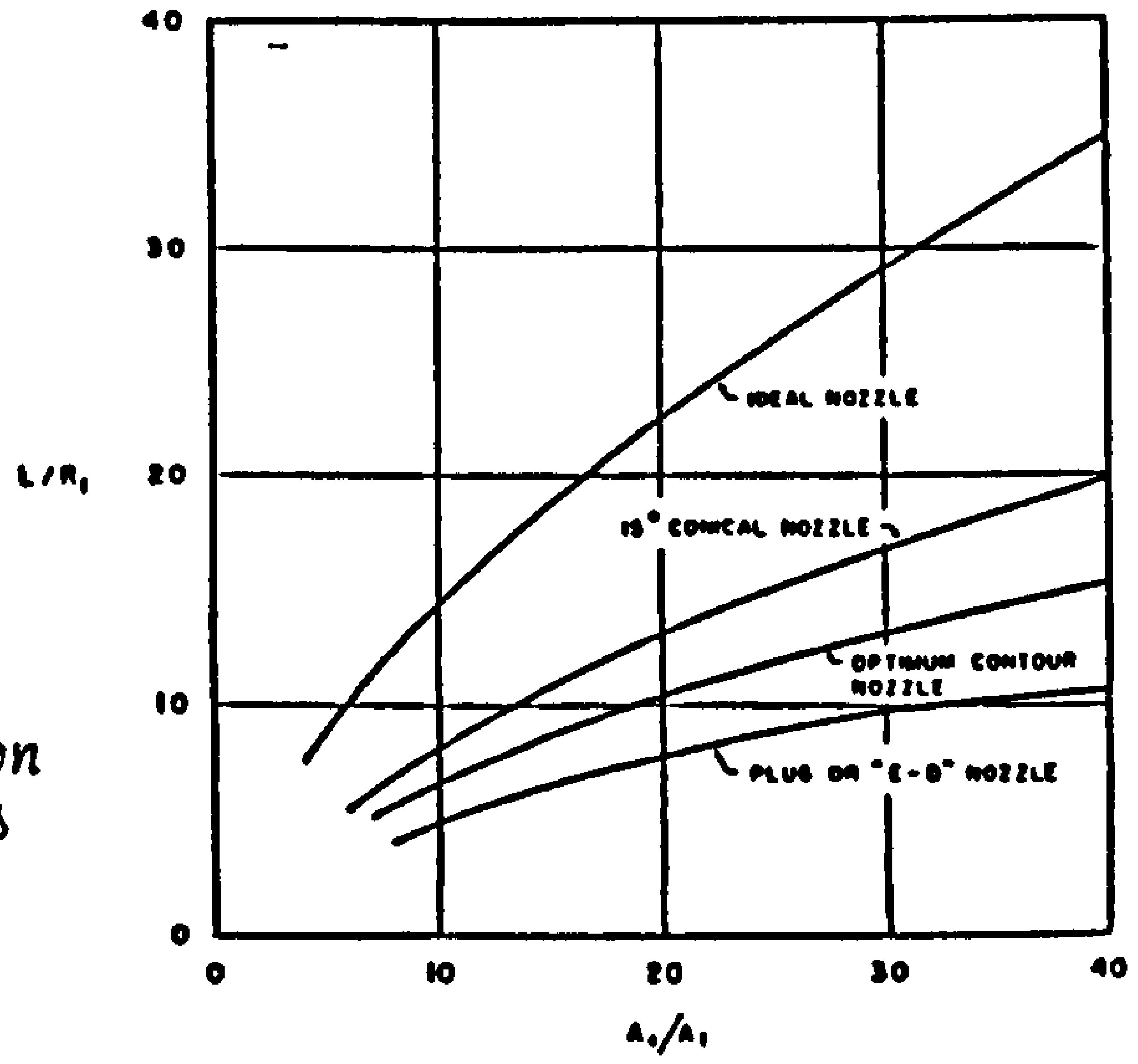

Fig. 2.1: Length comparison of various types of nozzles.

One way of reducing nozzle length, and therefore its weight, without appreciable loss in thrust performance is to alter its shape.

2.2.2.2 Conical nozzle

Though the exit velocity of a conical nozzle is essentially equal to the one-dimensional value corresponding to the area ratio, the flow direction is not all axial, and hence a thrust decrement arises due to the flow divergence.

(Malina, 1940) showed that the exit momentum is equal to the value from one-dimensional theory multiplied by a factor λ. The thrust coefficient of such a nozzle discharging into vacuum is :

$$C_{fv,\text{conical}} = \frac{\lambda \dot{m} V_e + P_e A_e}{P_{cc} A_{th}} \qquad \text{... (2.2)}$$

where : $$\lambda = \frac{1 + \cos\alpha}{2} \qquad \text{... (2.3)}$$

In the case of small rocket engines fitted with small area ratio nozzles, simple fabrication methods are prefered and it is common practice to use conical nozzles. Usually, a half cone of 15° is used for the divergent section (Figure 2.2).

Figure 2.1 shows that the length of a 15° conical nozzle is less than that of an ideal nozzle. The decrement in thrust coefficient of the latter, when compared to the uniform exit nozzle, is only about 1.7%.

2.2.2.3 Contoured nozzle

The reduction in thrust of a conical nozzle, due to flow divergence, becomes large with increasing cone angles associated with reduction in nozzle length. By contouring the nozzle wall, as shown in figure 2.3, the flow can be turned closer to axial direction and the loss in thrust is, to some extent, reduced.

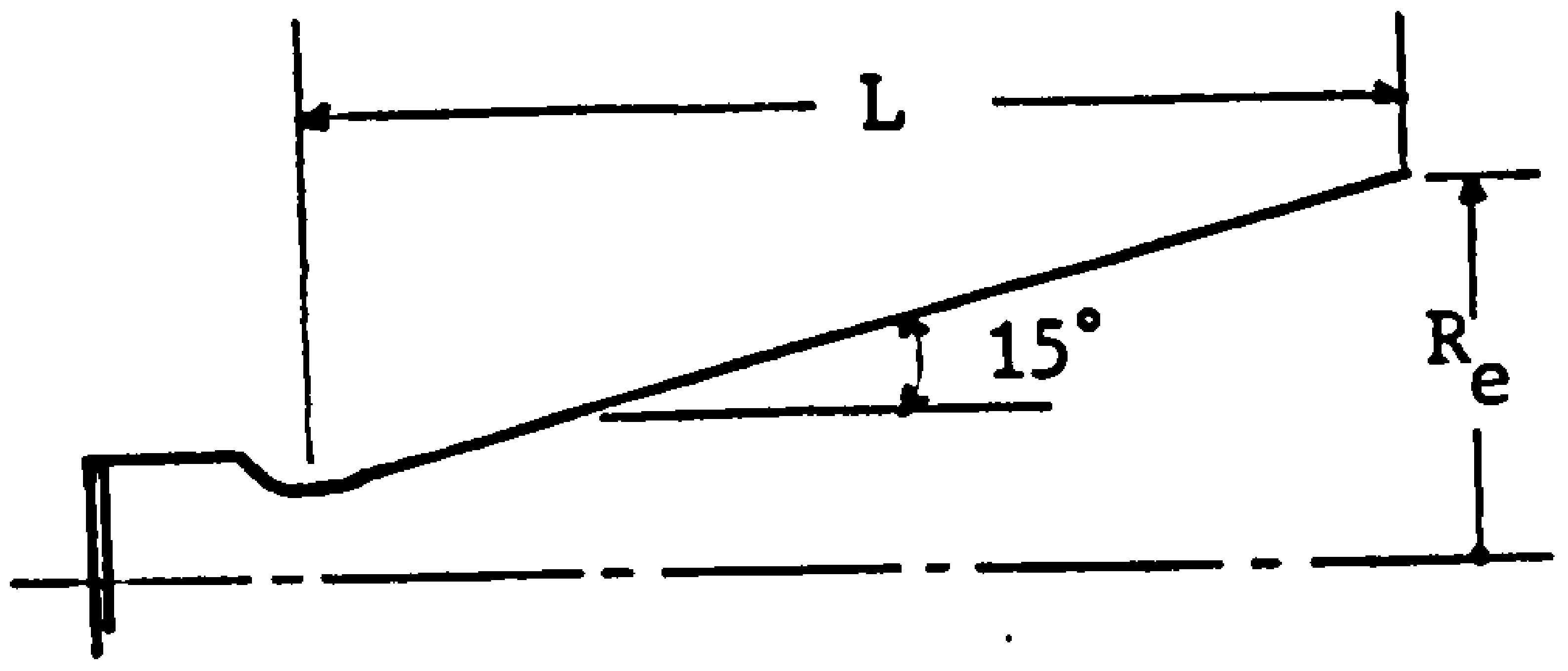

Fig. 2.2: Conical nozzle.

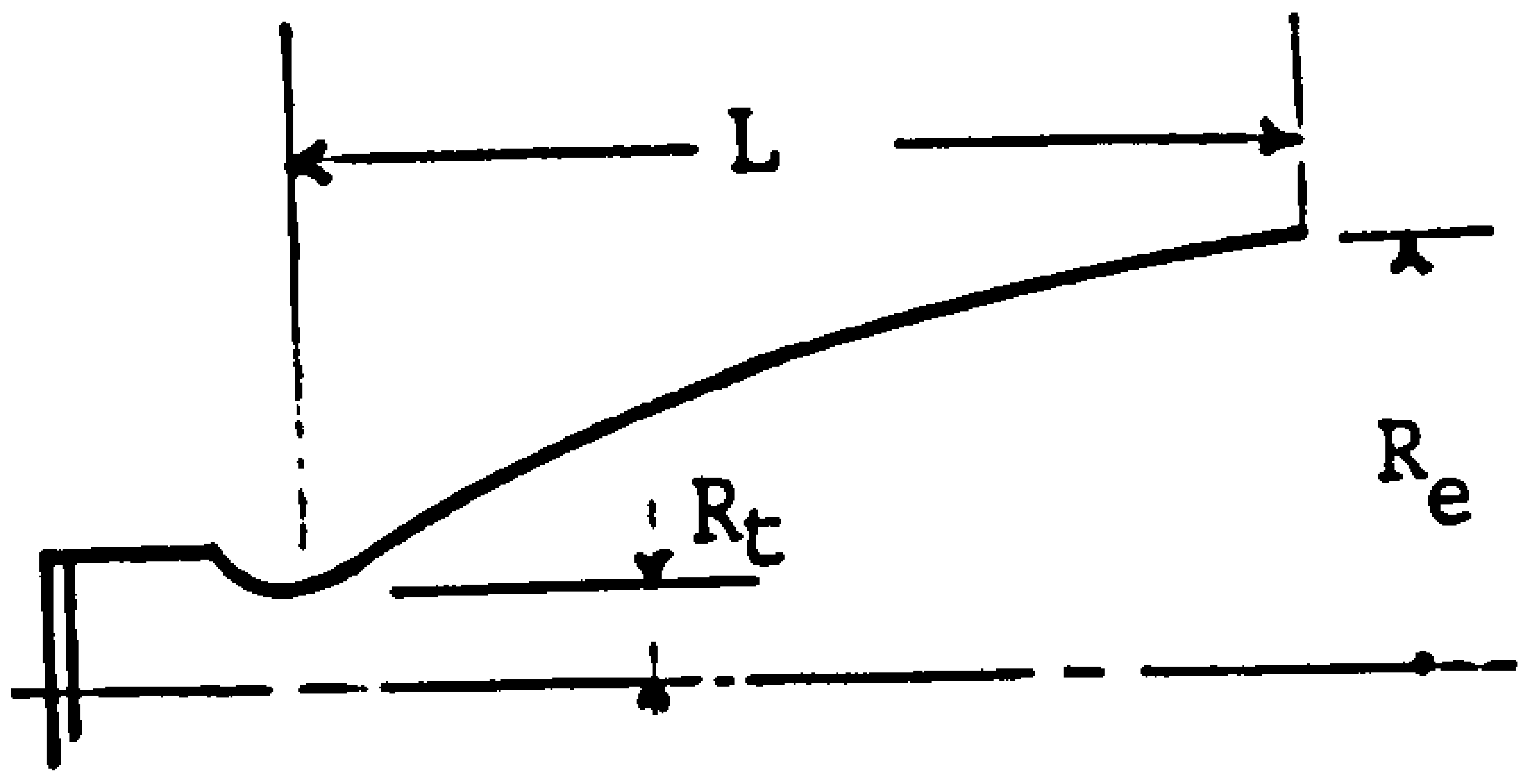

Fig. 2.3: Contoured nozzle.

A direct and elegant approach to nozzle contour design was first proposed by (Guderley & Hantsh, 1955). They formulated the problem of calculating the exit area and nozzle contour to yield optimum thrust subject to the nozzle length and ambient pressure assuming prescribed values. Using the calculus of variations, they solved the problem of the exit flow field required to deliver optimum thrust under the prescribed restrictions. After the required exit flow is achieved, the method of characteristics was used to develop the nozzle contour between the throat and exit.

Because of the complicated nature of the solution presented, optimum thrust contours for rocket nozzles were largely neglected until (Rao, 1958), in reformulating the problem, found a simplified approach to the contour calculation. Considering the nozzle length, ambient pressure and flow conditions in the immediate vicinity of the throat as governing conditions under which the thrust could be maximized and assuming the flow to be isentropic, he formulated the variational integral of this maximization problem with the aid of a suitably chosen control surface. The nozzle contour, giving the optimum flow, was again constructed using the method of characteristics.

In general, rocket nozzle contours chosen for optimum thrust performance require wall angles of about 28° to 30° downstream of the throat. The required wall inclination at the nozzle exit is about 10° to 14° depending upon the required area ratio and length. Nozzle contours having such parameters are widely used for liquid rocket engines and no specific difficulties attributable to the contour have been experienced with hot exhaust gases.

However, exhaust products of solid rocket engines often contain particles of metal oxides. (Kliegel & Nickerson, 1961) analysed flows of such gas particle mixtures through several contoured nozzles. They concluded that, in the case of highly curved nozzle walls, the gas particles impinge on the wall at the exit producing a decrement in thrust and aggravating the problems of erosion. Consequently, for solid rocket engine applications, they suggested the use of contours with less turning than the optimum thrust contours.

2.2.2.4 Annular nozzle

The throat section of such nozzle is an annulus formed between a central plug and an outer tail pipe (Figure 2.4). Downstream of the throat, the exhaust gases are made to expand in a diverging annulus formed between the diverging tail pipe and the converging central plug. The thrust loss due to flow divergence in an annular nozzle, with diverging walls formed by conical surfaces, would be less than that of a conical nozzle of the same area ratio and length (Rao, 1961).

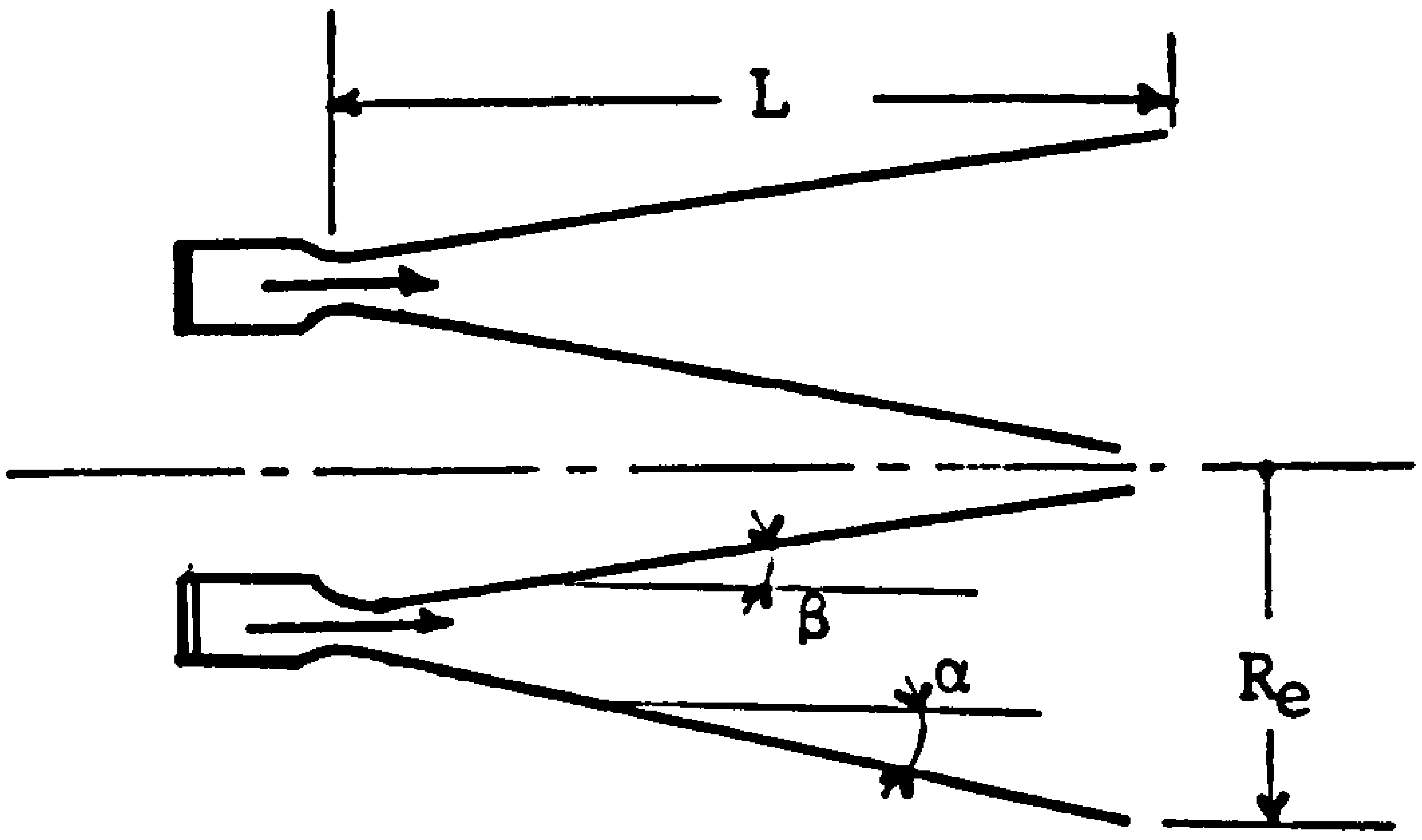

Fig. 2.4: Annular nozzle.

2.2.2.5 Self-adjusting type nozzle

The expansion process within the type of nozzle discussed above is exclusively governed by the diverging walls. The ambient pressure has practically no influence on the expansion and this latter would proceed to pressures considerably below the ambient pressure, until the flow separates. the nozzle wall pressure would then rise abruptly accross an oblique shock. Occurence of such a phenomenon was first observed by (Winpress, 1950) and later confirmed by (Summerfield et al., 1954). They indicated that the separation occured when the gas had been expanded to a static pressure approximatively 0.4 times the surrounding pressure. A similar result was obtained by (McKenny, 1949) whose spark-shadowgraph (Figure 2.5) shows clearly the oblique shock originating at the point of separation.

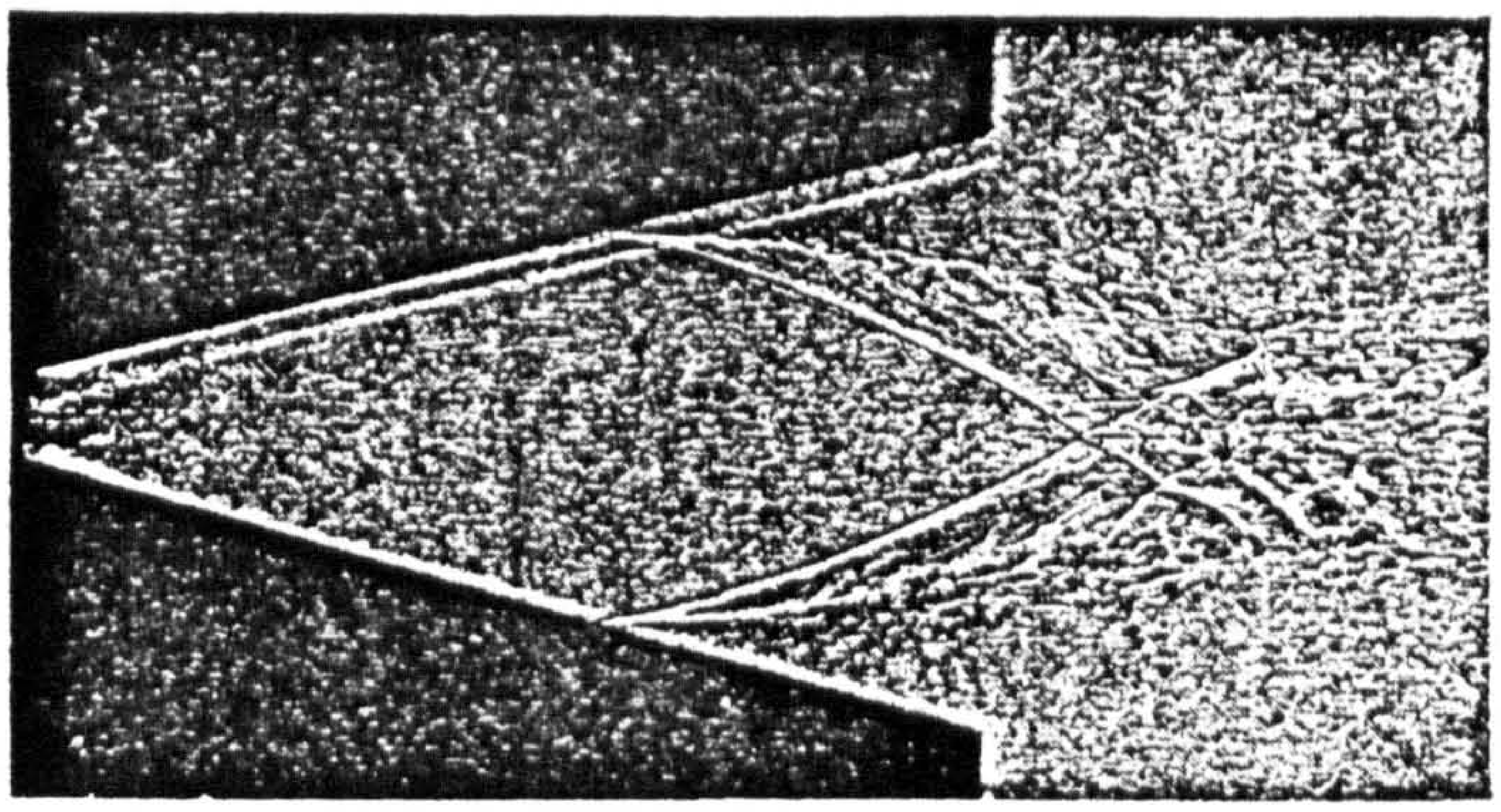

Fig. 2.5: Spark-shadowgraph of flow in overexpanded convergent-divergent nozzle.

Attention, for some time, turned towards developing nozzles in which the expansion process would be directly or indirectly regulated by the ambient pressure. (Rao, 1961) denoted them as a 'Self-adjusting' type and classified them into two categories :

1. Plug nozzles, and
2. Expansion-Deflection nozzles (E-D nozzles).

2.2.2.5.1 Plug nozzle

The throat of such nozzle, as shown in figure 2.6, is located as an annulus at the outer diameter. At the outer edge of the annulus, the exhaust gases expand abruptly to the ambient pressure. The plug surface may be designed in order to produce uniform exit flow parallel to the nozzle axis. The cowl-lip diameter would be the same as the exit diameter of a uniform flow of a Con-di nozzle expanding the gases to the same ambient pressure. However, the plug-type would be much shorter than the equivalent Con-di one.

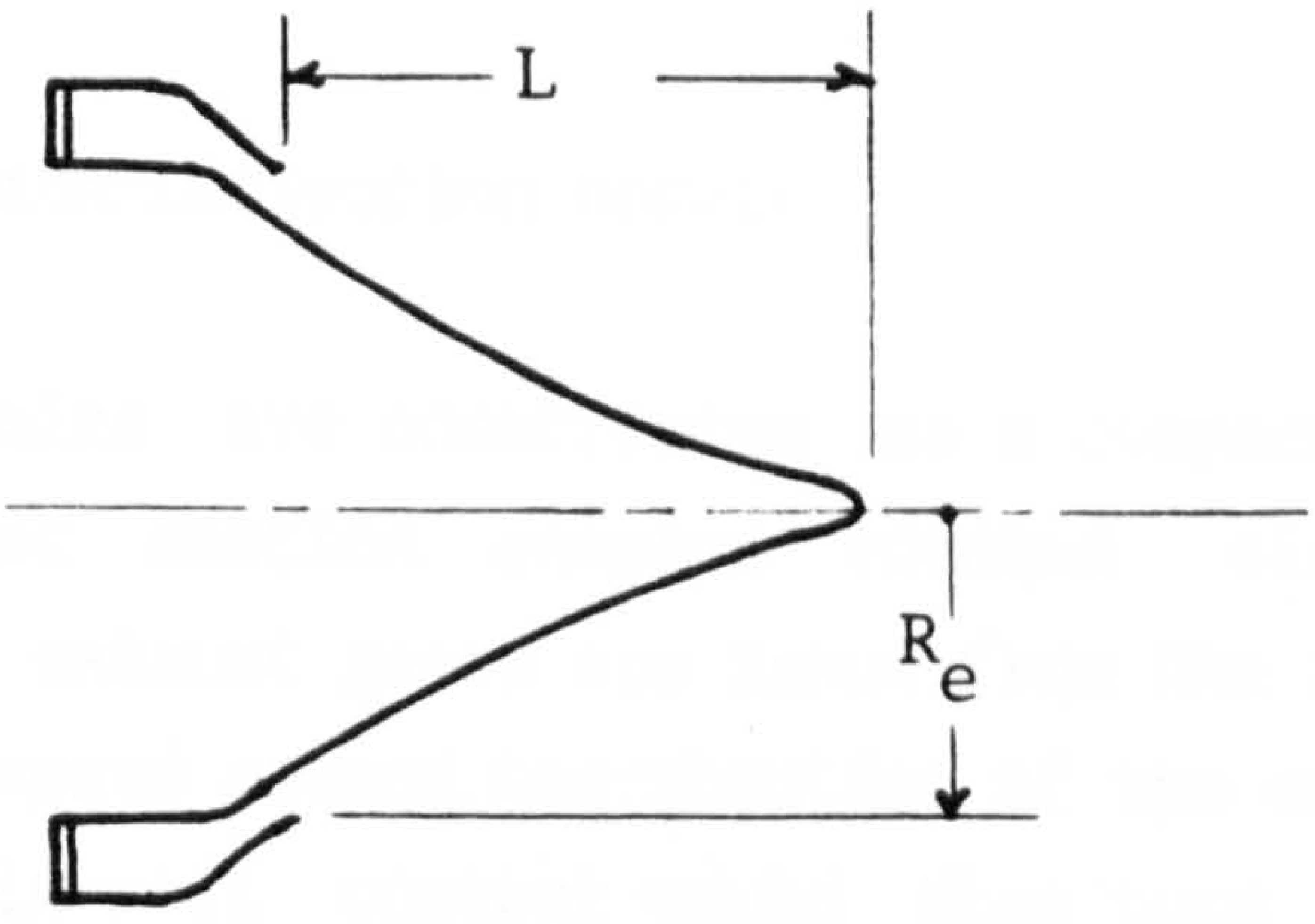

Fig. 2.6: Plug nozzle.

Performance comparisons between conventional and plug nozzles was reported by (Berman, 1960) from which figure 2.7 was reproduced. The plug-type nozzle shows a thrust advantage over its Con-di counterpart at pressure ratios below design. This is caused by the self-adjusting nature of the flow within such a nozzle.

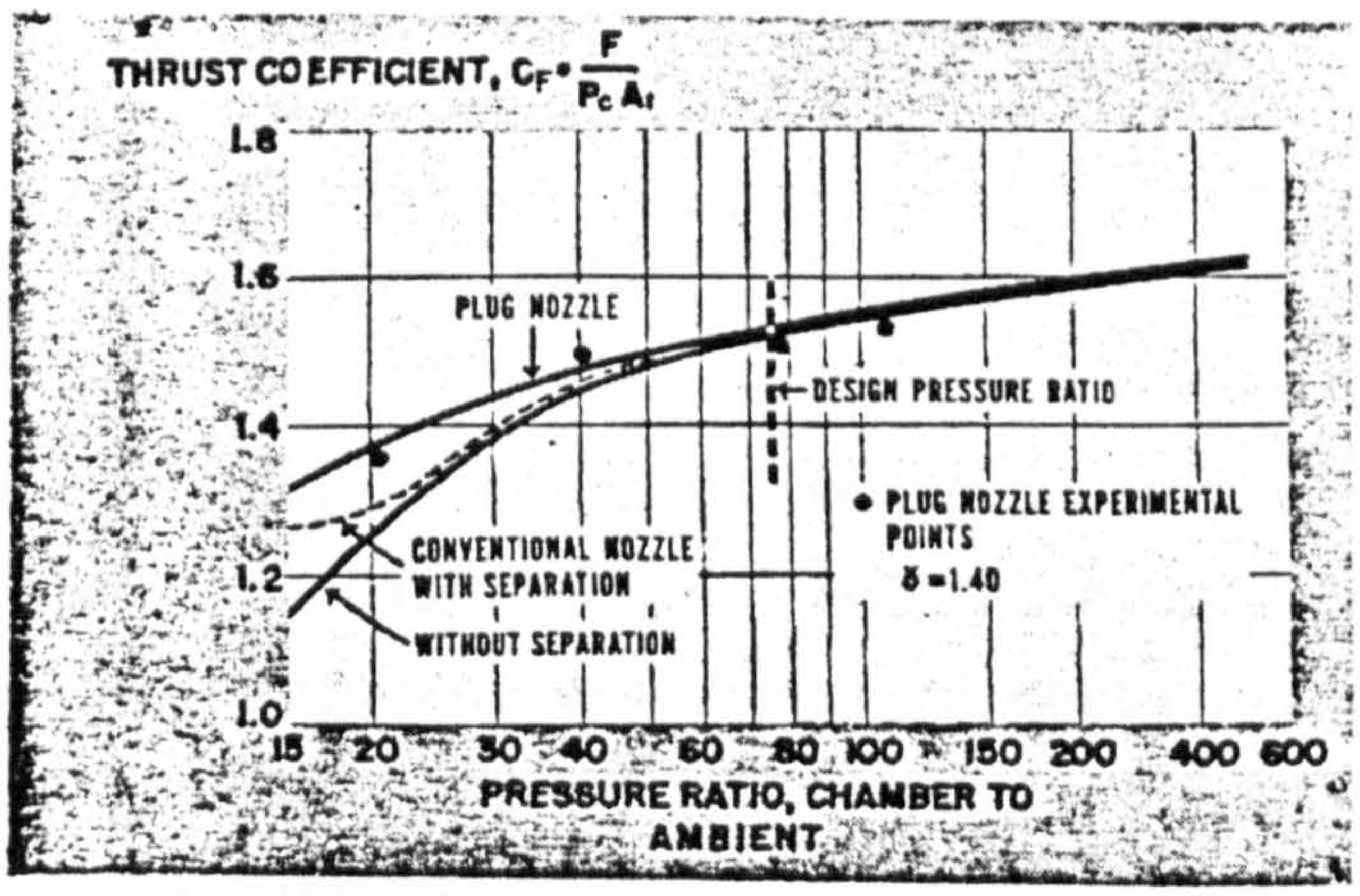

Fig. 2.7: Thrust comparison of plug and conventional nozzles.

At below design operating pressure ratios, the expansion wave intersects with the plug wall at a point where wall pressure is nearly equal to the ambient pressure. At that point, the expansion is interrupted and the convex surface of the plug downstream of this point causes a gradual compressive turning of the exhaust gases. Consequently, the wall pressure downstream of this location would rise to values higher than the ambient pressure. These increased pressures are the cause of the thrust increment of plug nozzles over that of a Con-di one.

2.2.2.5.2 Expansion-Deflection nozzle

E-D type nozzles are constructed as a compact combustion chamber with the throat section annulus located close to the nozzle centreline. The exhaust gases are issue from the throat in an outward direction and expand around the shoulder of the central plug (Figure 2.8). The nozzle wall contour would then turn them into a nearly axial direction.

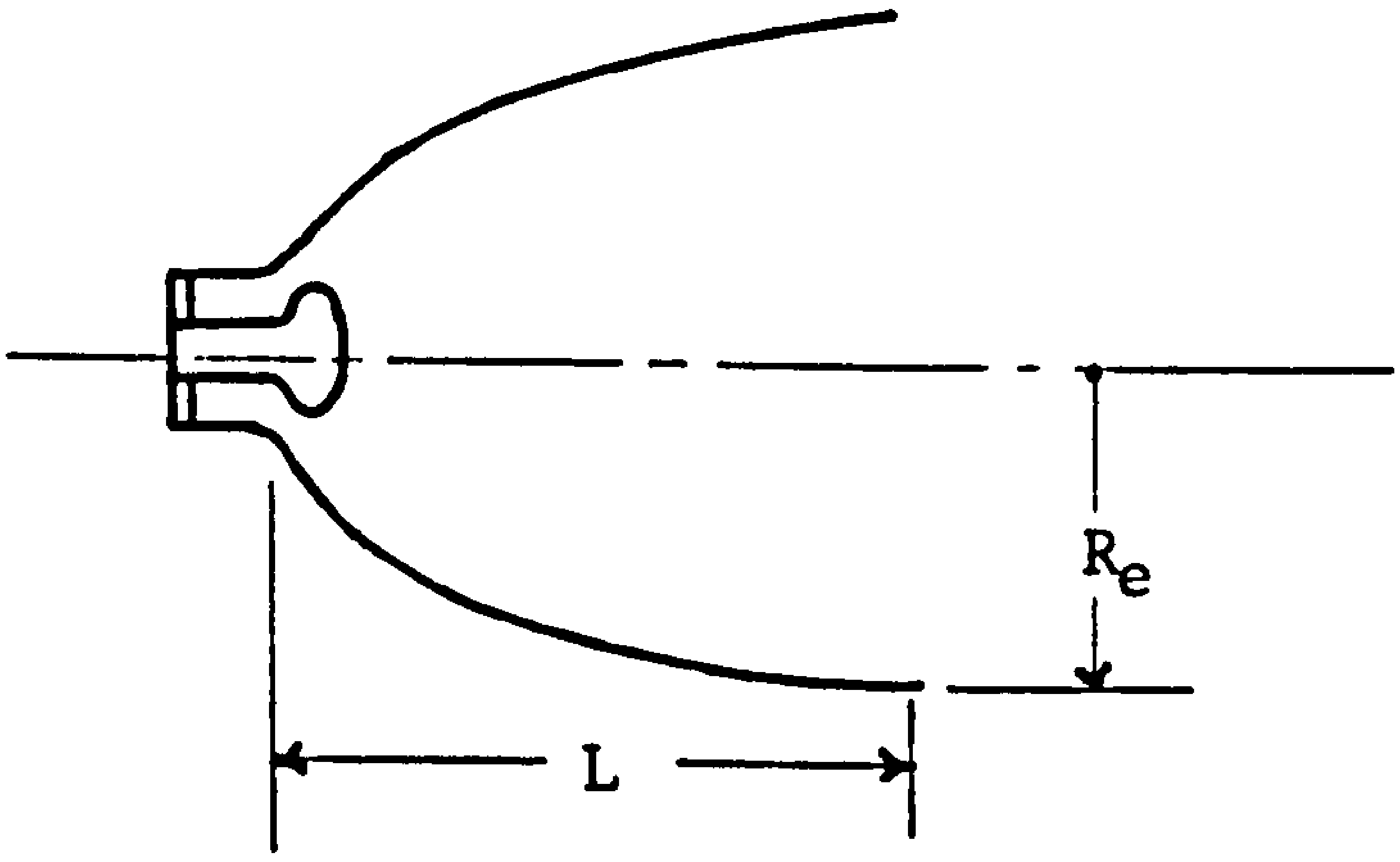

Fig. 2.8: Expansion-deflection nozzle.

The self adjustment of the flow in an E-D nozzle occurs because the pressure at the base of the central plug limits the amount of expansion of the exhaust gases. Hence, a certain amount of compressive turning takes place along the nozzle wall in a manner similar to that occuring in a plug nozzle.

The E-D type nozzle and its essential features were discussed by (Rao, 1960). He observed that, when the ratio of chamber pressure to ambient pressure is sufficiently high, the performance of an E-D nozzle would be the same as that of a plug nozzle designed with comparable parameters. However, when this operating pressure ratio is low, the E-D flow adjusts itself to the pressure occuring behind the central plug which can be lower than the ambient (whereas the plug flow adjusts itself to the pressure at the cowl-lip which is always equal to the ambient). Thus, under similar conditions, the E-D type may show lower thrust performance than that of a plug nozzle.

2.2.3 Design of contoured nozzles

Nozzle contour design procedures based on the calculus of variations developed by (Rao, 1958) have been shown to develop the highest thrusts. A major drawback of this procedure is that if the nozzle configuration or the gas dynamic model are changed, then the entire optimization analysis and corresponding computer program must be reworked.

(Allman & Hoffman, 1981) investigated a way of developing a method for the design of maximum thrust nozzle contours by direct optimization methods. The nozzle contour was specified as a second-order polynomial of the form :

$$y(x) = A_w + B_w x + C_w x^2$$

where the coefficients A_w, B_w, and C_w are determined by specifying the attachment angle, the exit radius and by requiring that the polynomial contour attach continuously to the circular-arc initial expansion contour.

In order to assess whether such a simulated shape can develop thrusts comparable to the ones developed by the calculus of variations contours, the authors compared thrusts developed by the latter contours (Rao's method) with the thrusts developed by polynomial contours. It was found that both methods predict essentially the same maximum thrust (i.e. for zero ambient pressure, agreement was within 0.2%) justifying the new proposed approach.

This approach was used to simulate the contoured wall of the axisymmetric nozzles investigated in this study.

2.3 Method of characteristics

Linearized approximation techniques have their place in the derivation of analytical relations enabling simplified solutions to be reached quickly. There are, however, many instances in which more accurate calculations are necessary. Such flow fields must, therefore, be analysed by methods that obtain solutions to the pertinent partial differential equations. These solutions are, generally, based on applying numerical methods of analysis which depend on the type of equations governing the flow.

For a subsonic flow, the governing equations are of elliptic form and their solution would depend on the specification of all the boundary conditions, that is those upstream and downstream of the region of interest. For these equations, the relaxation method is appropriate.

For supersonic flows, the governing equations are of hyperbolic form and the region of influence is restricted to a finite region upstream of the point of interest. In this case, marching type numerical methods may be applied, the most accurate one being the method of characteristics.

The method of characteristics permits the reduction of a system of partial differential equations to one of ordinary differential equations that are valid along the characteristic curves, which represent the path of propagation of disturbances in such flows. From a rigorous point of view, a characteristic may be defined as a curve along which the governing partial differential equations reduce to an 'interior operator', that is a total differential equation known as the compatibility equation. Thus, along a characteristic, the dependant variables may not be specified arbitrarily, being compelled to satisfy the compatibility equation.

When the flow involves three independant variables, the system of equations can no longer be reduced to a system of ordinary differential equations. Instead, the equations can only be reduced to a system of partial differential equations valid on characteristic surfaces. Consequently, any integration scheme must include numerical evaluation of the pertinent derivatives in two independant variables.

A review of the literature for the method of characteristics in two independant variables will not be given here as the volume of such literature is enormous, since the concept of characteristic directions was first discussed by (Massau, 1899) and has only indirect bearing with the problem at hand.

However, the method has been applied in this study to a steady, axisymmetric irrotational flow. The computer program generated from the implementation of the method of characteristics for this particular flow has been used to calculate the flowfield within the investigated axisymmetric contours.

Details of this particular application can be found in appendix A.

2.4 Boundary layer

2.4.1 General

Methods for calculating turbulent, compressible boundary layer development have been a topic of extensive research for many years. However, until the advent of high speed computers, most of this research effort was concerned with prediction methods which would be applied by using hand calculations or very simple machine computations. In recent years, rapid development of numerical techniques have been achieved.

Methods which solve the compressible, two-dimensional turbulent flow may be divided into two general categories: 1) traditional methods and 2) numerical solution procedures.

2.4.2 Traditional methods

The simplest of these methods are the correlation methods. They are applicable only for axisymmetric flows with zero pressure and wall temperature gradients. (Spalding & Chi, 1964) presented a good summary of available correlations methods for compressible turbulent flows and classified them as follows:

1. Methods using the Prandtl or Von Karman differential equation. In this category, the shear stress is assumed constant through the boundary layer and equal to its value at the wall. Van Driest used the two mixing length concepts as differential equations : (Van Driest, 1951) used the Prandtl's mixing length and (Van Driest, 1956) the Von Karman mixing length.

2. Theories based upon other differential equations. Also, in this category, the shear stress is assumed constant and equal to its wall value.

3. Theories based upon a fixed velocity profile assumed to be independant of compressibility.

4. Theories based upon incompressible formulae with reference properties. In this category, the incompressible relations are assumed to apply for compressible flows if the gas properties are evaluated at a reference temperature which is function of Mach number, ratio of wall to edge temperature, and recovery factor. This method has been used by (Sommer & Short, 1955) and by Eckert (Eckert, 1955).

The method of integral equations was originally developed as a tool for systematically reducing partial differential equations to a few coupled ordinary differential equations. All integral methods solve the Von-Karman integral momentum equation, along with various auxiliary relations.

Most earlier methods utilized a compressibility transformation, and then solve the equations in the incompressible plane. An example of these methods is the one developed by (Reshotko & Tucker, 1957). The authors solved the momentum integral and the moment of momentum equations in the transformed plane defined by using Stewartson's transformation (Stewartson, 1949). (Flaherty, 1968) improved the latter method by introducing an empirical expression for the shear stress integral through the boundary layer and, by providing for the calculation of the wall heat transfer.

In recent years, integral methods which do not use a compressibility transformation but rather auxiliary relations have found considerable favour. A second equation used in several methods is the mean energy integral equation. (Pickney, 1971) solved the momentum integral, the moment of momentum and the integral energy equation. Comparison of Pickney's results with experimental data, for an axisymmetric compression surface at both Mach 5 and Mach 8, were favorable (Stroud & Miller, 1965).

An alternate additional equation is derived from the notion that the turbulent boundary layer grows by a process of 'entrainment' of non turbulent fluids at the outer edge of the layer into the turbulent region. (Green et al, 1973) used the entrainment relation as an additional equation to close the boundary layer set of governing equations.

2.4.3 Numerical solution procedures

Numerical solution methods that solve the compressible turbulent boundary layer problem may be categorized as :

1. Conventional finite-difference methods,
2. Finite-difference variants, and
3. Methods employing analytical functions.

2.4.3.1 Conventional finite-difference methods

Conventional finite-difference methods have been the most popular. After the early techniques reviewed by (Rosenhead, 1963), emphasis turned to solutions of the boundary layer equations in the Crocco form. Using this approach, (Baxter & Flugge-Lotz, 1957) employed an explicit finite-difference scheme. The step size along the wall, in this procedure, was restricted by stability considerations. In order to avoid that, (Kramer & Liberstein, 1959) employed an implicit scheme.

By using the Von-Mises transformation, the continuity equation can be eliminated from the governing boundary layer equations. Such transformed system has been solved with an explicit scheme by (Mitchell, 1961). Using the stream function as an independant variable across the layer, (Patankar & Spalding, 1967) developed an implicit finite-difference scheme for solving the Von-Mises tranformed boundary layer equations. The nondimensional stream function was defined such that it varies from 0 to 1 from the wall to the outer edge respectively.

Solution of the boundary layer equations in untransformed or physical coordinates appears to be the next development in numerical procedures. In the Soviet Union, (Chudov & Brailovskaya, 1960) studied it using an implicit six-point finite-differece scheme.

(Paskonov, 1963), later, developed the method into a standard program in which a procedure was described which allows the step size accross the layer to vary. At about the same time, in the United States, a similar implicit technique was developed independantly by (Flugge-Lotz & Blottner, 1963).

2.4.3.2 Finite-difference variants

Three methods may be classified as variants of finite-difference techniques. The 'shooting method' uses finite differences in the flow direction but solves an ordinary difference equation in the transverse direction. Several users of this approach (i.e. Albers & Gregg, 1974) encountered stability problems, especially with wall heating or cooling.

With the 'box method', the equations are reduced to a first order system and then solved using a Newton iteration procedure and two-point differencing. This procedure which is of more recent vintage than other finite-difference methods, is quite efficient for boundary layers (Keller & Cebeci, 1972).

The last variant discussed has been developed at the Imperial College of Science and Technology. In the 'micro-integral' method (Patankar & Spalding, 1970), the boundary layer growth is accounted for by use of a stream function as a transverse variable. This permits the reduction of the required number of nodes. Although this solution is one of the most efficient ones available, use of the Couette flow analysis near the wall and an explicit formulae for grid control may give rise to problems when large longitudinal increments are used.

2.4.3.3 Methods employing analytical functions

The method of weighted residuals (or method of integral relations) uses weighting and approximating functions (Kuhn, 1970). The advantage of this procedure is the small number of nodes involved. For turbulent flows, the computation time can be of the same order as for the conventional finite-difference techniques.

2.4.4 Law of the wall

At a solid boundary at rest, the mean velocity is zero due to the no slip condition but so also are the fluctuations which are damped by the presence of the wall. Away from the wall, on the other hand, the turbulence generates Reynolds stresses which are large compared with viscous stresses.

This behaviour has led to a division of the turbulent boundary layer into inner and outer regions. The outer region contains 80 to 90% of the boundary layer thickness and its velocity profile is not influenced by viscous effects.

The thickness of the inner region is about 10 to 20% of the shear layer thickness. Analysis of the inner layer velocity profile is based on the plausible assumption that, in the near-wall region, the flow should be independant of the outer layer characteristics such as the boundary layer thickness and free stream velocity. It should instead depend on the distance from the wall, the surface shear stress and the fluid properties. Elementary dimensional analysis shows that the velocity is given by the 'law of the wall' (Cebeci & Bradshaw, 1977) :

$$u^+ = A \operatorname{Ln} y^+ + B$$

where :

$$u^+ = \frac{\bar{u}}{u_\tau} \quad ; \quad y^+ = \frac{y\, u_\tau}{\nu_w} \quad ; \quad u_\tau = \left(\frac{\tau_w}{\rho_w} \right)^{\frac{1}{2}} \quad \text{and} \quad A = \frac{1}{K}$$

K being the Von-Karman constant (found experimentally to be about 0.41), and B a constant of value 5.0-5.2 for a smooth surface.

Modifications to the law of the wall for surface roughness (Hama, 1954) and wall injection (Stevenson, 1963) are available.

The successful application of the law of the wall velocity profile for incompressible flows has naturally led to numerous attempts to apply similar concepts to compressible flows. (Sun & Childs, 1973), instead of assuming the shear stress constant, used the following relation :

$$\frac{\tau}{\tau_w} = 1 - \left(\frac{y}{\delta} \right)^b \quad .$$

The relation with b=1 was found to be a reasonable fit to experimental data for both subsonic and supersonic flows.

2.5. Nonaxisymmetric nozzle concept for advanced fighter aircraft

Because of the high internal performance attainable with axisymmetric nozzles, these have been used in past and current aircraft designs. During the 60's and early 70's the main concern, in the design of jet engine exhaust nozzles, was to reach configurations where the installed system did not cause excessive drag or thrust loss. Research and development programs have investigated various design variables including nozzle type, tail location and nozzle spacing. This has resulted in some interesting configurations using axisymmetric nozzle installations that are very efficient, with low drag and thrust penalties (F16 & F18). Other configurations, however, did not fare as well (i.e. the F-111 afterbody/nozzle was designed for optimum thrust but not necessarily for minimum drag. Tests attributed as much as 30 to 60% of the total aircraft drag to the afterbody/nozzle installation (Bergman et al, 1977)).

Among the more promising design techniques proposed to minimize the drag were concepts incorporating two-dimensional (2-D) nozzles into aircraft. Such nozzles integrate well with tapering, nearly rectangular afterbody fuselage contours, thereby improving thrust-minus-drag performance. Thrust vectoring and reversing, shown to be better suited for incorporation into 2-D nozzles, would further improve the aircraft manoeuvrability and reduce take-off and landing distances.

All these improvements are reflected in the design targets needed in future aircraft (Petty et Al, 1986). (Gal-Or, 1984) presented an excellent review of the available literature showing the advantages of the 2-D vectoring/reversing nozzles over current production configurations.

In a series of wind-tunnel tests, (Maiden & Petit, 1976) investigated 2-D wedge nozzle performance characteristics including cruise performance, aircraft manoeuvring and application for STOL. The investigation was conducted on an isolated nacelle integrated, in a first phase with a single 2-D nozzle and, in a second phase with twin 2-D nozzle.

The thrust-minus-afterbody drag performance of the twin 2-D nozzle integration was found to be significantly higher, for speeds greater than Mach 0.8, than the performance achieved with twin axisymmetric nozzle installations.

Figure 2.9 presents a comparison between twin axisymmetric and twin 2-D nozzles at Mach 1.20. These data show that the dry power 2-D nozzle performance is clearly superior to the axisymmetric one. This is very interesting because future aircaft design stresses supersonic persistence and, in this case, 2-D wedge nozzles seem to be an attractive installation.

For afterburner power, the nonaxisymmetric nozzles again exhibits high performance compared to axisymmetric convergent-divergent with similar expansion area ratio.

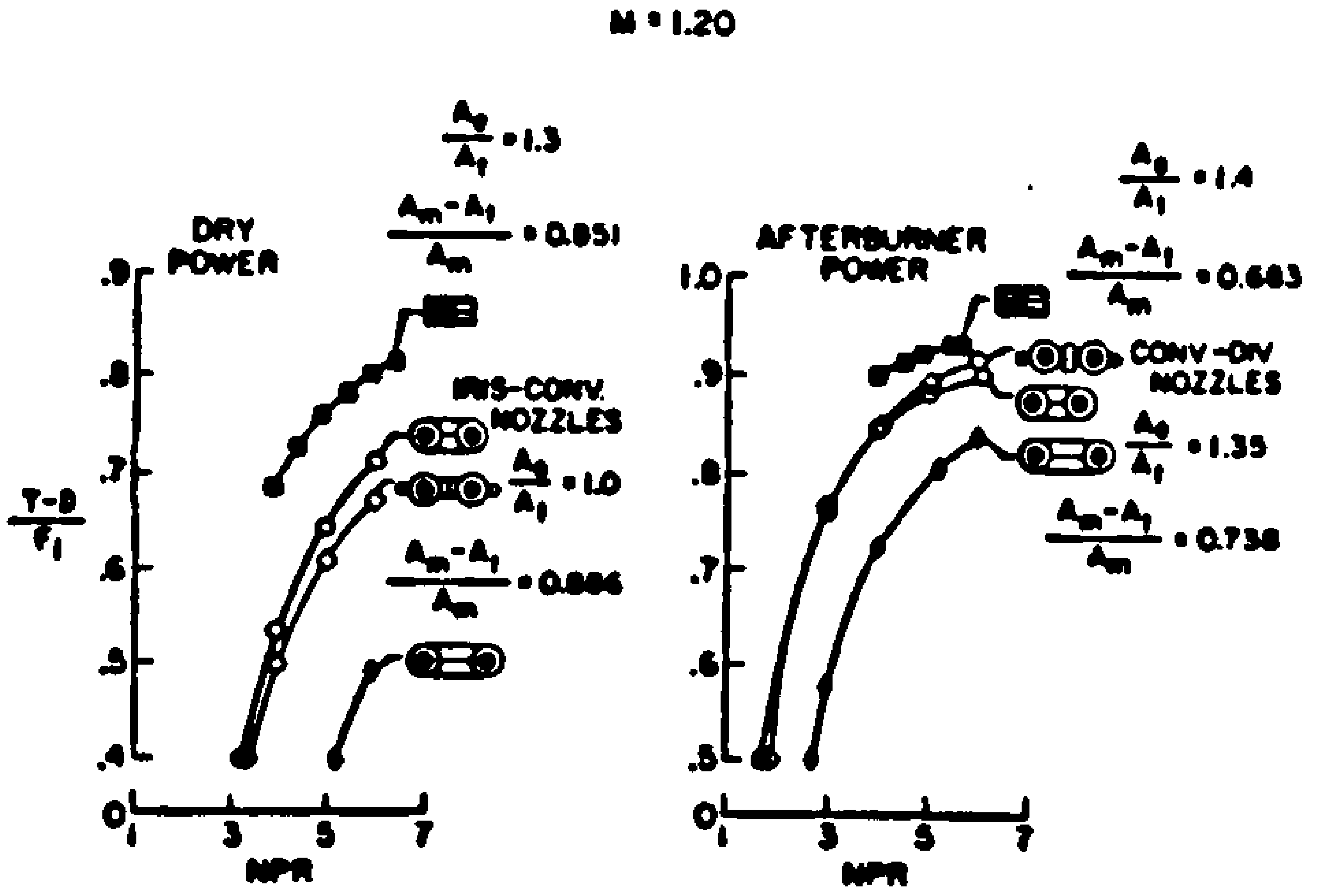

Fig. 2.9: Comparison of single and twin two-dimensional wedge nozzle performance.

But, when choosing a nozzle, aerodynamic considerations alone cannot be the final determinant in the selection. Considerations have to be turned towards total weight, cooling requirements and internal performance. The degree of thrust vectoring and reversing will also drive nozzle selection.

In 1981, trade-off studies were performed (Glidewell & Warburton, 1981) in order to determine the effects of the above factors. Nonaxisymmetric as well as axisymmetric nozzles were used. Comparisons were performed between three groups of configurations. 'Group 1' provided a comparison between axisymmetric and nonaxisymmetric nozzles with jet area and exit area controls only, whereas 'group 2' compares the same configurations with the added functions of thrust reversing. Finally 'group 3' compares the two types of nozzles with jet area control, exit area control, thrust vectoring and thrust reversing.

When considering nozzle weight, it has been found that the axisymmetric nozzle with jet area and exit area controls had a 10% advantage over the same nonaxisymmetric configuration. When thrust reversing is added to each of the nozzle concepts, the nonaxisymmetric one then showed a 9% advantage over the axisymmetric.

Flat surfaces resist internal performance loads in bending, which require a box structure with considerable depth. Round structures resist them in tension and, then, require only a thin skin. This seems to be the reason for finding the first nonaxisymmetric configuration heavier than the same axisymmetric one. When thrust reversing was added things changed, due probably to the better suitability of 2-D nozzles for reverser installation.

An overall advantage of nonaxisymmetric configurations was found when cooling requirements were involved. The nonaxisymmetric with area control required 28% less cooling than its axisymmetric counterpart. The same trend was found to be true when thrust reversing is added and the difference became 22%. Results also showed that no substantial additional cooling was required when thrust vectoring is added. This clear advantage may be found in the 'squared shape' of the 2-D wedge nozzle which lend itself better to more efficient cooling techniques.

The same main results were achieved during a program, completed in 1978 by McDonnell Aircraft Company (McDonnell Airc. Co.,1978). In this investigation, static as well as wind tunnel tests were conducted in order to determine the internal and installed performance characteristics of five selected nonaxisymmetric nozzles versus an axisymmetric baseline nozzle. The program, outlined in Figure 2.10, comprised three phases involving nozzles of three generic classes :

1) Internal expansion Con-di, 2) external expansion single ramp and 3)external expansion double ramp (or plug).

All the five nonaxisymmetric configurations, some with vectoring and some with both vectoring and reversing capabilities when full scale weights were estimated, were from about 60 to 900 lbs heavier than the nominal axisymmetric Con-di.

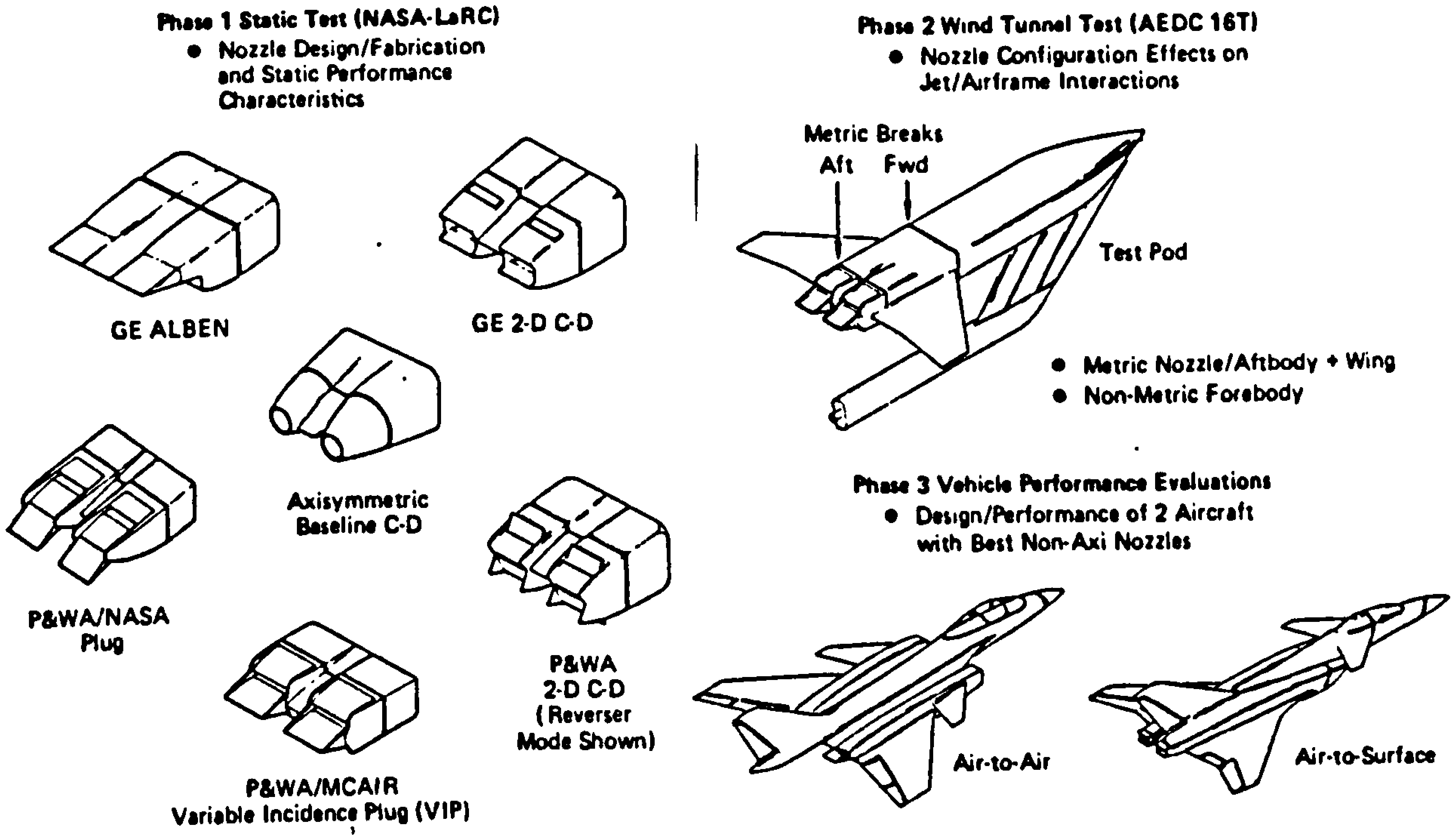

Fig. 2.10: Program elements. (Laughrey, 1979)

When cooling is considered, flat sidewall and flap systems of the 2-D design made it possible to use more efficient cooling and sealing systems.

Static tests were performed on all the full-scale nozzle concepts. The highest static internal performance was demonstrated for the nonaxisymmetric Con-di nozzle types which exhibited gross thrust coefficient values that were within 1% of the baseline axisymmetric nozzle.

Vectoring was found to improve the untrimmed lift-to-drag ratio for all nonaxisymmetric nozzles at all positive thrust vector angles.

Based on the concept of nonaxisymmetric nozzles of fixed external contours, wedge closure and a uniquely variable centrebody wedge, a 2-D Airframe Integrated Nozzle (2D-AIN), designed by Boeing (Figure 2.11) was put to transonic wind tunnel testing during the year 1974 (Goetz et al, 1976).

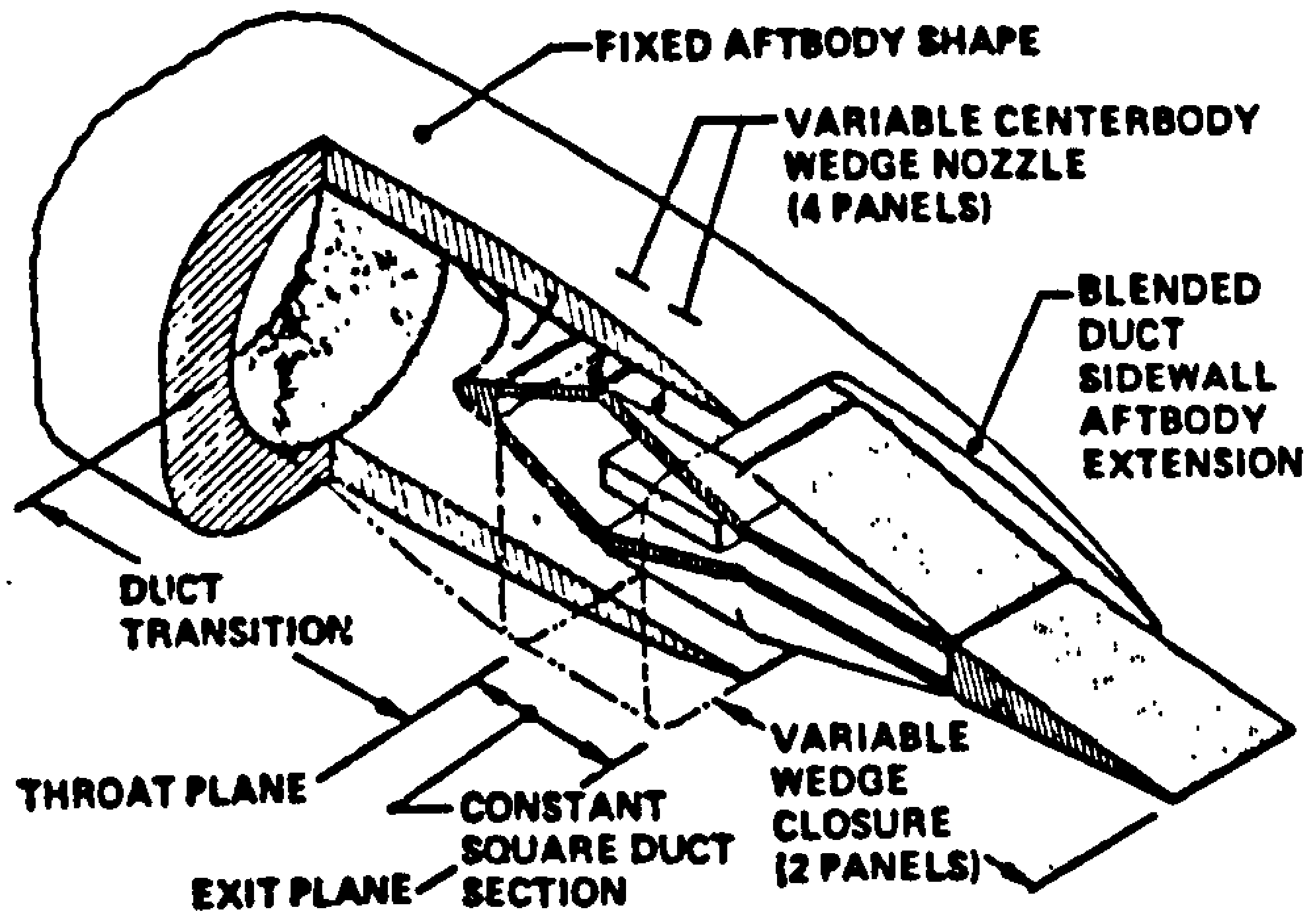

Fig. 2.11: Two-dimensional airframe integrated nozzle.

The tests demonstrated the 2D-AIN to have high levels of performance and the design approach showed a well suitability for closely spaced, twin engine installations. Figure 2.12 shows the extent of the afterbody structural arrangements for an example F-111 aircraft.

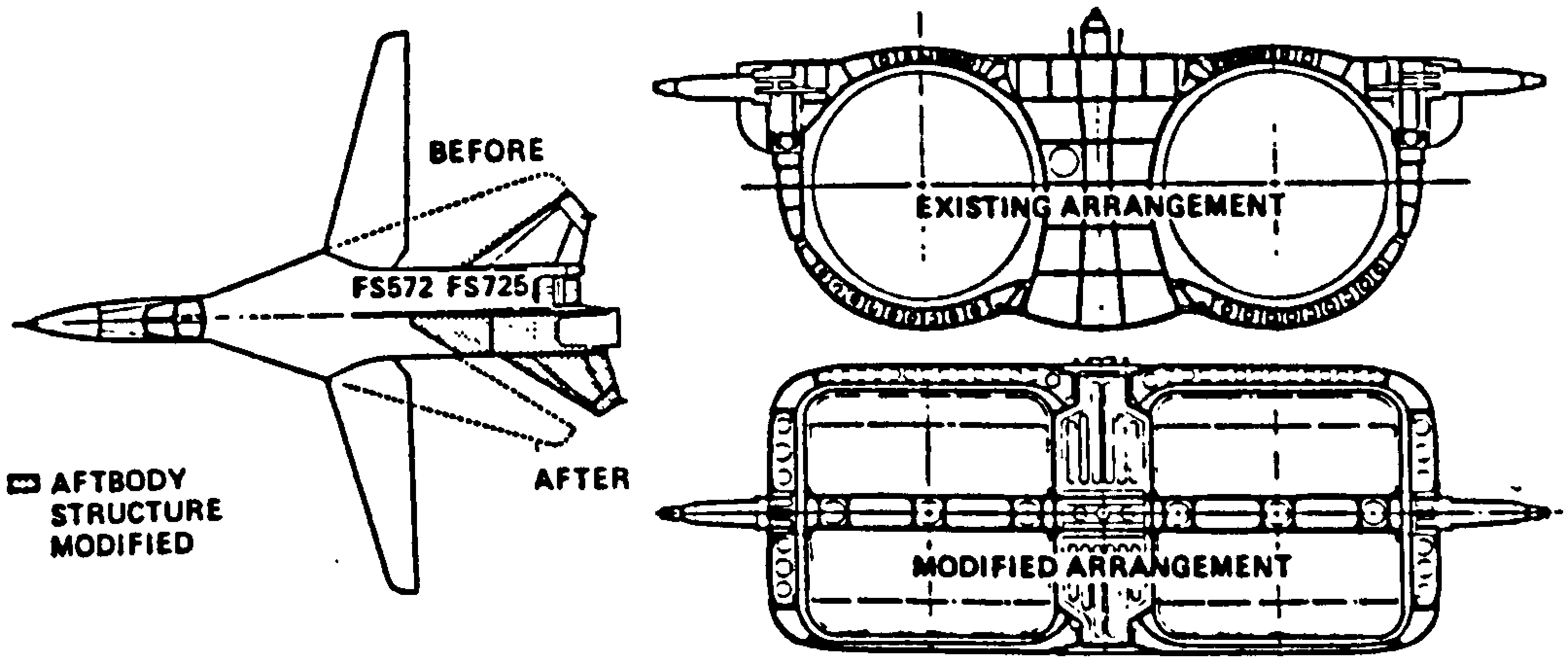

Fig. 2.12: F-111 afterbody modification and tail support structural comparison.

The F-111 has been selected for testing because of its characteristics such as fuel-to-weight fraction, wide Mach/altitude range and variable wing sweep capability which allow a multitude of aircraft types and configurations to be simulated.

Performance estimates showed a 0.8% to 11.7% (of ideal gross thrust) increase in installed performance when the 2D-AIN nozzles were installed, compared to the existing F-111 previous installation. When applying the estimated operating weight and drag changes related to the 2D-AIN airplane modification study, this resulted in a net improvement of 20 nautical miles to the total subsonic mission radius.

In 1984, the USAF has presented US engine makers with design targets of a new engine that would propel the new Advanced Tactical Fighter (ATF) required for the mid-1990s. The above estimates, test results and comparisons performed along the last 10 years have shown the advantages of the 2-D nozzles over their current production axisymmetric counterparts. The new engine will include a 2-D, converging-diverging, vectoring/reversing nozzle which will be fully integrated with aircraft flight controls.

In order to assess the performance of the method investigated in this thesis, a 2-D wedge Con-di nozzle will also be designed from a full-scale axisymmetric nozzle.

2.6 Measurement methods in compressible flows

2.6.1 General

In this section, we shall discuss briefly some of the methods used for measuring the properties of a compressible flow. Important variables that require measurement are pressure, temperature, velocity, flow direction and density.

We shall restrict ourselves to pressure measurement techniques, since it was the principal property which needed measurement in the tests performed in the present study.

2.6.2 Pressure measurement

Static pressure is the pressure indicated by a measuring device moving at the flow velocity or, in other words, by a device that introduces no disturbance or velocity change to the flow.

Along a wall, the usual method used for measuring a static pressure is to drill a small hole normal to the surface of the wall and connect it to a manometer, pressure gauge or any other similar device. The holes must be small with respect to the boundary layer thickness and must be free from roughness or burrs that might disturb the flow. Since there is no pressure change through the boundary layer in a direction normal to the wall, the pressure indicated is a true measure of the free-stream static pressure (Figure 2.13).

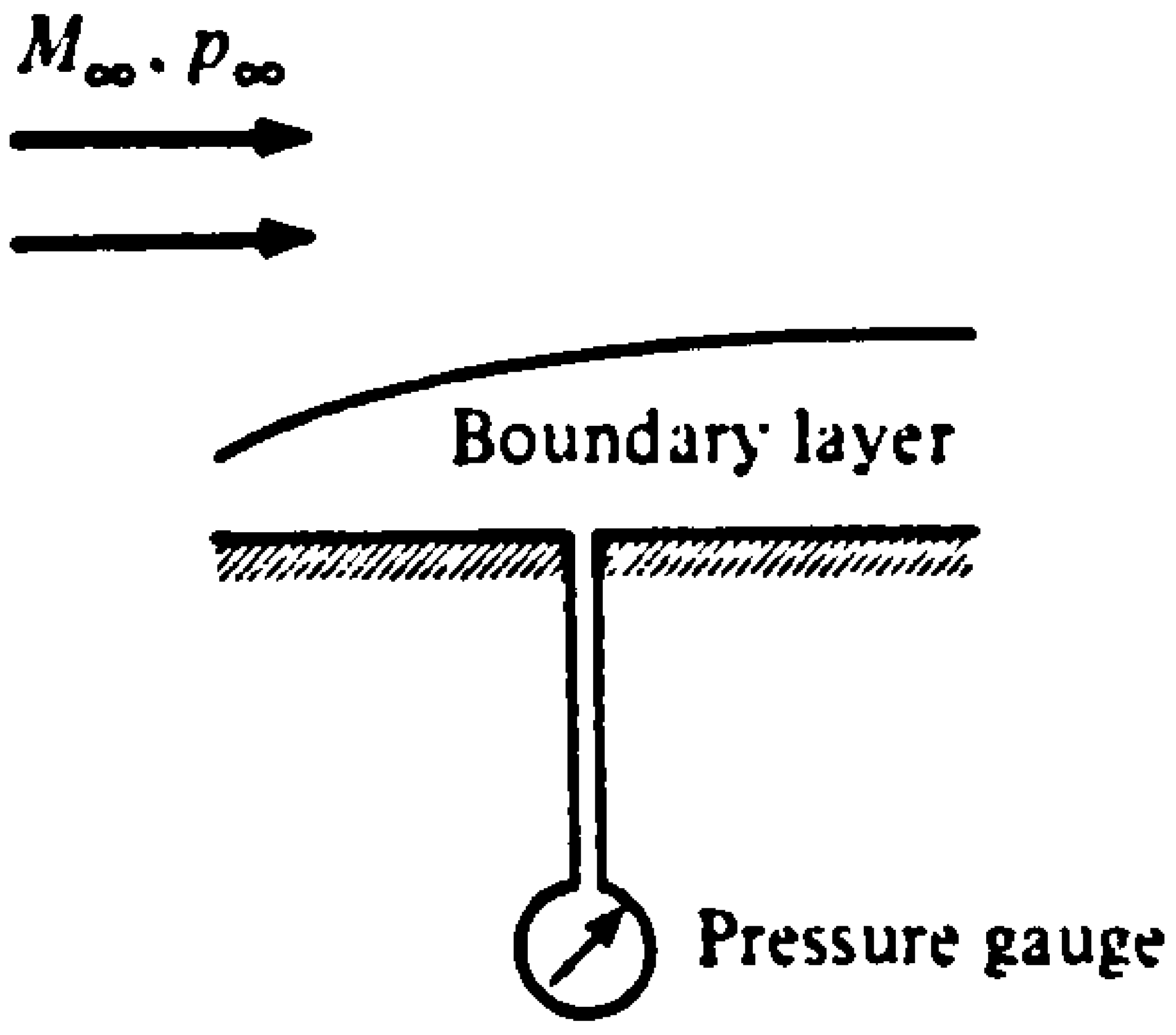

Fig. 2.13: Static pressure measurement along wall

In the interior of a flow, static pressure can be measured in a similar fashion by introducing a probe, which in a sense, creates a wall in the flow. A typical static pressure probe is shown in Figure 2.14.a.

The probe, generally, has a sharp, conical nose with the pressure tap located far enough downstream to be out of the influence of the disturbance introduced by the nose.

For supersonic flow, there will be an attached shock at the nose. There will also be an expansion where the nose joins the cylindrical section. So, the pressure measurement at the tap'P' of Figure 2.14.b, at least for a weak attached shock, will be very close to the free-stream static pressure.

The probe is very sensitive to flow alignment. This sensitivity can be reduced by drilling several holes around the circumference of the probe at the tap. Considerable care must be exercised in the interpretation of the results of static pressure probe measurements in a supersonic flow field in which a shock is present (cf. section 6).

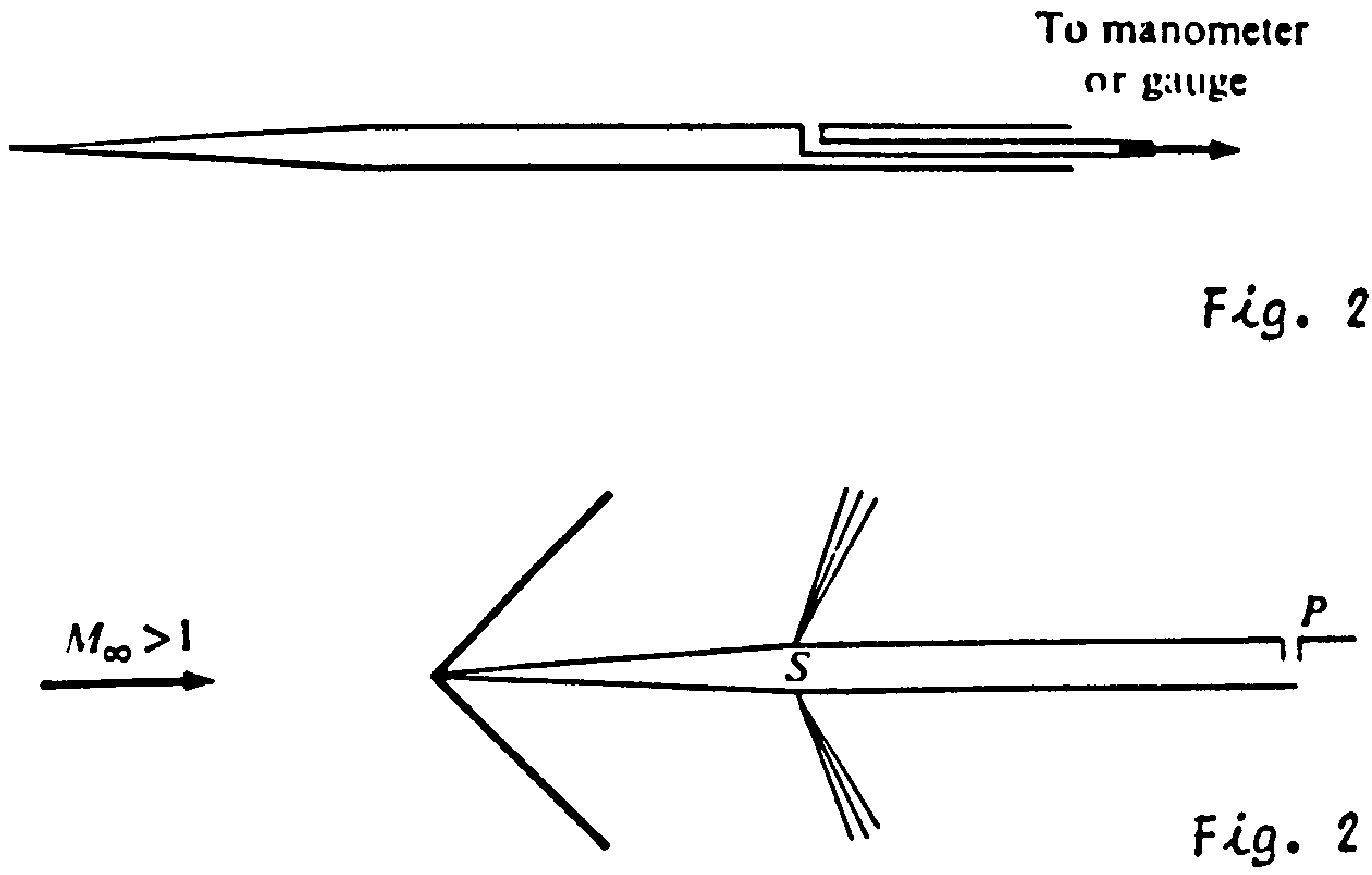

Fig. 2.14.a

Fig. 2.14.b

Fig. 2.14: Typical static pressure probe.

The stagnation pressure is the pressure measured by an instrument that brings the flow isentropically to rest. Such a device is a simple pitot tube (Figure 2.15.a)

In supersonic flow, since the probe is essentially a blunt-nosed body, there will be a detached normal shock in front of the probe (Figure 2.15.b).

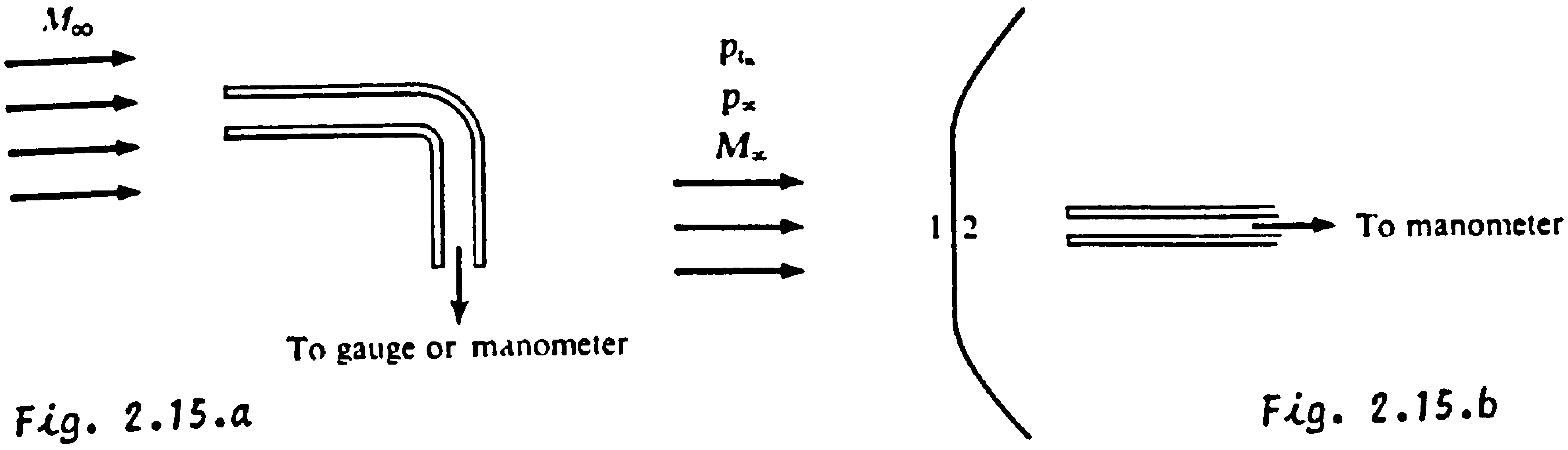

Fig. 2.15.a

Fig. 2.15.b

Fig. 2.15: Typical total pressure probe.

In this case, the stagnation pressure indicated on the manometer or gauge will be the stagnation pressure after a shock that is normal to the flow direction. However, in subsonic flow the stagnation pressure measured by the pitot tube is the true stagnation pressure (c.f. JOHN, 1984).

SECTION 3 : Inviscid flow computation using the method of characteristics.

3.1 General

The application of the method of characteristics to two-dimensional, steady, irrotational supersonic flow is described in detail in Appendix A. Although this method can describe a flowfield within a nozzle of any shape, the one implemented into the computer program in this study was bell-shaped.

As illustrated in Figure 3.1, the nozzle has a throat comprising of two circular arcs of different radii of curvature. The one downstream of the throat is joined tangentially, continuous in first derivative at the attachment point, to a simulated second order quadratic polynomial wall.

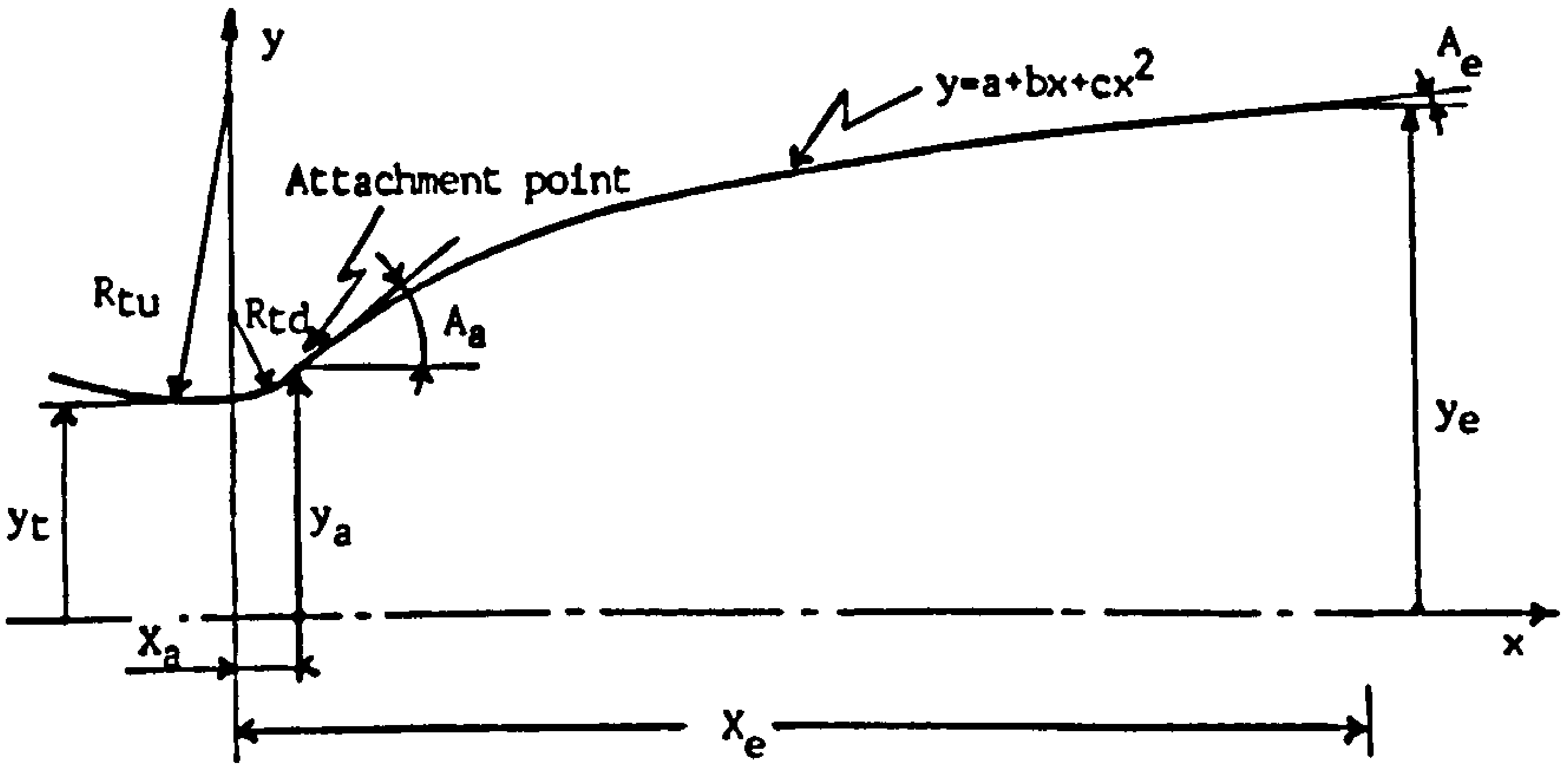

Fig. 3.1: Nozzle geometry implemented into the program.

3.2 Governing equations

Equations governing the flow described above are : the gas dynamic equation (Equation 3.1), the irrotationality condition (Equation

3.2) and the speed of sound relationship (Equation 3.3) :

$$(u^2-a^2) \frac{\partial u}{\partial x} + (v^2-a^2) \frac{\partial v}{\partial y} + 2\, uv \frac{\partial u}{\partial y} - \delta \frac{a^2 v}{y} = 0 \qquad \dots (3.1)$$

$$\frac{\partial u}{\partial y} - \frac{\partial v}{\partial x} = 0 \qquad \dots (3.2)$$

$$a = a (u,v) \qquad \dots (3.3)$$

where, in equation 3.1 :

$\delta = 0$ for planar flow,
$\delta = 1$ for axisymmetric flow.

Equation 3.1 is derived from the continuity, Navier-stokes equations and isentropic relationships, assuming the flow to be steady, two-dimensional and free from the action of any external work or body forces.

Equation 3.3 is obtained from the general thermodynamic properties of an homoenergetic flow. It may be algebraic (for a perfect gas), or in tabular form (for the case of an equilibrium gas mixture having variable specific heats, for example).

The above system comprises a set of two coupled partial differential equations involving the velocity components u and v. This system may be replaced by an equivalent one of two total differential equations, details of which are given in Appendix A.

3.3 Program description

The computer program consists of a core program (MAIN) and eight subroutines. 'MAIN' contains the overall logic for the nozzle flowfield analysis. It starts by reading the needed data which may be divided into three categories: 1) thermodynamic inputs, 2) geometrical inputs and 3) control inputs. The thermodynamic inputs include the data describing the state of the flow at the throat (e.g. the stagnation pressure and temperature). The geometrical data are the parameters describing the nozzle shape and boundaries (e.g. the throat radius, the upstream and downstream radii of curvature, the attachment and exit angles). The last category represent the choices open to the user (e.g. the number of stations along the initial-value line, the order of accuracy needed to stop the iterations of the corrector algorithm). A summary of the input data for the two axisymmetric configurations from which the elliptic and two-dimensional wedge nozzle designs were developed subsequently is given in chapter 3.4.4.

The output of 'MAIN' are the different thermodynamic and flow properties calculated at each station within the network described below (velocity, Mach number, pressure, temperature, density and flow direction).

3.3.1 Definition of the initial-value line

In order to start the computations of the flowfield by the method of characteristics, a starting line must be established that is everywhere supersonic. Along that line, the different stations at which the transonic flow would be computed are defined.

The transonic flow region in Con-di nozzles under chocked flow conditions has been widely studied. Different investigators, e.g. (Sauer, 1947), (Hall, 1962) and (Kliegel & Levine, 1969), have employed various expansion techniques ranging from double power series expansion to small parameter expansions about the sonic conditions. All of these methods are essentially the same, being perturbations about the one-dimensional flow solution.

Of the several methods that have been proposed for analyzing the flowfield in the throat region of a Con-di nozzle, that due to Sauer is the simplest and is used in the present study. Although it is not the most accurate of the methods mentionned above, it does have the desirable feature of being a closed form solution for the transonic flowfield (chapter 3.4.2.3).

Initial-value line computations have been incorporated into a single subroutine 'STARLINE', making easy any change or replacement of the method used, if needed.

3.3.2 Flowfield from the initial-value line

Having defined the geometrical inputs, the parameters defining the nozzle wall contour (attachment point coordinates, coefficients of the polynomial defining the wall) are determined by calling subroutine 'WALCON' summarized in Appendix C.

Using the finite-difference scheme (modified Euler, Appendix B), the network from the intial line is generated by 'MAIN'. It includes interior and axial stations defined in subroutines 'INTPOINT' and 'AXIPOINT' (appendix A).

Figure 3.2 presents the network of characteristics developed from the starting line of the axisymmetric nozzle from which the elliptic nozzle was developed subsequently.

3.3.3 Flowfield from the circular arc throat contour

In the throat region where the flow property gradients may be large, the spacing between successive intersections of the left-running characteristics and the wall (from which the stations defining the right-running characteristics are issue using the direct solution method presented in appendix A) may be too large for the desired accuracy. Therefore, the inverse method (also presented in appendix A) which enables the prescription of the number of these stations is used.

Once the solution is obtained, a right-running characteristic is originated from the wall, continuing until it intersects the centreline. For these computations, 'MAIN' calls subroutines 'INVPOINT', 'INTPOINT' and 'AXIPOINT'.

Figure 3.3 illustrates the network developed by the prespecified points at intervals of 0.18 mm along the contour.

3.3.4 Flowfield from the quadratic wall

Once the calculations along the characteristic issuing from the

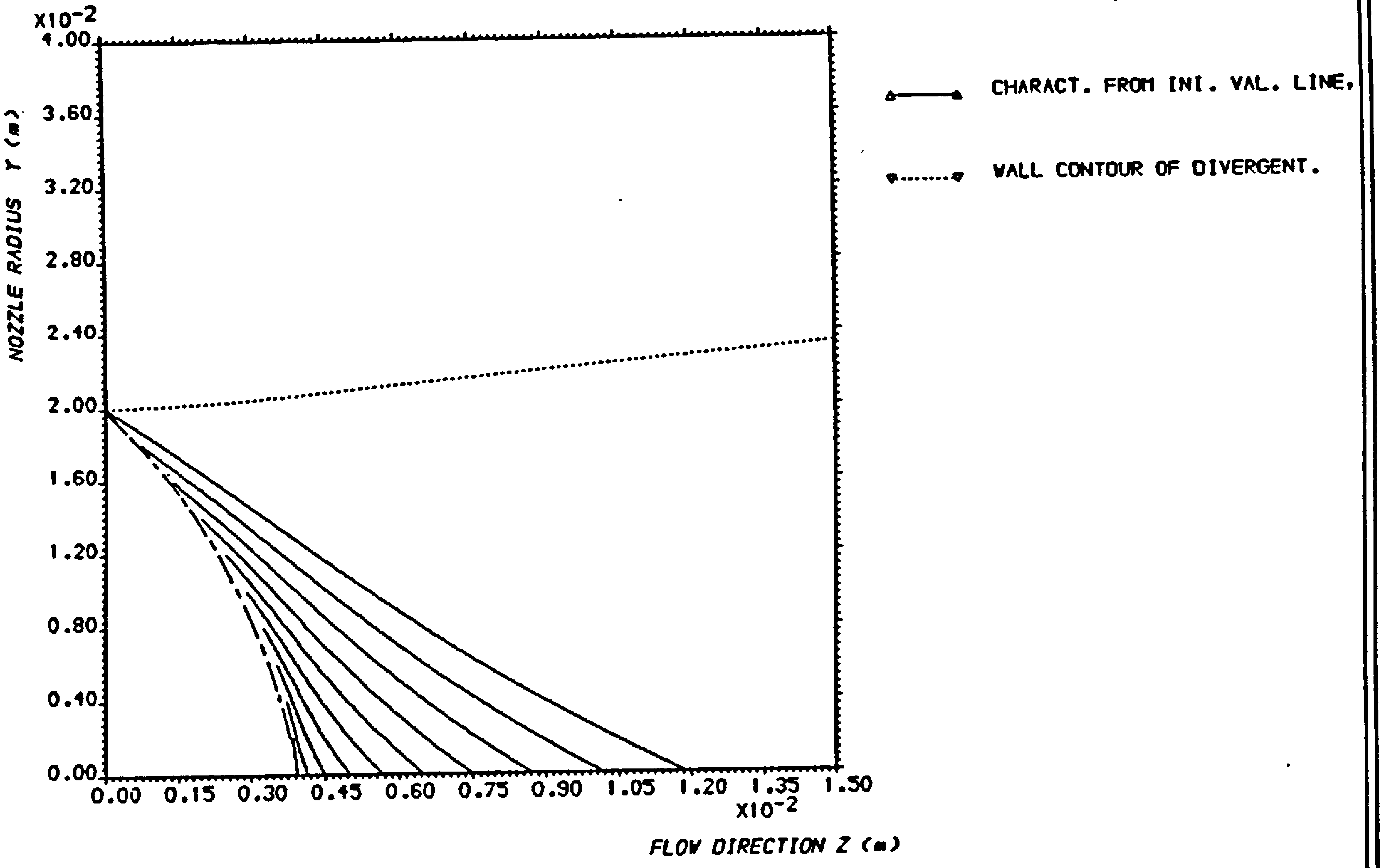

FIG : [3.2] NETWORK OF CHARACTERISTICS FROM THE INITIAL-VALUE LINE OF THE NOZZLE SUPERSONIC SECTION.

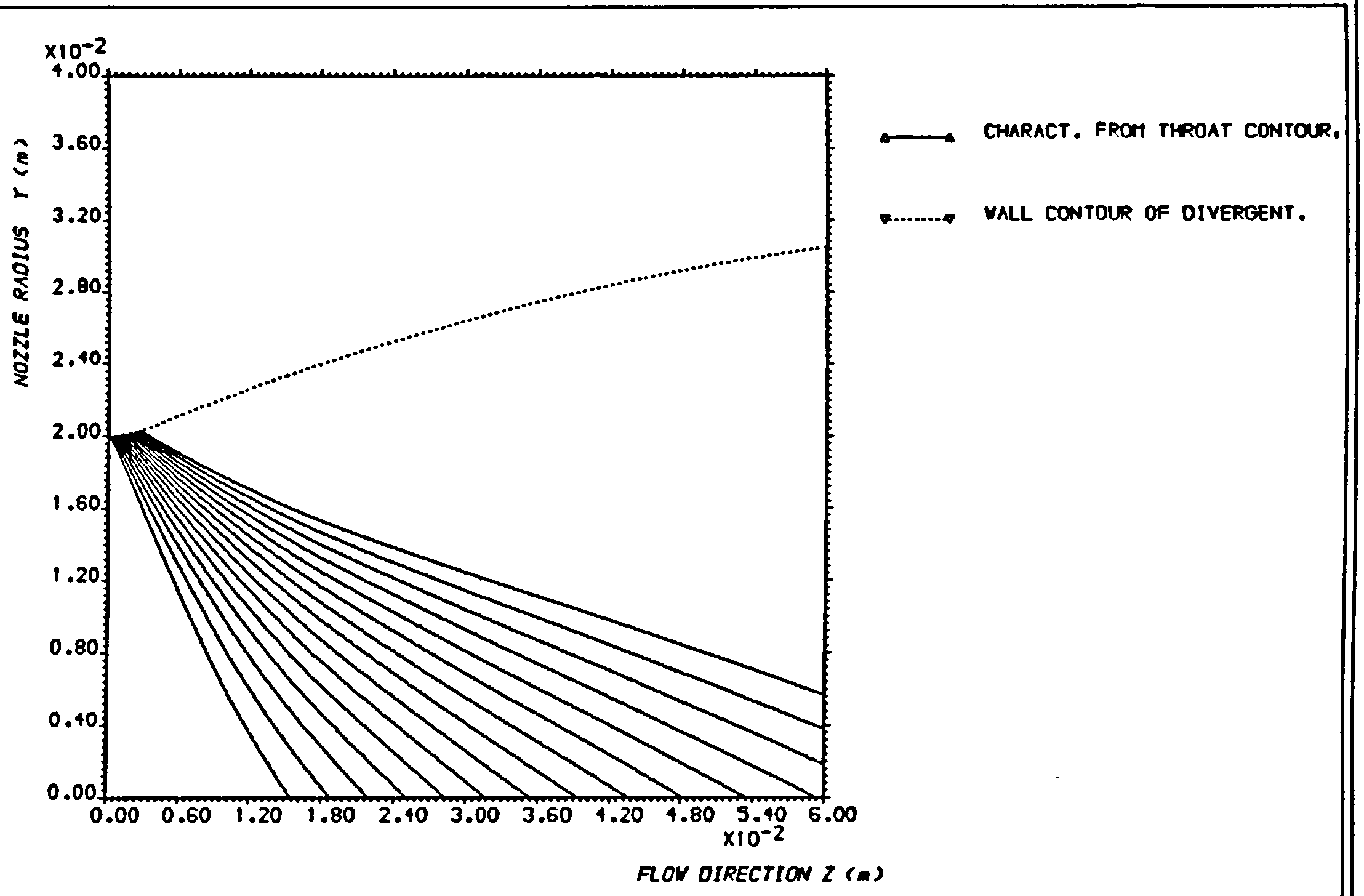

FIG : [3.3] NETWORK OF CHARACTERISTICS FROM THE CIRCULAR-ARC THROAT CONTOUR OF THE NOZZLE SUPERSONIC SECTION.

last prespecified point have been performed, the direct marching method may be applied along the wall. The procedure is the same as for the circular arc throat contour. The subroutines called are 'DIRPOINT', 'INTPOINT' and 'AXIPOINT'.

Figure 3.4 shows the network of characteristics issuing from the wall of the axisymmetric nozzle whose governing parameters are set out in chapter 3.4.4. At the start of the network, there is an overlapping of crossing characteristics. These coalescing characteristics are compression waves which may have been generated by either the concave surface turning or the discontinuity in the derivatives of the wall contour at discrete points. The attachment point, from which the first right-running characteristic is issued is such a point. at that position, the wall contour and the wall slope are both continuous but the wall curvature (i.e the rate of change of the wall slope) is discontinuous. That discontinuity created the weak compression waves observed in figure 3.4 which have been ignored in the flowfield computation, since they yield an almost isentropic compression.

The extent of the flowfield is determined by the nozzle exit lip point which is calculated by the inverse wall point procedure. Figure 3.5 shows the complete set of characteristics originating from the computations and Figure 3.6 the flow-chart of 'MAIN'.

3.4 Axisymmetric nozzle design

3.4.1 General

We are concerned here with the design of the supersonic section of two axisymmetric convergent-divergent nozzles. The first one is computed in detail in order to be transformed into a three-dimensional nozzle of elliptical cross-section using the streamline tracing technique described in section 5. In order that the nozzle so designed could be manufactured and submitted to experimental test, the model must evidently fit the available testing facilities. Nozzle flow analysis, using the computer program described previously, required the definition of certain initial parameters. The following sections will briefly discuss these parameters and how they have been

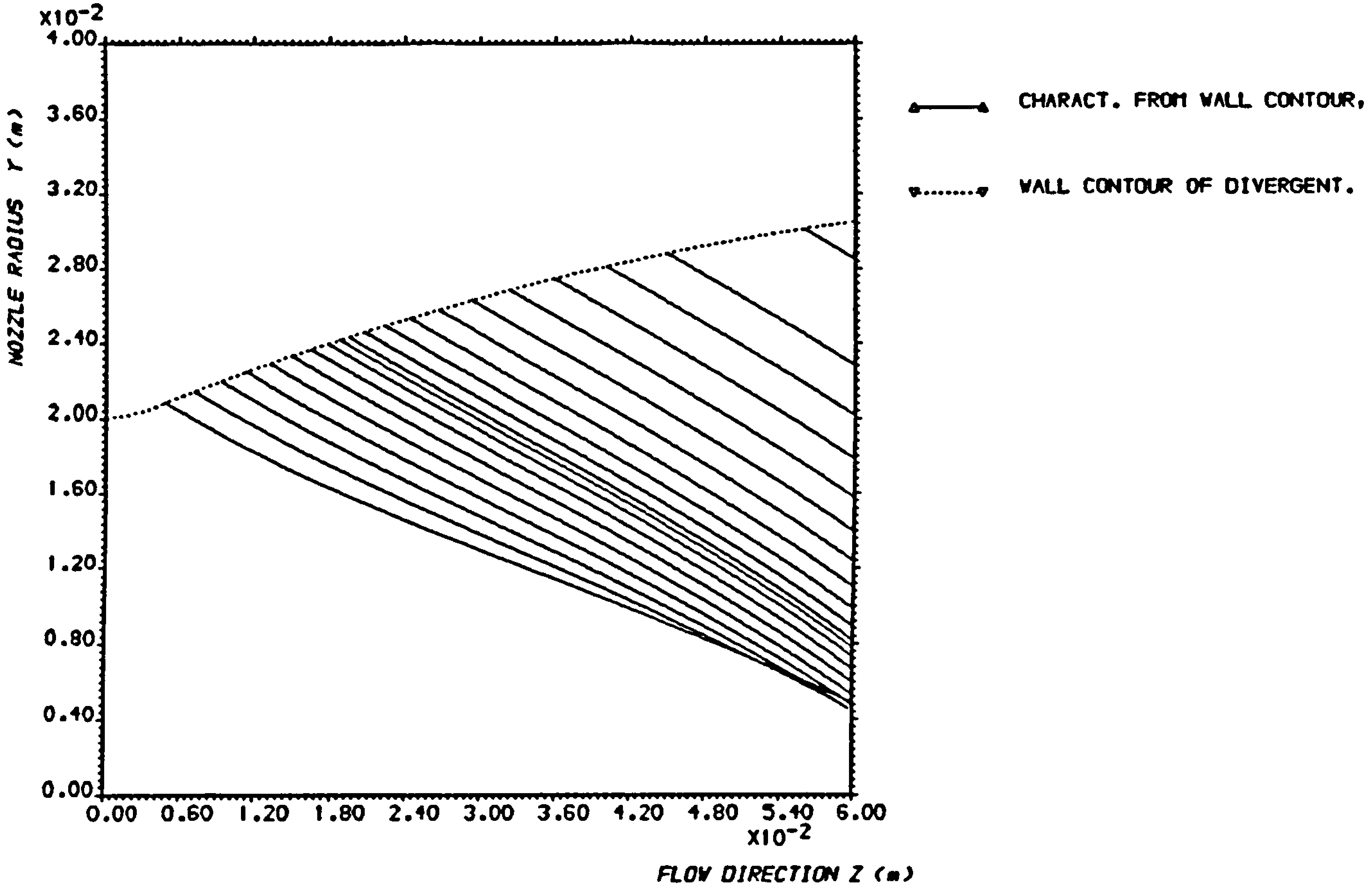

FIG : [3.4] NETWORK OF CHARACTERISTICS FROM THE SECOND-ORDER QUADRATIC WALL OF THE NOZZLE SUPERSONIC SECTION.

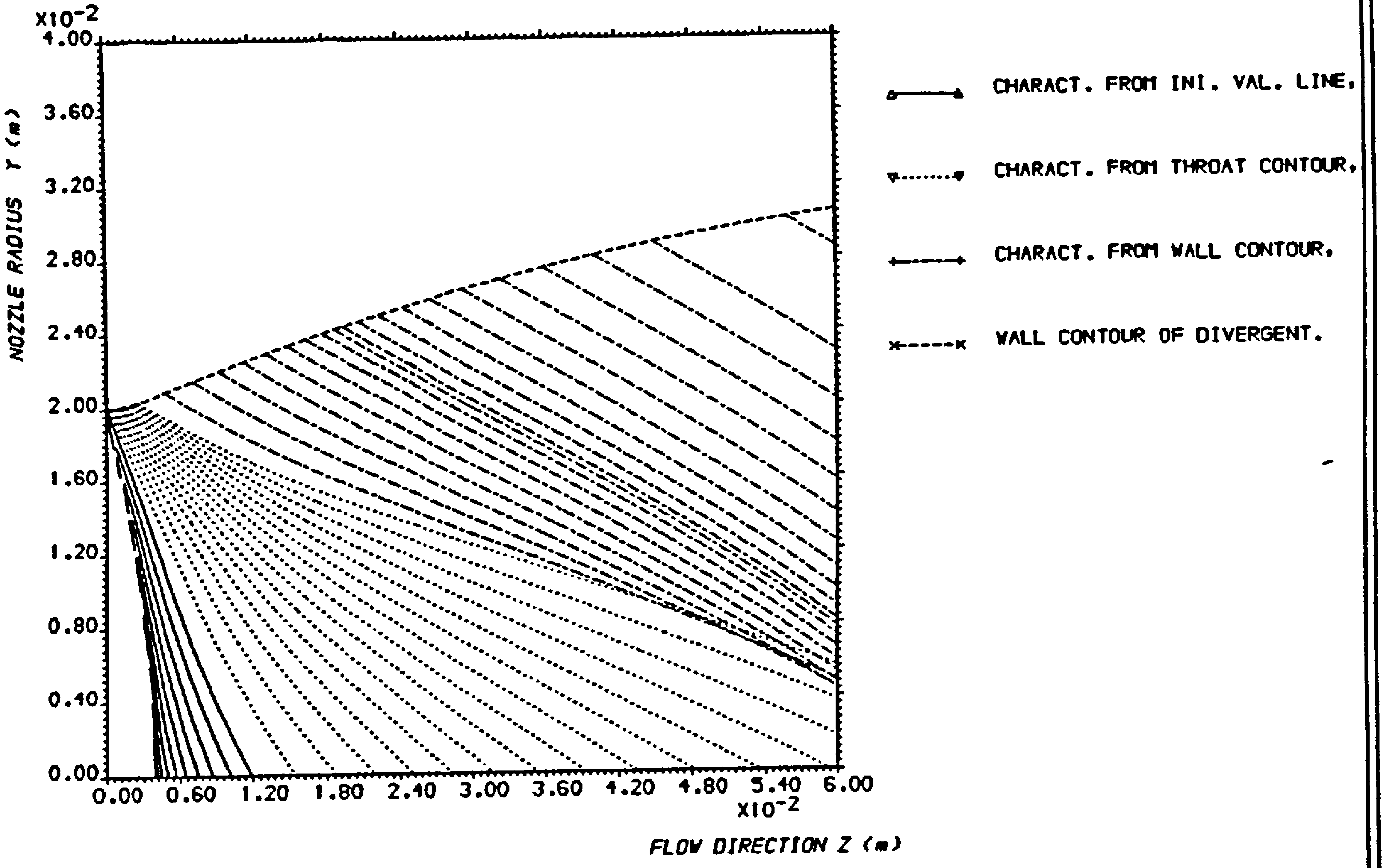

FIG : [3.5] COMPLETE NETWORK OF CHARACTERISTICS WITHIN NOZZLE SUPERSONIC SECTION.

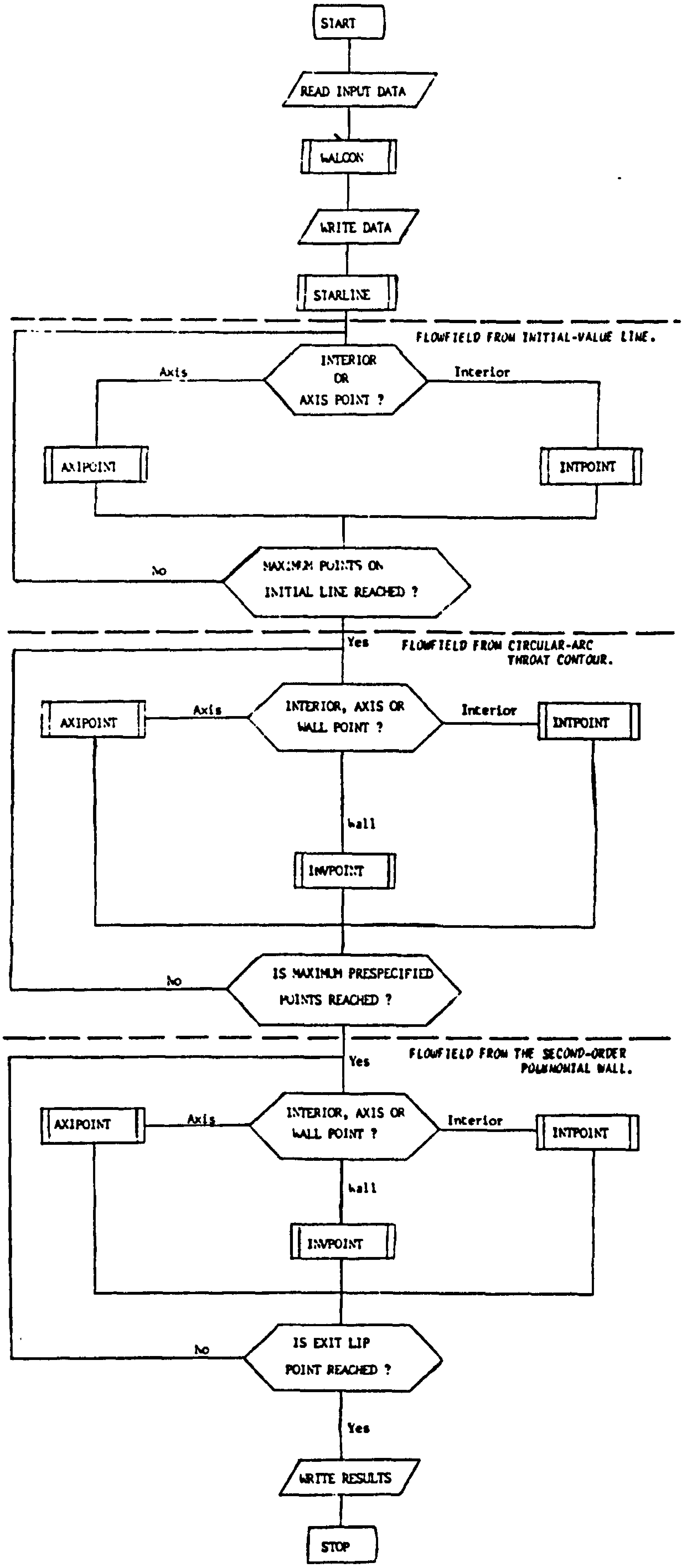

Fig. 3.6: Flow-chart of the main program.

determined.

Investigations carried out for the last ten years, involving the integration of the propulsion system with the airframe in a fighter aircraft (see chapter 2.5), have shown it is possible to improve fighter performance by incorporating non-axisymmetric nozzles. Because of this particular application for which the two-dimensional wedge configuration was designed, a different approach had to be followed in the determination of the starting parameters, which permitted the computation of the axisymmetric nozzle to be transformed into a two-dimensional wedge nozzle subsequently.

3.4.2 Axisymmetric-for-elliptic nozzle design

Test facilities in the School of Mechanical Engineering can make available a pressure and mass flow of up to 16 Atm. and 5 Kg/s respectively. Design calculations were carried out subject to the overall constraints which these values imply. Selected values for the stagnation pressure and temperature were 15 atm. and 403 °K respectively.

3.4.2.1 Exit Mach number and area ratio

Assuming a complete expansion of the flow to ambient atmospheric pressure in an isentropic manner and aiming to achieve an exit Mach number of 2.4 (made possible by the chosen pressure ratio of 14.8), the area ratio may be determined from standard isentropic flow tables (i.e. NACA, 1953). It was found equal to 2.32.

3.4.2.2 Throat and exit radii

In order to achieve a supersonic flow in the divergent section of the nozzle, the throat Mach number must clearly equal unity. At this position, the following expression for the choked mass flow rate :

$$\dot{m} = \left[\frac{\gamma}{R} \left(\frac{2}{\gamma+1} \right)^{\frac{\gamma+1}{\gamma-1}} \right]^{\frac{1}{2}} \frac{P_t \, \pi \, y_{th}^2}{T_t^{\frac{1}{2}}}$$

can be evaluated and for specified mass flow (whose value is determined by the test facility screw compressors when the pressure to be delivered is specified), stagnation pressure and stagnation temperature, the throat radius can be calculated.

Knowing the area ratio with which complete expansion may be achieved, the exit radius is calculated accordingly.

3.4.2.3 Upstream and downstream radii of curvature

An important parameter which governs the isentropic flowfield in the transonic region of a Con-di nozzle is the ratio of the throat radius of curvature to the throat radius. Figure 3.7 presents the calculated values of the geometrical contraction factor (C_c) as a function of this parameter (R_{tu}/y_t). The value of C_c measures the reduction in mass flow due to two-dimensional flow effects in the throat region, where $\dot{m}$ denotes the calculated value of the mass flow crossing the nozzle throat section and $\dot{m}_{1-D}$ the mass flow rate that would cross that section if the flow were one-dimensional.

It is evident from figure 3.7 that Sauer's analysis for $R_{tu}/y_t = 2$ (which is the value chosen in our case) agrees well with the experimental results.

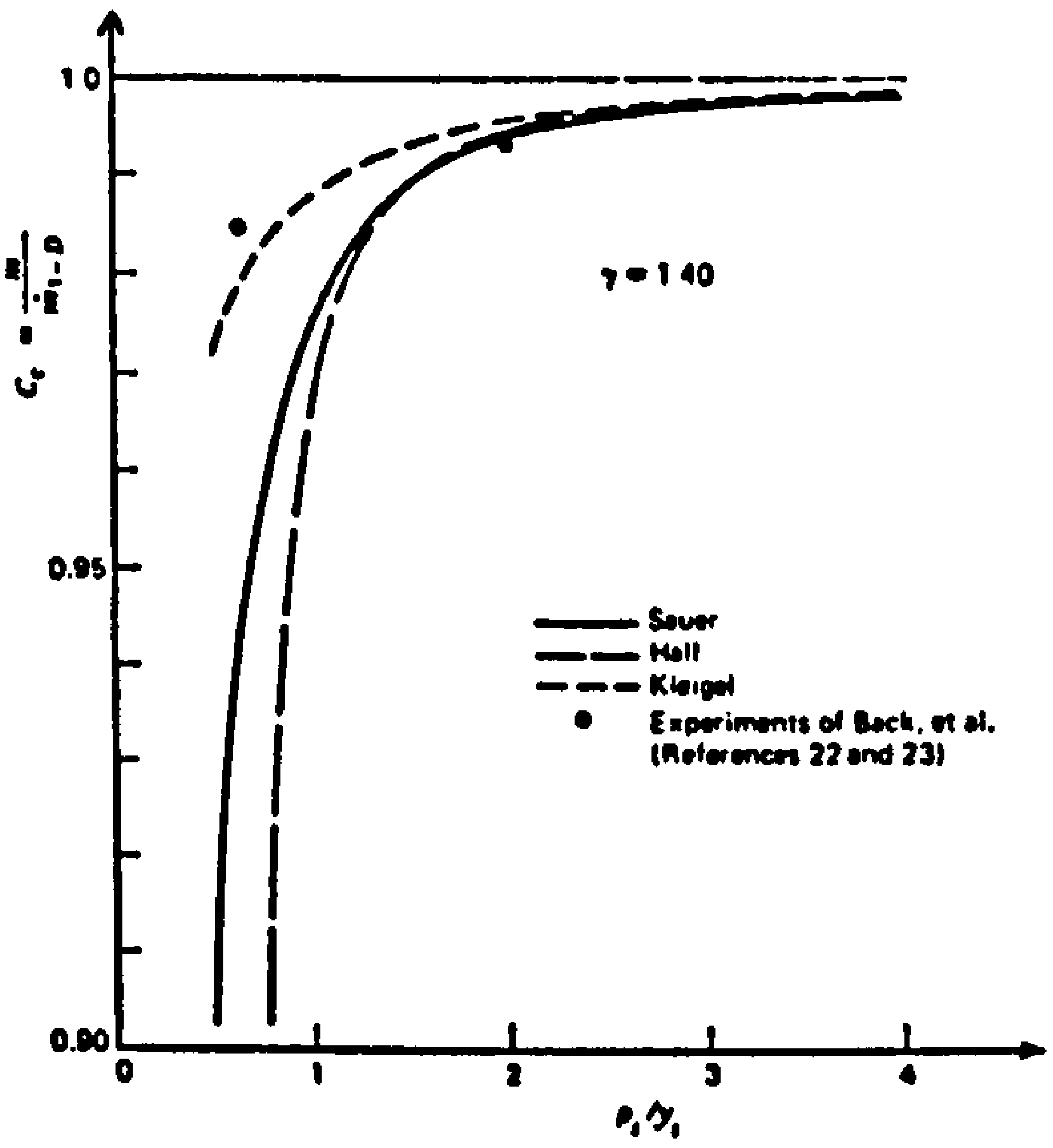

Fig. 3.7: Comparison of the different transonic flow prediction methods in terms of the throat concentration factor.

3.4.2.4 Maximum angle of divergence

The divergent part of a contoured nozzle may be divided into two sections. The first one permits a sharp expansion and is situated just after the throat. The second part, where the flow is still accelerating, tends to straighten the flow to achieve a near axial direction at the exit. The maximum angle of divergence is the contour angle at the attachment point, joining the downstream circular-arc contour to the quadratic wall. A high value for the contour angle increases the risks of flow separation from the walls. A small angle, however, may not permit the complete expansion of the gases within the desired length and would result in a longer nozzle and hence a weight penalty. The contour angle was chosen equal to 15°.

3.4.2.5 Flow uniformity and exit angle

For nozzles designed to supply wind tunnels, exit flow uniformity is of great importance and a primary design requirement. In our case, conditions are less demanding and exit flow uniformity though desirable is not a key factor. It is reasonable to assume that the circular-arc contours defining the throat will produce an acceptably uniform flow (Buseman, 1931). The bell-shaped wall downstream will further straighten the flow, resulting in satisfactory conditions at the exit. Furthermore, a low value of the exit angle would minimize the flow divergence and lead to a greater thrust. Subsequent measurement and detailed flow prediction confirm this to be achieved.

3.4.3 Axisymmetric-for-wedge nozzle design

The design of an aircraft (or certain of its components) is primarily based upon the flight conditions and types of mission it is required to perform. However, since the tendency is towards the design of 'multipurpose' aircraft which can fly at subsonic as well as supersonic speeds, an appropriate configuration seems to be the variable geometry Con-di nozzle (chapter 2.5).

In order to avoid the complexities involved in the design of such a nozzle, and since our objective is to check the capabilities of the simple method described earlier, emphasis has been placed on complete expansion bearing in mind that :

1. At sea level static conditions, maximum thrust is often used in take-off and complete expansion, therefore, needed,

2. Equally, efficient operation at low pressure levels associated with cruise, where an aircraft can spend a great deal of time and burn much of its fuel, also demands complete expansion.

A rather different concern which arises is whether the comparatively complicated Con-di nozzle is justified at all for use in such aircraft. Computer performance simulation, reported by Palmer (Palmer, 1985), was carried out for both convergent only and Con-di nozzles. The results supported the recommendation that a Con-di nozzle is only really justified for a nozzle pressure ratio (NPR) greater than 3. At higher NPRs, the utilization of a Con-di nozzle gave very large thrust increases (i.e. at maximum reheat, at 36,000 ft/1.6M for an NPR of 11, the increase in net thrust was approximatively 27%). At more modest levels of NPR, such as V/take-off, the NPR was 3 and the thrust increase only 1.8%.

Assuming an NPR of 11 at the altitude of 30,000 ft, the static and total pressures are calculated and found to be 0.297 and 3.267 atmospheres respectively. Knowledge of the ambient sea level pressure permits the determination of the NPR at this altitude (found equal to 3.22). Using the isentropic flow tables, the area ratio may be determined ($A_e/A^* = 1.12$).

Setting the mass flow which the engine would be required to deliver, assuming a sonic mach number at the throat and using the isentropic flow relationships, the different properties (temperature, pressure, density and velocity) may be calculated at the throat. Using the expressions for the mass flow and the area ratio, and assuming an attachment angle of 2° (in order to avoid any risk of separation), the radii of the circular shaped throat and exit areas are computed.

With these data in hand, nozzle flow computations were performed with a view to applying the technique to the design of a wedge nozzle appropriate to the aircraft propulsion application outlined. Not only did this introduce a quite different geometry but also further opportunities for detailed three-dimensional flowfield simulation. It was not however possible to submit the design to model test.

3.4.4 Summary properties of the input data used to perform the axisymmetric nozzle computation.

properties	axisymmetric-for-elliptic nozzle design	axisymmetric-for-2D wedge nozzle design
T_t	403 °K	1100 °K
P_t	$15\ 10^5\ N/m^2$	$3.26\ 10^5\ N/m^2$
P_a	$1.013\ 10^5\ N/m^2$	$1.013\ 10^5\ N/m^2$
y_t	0.020 m	0.325 m
R_{tu}	0.040 m	0.650 m
R_{td}	0.010 m	0.162 m
A_a	15°	2°
A_e	5°	2°
X_e	0.060 m	-
y_e	-	0.345 m

3.4.5 Axisymmetric results

Solutions for the two axisymmetric nozzles (for both elliptic and wedge designs) are represented in figures 3.8 and 3.9 respectively. Both the nozzle wall and centreline pressures are plotted in each case.

Due to the higher value of the attachment angle of the first configuration, a sharper expansion took place near the throat (along both the centreline and wall). Within the axisymmetric-for-wedge nozzle, the flow tends to expand gradually from the throat to the exit.

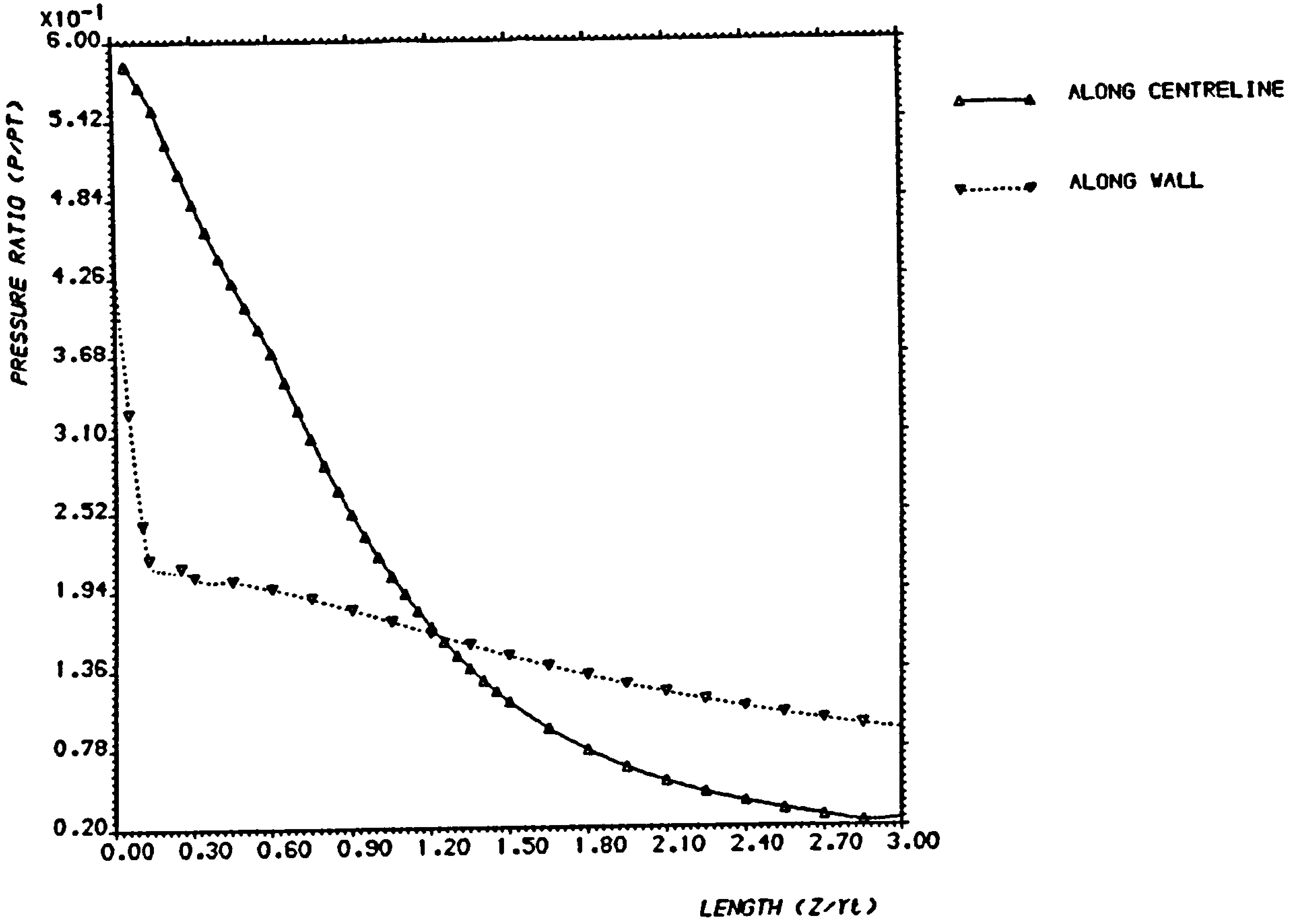

FIG : [3.8] STATIC PRESSURE PROFILE ALONG DIVERGENT SECTION OF AXISYMMETRIC-FOR-ELLIPTIC NOZZLE (AR = 2.32).

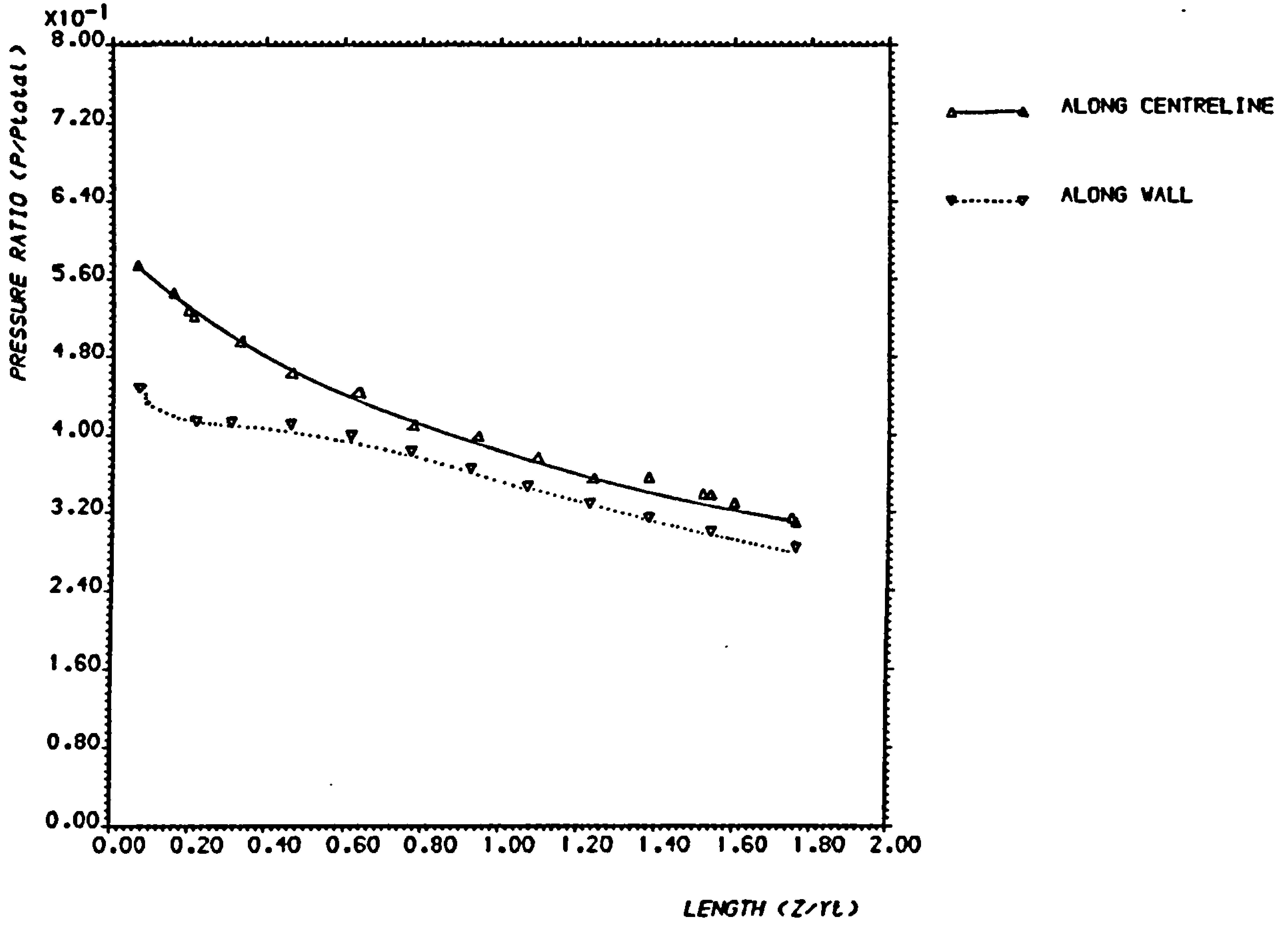

FIG : [3.9] STATIC PRESSURE DISTRIBUTION ALONG DIVERGENT SECTION OF AXISYMMETRIC-FOR-WEDGE NOZZLE (AR= 1.12).

SECTION 4 : Boundary layer computation

4.1 General

Current design and analysis requirements of the aerospace industry necessitate the development of accurate and efficient techniques for calculation of boundary layer development along physical walls. In rocket motor nozzles (with fixed initial and ambient conditions) for example, one is obviously interested in obtaining the maximum thrust in a given direction. The value of the thrust depends upon the viscous and heat conduction losses in the flowfield (generally assumed to be confined to a thin region near the wall: the boundary layer). Furthermore, non-symmetrical shapes give rise to significant transverse pressure gradients leading to the creation of cross flows around the contour.

There are two ways of taking into account the effects of viscous action and heat conduction, namely :

1. the effects of viscous action and heat conduction extend to the entire flowfield which is then governed by the complete Navier-Stokes equations for that nozzle configuration,
2. the effects of viscous action and heat conduction are confined to a narrow region at the nozzle wall. The flowfield is then governed by the boundary layer equations.

By following the second approach, the boundary layer may be considered in terms of integrated properties such as the displacement thickness. Calculated on the basis of a chosen reference velocity, the displacement thickness defines an effective surface outside which the flow is considered invicid. The edge of the displacement thickness is then utilized as a streamline separating the viscous and the invicid regions.

The displacement thickness, defined by :

$$\delta^* = \int_\infty^0 \left(1 - \frac{\rho\, u}{\rho_e u_e} \right) dy$$

is the distance by which the invicid flowfield in the neighbourhood of a wall has to be effectively displaced inwards into the fluid in order to compensate for the deficiency in mass flow arising from the action of viscosity at the wall.

The two regions, invicid external flow and viscous boundary layer, are described by different governing equations, thus needing different methods of solution. Invicid calculations have been carried out using the method of characteristics developed earlier. The viscous region is governed by the boundary layer equations defined in the next chapter.

4.2 Governing equations

The governing equations of fluid flow may be derived by equating the net rate of outward transfer of mass and momentum respectively through the faces of an infinitesimal, fixed volume to their net sources within it. The full derivation of these equations (i.e. Cebeci & Bradshaw, 1977) leads to the so-called conservation and Navier-Stokes equations.

While the Navier-Stokes equations are of elliptic type, the boundary layer equations are of parabolic type. That fact is due to the assumption that, in the boundary layer equations, the pressure in the direction normal to the body surface is considered constant while the pressure along the surface can be considered as being 'impressed' by the external flow.

The boundary layer equations for a steady, compressible flow of a perfect gas, in the (x,y) cartesian coordinate system are found to be (McDonald, 1979) :

$$\frac{\partial}{\partial x} (\overline{\rho u}) + \frac{\partial}{\partial y} (\overline{\rho v}) = 0 \qquad \ldots (4.1)$$

$$\frac{\partial \overline{P}}{\partial y} = 0 \qquad \ldots (4.2)$$

$$\frac{\partial}{\partial x}(\bar{\rho}\bar{u}^2) + \frac{\partial}{\partial y}(\bar{u}\,\overline{\rho v}) = -\frac{\partial \bar{P}}{\partial x} + \frac{\partial \bar{\tau}}{\partial y} \qquad \ldots (4.3)$$

$$\bar{\rho}\bar{u}\frac{\partial \bar{h}_t}{\partial x} + \overline{\rho v}\frac{\partial \bar{h}_t}{\partial y} = \frac{\partial}{\partial y}(\bar{q} + u\bar{\tau}) \qquad \ldots (4.4)$$

The equations apply to laminar and turbulent flow if the definition of $\bar{\tau}$ and $\bar{q}$ are taken to be :

$$\frac{\bar{\tau}}{\bar{\rho}} = \nu\frac{\partial \bar{u}}{\partial y} - \overline{u'v'} \qquad \ldots (4.5)$$

$$\frac{\bar{q}}{\bar{\rho}} = K\frac{\partial \bar{h}}{\partial y} - \overline{v'h'} \qquad \ldots (4.6)$$

where ($-u'v'$) and ($-v'h'$) are the kinematic Reynolds stress and heat flux respectively. Following the approximation made by (Boussinesq, 1877), the turbulent stress arising from the cross correlation of fluctuating velocities is replaced by the product of the mean velocity gradient and the 'turbulent viscosity', providing the framework for the construction of a turbulence model :

$$-\rho\,\overline{u'v'} = \mu_t\frac{\partial \bar{u}}{\partial y} \qquad \ldots (4.7)$$

In the same way, a 'turbulent conductivity' may be defined :

$$-\rho\,\overline{v'h'} = K_t\frac{\partial \bar{h}}{\partial y} \qquad \ldots (4.8)$$

An effective vicosity and an effective conductivity are defined next :

$$\frac{\bar{\tau}}{\bar{\rho}} = (\nu + \nu_t)\frac{\partial \bar{u}}{\partial y} = \nu_e\frac{\partial \bar{u}}{\partial y} \qquad \ldots (4.9)$$

$$\frac{q}{\rho} = (K + K_t) \frac{\partial h}{\partial y} = K_e \frac{\partial h}{\partial y} \qquad \ldots (4.10)$$

For convenience, it was useful to transform equations (4.1, 4.3, and 4.4) so that they appear closer to their planar form. For axisymmetric flows, (Herring & Mellor, 1972) showed that the governing equations, when expressed in the local (x,y) coordinate system illustrated by Figure 4.1, are of the form(*) :

$$\frac{1}{r_w} \frac{\partial}{\partial x} (r_w \rho u) + \frac{\partial}{\partial y} (\rho v) = 0 \qquad \ldots (4.11)$$

$$\rho u \frac{\partial u}{\partial x} + \rho v \frac{\partial u}{\partial y} = \rho_e u_e \frac{\partial u_e}{\partial x} + \frac{\partial}{\partial y} (\frac{r}{r_w} \tau) \qquad \ldots (4.12)$$

$$\rho u \frac{\partial h_t}{\partial x} + \rho v \frac{\partial h_t}{\partial y} = \frac{\partial}{\partial y} [\frac{r}{r_w} (q + u\tau)] \qquad \ldots (4.13)$$

where :

$$\frac{\tau}{\rho} = (\frac{r}{r_w}) \nu_e \frac{\partial u}{\partial y} \qquad \ldots (4.14)$$

$$\frac{q}{\rho} = (\frac{r}{r_w}) K_e \frac{\partial h}{\partial y} \qquad \ldots (4.15)$$

The above set of equations along with the boundary conditions (appendix D) are sufficient to calculate the development of the boundary layer. However, because the method was orientated towards turbulent flow, it was convenient to define a new set of variables in

---

(*) The dependent variables should, at all times, be interpreted as time-average quantities in turbulent flow.

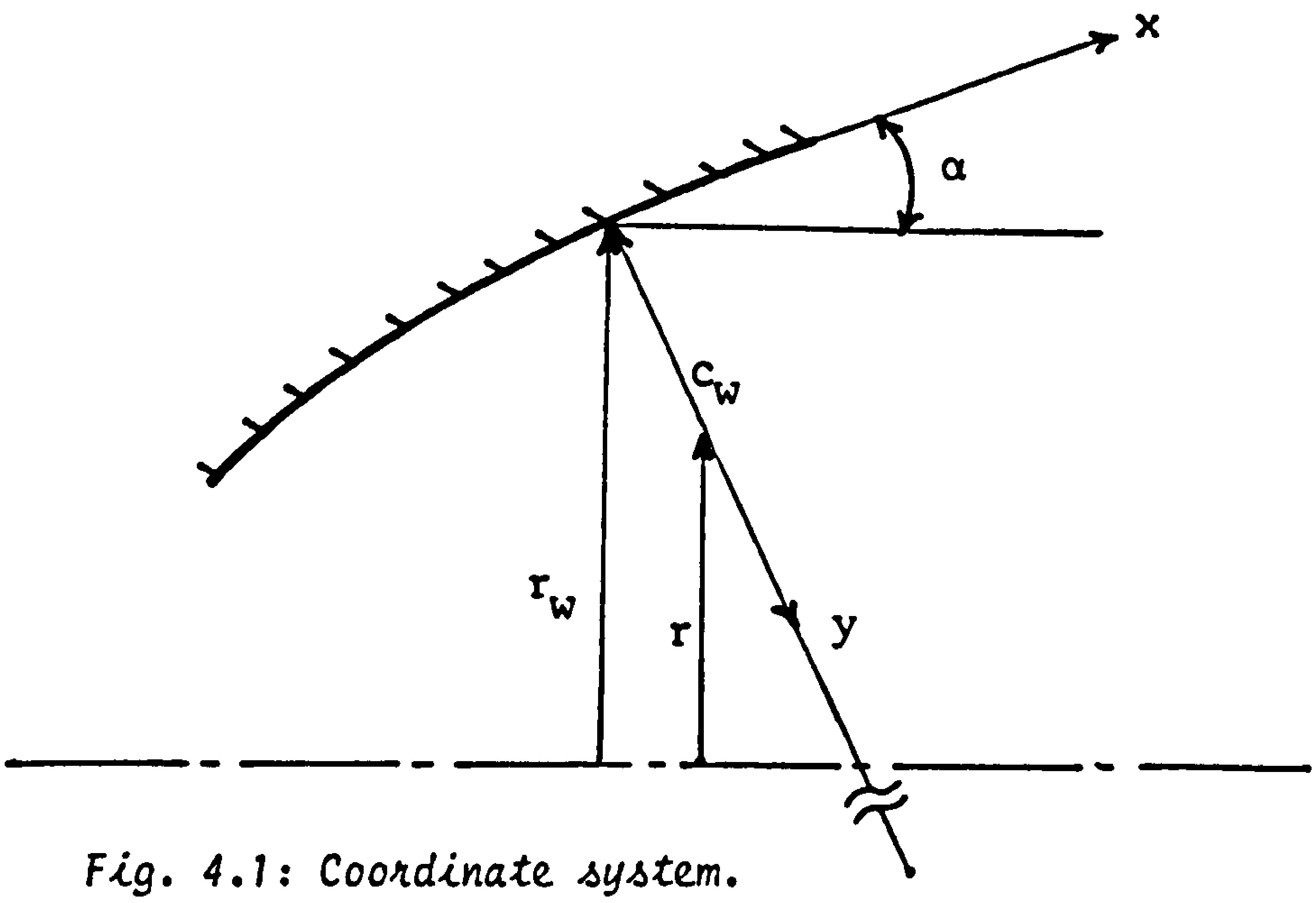

Fig. 4.1: Coordinate system.

which the velocity and enthalpy profiles were expressed in defect form (see appendix D). In terms of these variables, a new set of governing partial differential equations was defined. These equations were subsequently converted into ordinary differential equations and solved using finite-difference techniques.

In order to achieve greater accuracy (inaccuracies in the numerical solution which may be small enough after one step in x are frequently cumulative), the integral parameters such as δ^* and Θ were corrected by being referred to the solution of the Von-Karman momentum equation (Herring & Mellor, 1972 resumed in appendix D).

4.3 Program description

A computer program, initially developed by (Herring & Mellor, 1972) was employed in this study. Boundary layer calculations can be carried out for both laminar and turbulent flow for arbitrary Reynolds number and freestream Mach number distribution on planar or axisymmetric bodies.

The program divides into two parts. The first part deals with the preparation of an appropriate velocity and enthalpy profiles and associated parameters at the initial x-station. If the input profiles are provided simply by a rough guess, the program recalculates them using an appropriate similarity solution (either Falkner-Skan or Clauser, depending on whether the flow is respectively laminar or turbulent). The iterative loop performing the recalculation of the initial profiles may be skipped if the initial guess is satisfactory. A routine was developed and included into the program, enabling the user to simulate the necessary initial velocity and enthalpy profiles if they are not known (appendix E).

The forward motion of the program starts by storing the known profiles of the station before the one to be calculated. This is followed by an iterative loop which calculates the new set of profiles at the x-station considered. Within this loop, there are two inner loops, the first iterates for the velocity profile and the second for the enthalpy profile. When these calculations have converged, the integral parameters for that position are calculated and printed out. The process continues until profiles have been calculated at all x-stations.

4.4 Comparison with experimental data

4.4.1 General

In order to validate the program and the added routine (developed to guess the initial profiles, appendix E) by comparison with broadly relevant measurement, the former was used to compute the development of the boundary layer in the supersonic section of a conical nozzle having a 15° half-angle of divergence (Figure 4.2). Comparison was made between results of the experimental investigation carried out by (Boldman et al., 1969) and predictions of the above program.

4.4.2 Experimental investigation

Experimental tests were performed in the heated test facility shown in Figure 4.3 reproduced from (Boldman et al., 1969). The results used for comparison employed an adiabatic (uncooled) inlet. Velocity and temperature boundary layer surveys were obtained at three specific stations within the supersonic portion of the nozzle (Figure

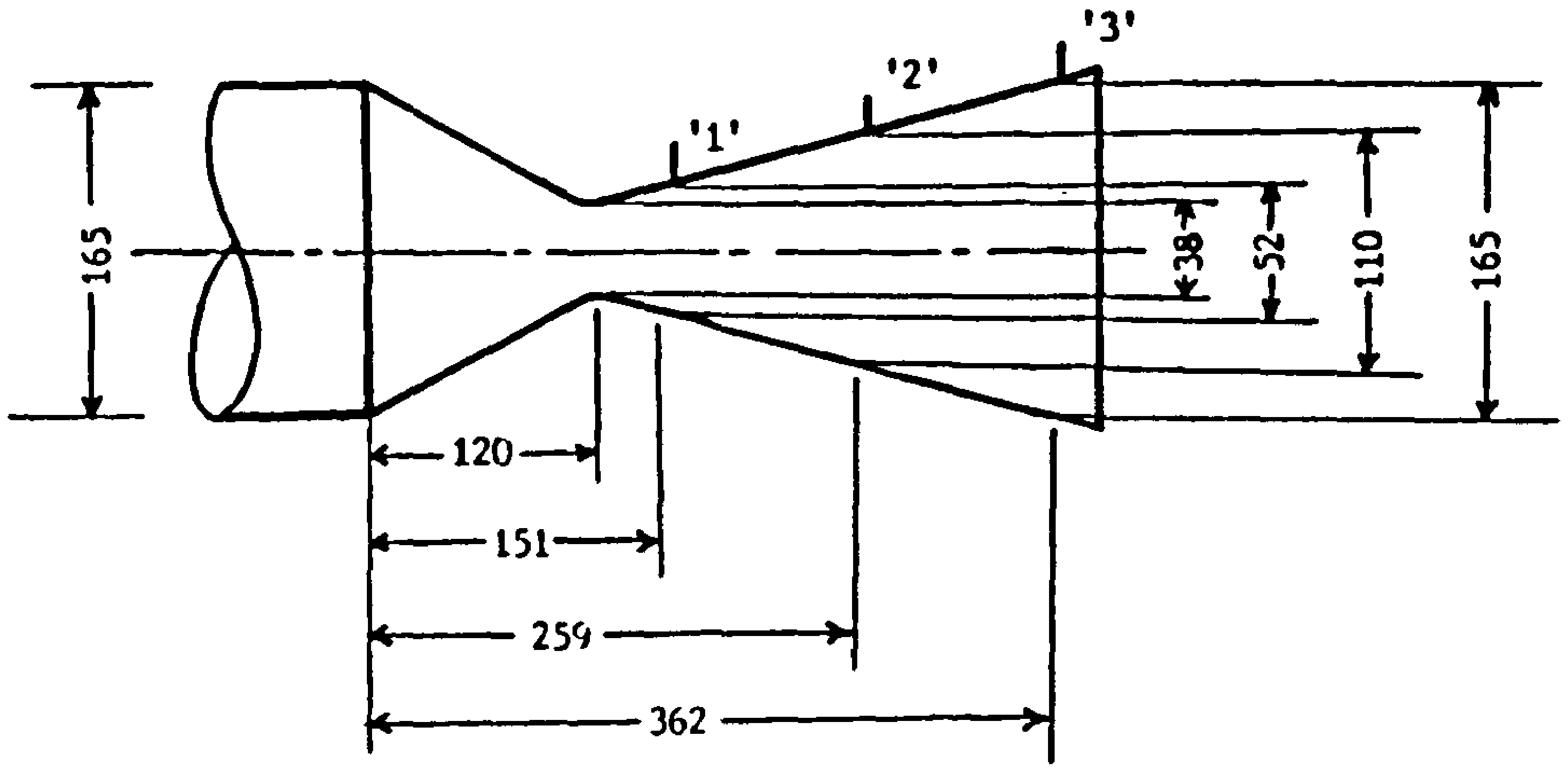

Fig. 4.2: Conical nozzle submitted to test.

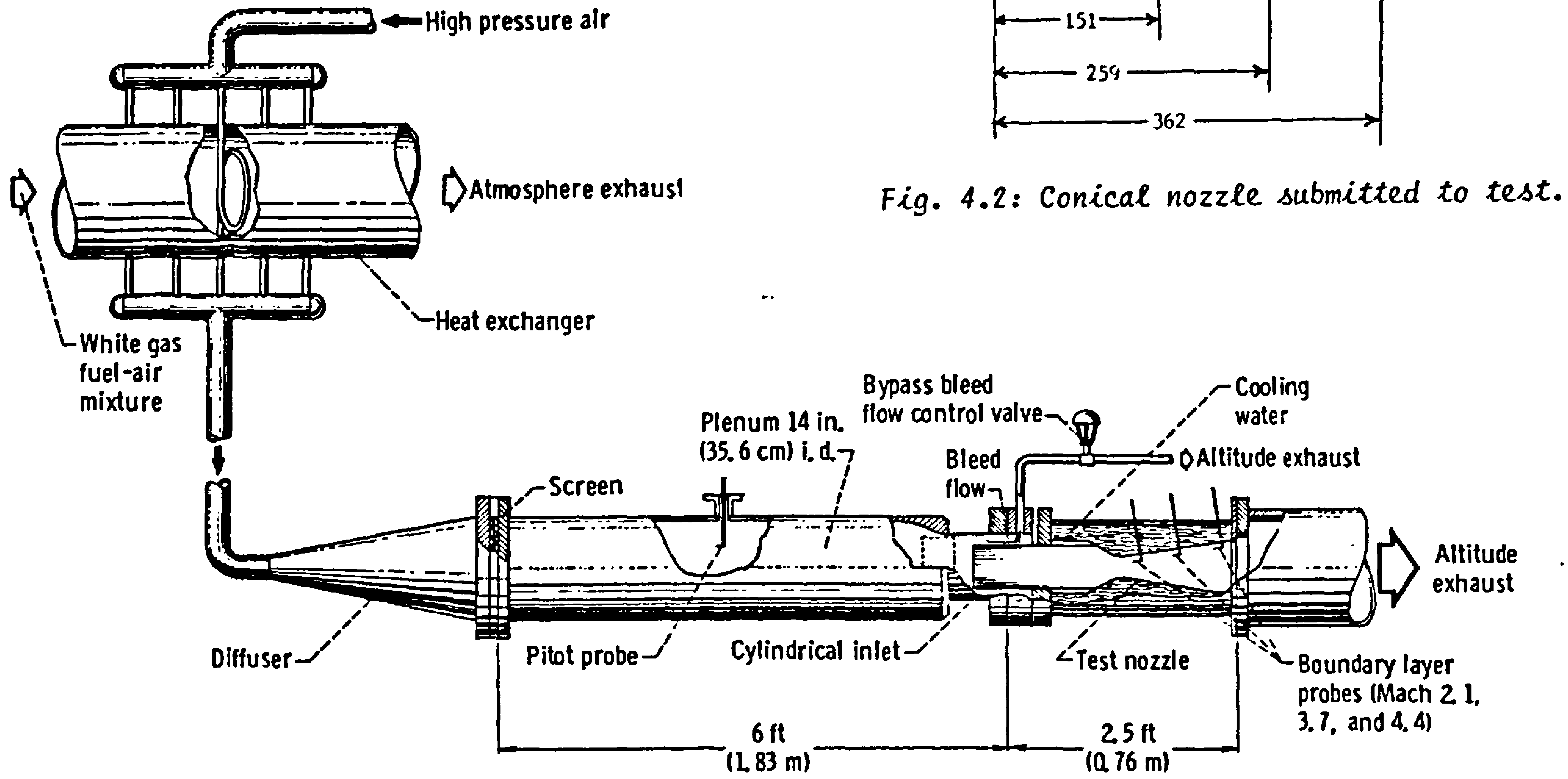

Fig. 4.3: Schematic diagram of nozzle heat transfer facility. (Boldman et al, 1969)

4.2). The freestream Mach numbers at the three stations were : 2.1, 3.7, and 4.4 respectively.

4.4.3 Theoretical investigation

In order to compute the development of the boundary layer within the nozzle section considered, initial profiles have to be defined. The first measurement station (numbered '1' in Figure 4.2) was taken as the initial computational position allowing the use of the measured external Mach number, velocity and boundary layer thickness as initial parameters. The initial velocity and temperature profiles were assumed to follow the 1/7-power and 1/4-power laws respectively (Appendix E). This permitted the determination of the input parameters to the program. They are reproduced in Table 4.1.

4.4.4 Summary of results and comparison

Results of the experimental investigation are shown in tables 4.2.a, 4.2.b, and 4.2.c. They, respectively, represent the three stations at which the measurements were performed. The theoretical predictions are presented in tables 4.3.a, 4.3.b, and 4.3.c.

The initial velocity profile, representing the 1/7-power law along with the experimental profile are shown in figure 4.4. The experimental and predicted profiles at the two other stations are shown in Figure 4.5 and 4.6. Good agreement is found between the predicted and measured profiles within the boundary layer which developed along the nozzle.

Figure 4.7 shows the distribution of the boundary layer displacement thickness at the three stations and those predicted by the program. The experimental value of the displacement thickness at station '1' has been taken as an initial condition in order to carry out the computations.

The development of the boundary layer seem to have been well predicted by the program. Good agreement between theoretical predictions and measured values is found. Calculated errors were within 1.5%.

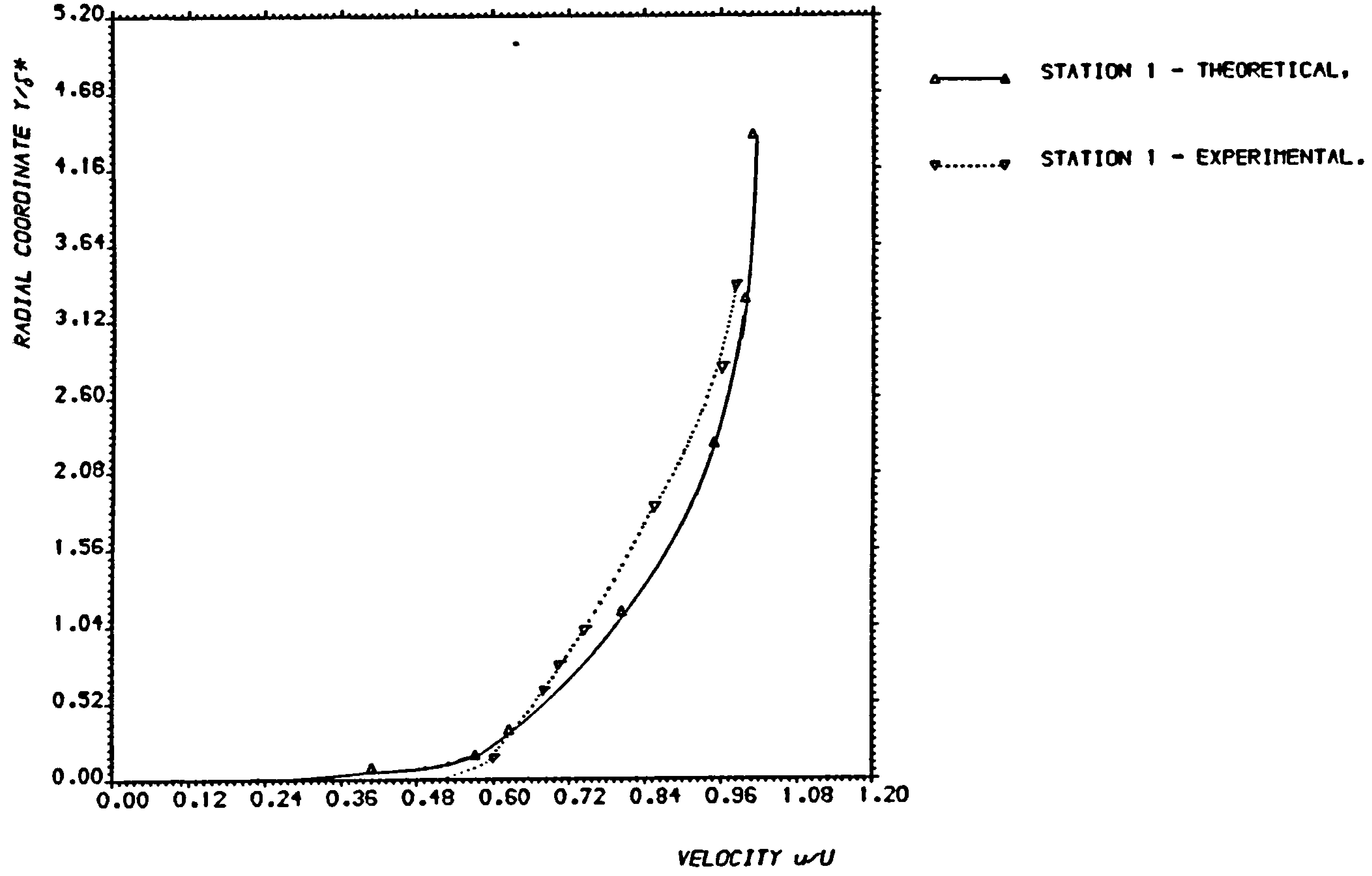

FIG : [4.4] VELOCITY PROFILE WITHIN BOUNDARY LAYER DEVELOPED ALONG DIVERGENT SECTION OF CONICAL NOZZLE.

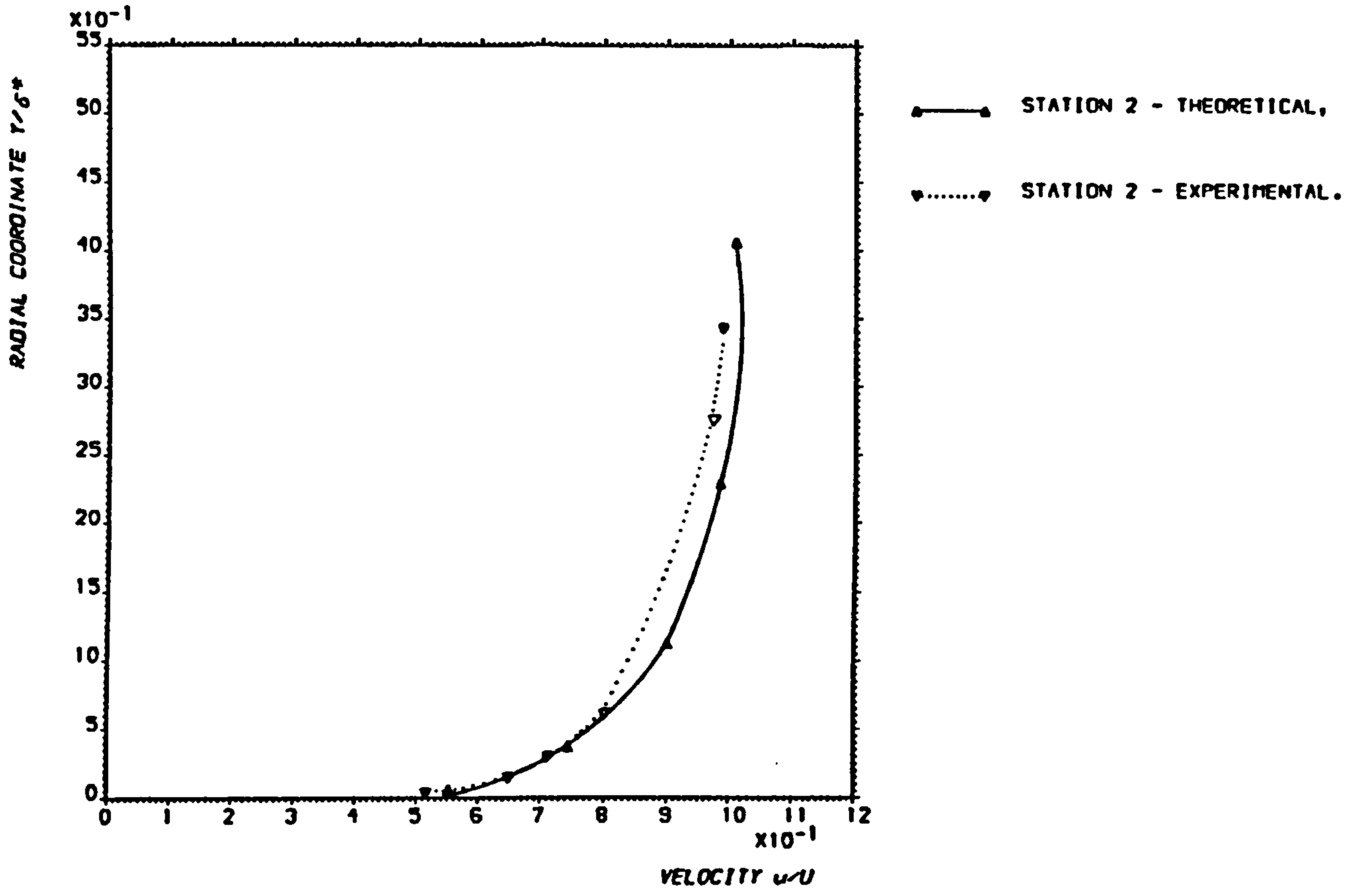

FIG : [4.5] VELOCITY PROFILE WITHIN BOUNDARY LAYER DEVELOPED ALONG DIVERGENT SECTION OF CONICAL NOZZLE.

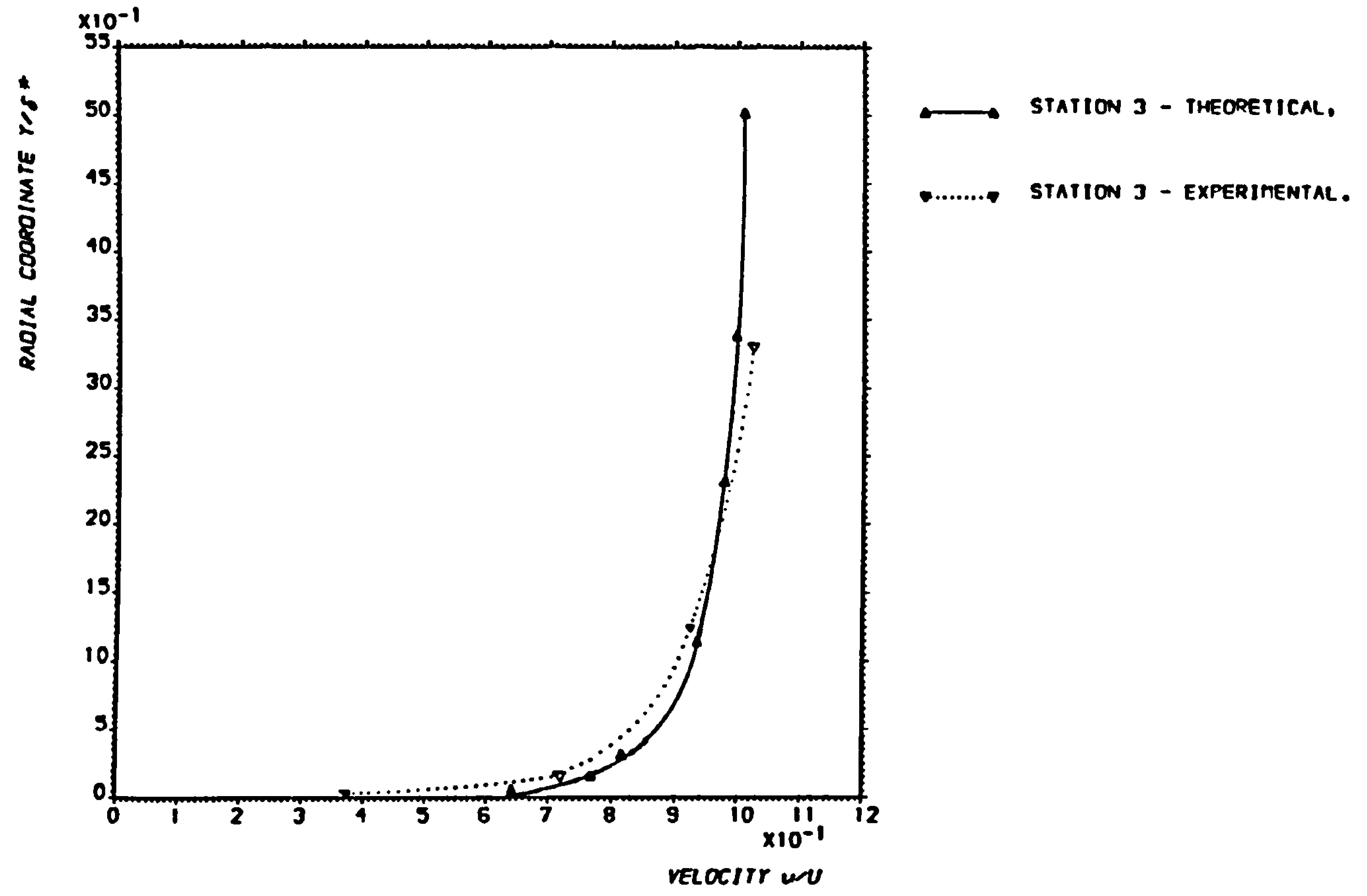

FIG : [4.6] VELOCITY PROFILE WITHIN BOUNDARY LAYER DEVELOPED ALONG DIVERGENT SECTION OF CONICAL NOZZLE.

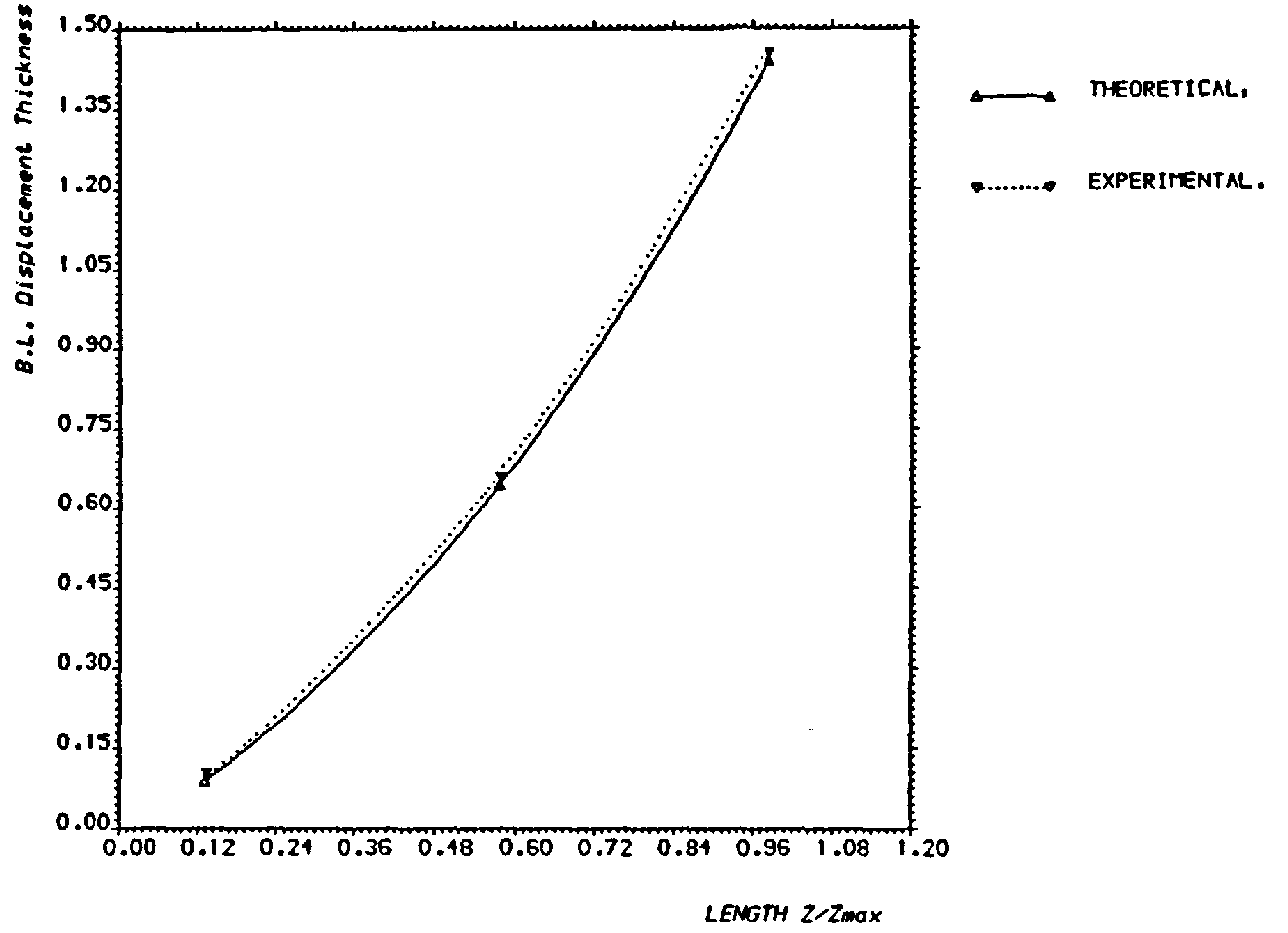

FIG : [4.7] BOUNDARY LAYER DEVELOPMENT ALONG DIVERGENT SECTION OF CONICAL NOZZLE.

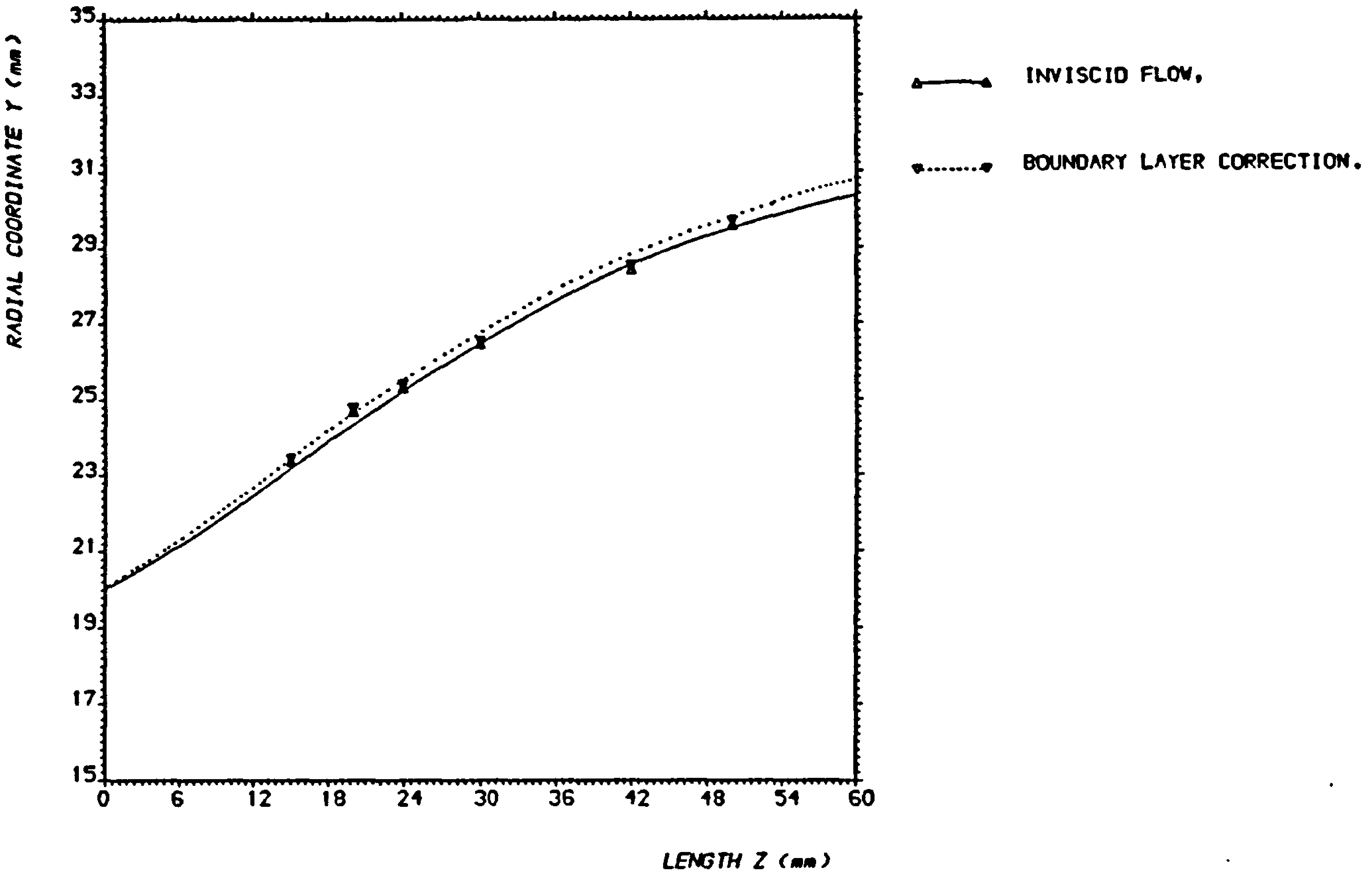

FIG : [4.8] BOUNDARY LAYER DEVELOPMENT ALONG DIVERGENT SECTION OF AXISYMMETRIC-FOR-ELLIPTIC NOZZLE (AR= 2.32).

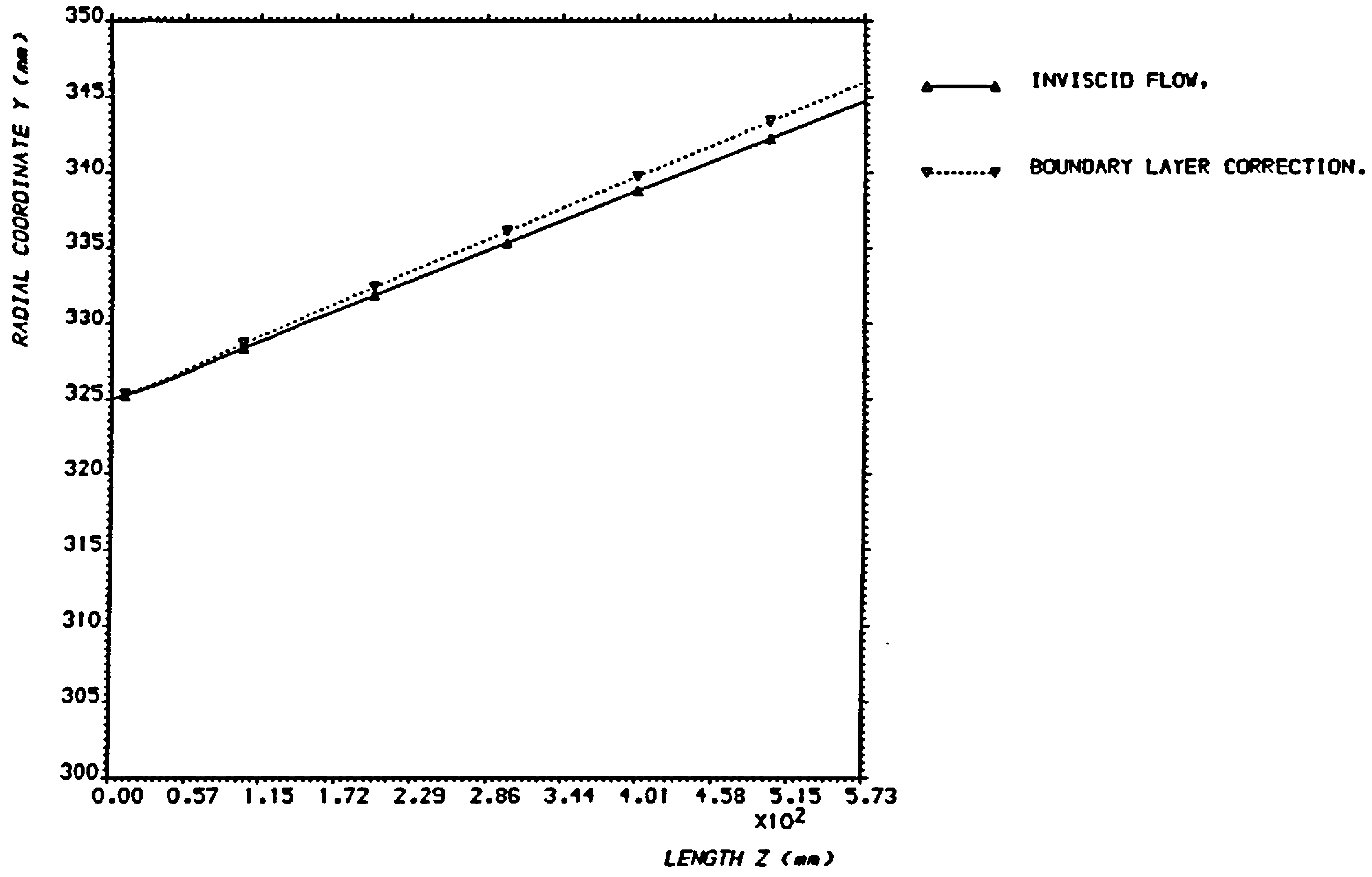

FIG : [4.9] BOUNDARY LAYER DEVELOPMENT ALONG DIVERGENT SECTION OF AXISYMMETRIC-FOR-WEDGE NOZZLE (AR=1.125).

4.5 Boundary layer computation for the axisymmetric nozzles designed in this study

The boundary layer development along the divergent section of the two axisymmetric nozzles investigated was predicted using the program described above. Initial profiles were produced using the routine developed for that purpose (appendix E). The starting parameters (edge Mach number at each station, wall temperature) were produced from the invicid flowfield computed by the method of characteristics. Figures 4.8 and 4.9 show the respective corrections needed (in terms of the displacement thickness) in order to include the viscous effects for the two axisymmetric configurations from which the elliptic and the two-dimensional wedge designs were developed subsequently.

The results obtained show that the corrections needed are very small (within 0.3% in terms of δ^*/R). Furthermore, the area occupied by the boundary layer did not exceed 0.7% of the total area, while blockage coefficients, defined as the ratio of the invicid flow area to the total flow area, were found to exceed 0.99.

In view of these results, it seems safe to neglect the viscosity effects for the two axisymmetric configurations investigated.

4.6 Boundary layer development prediction along the elliptic nozzle using axisymmetric results

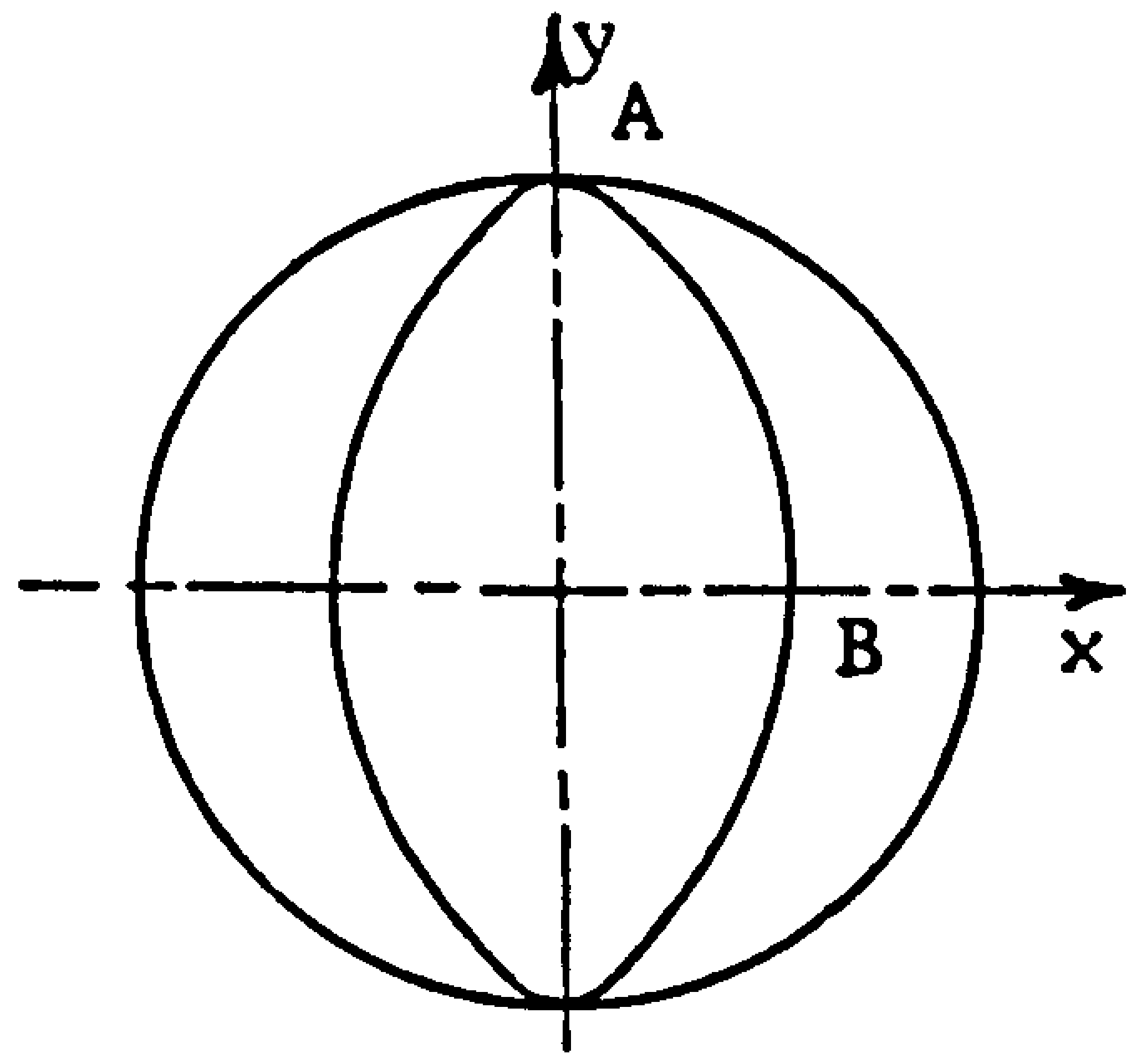

Fig. 4.10: Positions at which the boundary layer development was calculated.

Assuming the flow characteristics to remain nearly the same as the shape was transformed from the axisymmetric configuration to the corresponding elliptic one (Figure 4.10), the boundary layers along the major and minor axes (represented by points 'A' and 'B' of figure 4.10 respectively) were computed. Initial profiles and pressure gradients were calculated using the relations presented in appendix E. The starting parameters were produced from the invicid flowfield results obtained from the method of characteristics computation of the axisymmetric configuration.

Figure 4.11 presents a comparison in terms of the displacement thickness along the major and minor axes as a function of the axial position. It shows the boundary layer developing faster along the minor axis.

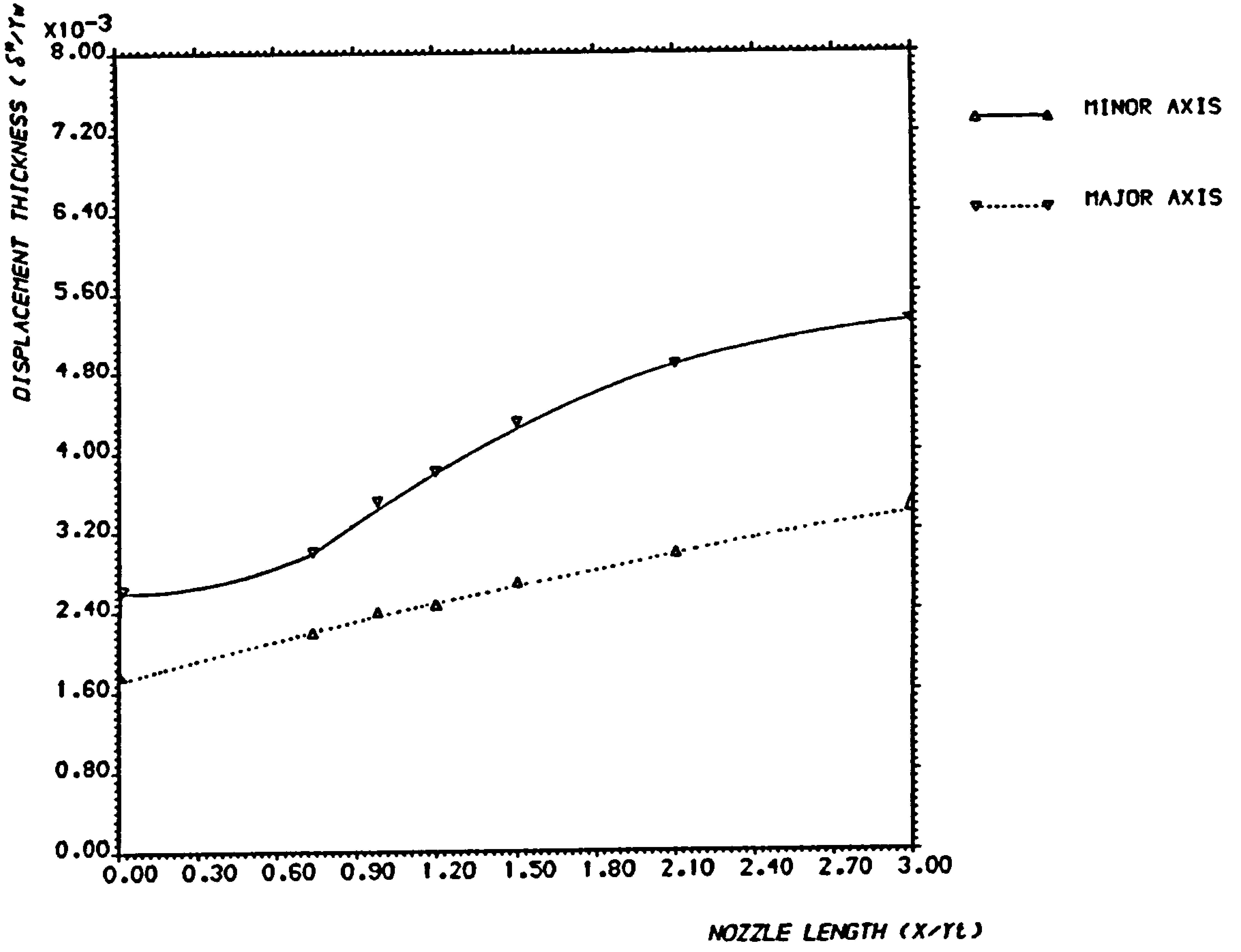

FIG : [4.11] BOUNDARY LAYER DEVELOPMENT ALONG THE MAJOR AND MINOR AXES OF THE ELLIPTIC NOZZLE (AR= 2.46).

TABLE 4.1 : FILE DATA FOR THE CONICAL NOZZLE CASE

```
3 69
0.0    0.0710 0.1421 0.2132 0.2843 0.3554 0.4265 0.4976 0.5687 0.6398
0.7109 0.7820 0.8531 0.9242 0.9953 1.0664 1.1374 1.2085 1.2793 1.3507
1.4218 1.5640 1.7062 1.8484 1.9906 2.1328 2.2749 2.4171 2.5593 2.7015
2.8437 2.9859 3.1281 3.2703 3.4124 3.5546 3.6968 3.8390 3.9812 4.1234
4.2656 4.4078 4.5499 4.6921 4.8343 4.8400 4.8450 4.8500 4.855  4.86
4.8650 4.8700 4.875  4.88   4.885  4.8900 4.8950 4.9000 4.905  4.91
4.915  4.9200 4.925  4.93   4.9350 4.9400 4.9450 4.9500 4.955
45
1.0000 0.5974 0.5449 0.5096 0.4821 0.4592 0.4394 0.4217 0.4057 0.3910
0.3773 0.3646 0.3526 0.3412 0.3304 0.3201 0.3102 0.3007 0.2915 0.2826
0.2741 0.2577 0.2422 0.2274 0.2133 0.1998 0.1868 0.1742 0.1621 0.1503
0.1389 0.1278 0.1169 0.1063 0.0960 0.0859 0.0759 0.0662 0.0567 0.0473
0.0381 0.0290 0.0201 0.0113 0.0027
6
0.1813 0.0672 0.0442 0.0290 0.01915 0.00152
6 3 -2 -1 2.1 0.086 9496.0 1.05 535.0 1.0
31.01  2.1 1.0 0.0 26.0 0.0 0.0 0.0
138.89 3.7 1.0 0.0 55.0 0.0 0.0 0.0
241.81 4.4 1.0 0.0 82.5 0.0 0.0 0.0
```

TABLE 4.2.a : Boundary layer survey at a nominal Mach number of 2.1 for adiabatic inlet. (Boldman et al., 1969)

[Free-stream velocity $u_\infty = 2319$ ft/sec (706 m/sec); wall temperature $T_w = 788^\circ$ R (438 K); free-stream stagnation temperature $T_0 = 973^\circ$ R (541 K); edge stagnation temperature $T_{t,e} = 964^\circ$ R (535 K); velocity boundary layer thickness $\delta = 0.021$ in. (0.053 cm); temperature boundary layer thickness $\Delta = 0.039$ in. (0.099 cm).]

Integration to edge condition				Integration to free-stream condition			
Momentum, θ		Displacement, δ^*		Momentum, θ		Displacement, δ^*	
in.	cm	in.	cm	in.	cm	in.	cm
0.0014	0.0036	0.0034	0.0086	0.0030	0.0076	0.0040	0.0102

Distance from nozzle wall, y		Local static temperature, T		Local stagnation temperature, T_t		Local velocity, u		Local Mach number, M	Velocity ratio, u/u_∞	Temperature difference ratio, $\frac{T_t - T_w}{T_0 - T_w}$	Distance ratio, y/δ	Velocity ratio, u/u_e	Distance ratio, y/Δ	Temperature difference ratio, $\frac{T_t - T_w}{T_{t,e} - T_w}$
in.	cm	°R	K	°R	K	ft/sec	m/sec							
0.0012	0.0032	694	386	851	473	1374	419	1.1	0.592	0.342	0.059	0.598	0.032	0.361
0.0024	0.0062	659	366	860	478	1554	473	1.2	0.670	0.388	0.115	0.677	0.063	0.409
0.0034	0.0088	634	352	867	482	1675	510	1.4	0.722	0.426	0.162	0.730	0.089	0.450
0.0044	0.0113	609	338	874	486	1786	544	1.5	0.770	0.464	0.209	0.778	0.115	0.490
0.0064	0.0164	566	315	888	494	1967	599	1.7	0.848	0.541	0.302	0.857	0.167	0.571
0.0084	0.0215	532	295	902	501	2110	643	1.9	0.910	0.617	0.396	0.919	0.219	0.651
0.0089	0.0227	525	292	906	503	2139	651	1.9	0.923	0.636	0.420	0.932	0.232	0.672
0.0094	0.0240	519	289	910	505	2165	659	1.9	0.934	0.655	0.443	0.943	0.245	0.692
0.0099	0.0253	518	288	913	507	2178	663	2.0	0.940	0.674	0.467	0.949	0.257	0.712
0.0104	0.0265	521	290	917	509	2179	664	1.9	0.940	0.694	0.490	0.949	0.270	0.732
0.0109	0.0278	526	292	920	511	2176	663	1.9	0.938	0.713	0.514	0.948	0.283	0.752
0.0114	0.0291	528	294	924	513	2179	664	1.9	0.940	0.732	0.537	0.949	0.296	0.772
0.0119	0.0304	529	294	926	514	2184	665	1.9	0.942	0.741	0.560	0.951	0.309	0.782
0.0124	0.0316	527	293	927	515	2192	668	1.9	0.946	0.750	0.584	0.955	0.322	0.791
0.0134	0.0342	523	290	930	517	2213	674	2.0	0.954	0.767	0.631	0.964	0.346	0.809
0.0144	0.0367	520	289	933	519	2229	679	2.0	0.961	0.784	0.678	0.971	0.374	0.827
0.0154	0.0392	517	287	937	520	2246	684	2.0	0.969	0.801	0.725	0.978	0.403	0.845
0.0164	0.0418	515	286	940	522	2258	688	2.0	0.974	0.818	0.771	0.984	0.425	0.863
0.0184	0.0469	514	285	946	526	2279	694	2.1	0.983	0.852	0.865	0.993	0.477	0.859
0.0204	0.0519	515	286	952	529	2292	698	2.1	0.989	0.986	0.959	0.999	0.523	0.935
0.0209	0.0532	515	286	954	530	2295	699	2.1	0.990	0.894	0.982	1.000	0.542	0.944
0.0404	0.1027	521	290	965	536	2308	703	2.1	0.996	0.953	1.897	1.000	1.047	1.000
0.1897	0.4820	526	292	973	540	2318	706	2.1	1.000	0.996	8.899	1.000	4.913	1.000
0.3397	0.8630	526	292	973	541	2319	706	2.1	1.000	1.000	15.933	1.000	8.792	1.000

TABLE 4.2.b : Boundary layer survey at a nominal Mach number of 3.7 for adiabatic inlet.(Boldman et al., 1969)

[Free-stream velocity u_∞ = 2925 ft/sec (891 m/sec); wall temperature T_w = 637° R (354 K); free-stream stagnation temperature T_0 = 970° R (539 K); edge stagnation temperature $T_{t,e}$ = 960° R (533 K); velocity boundary layer thickness δ = 0.087 in. (0.221 cm); temperature boundary layer thickness Δ = 0.083 in. (0.211 cm).]

Integration to edge condition				Integration to free-stream condition			
Momentum, θ		Displacement, δ*		Momentum, θ		Displacement, δ*	
in.	cm	in.	cm	in.	cm	in.	cm
0.0050	0.013	0.024	0.061	0.0055	0.014	0.026	0.066

Distance from nozzle wall, y		Local static temperature, T		Local stagnation temperature, T_t		Local velocity, u		Local Mach number, M	Velocity ratio, u/u_∞	Temperature difference ratio, $\frac{T_t - T_w}{T_0 - T_w}$	Distance ratio, y/δ	Velocity ratio, u/u_e	Distance ratio, y/Δ	Temperature difference ratio, $\frac{T_t - T_w}{T_{t,e} - T_w}$
in.	cm	°R	K	°R	K	ft/sec	m/sec							
0.0012	0.0032	566	315	740	411	1444	440	1.2	0.494	0.309	0.014	0.495	0.015	0.318
0.0017	0.0044	553	307	750	417	1538	468	1.3	0.526	0.340	0.020	0.531	0.021	0.350
0.0022	0.0057	539	299	761	423	1632	497	1.4	0.558	0.371	0.026	0.564	0.027	0.383
0.0027	0.0070	527	293	771	428	1713	522	1.5	0.586	0.403	0.031	0.592	0.033	0.415
0.0032	0.0083	516	287	781	434	1786	544	1.6	0.611	0.434	0.037	0.617	0.039	0.447
0.0037	0.0095	505	281	792	440	1854	565	1.7	0.634	0.465	0.043	0.641	0.045	0.479
0.0042	0.0108	501	278	802	446	1901	579	1.7	0.650	0.497	0.049	0.657	0.051	0.511
0.0047	0.0121	491	273	811	450	1960	597	1.8	0.670	0.522	0.054	0.677	0.057	0.538
0.0052	0.0133	485	270	817	454	1995	607	1.8	0.682	0.540	0.060	0.685	0.063	0.556
0.0062	0.0159	467	259	826	459	2078	633	2.0	0.711	0.569	0.072	0.718	0.075	0.586
0.0072	0.0184	452	251	832	462	2135	650	2.0	0.730	0.586	0.083	0.737	0.087	0.603
0.0077	0.0197	445	247	834	463	2161	658	2.1	0.739	0.592	0.089	0.746	0.093	0.610
0.0082	0.0210	441	245	836	464	2179	664	2.1	0.745	0.599	0.094	0.753	0.099	0.617
0.0112	0.0286	422	234	849	472	2264	690	2.2	0.774	0.637	0.129	0.782	0.135	0.656
0.0132	0.0337	413	229	856	476	2307	703	2.3	0.789	0.659	0.152	0.797	0.159	0.679
0.0172	0.0438	397	221	870	483	2382	726	2.4	0.815	0.700	0.198	0.823	0.207	0.721
0.0297	0.0756	359	199	897	498	2542	774	2.7	0.869	0.782	0.341	0.878	0.357	0.806
0.0422	0.1073	327	182	919	510	2667	812	3.0	0.912	0.848	0.484	0.921	0.507	0.873
0.0552	0.1403	301	167	937	520	2762	841	3.2	0.945	0.901	0.633	0.954	0.662	0.928
0.0672	0.1708	283	157	949	527	2829	862	3.4	0.967	0.938	0.770	0.977	0.806	0.967
0.0802	0.2038	268	149	959	533	2880	877	3.6	0.985	0.967	0.919	0.995	0.962	0.996
0.0927	0.2356	260	144	963	535	2907	886	3.7	0.994	0.982	1.062	1.000	1.112	1.000
0.1052	0.2673	258	143	966	537	2917	889	3.7	0.997	0.990	1.205	1.000	1.262	1.000
0.1182	0.3004	257	143	967	537	2920	890	3.7	0.998	0.993	1.354	1.000	1.418	1.000
0.1302	0.3308	257	143	968	538	2922	890	3.7	0.999	0.996	1.492	1.000	1.562	1.000
0.1432	0.3639	257	143	969	538	2923	890	3.7	0.999	0.997	1.641	1.000	1.717	1.000
0.1557	0.3956	257	143	969	538	2924	891	3.7	1.000	0.999	1.784	1.000	1.867	1.000
0.1682	0.4274	257	143	969	538	2924	891	3.7	1.000	0.999	1.927	1.000	2.017	1.000
0.1932	0.4909	257	143	969	539	2925	891	3.7	1.000	1.000	2.213	1.000	2.317	1.000
0.2482	0.6306	257	143	969	539	2925	891	3.7	1.000	1.000	2.843	1.000	2.976	1.000

TABLE 4.2.c : Boundary layer survey at a nominal Mach number of 4.4 for adiabatic inlet.(Boldman et al., 1969)

[Free-stream velocity u_∞ = 3043 ft/sec (927 m/sec); wall temperature T_w = 570° R (317 K); free-stream stagnation temperature T_0 = 970° R (539 K); edge stagnation temperature $T_{t,e}$ = 960° R (533 K); velocity boundary layer thickness δ = 0.161 in. (0.409 cm); temperature boundary layer thickness Δ = 0.161 in. (0.409 cm).]

Integration to edge condition				Integration to free-stream condition			
Momentum, θ		Displacement, δ^*		Momentum, θ		Displacement, δ^*	
in.	cm	in.	cm	in.	cm	in.	cm
0.0090	0.0229	0.056	0.142	0.010	0.025	0.061	0.155

Distance from nozzle wall, y		Local static temperature, T		Local stagnation temperature, T_t		Local velocity, u		Local Mach number, M	Velocity ratio, u/u_∞	Temperature difference ratio, $\frac{T_t - T_w}{T_0 - T_w}$	Distance ratio, y/δ	Velocity ratio, u/u_e	Distance ratio, y/Δ	Temperature difference ratio, $\frac{T_t - T_w}{T_{t,e} - T_w}$
in.	cm	°R	K	°R	K	ft/sec	m/sec							
0.0012	0.0032	654	363	694	385	691	210	0.6	0.227	0.309	0.008	0.229	0.008	0.317
0.0030	0.0076	591	328	719	400	1244	379	1.0	0.409	0.374	0.019	0.412	0.019	0.383
0.0032	0.0083	537	299	723	402	1494	455	1.3	0.491	0.383	0.020	0.496	0.020	0.393
0.0052	0.0133	513	285	752	418	1697	517	1.5	0.558	0.457	0.033	0.562	0.033	0.468
0.0072	0.0184	487	270	773	430	1855	565	1.7	0.610	0.508	0.045	0.616	0.045	0.521
0.0092	0.0235	459	255	784	436	1976	602	1.9	0.650	0.536	0.058	0.656	0.057	0.549
0.0132	0.0337	436	242	798	443	2084	635	2.0	0.685	0.570	0.083	0.692	0.082	0.584
0.0172	0.0438	415	230	808	449	2173	662	2.2	0.714	0.595	0.107	0.721	0.107	0.610
0.0232	0.0591	398	221	823	457	2259	688	2.3	0.742	0.632	0.145	0.750	0.144	0.648
0.0282	0.0718	384	214	832	462	2318	706	2.4	0.762	0.655	0.175	0.765	0.175	0.671
0.0412	0.1048	352	196	854	474	2454	748	2.7	0.807	0.710	0.257	0.815	0.256	0.727
0.0652	0.1657	303	168	886	492	2647	806	3.1	0.870	0.791	0.405	0.875	0.405	0.810
0.0862	0.2191	269	150	910	506	2774	845	3.4	0.912	0.851	0.537	0.921	0.535	0.872
0.1032	0.2623	248	138	927	515	2856	870	3.7	0.939	0.894	0.643	0.948	0.640	0.916
0.1212	0.3080	230	128	940	522	2921	890	3.9	0.960	0.927	0.755	0.970	0.752	0.950
0.1417	0.3600	214	119	952	529	2978	907	4.2	0.979	0.957	0.883	0.988	0.879	0.980
0.1497	0.3804	209	116	956	531	2995	912	4.2	0.984	0.966	0.932	0.994	0.928	0.990
0.1592	0.4045	205	114	959	533	3011	917	4.3	0.989	0.974	0.992	0.999	0.987	0.999
0.1672	0.4248	202	112	962	534	3020	920	4.3	0.993	0.980	1.041	1.000	1.037	1.000
0.1732	0.4401	200	111	963	535	3026	922	4.4	0.994	0.982	1.079	1.000	1.074	1.000
0.1782	0.4528	199	111	963	535	3029	923	4.4	0.995	0.984	1.110	1.000	1.105	1.000
0.1832	0.4655	199	110	964	535	3031	923	4.4	0.996	0.985	1.141	1.000	1.136	1.000
0.1972	0.5010	198	110	965	536	3033	924	4.4	0.997	0.987	1.228	1.000	1.223	1.000
0.4832	1.2275	199	110	970	539	3043	927	4.4	1.000	1.000	3.001	1.000	2.996	1.000

TABLE 4.3.a : BOUNDARY LAYER SURVEY AT THE FIRST STATION (M=2.1)

```
                 X =   31.010    U =     1.000    M =   2.10    RDT = 9.50E+03
      TURB =1.000      RW = 2.60E+01     VW = 0.00E+00    SW = 0.00E+00    CW = 0.00E+00
  DT = 8.60E-02 MT = 2.41E-02 HT =-3.56E-06 SF = 3.57E+00 CF = 2.23E-03 ST = 0.00E+00
             HR = 1.00E+00     PR = 7.80E-01     PRT = 1.00E+00     SHR = 1.40

  J      YY       u/U        F        FP        FPP        D        GP        GPP       TAU       VE
   1  0.00E+00 0.00E+00 0.00E+00 1.00E+00 -3.68E+00 1.85E+00 1.80E-02  0.00E+00 1.12E-03 3.03E-04
   4  7.10E-02 4.13E-01 6.20E-02 7.60E-01 -2.21E+00 1.72E+00 4.24E-03 -1.60E-01 1.08E-03 5.67E-04
   7  1.42E-01 5.25E-01 1.13E-01 6.79E-01 -6.93E-01 1.64E+00 6.86E-04 -1.34E-02 1.24E-03 2.30E-03
  10  2.13E-01 5.72E-01 1.59E-01 6.41E-01 -4.39E-01 1.59E+00 1.74E-04 -4.33E-03 1.26E-03 3.88E-03
  13  2.84E-01 6.03E-01 2.04E-01 6.14E-01 -3.41E-01 1.56E+00-4.32E-05 -2.23E-03 1.29E-03 5.32E-03
  16  3.55E-01 6.27E-01 2.47E-01 5.92E-01 -2.85E-01 1.54E+00-1.66E-04 -1.35E-03 1.32E-03 6.70E-03
  19  4.26E-01 6.47E-01 2.88E-01 5.73E-01 -2.48E-01 1.51E+00-2.44E-04 -8.94E-04 1.35E-03 8.06E-03
  22  4.98E-01 6.63E-01 3.28E-01 5.56E-01 -2.31E-01 1.49E+00-2.86E-04  8.72E-06 1.38E-03 9.08E-03
  25  5.69E-01 6.79E-01 3.67E-01 5.40E-01 -2.39E-01 1.48E+00-2.69E-04  2.38E-04 1.39E-03 9.08E-03
  28  6.40E-01 6.95E-01 4.05E-01 5.22E-01 -2.46E-01 1.46E+00-2.53E-04  2.31E-04 1.41E-03 9.08E-03
  31  7.11E-01 7.11E-01 4.41E-01 5.05E-01 -2.53E-01 1.44E+00-2.37E-04  2.23E-04 1.41E-03 9.08E-03
  34  7.82E-01 7.27E-01 4.76E-01 4.86E-01 -2.60E-01 1.42E+00-2.21E-04  2.15E-04 1.42E-03 9.08E-03
  37  8.53E-01 7.43E-01 5.10E-01 4.68E-01 -2.65E-01 1.40E+00-2.06E-04  2.07E-04 1.41E-03 9.08E-03
  40  9.24E-01 7.58E-01 5.43E-01 4.49E-01 -2.70E-01 1.38E+00-1.92E-04  1.98E-04 1.40E-03 9.08E-03
  43  9.95E-01 7.73E-01 5.74E-01 4.30E-01 -2.73E-01 1.36E+00-1.78E-04  1.89E-04 1.39E-03 9.08E-03
  46  1.07E+00 7.88E-01 6.04E-01 4.10E-01 -2.76E-01 1.34E+00-1.65E-04  1.80E-04 1.37E-03 9.08E-03
  49  1.14E+00 8.02E-01 6.32E-01 3.91E-01 -2.77E-01 1.32E+00-1.52E-04  1.71E-04 1.34E-03 9.08E-03
  52  1.21E+00 8.15E-01 6.59E-01 3.71E-01 -2.77E-01 1.30E+00-1.41E-04  1.62E-04 1.32E-03 9.08E-03
  55  1.28E+00 8.28E-01 6.84E-01 3.51E-01 -2.76E-01 1.28E+00-1.29E-04  1.53E-04 1.28E-03 9.08E-03
  58  1.35E+00 8.41E-01 7.09E-01 3.32E-01 -2.74E-01 1.26E+00-1.19E-04  1.44E-04 1.24E-03 9.08E-03
  61  1.42E+00 8.53E-01 7.31E-01 3.12E-01 -2.70E-01 1.24E+00-1.09E-04  1.34E-04 1.20E-03 9.08E-03
  64  1.56E+00 8.75E-01 7.73E-01 2.75E-01 -2.62E-01 1.21E+00-9.09E-05  1.19E-04 1.12E-03 9.08E-03
  67  1.71E+00 8.95E-01 8.09E-01 2.39E-01 -2.49E-01 1.18E+00-7.52E-05  1.03E-04 1.02E-03 9.08E-03
  70  1.85E+00 9.13E-01 8.41E-01 2.05E-01 -2.32E-01 1.15E+00-6.17E-05  8.86E-05 9.17E-04 9.08E-03
  73  1.99E+00 9.28E-01 8.67E-01 1.73E-01 -2.13E-01 1.12E+00-5.01E-05  7.54E-05 8.15E-04 9.08E-03
  76  2.13E+00 9.41E-01 8.90E-01 1.44E-01 -1.92E-01 1.10E+00-4.03E-05  6.35E-05 7.14E-04 9.08E-03
  79  2.27E+00 9.53E-01 9.08E-01 1.19E-01 -1.70E-01 1.08E+00-3.21E-05  5.29E-05 6.16E-04 9.08E-03
  82  2.42E+00 9.62E-01 9.23E-01 9.65E-02 -1.48E-01 1.07E+00-2.54E-05  4.37E-05 5.25E-04 9.08E-03
  85  2.56E+00 9.70E-01 9.36E-01 7.72E-02 -1.26E-01 1.05E+00-1.98E-05  3.57E-05 4.40E-04 9.08E-03
  88  2.70E+00 9.77E-01 9.45E-01 6.09E-02 -1.06E-01 1.04E+00-1.52E-05  2.88E-05 3.64E-04 9.08E-03
  91  2.84E+00 9.82E-01 9.53E-01 4.73E-02 -8.74E-02 1.03E+00-1.16E-05  2.30E-05 2.96E-04 9.08E-03
  94  2.99E+00 9.87E-01 9.59E-01 3.62E-02 -7.08E-02 1.02E+00-8.73E-06  1.81E-05 2.38E-04 9.08E-03
  97  3.13E+00 9.90E-01 9.63E-01 2.72E-02 -5.64E-02 1.02E+00-6.48E-06  1.41E-05 1.88E-04 9.08E-03
 100  3.27E+00 9.93E-01 9.66E-01 2.02E-02 -4.41E-02 1.01E+00-4.73E-06  1.08E-05 1.46E-04 9.08E-03
 103  3.41E+00 9.95E-01 9.69E-01 1.47E-02 -3.39E-02 1.01E+00-3.40E-06  8.28E-06 1.12E-04 9.08E-03
 106  3.55E+00 9.96E-01 9.71E-01 1.06E-02 -2.56E-02 1.01E+00-2.38E-06  6.31E-06 8.40E-05 9.08E-03
 109  3.70E+00 9.97E-01 9.72E-01 7.46E-03 -1.90E-02 1.00E+00-1.61E-06  4.73E-06 6.22E-05 9.08E-03
 112  3.84E+00 9.98E-01 9.73E-01 5.17E-03 -1.39E-02 1.00E+00-1.04E-06  3.44E-06 4.53E-05 9.08E-03
 115  3.98E+00 9.99E-01 9.73E-01 3.51E-03 -9.97E-03 1.00E+00-6.27E-07  2.45E-06 3.24E-05 9.08E-03
 118  4.12E+00 9.99E-01 9.74E-01 2.33E-03 -7.03E-03 1.00E+00-3.39E-07  1.71E-06 2.28E-05 9.08E-03
 121  4.27E+00 9.99E-01 9.74E-01 1.50E-03 -4.87E-03 1.00E+00-1.40E-07  1.17E-06 1.58E-05 9.08E-03
 124  4.41E+00 1.00E+00 9.74E-01 9.35E-04 -3.31E-03 1.00E+00-4.35E-10  8.21E-07 1.07E-05 9.08E-03
 127  4.55E+00 1.00E+00 9.74E-01 5.54E-04 -2.21E-03 1.00E+00 1.03E-07  6.96E-07 7.13E-06 9.08E-03
 130  4.69E+00 1.00E+00 9.74E-01 3.01E-04 -1.45E-03 1.00E+00 1.94E-07  6.11E-07 4.67E-06 9.08E-03
 133  4.83E+00 1.00E+00 9.74E-01 1.35E-04 -1.04E-03 1.00E+00 2.79E-07  6.32E-07 3.35E-06 9.08E-03
 136  4.84E+00 1.00E+00 9.74E-01 1.30E-04 -9.65E-04 1.00E+00 2.89E-07  2.67E-06 3.05E-06 9.08E-03
 139  4.84E+00 1.00E+00 9.74E-01 1.25E-04 -1.03E-03 1.00E+00 3.01E-07  1.80E-06 3.17E-06 9.08E-03
 142  4.85E+00 1.00E+00 9.74E-01 1.20E-04 -1.09E-03 1.00E+00 3.07E-07  1.24E-06 3.25E-06 9.08E-03
 145  4.86E+00 1.00E+00 9.74E-01 1.14E-04 -1.11E-03 1.00E+00 3.13E-07  1.24E-06 3.44E-06 9.08E-03
 148  4.86E+00 1.00E+00 9.74E-01 1.08E-04 -1.17E-03 1.00E+00 3.18E-07  1.77E-07 3.61E-06 9.08E-03
 151  4.86E+00 1.00E+00 9.74E-01 1.03E-04 -1.23E-03 1.00E+00 3.19E-07  1.39E-07 3.81E-06 9.08E-03
 154  4.87E+00 1.00E+00 9.74E-01 9.65E-05 -1.26E-03 1.00E+00 3.19E-07  1.38E-07 3.98E-06 9.08E-03
 157  4.88E+00 1.00E+00 9.74E-01 9.02E-05 -1.30E-03 1.00E+00 3.16E-07 -1.04E-06 4.17E-06 9.08E-03
 160  4.88E+00 1.00E+00 9.74E-01 8.37E-05 -1.32E-03 1.00E+00 3.11E-07 -1.07E-06 4.01E-06 9.08E-03
 163  4.89E+00 1.00E+00 9.74E-01 7.73E-05 -1.26E-03 1.00E+00 3.06E-07 -1.57E-06 3.57E-06 9.08E-03
 166  4.89E+00 1.00E+00 9.74E-01 7.13E-05 -1.18E-03 1.00E+00 2.96E-07 -2.17E-06 2.90E-06 9.08E-03
 169  4.89E+00 1.00E+00 9.74E-01 6.56E-05 -1.11E-03 1.00E+00 2.85E-07 -2.17E-06 2.79E-06 9.08E-03
 172  4.90E+00 1.00E+00 9.74E-01 6.02E-05 -1.10E-03 1.00E+00 2.73E-07 -3.27E-06 2.95E-06 9.08E-03
 175  4.91E+00 1.00E+00 9.74E-01 5.48E-05 -1.11E-03 1.00E+00 2.57E-07 -3.27E-06 3.24E-06 9.08E-03
 178  4.91E+00 1.00E+00 9.74E-01 4.95E-05 -1.07E-03 1.00E+00 2.41E-07 -3.31E-06 3.22E-06 9.08E-03
 181  4.91E+00 1.00E+00 9.74E-01 4.43E-05 -1.07E-03 1.00E+00 2.21E-07 -4.48E-06 3.34E-06 9.08E-03
 184  4.92E+00 1.00E+00 9.74E-01 3.87E-05 -1.18E-03 1.00E+00 1.99E-07 -4.45E-06 3.89E-06 9.08E-03
 187  4.93E+00 1.00E+00 9.74E-01 3.30E-05 -1.13E-03 1.00E+00 1.78E-07 -4.41E-06 3.77E-06 9.08E-03
 190  4.93E+00 1.00E+00 9.74E-01 2.75E-05 -1.09E-03 1.00E+00 1.52E-07 -5.54E-06 3.71E-06 9.08E-03
 193  4.93E+00 1.00E+00 9.74E-01 2.22E-05 -1.10E-03 1.00E+00 1.25E-07 -5.58E-06 3.94E-06 9.08E-03
 196  4.94E+00 1.00E+00 9.74E-01 1.66E-05 -1.15E-03 1.00E+00 9.76E-08 -5.58E-06 4.42E-06 9.08E-03
 199  4.95E+00 1.00E+00 9.74E-01 1.09E-05 -1.19E-03 1.00E+00 6.67E-08 -6.72E-06 4.76E-06 9.08E-03
 202  4.95E+00 1.00E+00 9.74E-01 5.03E-06 -1.18E-03 1.00E+00 3.36E-08 -6.72E-06 4.62E-06 9.08E-03
 205  4.95E+00 1.00E+00 9.74E-01 0.00E+00  0.00E+00 1.00E+00 0.00E+00  0.00E+00 0.00E+00 9.08E-03
```

TABLE 4.3.b : BOUNDARY LAYER SURVEY AT THE SECOND STATION (M=3.7)

X = 138.890   U =   1.250   M = 3.70   RDT = 2.76E+04
TURB =1.000   RW = 5.50E+01   VW = 0.00E+00   SW = 0.00E+00   CW = 0.00E+00
DT = 6.19E-01 MT = 8.31E-02 HT =-1.79E-05 SF = 7.45E+00 CF = 1.95E-03 ST = 0.00E+00
HR = 1.00E+00   PR = 7.80E-01   PRT = 1.00E+00   SHR = 1.40

J	YY	u/U	F	FP	FPP	D	GP	GPP	TAU	VE
1	0.00E+00	0.00E+00	0.00E+00	1.00E+00	-3.00E+00	3.59E+00	3.89E-02	0.00E+00	9.75E-04	3.25E-04
4	7.10E-02	5.46E-01	6.37E-02	8.12E-01	-1.47E+00	2.90E+00	3.94E-03	-2.43E-01	9.83E-04	1.00E-03
7	1.42E-01	6.44E-01	1.19E-01	7.52E-01	-5.97E-01	2.60E+00	5.20E-04	-1.53E-02	8.58E-04	2.68E-03
10	2.13E-01	6.89E-01	1.71E-01	7.17E-01	-4.23E-01	2.43E+00	-1.01E-04	-5.38E-03	8.08E-04	3.95E-03
13	2.85E-01	7.19E-01	2.21E-01	6.90E-01	-3.43E-01	2.32E+00	-3.69E-04	-2.01E-03	7.81E-04	5.07E-03
16	3.56E-01	7.42E-01	2.69E-01	6.66E-01	-3.29E-01	2.23E+00	-3.71E-04	4.73E-04	7.39E-04	5.33E-03
19	4.27E-01	7.63E-01	3.16E-01	6.43E-01	-3.34E-01	2.14E+00	-3.39E-04	4.23E-04	7.09E-04	5.33E-03
22	4.99E-01	7.83E-01	3.60E-01	6.19E-01	-3.39E-01	2.05E+00	-3.10E-04	3.85E-04	6.80E-04	5.33E-03
25	5.70E-01	8.01E-01	4.04E-01	5.95E-01	-3.43E-01	1.98E+00	-2.84E-04	3.58E-04	6.52E-04	5.33E-03
28	6.42E-01	8.17E-01	4.45E-01	5.70E-01	-3.46E-01	1.90E+00	-2.59E-04	3.33E-04	6.25E-04	5.33E-03
31	7.13E-01	8.33E-01	4.84E-01	5.46E-01	-3.49E-01	1.83E+00	-2.37E-04	3.09E-04	5.99E-04	5.33E-03
34	7.85E-01	8.47E-01	5.22E-01	5.21E-01	-3.50E-01	1.77E+00	-2.16E-04	2.86E-04	5.73E-04	5.33E-03
37	8.56E-01	8.60E-01	5.58E-01	4.96E-01	-3.51E-01	1.71E+00	-1.96E-04	2.65E-04	5.48E-04	5.33E-03
40	9.28E-01	8.72E-01	5.93E-01	4.71E-01	-3.50E-01	1.65E+00	-1.78E-04	2.45E-04	5.24E-04	5.33E-03
43	1.00E+00	8.83E-01	6.25E-01	4.46E-01	-3.48E-01	1.60E+00	-1.61E-04	2.25E-04	5.00E-04	5.33E-03
46	1.07E+00	8.94E-01	6.56E-01	4.22E-01	-3.45E-01	1.55E+00	-1.46E-04	2.07E-04	4.76E-04	5.33E-03
49	1.14E+00	9.03E-01	6.85E-01	3.97E-01	-3.41E-01	1.50E+00	-1.32E-04	1.91E-04	4.53E-04	5.33E-03
52	1.22E+00	9.12E-01	7.12E-01	3.73E-01	-3.36E-01	1.46E+00	-1.19E-04	1.75E-04	4.30E-04	5.33E-03
55	1.29E+00	9.20E-01	7.38E-01	3.50E-01	-3.30E-01	1.42E+00	-1.07E-04	1.60E-04	4.07E-04	5.33E-03
58	1.36E+00	9.27E-01	7.62E-01	3.27E-01	-3.22E-01	1.38E+00	-9.62E-05	1.46E-04	3.85E-04	5.33E-03
61	1.43E+00	9.34E-01	7.84E-01	3.04E-01	-3.10E-01	1.34E+00	-8.64E-05	1.31E-04	3.59E-04	5.33E-03
64	1.57E+00	9.46E-01	8.24E-01	2.62E-01	-2.92E-01	1.28E+00	-6.92E-05	1.10E-04	3.20E-04	5.33E-03
67	1.72E+00	9.57E-01	8.58E-01	2.22E-01	-2.68E-01	1.23E+00	-5.51E-05	9.01E-05	2.79E-04	5.33E-03
70	1.86E+00	9.65E-01	8.87E-01	1.86E-01	-2.42E-01	1.19E+00	-4.36E-05	7.32E-05	2.41E-04	5.33E-03
73	2.01E+00	9.72E-01	9.11E-01	1.54E-01	-2.15E-01	1.15E+00	-3.43E-05	5.88E-05	2.05E-04	5.33E-03
76	2.15E+00	9.78E-01	9.31E-01	1.25E-01	-1.87E-01	1.12E+00	-2.69E-05	4.67E-05	1.73E-04	5.33E-03
79	2.30E+00	9.83E-01	9.47E-01	1.01E-01	-1.61E-01	1.09E+00	-2.10E-05	3.67E-05	1.44E-04	5.33E-03
82	2.44E+00	9.87E-01	9.59E-01	7.97E-02	-1.35E-01	1.07E+00	-1.64E-05	2.85E-05	1.18E-04	5.33E-03
85	2.59E+00	9.90E-01	9.69E-01	6.23E-02	-1.12E-01	1.06E+00	-1.29E-05	2.20E-05	9.62E-05	5.33E-03
88	2.73E+00	9.92E-01	9.77E-01	4.80E-02	-9.13E-02	1.04E+00	-1.02E-05	1.70E-05	7.70E-05	5.33E-03
91	2.88E+00	9.94E-01	9.83E-01	3.65E-02	-7.31E-02	1.03E+00	-8.08E-06	1.29E-05	6.09E-05	5.33E-03
94	3.03E+00	9.96E-01	9.87E-01	2.73E-02	-5.77E-02	1.02E+00	-6.51E-06	9.44E-06	4.74E-05	5.33E-03
97	3.17E+00	9.97E-01	9.91E-01	2.01E-02	-4.47E-02	1.02E+00	-5.39E-06	6.83E-06	3.65E-05	5.33E-03
100	3.32E+00	9.98E-01	9.93E-01	1.46E-02	-3.41E-02	1.01E+00	-4.57E-06	4.80E-06	2.76E-05	5.33E-03
103	3.47E+00	9.98E-01	9.95E-01	1.04E-02	-2.57E-02	1.01E+00	-4.00E-06	3.38E-06	2.06E-05	5.33E-03
106	3.61E+00	9.99E-01	9.96E-01	7.32E-03	-1.90E-02	1.01E+00	-3.61E-06	2.25E-06	1.52E-05	5.33E-03
109	3.76E+00	9.99E-01	9.97E-01	5.04E-03	-1.38E-02	1.00E+00	-3.35E-06	1.49E-06	1.10E-05	5.33E-03
112	3.91E+00	9.99E-01	9.98E-01	3.39E-03	-9.90E-03	1.00E+00	-3.19E-06	8.82E-07	7.86E-06	5.33E-03
115	4.05E+00	1.00E+00	9.98E-01	2.22E-03	-6.98E-03	1.00E+00	-3.10E-06	3.41E-07	5.52E-06	5.33E-03
118	4.20E+00	1.00E+00	9.98E-01	1.40E-03	-4.85E-03	1.00E+00	-3.07E-06	1.44E-07	3.80E-06	5.33E-03
121	4.35E+00	1.00E+00	9.98E-01	8.31E-04	-3.31E-03	1.00E+00	-3.05E-06	6.41E-08	2.58E-06	5.33E-03
124	4.50E+00	1.00E+00	9.98E-01	4.48E-04	-2.23E-03	1.00E+00	-3.06E-06	-1.55E-07	1.73E-06	5.33E-03
127	4.65E+00	1.00E+00	9.98E-01	1.93E-04	-1.47E-03	1.00E+00	-3.08E-06	-5.73E-08	1.14E-06	5.33E-03
130	4.79E+00	1.00E+00	9.98E-01	2.58E-05	-9.63E-04	1.00E+00	-3.09E-06	-9.47E-08	7.29E-07	5.33E-03
133	4.94E+00	1.00E+00	9.98E-01	-8.69E-05	-7.24E-04	1.00E+00	-3.12E-06	-2.50E-07	5.43E-07	5.33E-03
136	4.95E+00	1.00E+00	9.98E-01	-9.05E-05	-5.63E-04	1.00E+00	-3.11E-06	5.87E-06	6.89E-07	5.33E-03
139	4.95E+00	1.00E+00	9.98E-01	-9.26E-05	-3.61E-04	1.00E+00	-3.08E-06	6.96E-06	6.59E-07	5.33E-03
142	4.96E+00	1.00E+00	9.98E-01	-9.39E-05	-1.43E-04	1.00E+00	-3.04E-06	8.10E-06	5.71E-07	5.33E-03
145	4.97E+00	1.00E+00	9.98E-01	-9.40E-05	9.23E-05	1.00E+00	-3.00E-06	9.24E-06	6.19E-07	5.33E-03
148	4.97E+00	1.00E+00	9.98E-01	-9.33E-05	1.71E-04	1.00E+00	-2.94E-06	1.51E-05	7.10E-07	5.33E-03
151	4.98E+00	1.00E+00	9.98E-01	-9.18E-05	4.22E-04	1.00E+00	-2.85E-06	1.84E-05	2.88E-07	5.33E-03
154	4.98E+00	1.00E+00	9.98E-01	-8.94E-05	5.68E-04	1.00E+00	-2.76E-06	1.96E-05	4.13E-07	5.33E-03
157	4.99E+00	1.00E+00	9.98E-01	-8.63E-05	6.91E-04	1.00E+00	-2.66E-06	1.95E-05	3.17E-07	5.33E-03
160	4.99E+00	1.00E+00	9.98E-01	-8.25E-05	7.97E-04	1.00E+00	-2.56E-06	2.40E-05	3.09E-07	5.33E-03
163	5.00E+00	1.00E+00	9.98E-01	-7.87E-05	7.68E-04	1.00E+00	-2.44E-06	2.30E-05	4.85E-07	5.33E-03
166	5.00E+00	1.00E+00	9.98E-01	-7.48E-05	7.83E-04	1.00E+00	-2.32E-06	2.41E-05	4.01E-07	5.33E-03
169	5.01E+00	1.00E+00	9.98E-01	-7.09E-05	8.19E-04	1.00E+00	-2.20E-06	2.63E-05	2.18E-07	5.33E-03
172	5.01E+00	1.00E+00	9.98E-01	-6.68E-05	8.59E-04	1.00E+00	-2.07E-06	2.76E-05	1.10E-07	5.33E-03
175	5.02E+00	1.00E+00	9.98E-01	-6.25E-05	9.32E-04	1.00E+00	-1.93E-06	2.98E-05	-9.74E-08	5.33E-03
178	5.02E+00	1.00E+00	9.98E-01	-5.76E-05	1.04E-03	1.00E+00	-1.77E-06	3.20E-05	-2.42E-07	5.33E-03
181	5.03E+00	1.00E+00	9.98E-01	-5.23E-05	1.09E-03	1.00E+00	-1.61E-06	3.53E-05	-1.37E-07	5.33E-03
184	5.03E+00	1.00E+00	9.98E-01	-4.68E-05	1.18E-03	1.00E+00	-1.43E-06	3.66E-05	-1.24E-07	5.33E-03
187	5.04E+00	1.00E+00	9.98E-01	-4.08E-05	1.22E-03	1.00E+00	-1.25E-06	3.78E-05	7.58E-08	5.33E-03
190	5.04E+00	1.00E+00	9.98E-01	-3.47E-05	1.30E-03	1.00E+00	-1.06E-06	3.90E-05	-6.42E-08	5.33E-03
193	5.05E+00	1.00E+00	9.98E-01	-2.81E-05	1.38E-03	1.00E+00	-8.62E-07	4.00E-05	3.29E-08	5.33E-03
196	5.05E+00	1.00E+00	9.98E-01	-2.11E-05	1.47E-03	1.00E+00	-6.65E-07	4.23E-05	-3.15E-08	5.33E-03
199	5.06E+00	1.00E+00	9.98E-01	-1.35E-05	1.62E-03	1.00E+00	-4.45E-07	4.57E-05	-1.40E-07	5.33E-03
202	5.06E+00	1.00E+00	9.98E-01	-5.28E-06	1.62E-03	1.00E+00	-2.22E-07	4.46E-05	-3.65E-07	5.33E-03
205	5.07E+00	1.00E+00	9.98E-01	0.00E+00	0.00E+00	1.00E+00	0.00E+00	0.00E+00	0.00E+00	5.33E-03

TABLE 4.3.c : BOUDARY LAYER SURVEY AT THE THIRD STATION (M=4.4)

X = 241.810   U =   1.302   M = 4.40   RDT = 4.39E+04
TURB =1.000   RW = 8.25E+01   VW = 0.00E+00   SW = 0.00E+00   CW = 0.00E+00
DT = 1.42E+00 MT = 1.47E-01 HT =-4.49E-05 SF = 9.64E+00 CF = 2.08E-03 ST = 0.00E+00
HR = 1.00E+00   PR = 7.80E-01   PRT = 1.00E+00   SHR = 1.40

J	YY	u/U	F	FP	FPP	D	GP	GPP	TAU	VE
1	0.00E+00	0.00E+00	0.00E+00	1.00E+00	-3.69E+00	4.64E+00	4.71E-02	0.00E+00	1.04E-03	2.82E-04
4	7.11E-02	6.42E-01	6.28E-02	8.04E-01	-1.31E+00	3.27E+00	2.83E-03	-1.48E-01	1.02E-03	1.50E-03
7	1.42E-01	7.27E-01	1.18E-01	7.43E-01	-6.66E-01	2.83E+00	7.11E-04	-1.30E-02	7.42E-04	2.72E-03
10	2.14E-01	7.69E-01	1.69E-01	7.02E-01	-4.95E-01	2.58E+00	1.34E-04	-4.53E-03	6.60E-04	3.70E-03
13	2.86E-01	7.97E-01	2.18E-01	6.70E-01	-4.47E-01	2.41E+00	2.53E-05	-7.20E-04	5.83E-04	3.99E-03
16	3.57E-01	8.21E-01	2.64E-01	6.38E-01	-4.36E-01	2.27E+00	-2.03E-05	-5.62E-04	5.21E-04	3.99E-03
19	4.29E-01	8.40E-01	3.08E-01	6.08E-01	-4.24E-01	2.14E+00	-5.52E-05	-4.29E-04	4.70E-04	3.99E-03
22	5.01E-01	8.57E-01	3.50E-01	5.78E-01	-4.11E-01	2.03E+00	-8.17E-05	-3.23E-04	4.25E-04	3.99E-03
25	5.74E-01	8.72E-01	3.90E-01	5.49E-01	-3.98E-01	1.93E+00	-1.01E-04	-2.37E-04	3.85E-04	3.99E-03
28	6.46E-01	8.84E-01	4.28E-01	5.22E-01	-3.84E-01	1.85E+00	-1.16E-04	-1.68E-04	3.51E-04	3.99E-03
31	7.19E-01	8.95E-01	4.64E-01	4.95E-01	-3.71E-01	1.77E+00	-1.26E-04	-1.11E-04	3.20E-04	3.99E-03
34	7.91E-01	9.05E-01	4.99E-01	4.69E-01	-3.57E-01	1.70E+00	-1.32E-04	-6.62E-05	2.93E-04	3.99E-03
37	8.64E-01	9.13E-01	5.31E-01	4.44E-01	-3.43E-01	1.64E+00	-1.35E-04	-2.97E-05	2.69E-04	3.99E-03
40	9.37E-01	9.21E-01	5.62E-01	4.21E-01	-3.29E-01	1.59E+00	-1.36E-04	-7.93E-07	2.47E-04	3.99E-03
43	1.01E+00	9.28E-01	5.91E-01	3.98E-01	-3.15E-01	1.54E+00	-1.35E-04	2.16E-05	2.27E-04	3.99E-03
46	1.08E+00	9.34E-01	6.18E-01	3.76E-01	-3.01E-01	1.50E+00	-1.33E-04	3.91E-05	2.10E-04	3.99E-03
49	1.16E+00	9.39E-01	6.44E-01	3.55E-01	-2.88E-01	1.46E+00	-1.30E-04	5.22E-05	1.94E-04	3.99E-03
52	1.23E+00	9.44E-01	6.68E-01	3.35E-01	-2.75E-01	1.42E+00	-1.26E-04	6.22E-05	1.79E-04	3.99E-03
55	1.30E+00	9.49E-01	6.91E-01	3.16E-01	-2.63E-01	1.39E+00	-1.21E-04	6.93E-05	1.66E-04	3.99E-03
58	1.38E+00	9.53E-01	7.13E-01	2.98E-01	-2.50E-01	1.36E+00	-1.16E-04	7.45E-05	1.54E-04	3.99E-03
61	1.45E+00	9.57E-01	7.34E-01	2.81E-01	-2.34E-01	1.33E+00	-1.11E-04	7.75E-05	1.40E-04	3.99E-03
64	1.60E+00	9.63E-01	7.71E-01	2.49E-01	-2.16E-01	1.28E+00	-9.96E-05	7.88E-05	1.23E-04	3.99E-03
67	1.75E+00	9.68E-01	8.04E-01	2.20E-01	-1.96E-01	1.24E+00	-8.86E-05	7.65E-05	1.07E-04	3.99E-03
70	1.90E+00	9.73E-01	8.33E-01	1.93E-01	-1.78E-01	1.21E+00	-7.81E-05	7.17E-05	9.36E-05	3.99E-03
73	2.05E+00	9.77E-01	8.59E-01	1.69E-01	-1.61E-01	1.18E+00	-6.83E-05	6.59E-05	8.19E-05	3.99E-03
76	2.21E+00	9.80E-01	8.81E-01	1.48E-01	-1.45E-01	1.15E+00	-5.95E-05	5.96E-05	7.18E-05	3.99E-03
79	2.36E+00	9.83E-01	9.01E-01	1.28E-01	-1.31E-01	1.13E+00	-5.15E-05	5.32E-05	6.31E-05	3.99E-03
82	2.51E+00	9.86E-01	9.18E-01	1.11E-01	-1.18E-01	1.11E+00	-4.45E-05	4.68E-05	5.53E-05	3.99E-03
85	2.67E+00	9.88E-01	9.32E-01	9.49E-02	-1.05E-01	1.09E+00	-3.83E-05	4.08E-05	4.83E-05	3.99E-03
88	2.82E+00	9.90E-01	9.44E-01	8.09E-02	-9.37E-02	1.08E+00	-3.29E-05	3.54E-05	4.21E-05	3.99E-03
91	2.98E+00	9.92E-01	9.55E-01	6.85E-02	-8.27E-02	1.06E+00	-2.83E-05	3.06E-05	3.65E-05	3.99E-03
94	3.13E+00	9.93E-01	9.64E-01	5.76E-02	-7.24E-02	1.05E+00	-2.43E-05	2.62E-05	3.14E-05	3.99E-03
97	3.29E+00	9.94E-01	9.71E-01	4.81E-02	-6.28E-02	1.04E+00	-2.09E-05	2.23E-05	2.68E-05	3.99E-03
100	3.45E+00	9.95E-01	9.77E-01	3.99E-02	-5.40E-02	1.04E+00	-1.80E-05	1.89E-05	2.27E-05	3.99E-03
103	3.61E+00	9.96E-01	9.83E-01	3.28E-02	-4.61E-02	1.03E+00	-1.55E-05	1.61E-05	1.91E-05	3.99E-03
106	3.77E+00	9.97E-01	9.87E-01	2.69E-02	-3.89E-02	1.02E+00	-1.34E-05	1.36E-05	1.59E-05	3.99E-03
109	3.93E+00	9.97E-01	9.90E-01	2.19E-02	-3.26E-02	1.02E+00	-1.17E-05	1.12E-05	1.32E-05	3.99E-03
112	4.09E+00	9.98E-01	9.93E-01	1.77E-02	-2.71E-02	1.02E+00	-1.03E-05	9.42E-06	1.09E-05	3.99E-03
115	4.26E+00	9.98E-01	9.95E-01	1.42E-02	-2.24E-02	1.01E+00	-9.06E-06	7.78E-06	8.88E-06	3.99E-03
118	4.42E+00	9.99E-01	9.97E-01	1.14E-02	-1.84E-02	1.01E+00	-8.06E-06	6.68E-06	7.22E-06	3.99E-03
121	4.58E+00	9.99E-01	9.98E-01	9.01E-03	-1.51E-02	1.01E+00	-7.17E-06	5.91E-06	5.89E-06	3.99E-03
124	4.75E+00	9.99E-01	9.99E-01	7.08E-03	-1.27E-02	1.01E+00	-6.36E-06	5.96E-06	4.90E-06	3.99E-03
127	4.92E+00	9.99E-01	1.00E+00	5.41E-03	-1.14E-02	1.00E+00	-5.48E-06	7.02E-06	4.40E-06	3.99E-03
130	5.08E+00	1.00E+00	1.00E+00	3.80E-03	-1.20E-02	1.00E+00	-4.29E-06	1.08E-05	4.61E-06	3.99E-03
133	5.25E+00	1.00E+00	1.00E+00	1.98E-03	-1.38E-02	1.00E+00	-2.16E-06	1.88E-05	5.34E-06	3.99E-03
136	5.26E+00	1.00E+00	1.00E+00	1.89E-03	-1.60E-02	1.00E+00	-2.06E-06	1.81E-05	6.00E-06	3.99E-03
139	5.27E+00	1.00E+00	1.00E+00	1.81E-03	-1.63E-02	1.00E+00	-1.98E-06	1.54E-05	5.69E-06	3.99E-03
142	5.27E+00	1.00E+00	1.00E+00	1.73E-03	-1.63E-02	1.00E+00	-1.91E-06	1.34E-05	5.69E-06	3.99E-03
145	5.28E+00	1.00E+00	1.00E+00	1.65E-03	-1.63E-02	1.00E+00	-1.85E-06	1.02E-05	5.54E-06	3.99E-03
148	5.28E+00	1.00E+00	1.00E+00	1.57E-03	-1.64E-02	1.00E+00	-1.81E-06	8.94E-06	5.28E-06	3.99E-03
151	5.29E+00	1.00E+00	1.00E+00	1.49E-03	-1.63E-02	1.00E+00	-1.76E-06	9.85E-06	4.91E-06	3.99E-03
154	5.30E+00	1.00E+00	1.00E+00	1.41E-03	-1.63E-02	1.00E+00	-1.73E-06	5.49E-06	4.79E-06	3.99E-03
157	5.30E+00	1.00E+00	1.00E+00	1.33E-03	-1.62E-02	1.00E+00	-1.72E-06	1.93E-06	4.50E-06	3.99E-03
160	5.31E+00	1.00E+00	1.00E+00	1.25E-03	-1.64E-02	1.00E+00	-1.70E-06	2.88E-06	4.84E-06	3.99E-03
163	5.31E+00	1.00E+00	1.00E+00	1.17E-03	-1.66E-02	1.00E+00	-1.69E-06	1.60E-07	4.94E-06	3.99E-03
166	5.32E+00	1.00E+00	1.00E+00	1.09E-03	-1.68E-02	1.00E+00	-1.70E-06	-4.39E-06	5.24E-06	3.99E-03
169	5.33E+00	1.00E+00	1.00E+00	1.00E-03	-1.70E-02	1.00E+00	-1.72E-06	-5.38E-06	5.50E-06	3.99E-03
172	5.33E+00	1.00E+00	1.00E+00	9.18E-04	-1.71E-02	1.00E+00	-1.75E-06	-6.21E-06	5.61E-06	3.99E-03
175	5.34E+00	1.00E+00	1.00E+00	8.34E-04	-1.71E-02	1.00E+00	-1.79E-06	-7.24E-06	5.71E-06	3.99E-03
178	5.34E+00	1.00E+00	1.00E+00	7.50E-04	-1.72E-02	1.00E+00	-1.82E-06	-1.52E-06	5.79E-06	3.99E-03
181	5.35E+00	1.00E+00	1.00E+00	6.65E-04	-1.74E-02	1.00E+00	-1.81E-06	6.53E-06	6.05E-06	3.99E-03
184	5.36E+00	1.00E+00	1.00E+00	5.79E-04	-1.75E-02	1.00E+00	-1.75E-06	1.56E-05	6.18E-06	3.99E-03
187	5.36E+00	1.00E+00	1.00E+00	4.92E-04	-1.76E-02	1.00E+00	-1.66E-06	2.35E-05	6.30E-06	3.99E-03
190	5.37E+00	1.00E+00	1.00E+00	4.05E-04	-1.78E-02	1.00E+00	-1.52E-06	3.49E-05	6.58E-06	3.99E-03
193	5.37E+00	1.00E+00	1.00E+00	3.18E-04	-1.79E-02	1.00E+00	-1.32E-06	4.43E-05	6.72E-06	3.99E-03
196	5.38E+00	1.00E+00	1.00E+00	2.29E-04	-1.79E-02	1.00E+00	-1.08E-06	5.36E-05	6.86E-06	3.99E-03
199	5.39E+00	1.00E+00	1.00E+00	1.41E-04	-1.78E-02	1.00E+00	-7.88E-07	6.62E-05	6.69E-06	3.99E-03
202	5.39E+00	1.00E+00	1.00E+00	5.61E-05	-1.61E-02	1.00E+00	-4.28E-07	7.99E-05	6.37E-06	3.99E-03
205	5.40E+00	1.00E+00	1.00E+00	0.00E+00	0.00E+00	1.00E+00	0.00E+00	0.00E+00	0.00E+00	3.99E-03

SECTION 5 : Three dimensional design

5.1 General

In order to transform the axisymmetric nozzles computed above to more general non-axisymmetric ones, the desired shapes are chosen at the exit cross-section. The streamlines, whose intersection with the exit plane defines the particular profile shape, are then calculated and traced back to the throat. The resulting streamsheets then form the walls of the new nozzle shapes. Such a method would allow the simple design of non-axisymmetric nozzles without the complications involved when using three-dimensional methods (section 1).

5.2 Streamline calculation method

For a steady two-dimensional axisymmetric flow, the stream function and velocity are related through :

$$\frac{\partial\psi}{\partial z} = - \rho vy \qquad \text{and} \qquad \frac{\partial\psi}{\partial y} = \rho uy \qquad \dots (5.1)$$

where z and y represent the axial and radial coordinates respectively. The streamlines (defined as the lines for which $\psi(z,y) =$ constant) can be determined either by constructing them from the known local flow directions or more systematically by integrating the axisymmetric stream function. The second procedure was used and may be described as follows :

1. By considering a particular cross-section (the exit for example), the axial coordinate z is prescribed and therefore the problem is transformed from a two-dimensional one where the stream function depends on both the coordinates to effectively a

one-dimensional problem where it only depends on y :

$$\psi = \int_0^y \rho\ u\ y\ dy \qquad \ldots\ (\ 5.2\ )$$

2. Along the cross-section considered, the density and streamwise (axial) velocity are evaluated at several stations (10, in this case). This is effected by performing a plane interpolation between the results obtained by the method of characteristics program,

3. Using the calculated values of the velocity and density, the stream function is evaluated by performing a numerical integration of equation 5.2 at each station defined above,

4. By repeating the same procedure at further cross-sections, a set of stream functions is defined at each of them. This permits, by means of interpolation, the determination of the position of any stream function value along each of the cross-sections considered. The streamlines, defined as the lines of constant ψ, may therefore be constructed by joining the positions of each cross-section at which the stream functions have the same value,

5. One particular case which arises is concerned with the determination of the stream functions at the nozzle throat cross-section. Since the computations using the method of characteristics have been initiated from the initial-value line situated beyond the throat, the necessary parameters (density & velocity) for their evaluation cannot be computed at that position. Determination of the stream function, at the throat cross-section, has then been achieved by extrapolation of the known values from the other sections within the nozzle.

5.3 Elliptical nozzle design

The elliptical case presented is not directed towards any specific application but is typical of the types of nozzles wich might be used as either rocket, ramjet or scramjet nozzles. It may be connected to the pebble-bed heater which may then used as a combustion or heat transfer facility. Furthermore, since the investigation was carried out with a view to simple 'proof of concept', the elliptical exit plane presenting a smooth transition from the axisymmetric configuration seemed the appropriate choice.

5.3.1 Supersonic section design

Figure 5.1 shows the initial axisymmetric shape computed by the method of characteristics, outlined earlier, and the elliptical shape chosen at the exit cross-section. The equation of the ellipse was determined by selecting the ratio of the major axis to the minor one of b/a = 1.5.

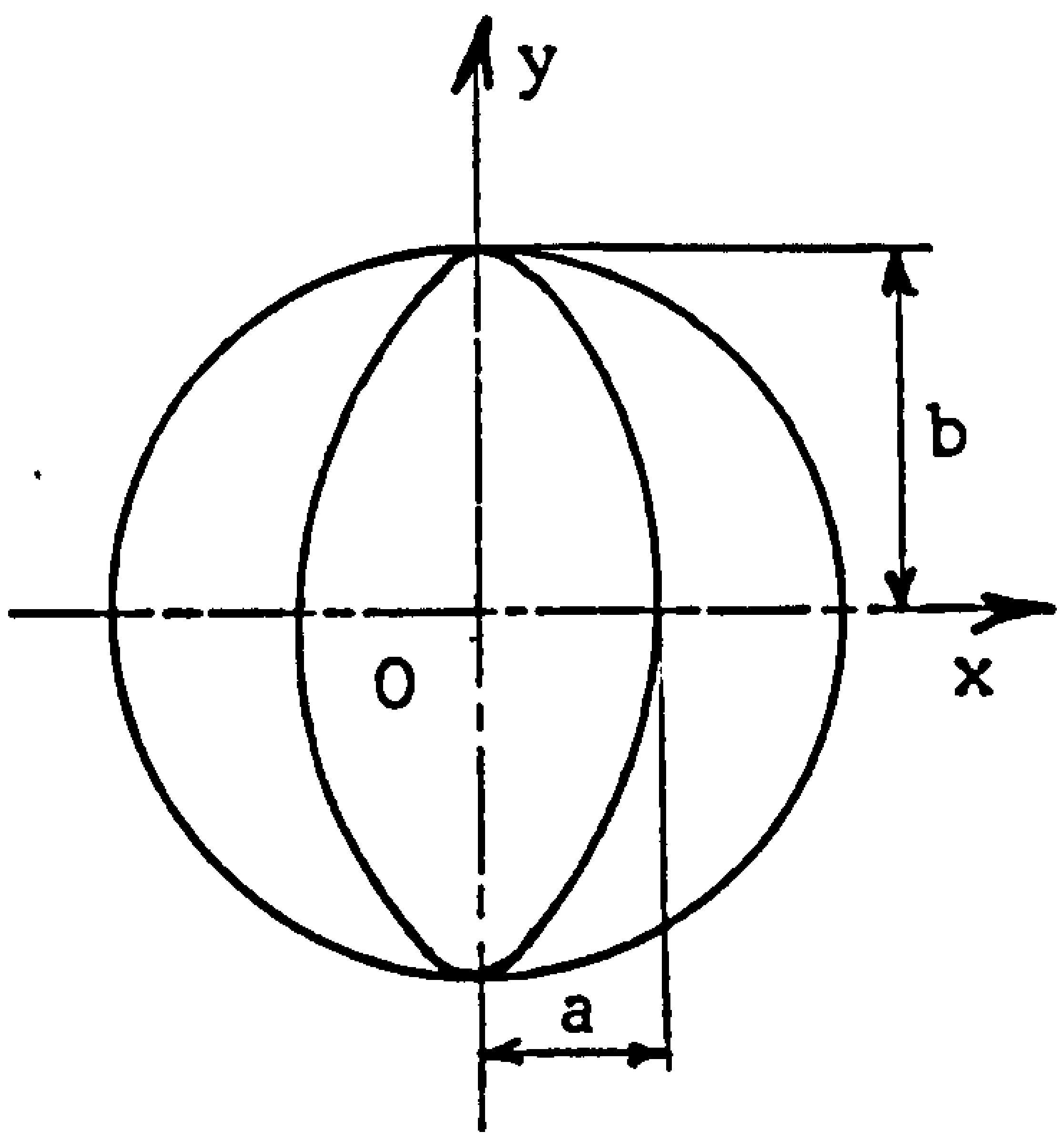

Fig. 5.1: Axisymmetric and elliptical exit cross-sections.

This permitted the discretization of the elliptical contour into several stations leading to the array of points presented in table 5.1. These points are traced along their respective streamlines back to the throat. Table 5.2 shows the defining points at the throat and exit cross-sections and figure 5.2 the streamline network.

5.3.2 Subsonic section design

The convergent section must effect a smooth transition from the elliptical throat to the axisymmetric supply pipe. This transition is carried out by arcs of circles starting from the stations defining the

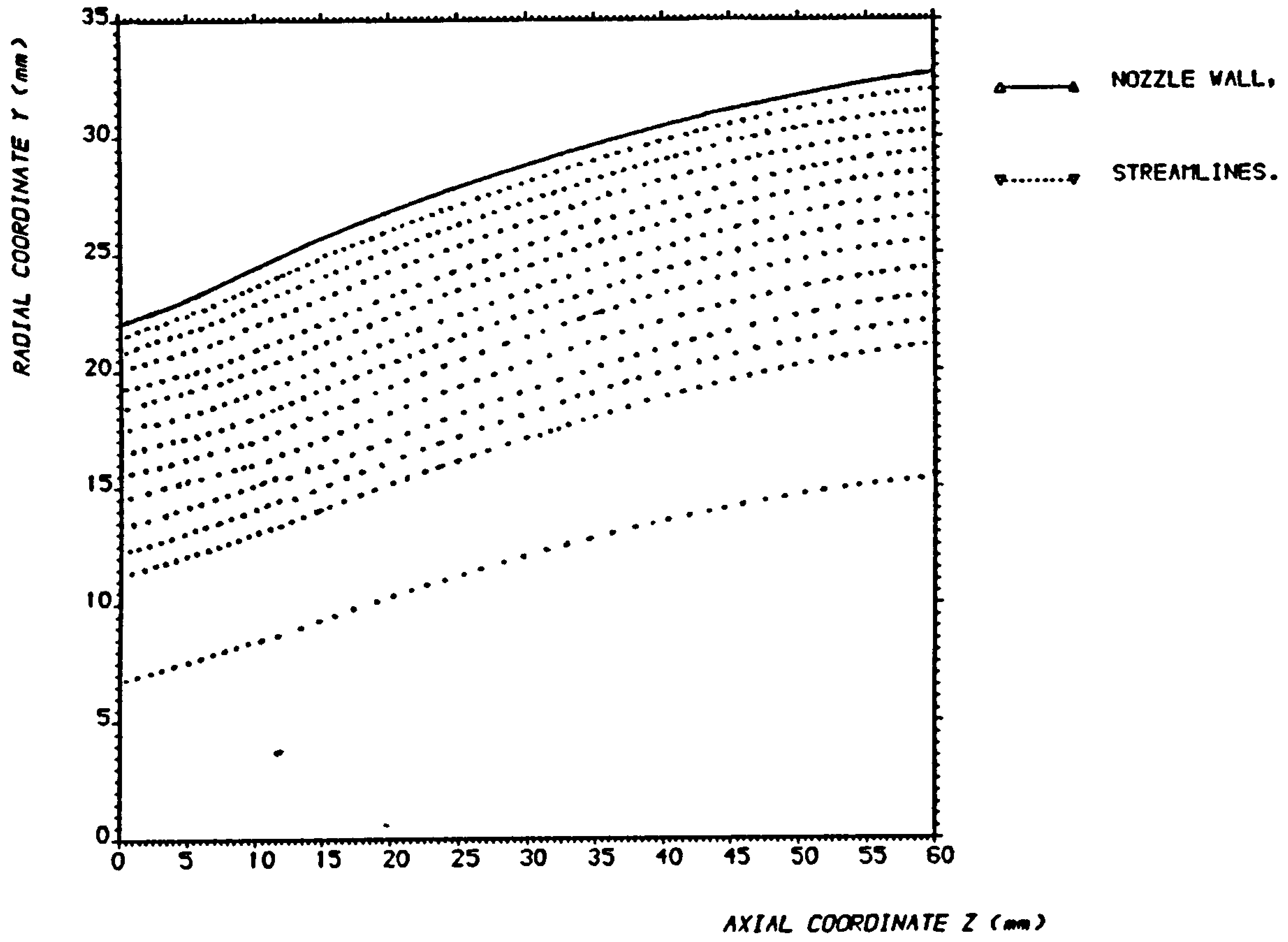

FIG : [5.2] STREAMLINES WITHIN THE DIVERGENT SECTION OF THE AXISYMMETRIC-FOR-EL LIPTIC NOZZLE.(AR=2.327) elliptical throat (points 1 to N in Figure 5.3 calculated within the supersonic section design and presented in table 5.2) and meeting the axisymmetric supply contour (point M in Figure 5.3). The circles having as radii R_i are centered on C. The equations defining the different circles to which the arcs belong are derived in appendix J. Table 5.3 shows the circle characteristics (centre position, radii).

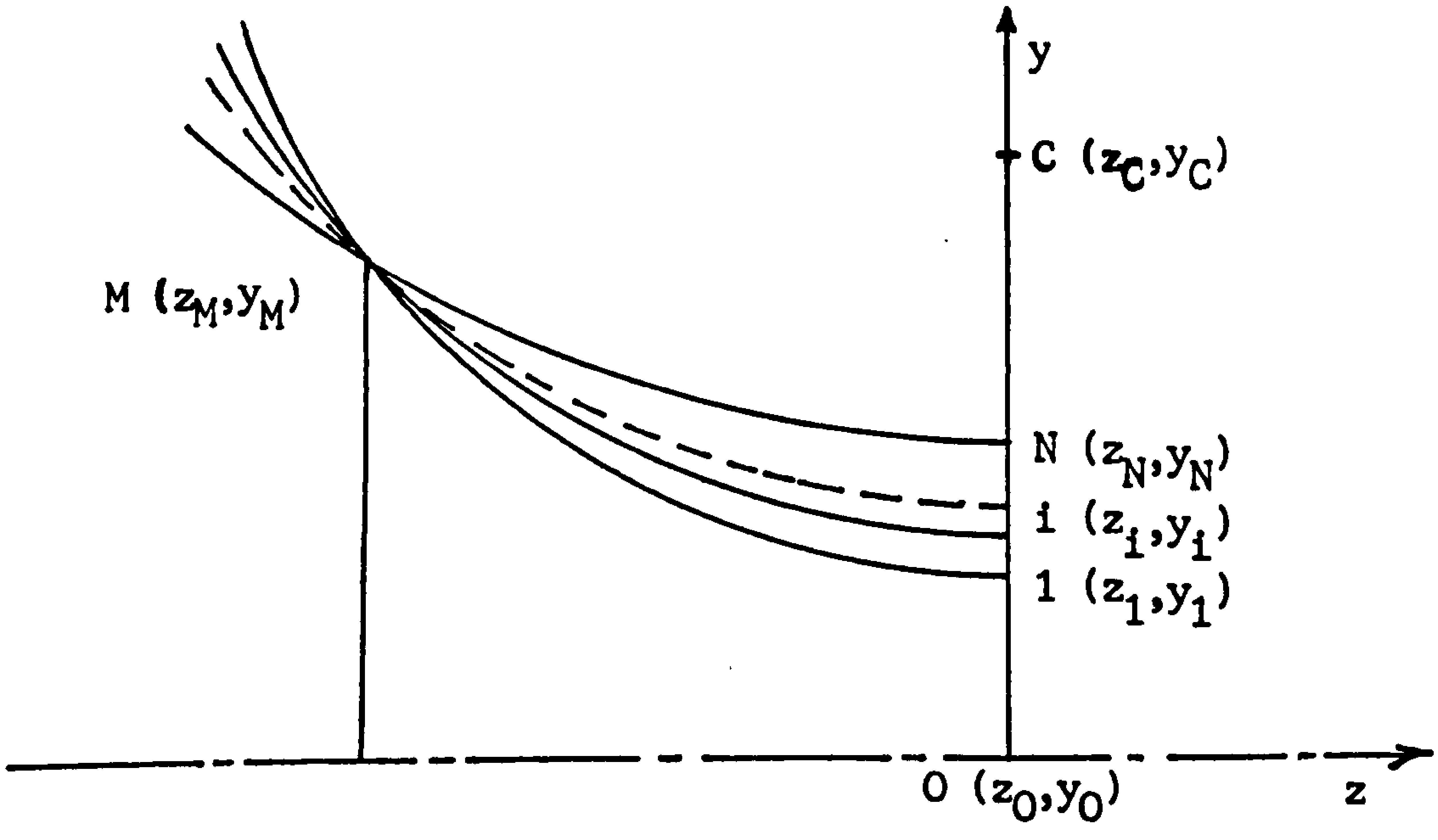

Fig. 5.3: Subsonic section design.

5.3.3 Inlet design

The inlet is the part of the nozzle which links the convergent section to the test section . It must match the dimensions of the latter's exit section (whose radius equals 44 mm) and was designed to do so. The inlet is shown in Figure 5.4 along with the convergent and divergent sections.

5.4 Two-dimensional wedge nozzle design

The two-dimensional wedge nozzle represents the new technology propulsion nozzle which would be integrated into future fighter aircrafts. Its characteristics and performance are described in section 2.5.

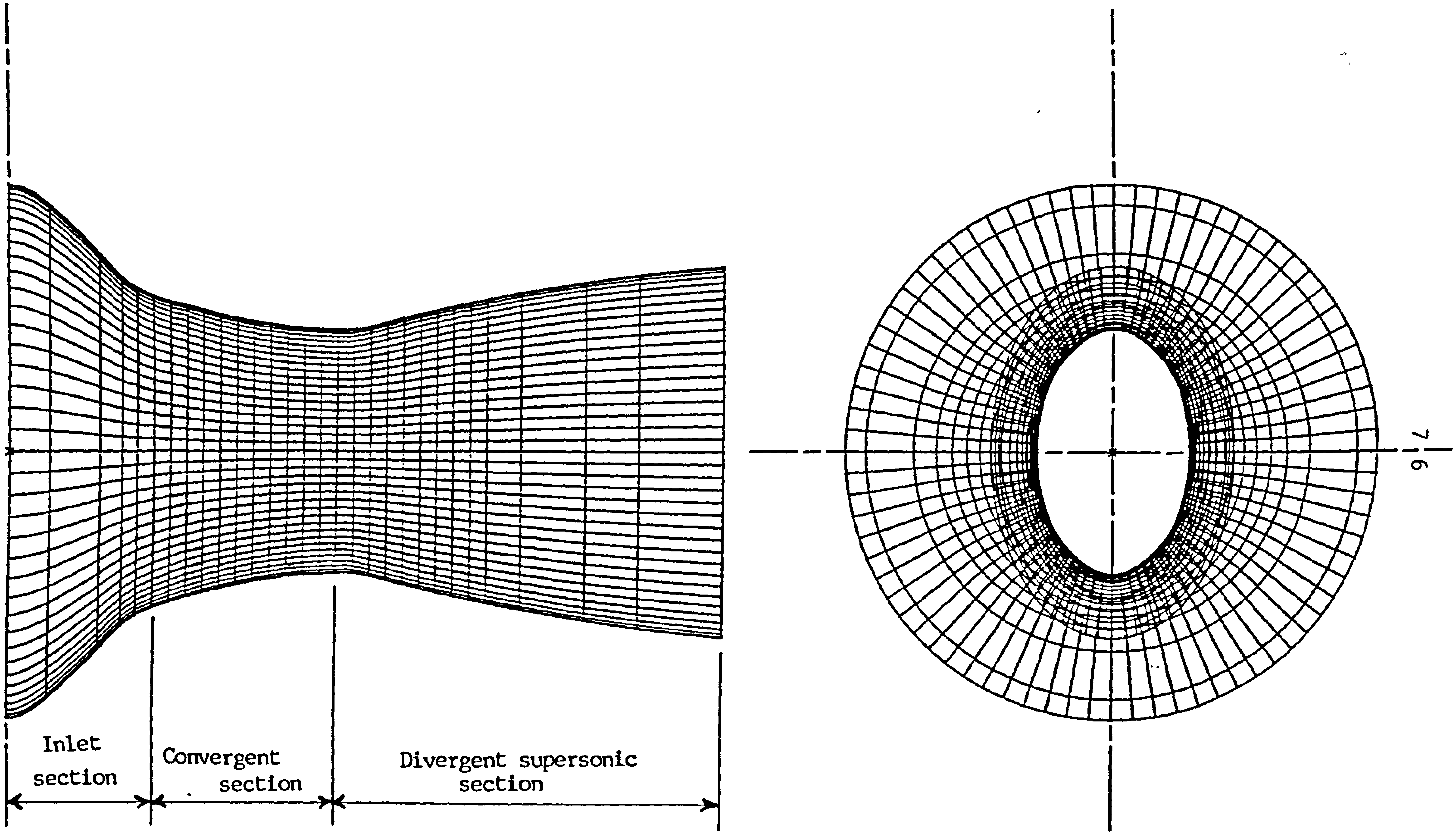

Fig. 5.4: Final design of the elliptical nozzle.

Since the configuration designed in this study will only be subjected to a theoretical three-dimensional simulation, a similarly matching convergent section is not required and the nozzle divergent alone was designed.

Figure 5.5 shows the initial axisymmetric shape computed by the method of characteristics and the 2-D wedge one defined by points A, B_1, B_2, B_3 and C. The coordinates of the different stations (derived in appendix J) were determined by selecting the ratio of the internal radius y_i to the external radius y_e of 9/10.

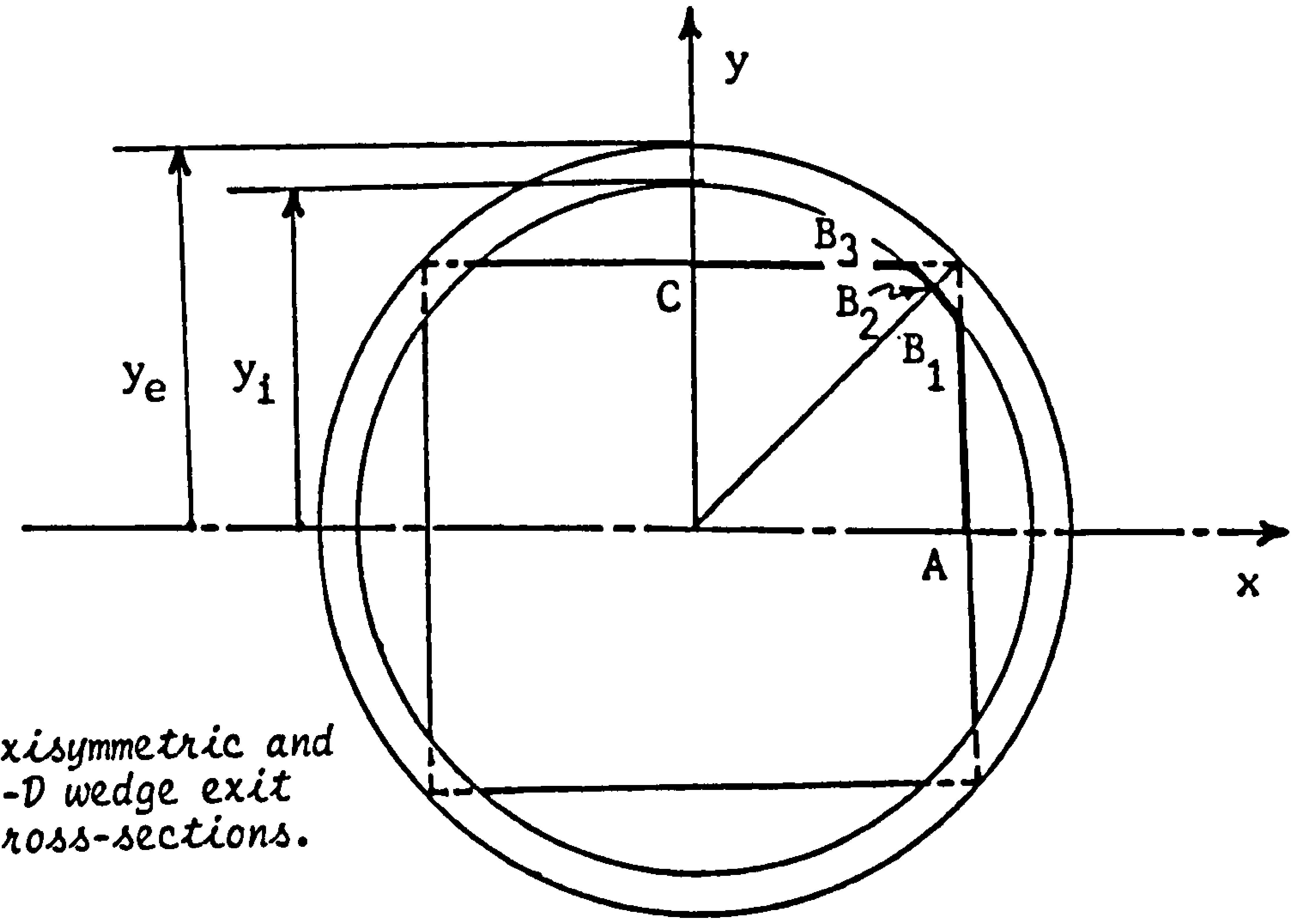

Fig. 5.5: Axisymmetric and 2-D wedge exit cross-sections.

Following the same procedure as for the elliptical case, the stream function values were calculated at the above stations. These latters were then traced back to the throat along their respective streamline, forming the final 2-D wedge shape. Table 5.4 shows the defining points at the throat and exit cross-sections and Figure 5.6 the streamline network.

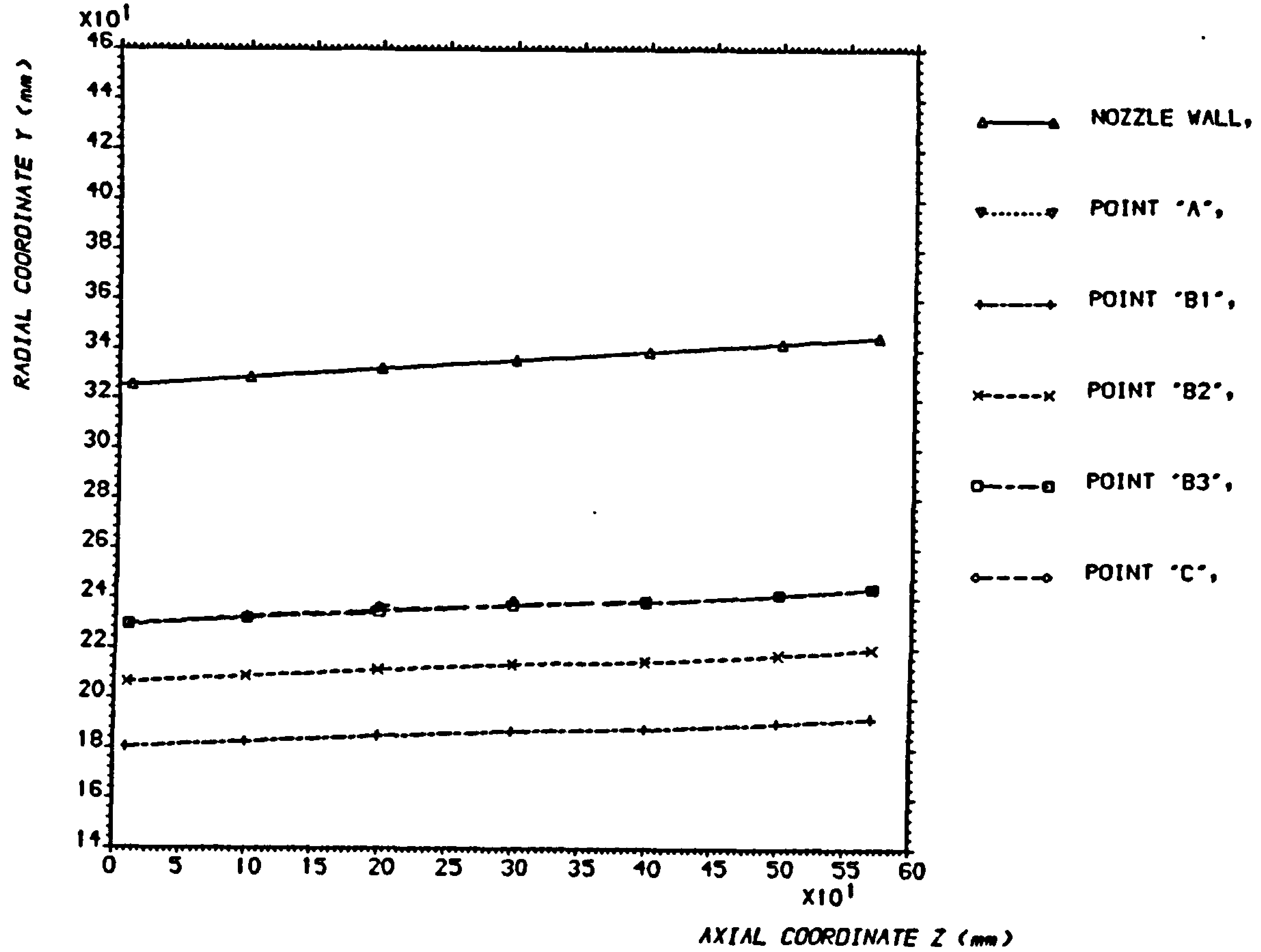

FIG : [5.6] STREAMLINES WITHIN THE DIVERGENT SECTION OF THE AXISYMMETRIC-FOR-WE DGE NOZZLE. (AR=1.125)

Table 5.1

I	y (mm)	x (mm)	h (mm)	α	ψ
1	0.000	20.000	20.000	0.00	0.2307959
2	2.500	19.993	20.089	7.15	0.2331224
3	5.000	19.729	20.353	14.22	0.2401018
4	7.500	19.386	20.786	21.15	0.2518043
5	10.000	18.895	21.378	27.89	0.2683184
6	12.500	18.244	22.115	34.42	0.2897090
7	15.000	17.415	22.984	40.74	0.3161183
8	17.500	16.382	23.971	46.89	0.3476768
9	20.000	15.102	25.061	52.94	0.3845091
10	22.500	13.506	26.242	59.02	0.4269227
11	25.000	11.462	27.502	65.37	0.4752550
12	27.500	8.658	28.831	72.52	0.5295898
13	30.507	0.000	30.507	90.00	0.6019856

Table 5.2

Throat cross-section : (z = 0 mm)

I	y (mm)	x (mm)
1	0.000	12.376
2	1.547	12.347
3	3.114	12.237
4	4.663	12.048
5	6.230	11.776
6	7.527	10.993
7	9.028	10.485
8	11.070	10.363
9	12.696	9.585
10	14.274	8.567
11	15.848	7.263
12	17.560	5.523
13	20.000	0.000

Exit cross-section : (z = 60 mm)

I	y (mm)	x (mm)
1	0.000	20.000
2	2.500	19.993
3	5.000	19.729
4	7.500	19.386
5	10.000	18.895
6	12.500	18.244
7	15.000	17.415
8	17.500	16.382
9	20.000	15.102
10	22.500	13.506
11	25.000	11.462
12	27.500	8.658
13	30.507	0.000

Table 5.3

Position	Station at throat	Circle centre	Circle radius
I	y_i (mm)	y_o (mm)	R_i (mm)
1	20.000	105.000	85.000
2	18.408	90.760	72.352
3	17.433	84.039	66.606
4	16.648	79.406	62.758
5	15.908	75.543	59.635
6	15.163	72.061	56.898
7	14.458	69.080	54.622
8	13.836	66.668	52.832
9	13.323	64.812	51.489
10	12.919	63.427	50.508
11	12.627	64.425	49.838
12	12.443	61.875	49.432
13	12.376	61.663	49.287

Table 5.4

Throat cross-section (z = 0 mm)			Exit cross-section (z = 572.7 mm)		
I	y (mm)	x (mm)	I	y (mm)	x (mm)
A	0.000	229.160	A	0.000	243.801
B_1	179.400	229.160	B_1	191.989	243.801
B_2	205.140	205.140	B_2	219.429	219.429
B_3	229.160	179.400	B_3	243.801	191.989
C	229.16	0.000	C	243.801	0.000

SECTION 6 : Experimental apparatus and procedure

6.1 General

The design approach, developed in this thesis, is based on the computation of the flowfield using the method of characteristics in two dimensions (section 3). However, the final design (elliptical and 2-D wedge) are three-dimensional. In order to validate the approach investigated, real simulation of the three-dimensional flow had to be undertaken.

With a view towards a simple 'proof of concept', the elliptical cross-section nozzle was manufactured and submitted to cold flow testing using compressed air. Though the pressure was the main parameter measured, the thrust, thrust coefficient and exit Mach number were also determined to compare the different configurations.

The actual chapter shall focus on test hardware and methodology. The detailed results are presented and discussed, together with the theoretical study, in section 8.

6.2 Experimental apparatus

In order to compare the pressure distribution along the supersonic section of the nozzle and at the exit, pressures were measured at different equally spaced stations (the step being 5 mm) along the centreline and the exit major and minor axes. The pressure, along the centreline, was measured by what we shall call the 'internal' probe. The pressure along the exit major and minor nozzle axes was measured by the 'external' probe. These will be described in more detail in the following chapters.

The experimental apparatus may be divided into four parts: the flow system, the pressure measuring system, the flow instrumentation and the test articles.

6.2.1 Flow system

To minimize complexity and test cost, the flow medium was compressed air supplied by the compressor house situated within the Mechanical Engineering test area. Pressures may be adjusted within the range from 4 10^5 to 18 10^5 N/m^2 with a mass flow of up to 5 Kg/s (Typical design conditions were 16 10^5 N/m^2 and 2.25 Kg/s).

The nozzle was attached to the end of the pebble-bed heater test section. Because of the required mass flow (2.25 Kg/s) which exceeds the limit allowed before the pebbles 'lift-off' (Cookson, 1967), the pebble-bed was by-passed and air supply was connected directly to the test section (overall schematic in Figure 6.1). An axisymmetric extension flange was used to adjust the nozzle inlet to the test section exit. An O-ring made the connection tight. A thermocouple and a pressure tap were available for measurement of the inlet pressure and temperature (Figure 6.1).

6.2.2 Pressure measuring system

6.2.2.1 General

The pressure measuring system consists of two probes. An internal probe designed to measure the static pressure along the nozzle centreline and an external conical probe to be used at the exit cross-section of the elliptical nozzle. The probes were designed, but not tested under the conditions appropriate here, in an earlier related study (Khalil, 1987)

6.2.2.2 The internal probe

The internal probe (Figure 6.2 and plate 2) was designed in order to measure the static pressure along the centreline of the supersonic section of the elliptical nozzle. It mainly consists of a hypodermic tube of 300 mm length and 2 mm diameter. Four pressure

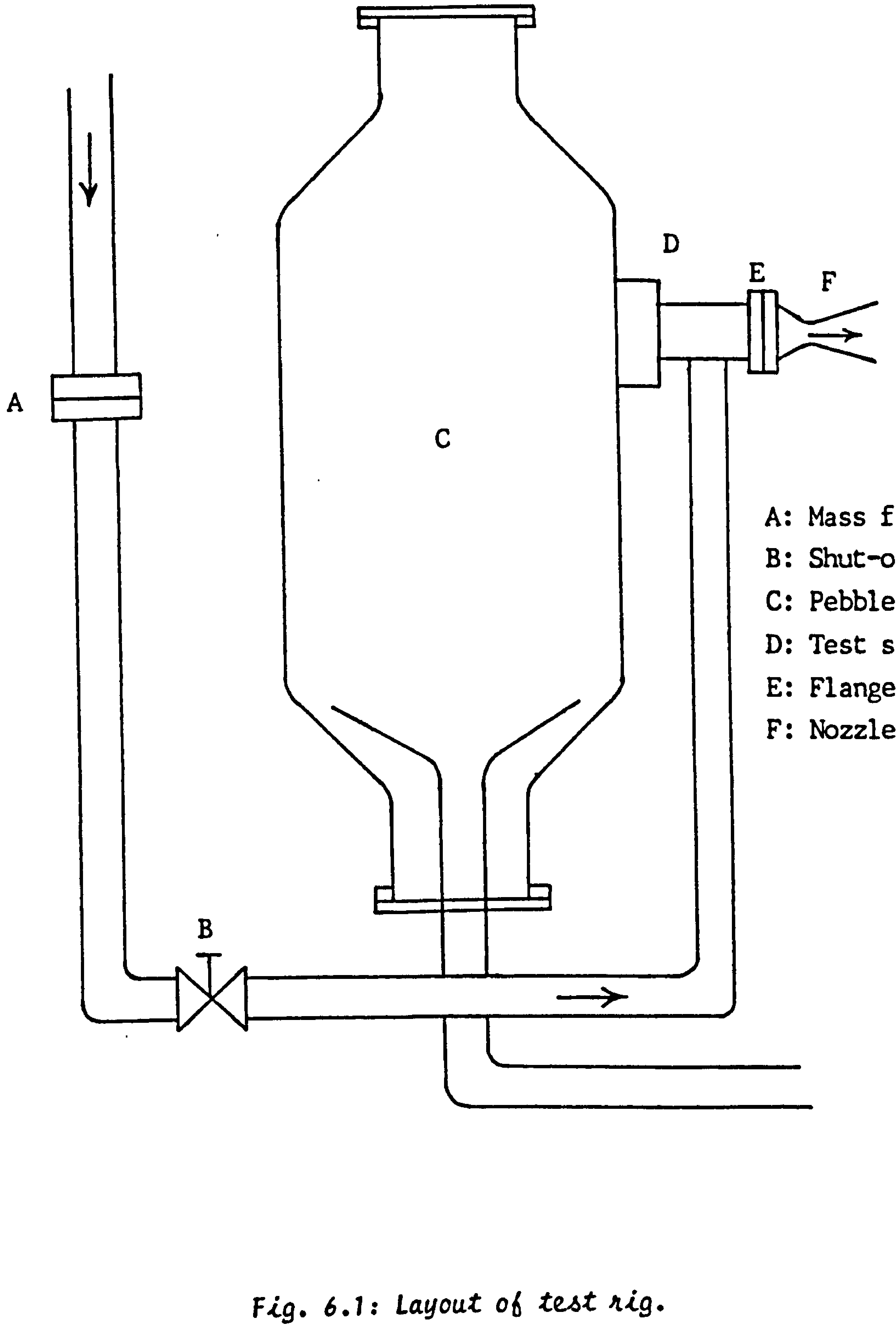

A: Mass flow meter
B: Shut-off valve
C: Pebble bed heater
D: Test section
E: Flange
F: Nozzle

Fig. 6.1: Layout of test rig.

taps, 0.25 mm in diameter and drilled at 90° intervals, are used to measure the static pressure. They are situated at 12 probe diameters distance from the tube nose (Figure 6.2).

The rear of the hypodermic probe is strenghtened by a larger tube, 50 mm in length and 6 mm in diameter, which is soldered to a 100 mm long bar of losenge cross-section. The bar's upper end is designed to adapt to the existing traverse (plate 1) moving the probe to the required position. The bar is drilled inside (Figure 6.2) providing an air passage connected to a tube of 15 mm length (plate 2). The latter tube may be connected to the pressure gauge or manometer by a flexible pipe.

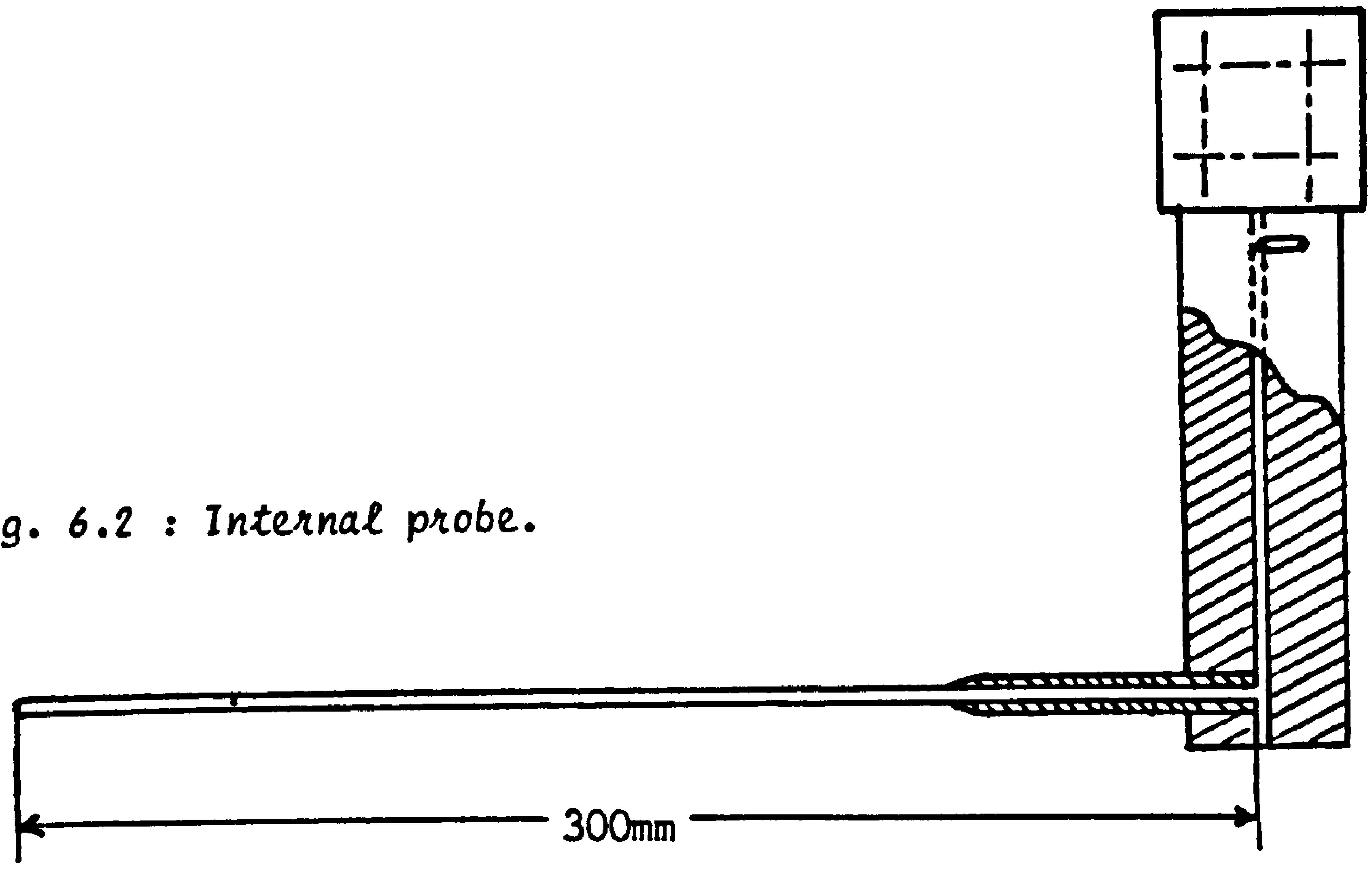

Fig. 6.2 : Internal probe.

6.2.2.3 The upstream probe holder

Internal measurements are bedevilled by the attached shock on any entrant probe. In order to minimize flow disturbance inside the nozzle, the probe therefore runs along the complete length of the axis from the entry section of the convergent to the exit. Because of the probe length and in order to avoid the vibrations which may occur if it were fixed at only one end, the forward part of the hypodermic tube was made to slide inside a fixed probe holder mounted upstream of the nozzle (Figure 6.3 and plate 3). The probe holder consists of a main tube of 70 mm length, 5 mm outer diameter and 2 mm bore. It is positioned upstream of the nozzle in a flanged section and is maintained on the central axis by means of three legs positioned at 120° intervals (Figure 6.3 and plate 3). The upstream end of the probe holder's bore is closed and represent the sliding end of the internal probe. At that position, the static pressure tappings will be positioned at the throat. By moving the probe downstream, the tappings are moved along the nozzle centreline. When they reach the exit section, the forward end of the probe would still be retained inside the probe holder (length of the retained part is 5 mm).

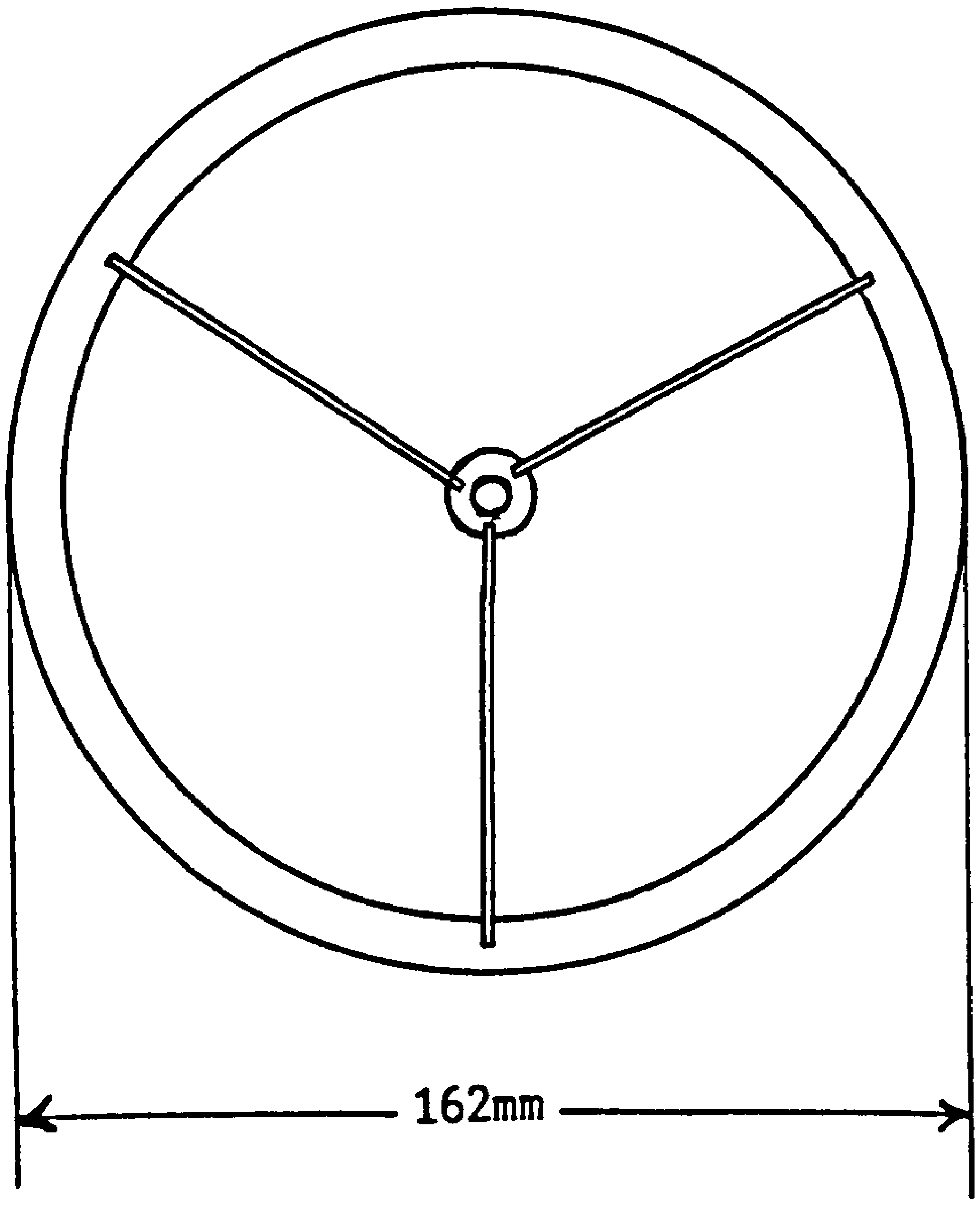

Fig. 6.3 : Probe holder.

6.2.2.4 The external probe

In order to measure the exit static pressure along the minor and major axes of the elliptical nozzle, an external probe is provided (Figure 6.4 and plate 4). It consists of a hypodermic tube, 114 mm in length and 2 mm in diameter, provided with a conical nose of 4 half-angle. The tube is strenghtened in the same way as for the internal probe. It is soldered to a bar having the same shape and dimensions as the one used for the internal probe.

Four taps of 0.25 mm diameter are used to measure the static pressure. They are located at 12 probe diameters distance from the tip of the cone.

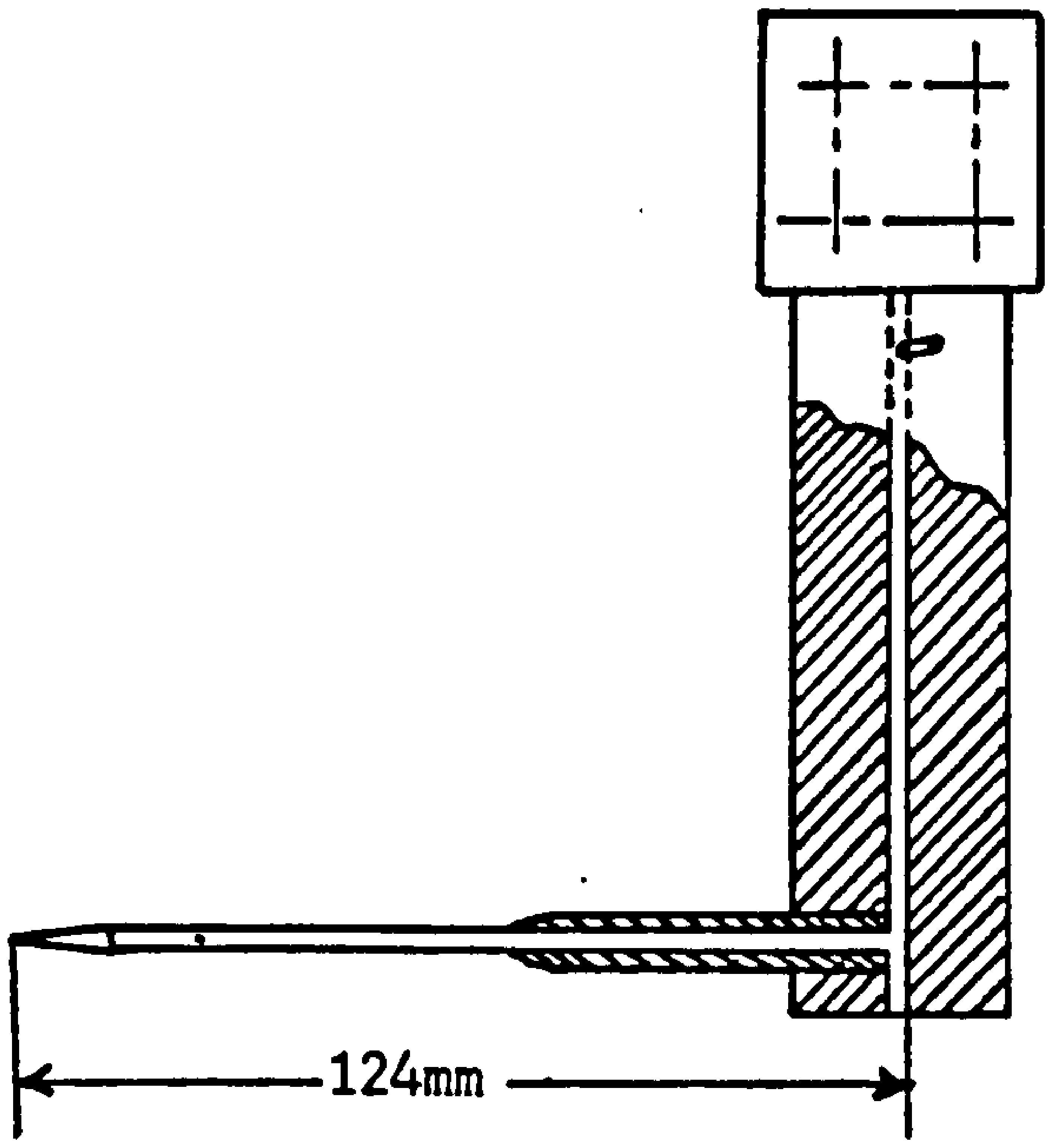

Fig. 6.4 : External probe.

6.2.3 Flow instrumentation

An orifice flow meter located upstream of the pebble-bed heater (Figure 6.1) was, in principle, available for the measurement of the mass flow. The meter requires measurement of the pressure difference across the orifice which is performed by a U-tube manometer connected to two pressure taps. However, because of the rust accumulated around the orifice, its precise dimensions could not be evaluated and the absolute determination of mass flow rate proved unsatisfactory. The mass flow was therefore determined using the isentropic relationships (see Appendix F). Typical mass flow supplied by the compressor house was 2.8 Kg/s.

6.2.4 Test articles

The test articles are principally represented by the elliptical nozzle necessary for the study (Figure 5.4 of section 5 and plate 5). Designed from an axisymmetric shape using the method investigated in this thesis, the nozzle was manufactured at RAE Bedford.

In order to achieve the necessary finish (N7 or better) of the bore (any protuberance in the surface may disturb the supersonic flow), the internal elliptical shape was cast in an epoxy resin (Araldite MY 750) filled with aluminium. The hardener used is HT 972 and the maximum working temperature 130°C.

The elliptical shape of the divergent section of the nozzle was described,at each cross-section, by the stations defined at the exit and traced back to the throat (section 5). The subsonic section, effecting a smooth transition from the elliptical throat to the axisymmetric supply pipe, was defined in the same way (Appendix J). Fourty cross-sections were used, each cross-section being defined by fifty two stations. Tolerance was of the order of the micron.

The external body, used to support the internal resin shape and designed to fit the pebble-bed test section to which it is bolted, was all machined in an aluminium alloy. Tolerance was of the order of 0.1 mm.

The two parts (elliptical internal shape and external body) were assembled and received the necessary heat treatments.

Static pressure tappings along the nozzle wall were meant to be provided. The usual method for measuring the pressure along a wall is to drill a small hole normal to the surface of the wall and connect it to a manometer, pressure gauge of similar other device (see chapter 2.6). Drilling a hole, in this case where the internal shape is elliptical (difficulty in drilling satisfactory static pressure tappings normal to the elliptical internal surface) and constituted by a resin, may give rise to imperfections (such as burrs) around the tappings which would probably disurb the flow locally. Because of this, wall tapping of the elliptical nozzle was avoided and only static pressure measurement along the centreline and at the exit were performed.

6.3 Experimental procedure

The experimental procedure consists of calibrating the instrumentation and running the tests.

6.3.1 Calibration

The internal probe runs along the complete length of the nozzle from the entry section of the convergent to the exit. Its forward end is blocked off inside the probe holder situated upstream of the nozzle (chapter 6.2) and consequently the measurements it performs give the true value of the pressure.

The external probe, being inserted into a supersonic flow, will have an attached shock at the nose. Due to the compression caused by the shock, the static pressure readings will be higher than the true pressure in the absence of the probe. In order to demonstrate this, the internal and external probes were used simultaneously to measure the static pressure at the centre of the exit cross-section. The corections needed were of the order of 1.5%.

The correction was carried out by adopting the following procedure :

1. Using the isentropic relationships, the Mach number (M_1 in figure 6.5) just before the shock is calculated,
2. The cone half-angle of the forward part of the extenal probe (δ_c in figure 6.5) is designed equal to 4°,
3. From figure 6.5, for a given value of M_1 and a cone half-angle δ_c, the ratio of the measured pressure to the real pressure (P_c/P_1 in figure 6.5) may be determined.

The ratio of the measured pressure to the real one is found close to 1 ($P_c/P_1 = 1.1$). It can be seen, in figure 6.5 that for Mach numbers comprised between 1 and 2.5 (which is the range of change of the Mach number within the divergent section of the elliptical nozzle where the measurements are taking place), the curve representing the cone half-angle of 4° is very close to the Mach line. Hence, the close-to-1 ratio of the measured to the real static pressures.

6.3.3 Test procedure

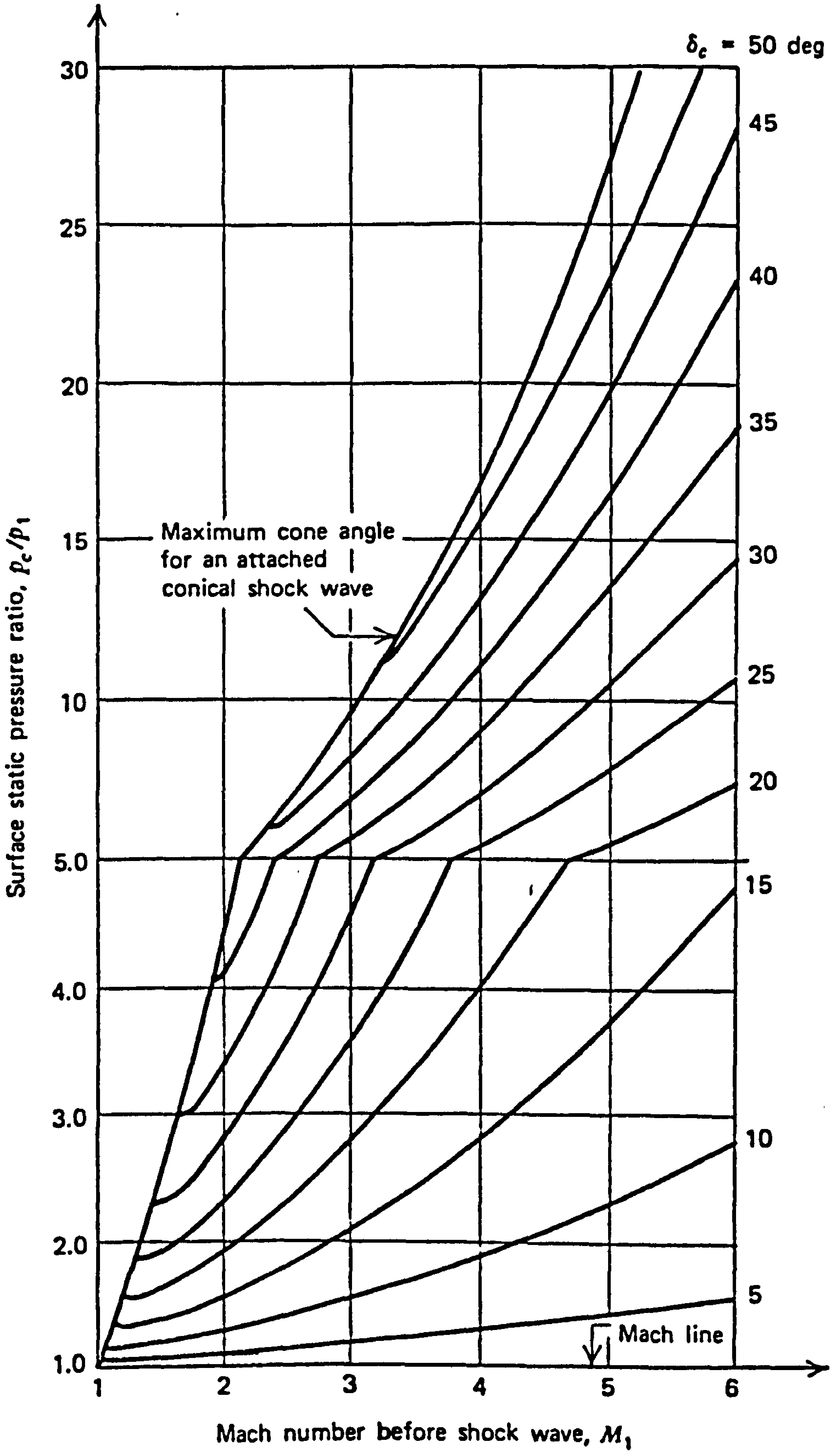

Fig. 6.5: Static pressure ratio P_c/P_1 for a conical wave as a function of the initial Mach number M_1 for different values of the cone angle δ_c for =1.40. (Zucrow & Hoffman, 1976)

Tests involving the internal and external probes were performed separately. When measuring the pressure distribution along the nozzle centreline, the internal probe is centered by inserting its forward extremity into the probe holder. The tests start with the measurements at the throat. The compressed air supply is then released and, using the traverse, the probe static pressure tap is moved from one station to another (the step being 5 mm) until the exit is reached. Near the throat, the static pressure is relatively high and the transducer was used. Close to the exit, pressure measurements were switched to be performed by U-tube manometer.

Only the U-tube manometer was used when measuring the exit pressure with the external probe. The axis along which the measurements are performed is restricted to the vertical position, since the traverse can only move in that direction. The nozzle must therefore be rotated through 90° to measure the pressure distribution along both the major and minor axes.

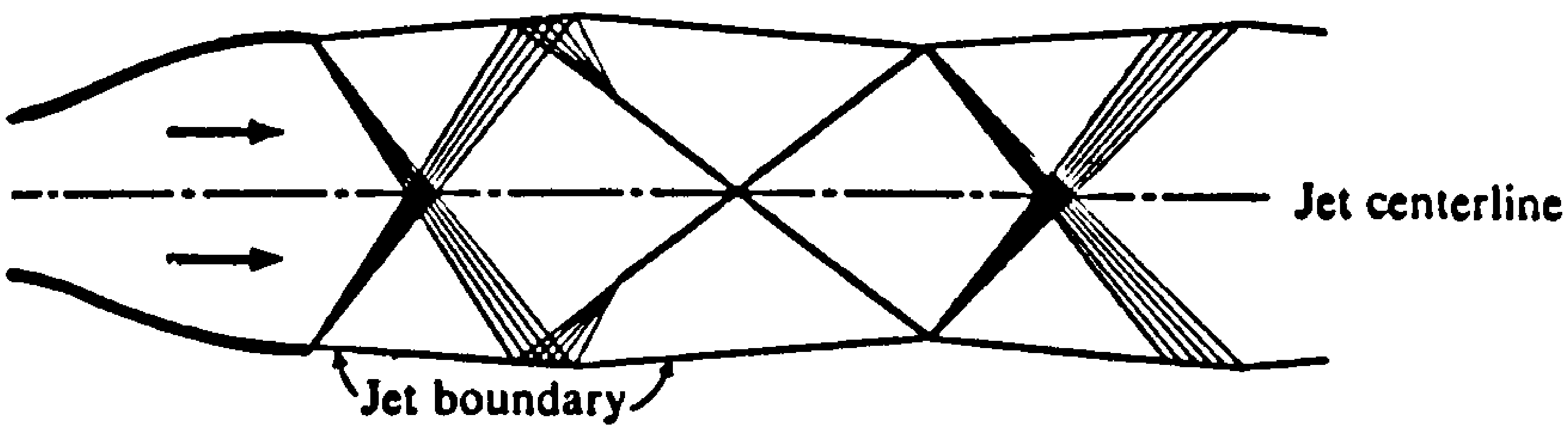

Fig. 6.6 : Underexpanded supersonic nozzle.

A schlieren picture of the elliptical nozzle/external probe is shown in plate 6. The elliptical nozzle is designed to expand the flow from an inlet pressure of 15 atm to a back pressure of 1 atm. The compressed air supply was provided with a total pressure of 16.3 atm. Consequently, the elliptical nozzle was not able to perform a complete expansion of the flow and expansion fans formed at the nozzle exit plane (Figure 6.6 and plate 6).

At the centreline of the exhaust jet, pictured in plate 6, two relatively weak waves can be seen. These waves represent an oblique shock which may have been generated by either an irregularity in the surface finish or the discontinuous concave surface turning at the attachment point A (chapter 3.3.4 & Figure 6.7).

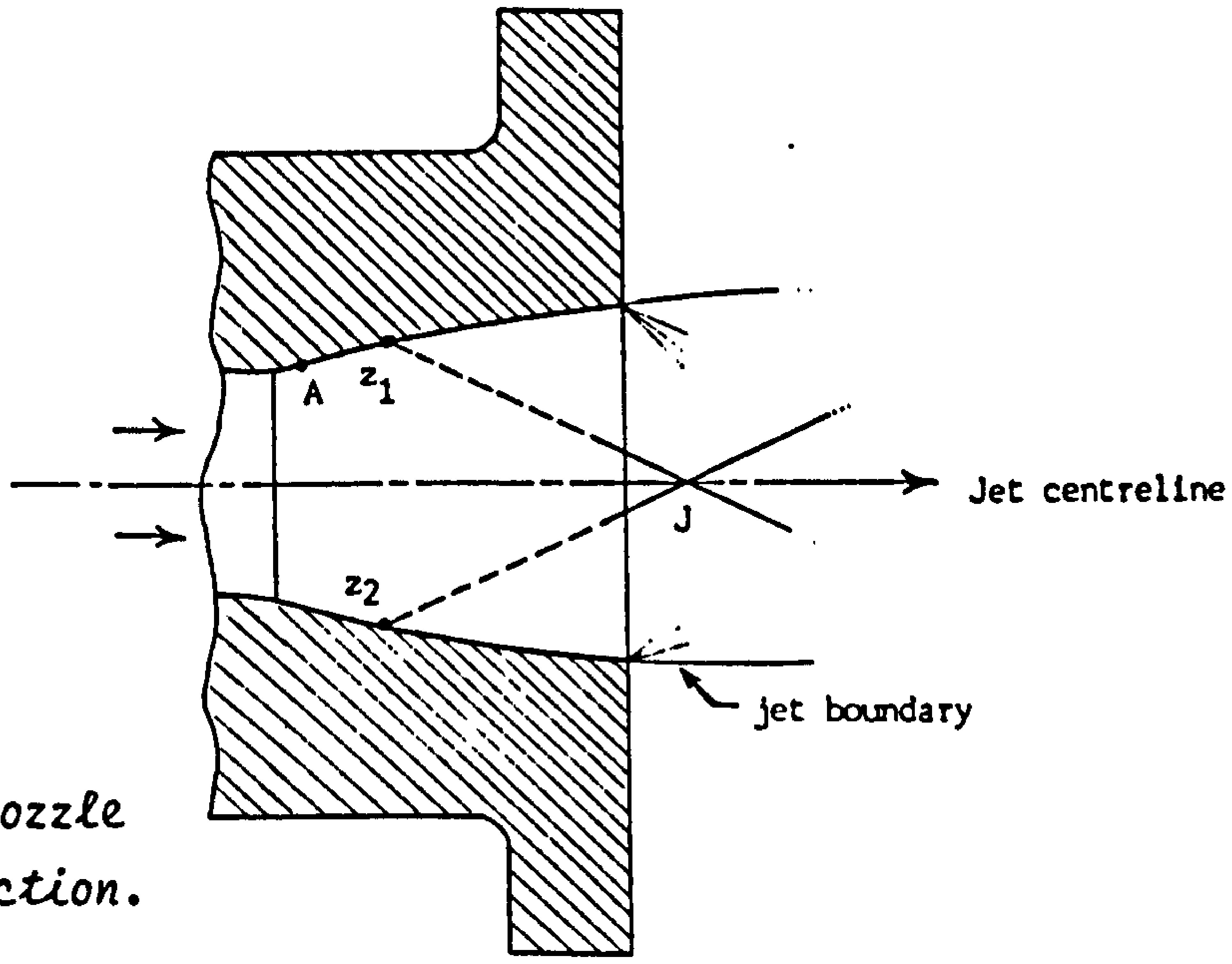

Fig. 6.7 : Elliptical nozzle divergent section.

Figure 6.7 traces the two waves back into the supersonic section of the elliptical nozzle where they are found to interssect the nozzle wall at a distance $z_1 = z_2 = 19.8$ mm from the throat. On that basis and knowing that the attachment point is situated 2.6 mm far from the throat, it seems unlikely that the internal oblique shock wave is generated by the discontinuity in the wall curvature.

SECTION 7 : Three-dimensional simulation

7.1 General

In order to validate the performance of the design approach developed in this thesis, detailed analysis of the flowfield within the nonaxisymmetric nozzle configurations designed should be performed. This analysis may be carried out in two ways: by extensive experimental testing and/or computational modelling and simulation using a generalized three-dimensional method. In either case, the study of the results would show the real nature of the flow. In particular, comparison of these results against their axisymmetric counterparts would demonstrate the performance of the designed shapes.

Both procedures have been adopted in the present study. The elliptical nozzle was manufactured and submitted to the appropriate tests (cf. Section 6). In addition, the flowfield within the two configurations (elliptical and two-dimensional wedge) was computed using finite-difference techniques. The appropriate grids were generated by the I-Deas Supertab module (Appendix G). 'Phoenics' (Appendix H) was used to simulate and compute the three-dimensional flow.

The two approaches (experimental testing and computational modelling and simulation) are in part complementary. Indeed, one of the main problem faced when carrying out numerical computations is concerned with the selection of the appropriate initial flow data. Generating accurate internal flow data in an accelerating supersonic flow in particular is one of the most difficult tasks. In the present case, test results (ie. initial static pressure) were used as initial conditions for the three-dimensional computations performed by 'Phoenics'.

The present chapter shall focus on the methodology followed to simulate and compute the flowfield within the elliptical and two-dimensional wedge nozzles. The detailed results are presented and discussed, together with the experimental study, in the following section.

7.2 The elliptical nozzle

Because of their symmetry, relative to the zx and zy planes, the elliptical and the two-dimensional wedge nozzles were divided into four identical quadrants. The computation, carried out within one quarter of the flowfield, shall then be sufficient to simulate the whole flow: the other three quarters being images of the calculated one.

7.2.1 Grid generation

The elliptical configuration was generated using the I-Deas engineering analysis Supertab module (Appendix G). The different steps involved are described by Figures 7.1 to 7.7.

The shape is originally defined by the discrete points (shown in Figure 7.1) describing the different cross-sections and boundaries of one quadrant of the elliptical nozzle. The coordinates of these stations are determined in section 5 where the three-dimensional design is performed. Figure 7.1 shows the stations defining the throat and exit sections as well as those defining the major and minor axes. Both the throat and exit sections, which are elliptic in shape, are described by the stations whose position are represented in table 5.2 of section 5.

The following step consists of joining the different stations described above in order to define the outer edge of the nozzle contour (Figure 7.2). This may be performed by using arcs, lines or splines. The throat and exit sections are described by one spline and two lines each. The splines are used to join the points defining the ellipse shaped section. The lines join the extremities of the one quarter of the ellipse to its centre. The stations defining the major and minor axes are joined by splines (Figure 7.2).

Surfaces are needed to close the contour and define the volume. Figure 7.3 shows the different surfaces (denoted SF1 to SF6) and Figure 7.4 the volume they enclose.

The mesh, shown in Figure 7.5, was generated by prescribing the number of elements required along the external edges (5 along x, 5 along y and 15 along z). The degree of concentration of the elements may clearly be chosen to match the requirements of particular flow problems. Since it was expected that the flow property gradients would be large in the throat region, a concentration of degree 2 (implicating that the distance between the sections along which the flow is computed will be closer) was generated immediately downstream of that particular section.

The last step in the procedure is the division of the volume describing the one quadrant of the elliptical nozzle into elements (or cells). Since the edges along the radial and azimutal directions were divided into 5 stations each, the total number of elements describing a cross-section is 25. The number of sections in the axial direction was selected equal to 15 making the total number of elements 375. Figure 7.6 shows the different nodes (or grid points) and figure 7.7 the different elements constituting one quater of the elliptical nozzle.

Results from this simulation represent the necessary geometrical data. Stored in a special file, these data along with the control data file (comprising the thermodynamic boundary conditions, i.e. pressure, density, mass flow) form the input to 'Phoenics' enabling the use of its body fitted coordinate version.

7.2.2 Flow simulation

Simulation of the flowfield within the supersonic section of the elliptical nozzle designed using the method investigated in this thesis has been undertaken. The initial conditions were prescribed by the total pressure and total temperature measured during the experimental tests (section 6). The inlet static pressure was established by prescribing the mass flow rate and the nozzle inlet dimensions.

The governing equations, in the form presented in appendix H and shown in more detail in CHAM report TR/99, were solved for the pressure and the velocity (as dependent variables) involving the three coordinate directions (as independent variables). The remaining thermodynamic properties (auxiliary variables, i.e. density) were then calculated using the isentropic and perfect gas relationships (Appendix H).

Using the graphics post-processor 'Photon' (CHAM report TR/140), the velocity vectors resulting from the flowfield computation were drawn and represented in Figure 7.8 and 7.9. At the level of visualization, the figures show the smooth acceleration of the flow along the walls and at some specified cross-sections respectively. They demonstrate the satisfactory convergence of the procedure.

Further detailed results from the I-Deas-Phoenics analysis and the experimental study are presented and discussed in the following section.

7.3 Two-dimensional wedge nozzle

Two-dimensional wedge nozzles are specifically designed to be integrated into advanced fighter aircraft (section 2.5). These latter are needed to operate over a wide range of altitudes and Mach numbers. In order to expand at maximum efficiency throughout the different flight conditions, the nozzles need to compensate for the environmental conditions and power settings by continuously optimizing their geometry. At low power settings, the angle of divergence is small and has been selected equal to 2° (section 3.4.3).

In order to simulate the nozzle flow using the approach outlined earlier, one quarter of the divergent section of a two-dimensional nozzle has been designed and a geometrical specification generated. Because of the small value of the divergence angle, the flow is expected to accelerate gradually to the exit Mach number of 1.4 (Compared to 2.4 for the elliptical nozzle). Therefore, fewer elements were used to describe the generated volume (figure 7.10). The number of elements was selected equal to 5 along both the radial and azimuthal directions while the axial direction was divided into 10 elements making the total number of elements 250. Similarly to the elliptical case, the grid was concentrated in the throat region.

The graphics post-processor 'Photon' allowed the representation of the velocity vectors along the wall and at specified cross-sections. They are shown by figures 7.11 and 7.12 respectively, indicating a smooth acceleration of the flow within the nozzle to the designed exit Mach number of 1.4 and demonstrating that a satisfactory convergence has been achieved.

Further detailed results for the flowfield simulation along with the performance comparison of the two-dimensional wedge nozzle and its axisymmetric counterpart are presented and discussed in the following section.

7.4 Closing remarks

1. The design of the nozzle configurations presented in this section has been carried out iteratively, the objective being to achieve a good description of the flowfield with a minimum number of cells (or elements), therefore economizing computer time and storage.

2. Simulation of the whole flowfield within the elliptical nozzle (Figure 7.13) has been undertaken. The initial conditions were prescribed by the total pressure and total temperature measured during the experimental test. A satisfactory convergence of the procedure could not be achieved within the limited time available for this aspect of the simulation. The reasons for that may be of geometrical order: i.e. loss of orthogonality within the designed grid, especially at the inlet section (cell A in Figure 7.14). Grid nonorthogonality may be reduced by either increasing the number of grid points or by redesigning the complete grid altogether (Figure 7.15).

The failure to achieve a satisfactory convergence may also be due to the complex nature of the flow which is accelerating from low subsonic to transonic and later achieving high supersonic velocities. Numerical simulation of such a flowfield (whose governing equations takes two forms, depending whether the flow is subsonic or

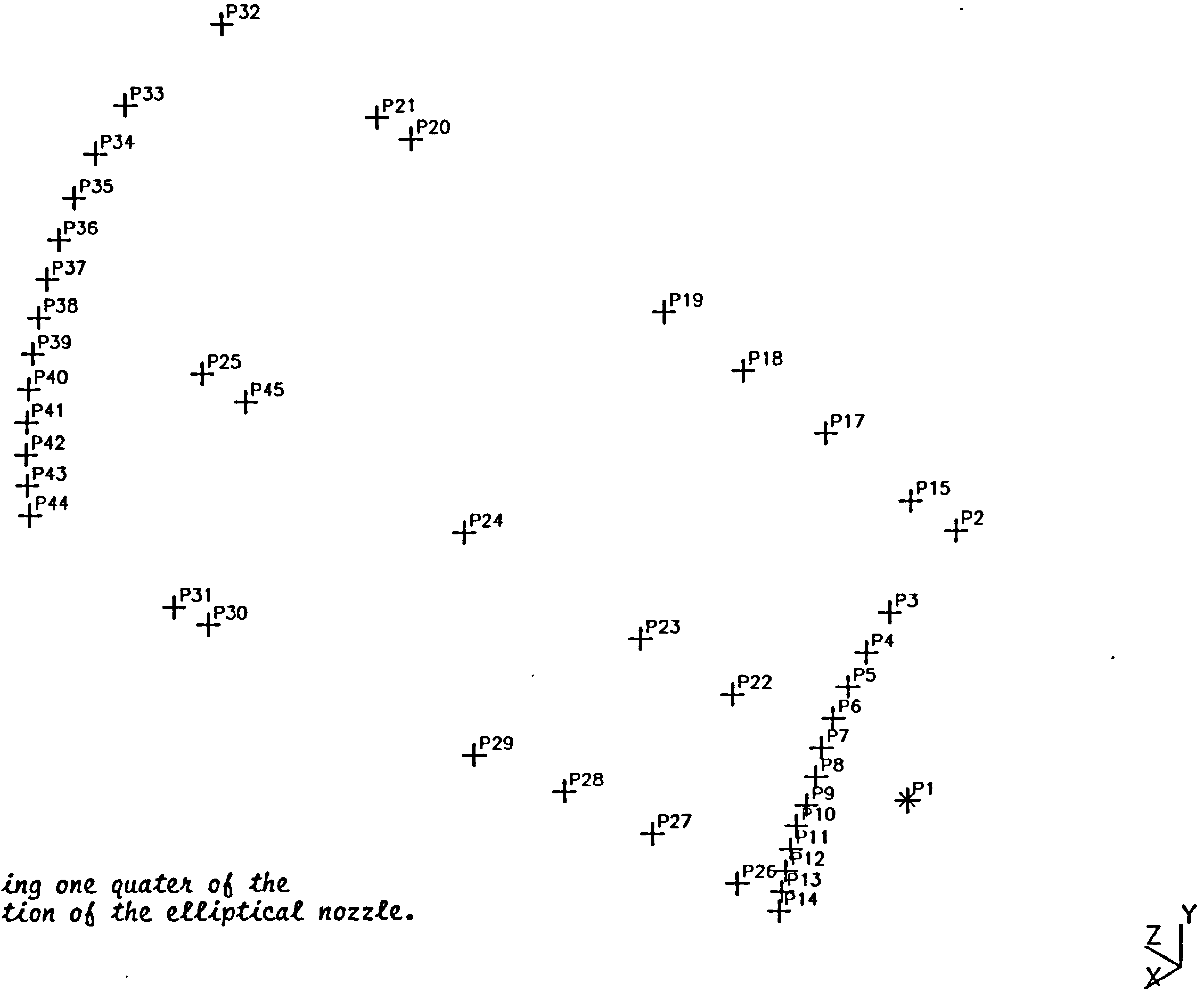

Fig 7.1: Stations defining one quater of the supersonic section of the elliptical nozzle.

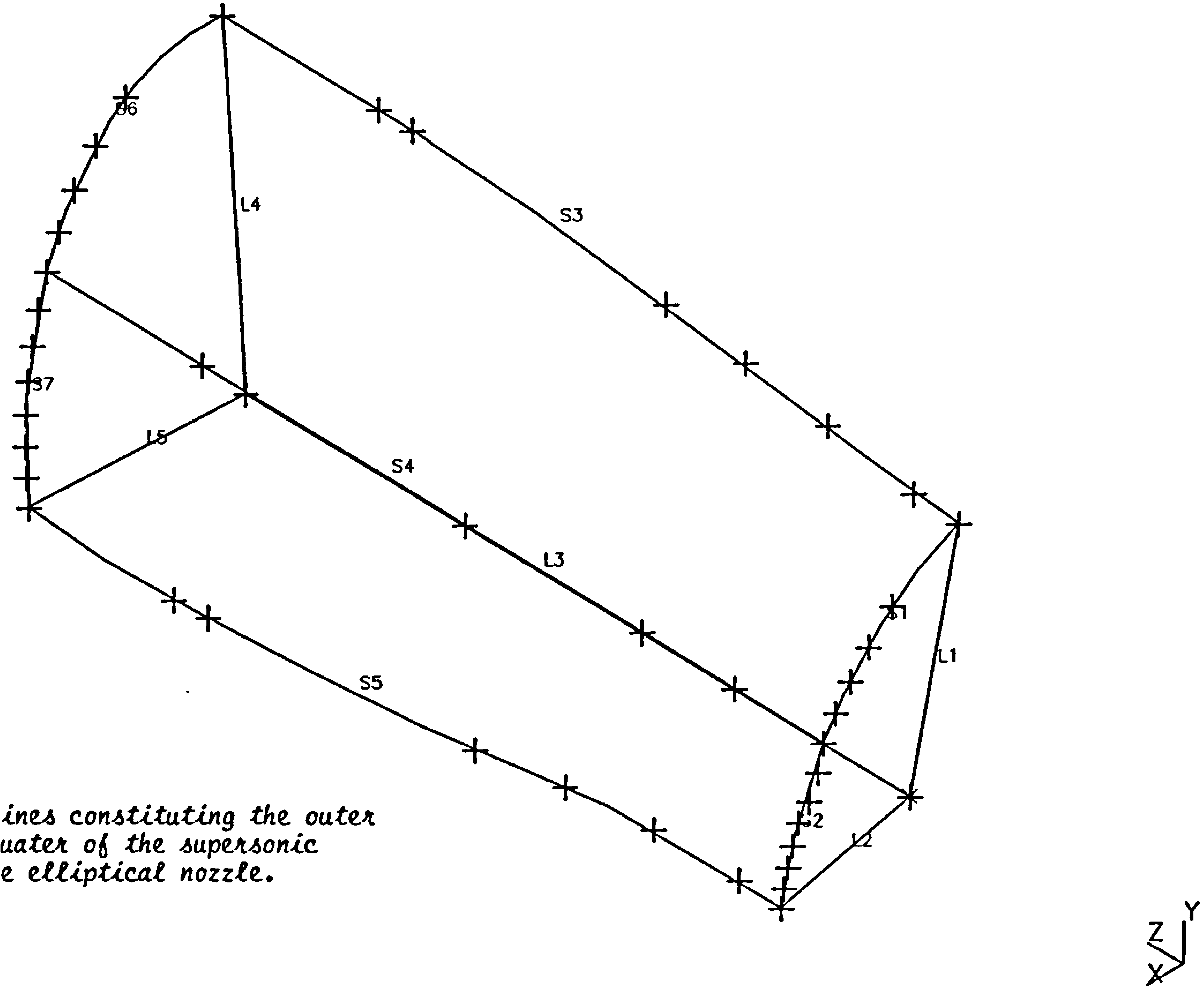

Fig. 7.2: Lines and splines constituting the outer edge of one quater of the supersonic section of the elliptical nozzle.

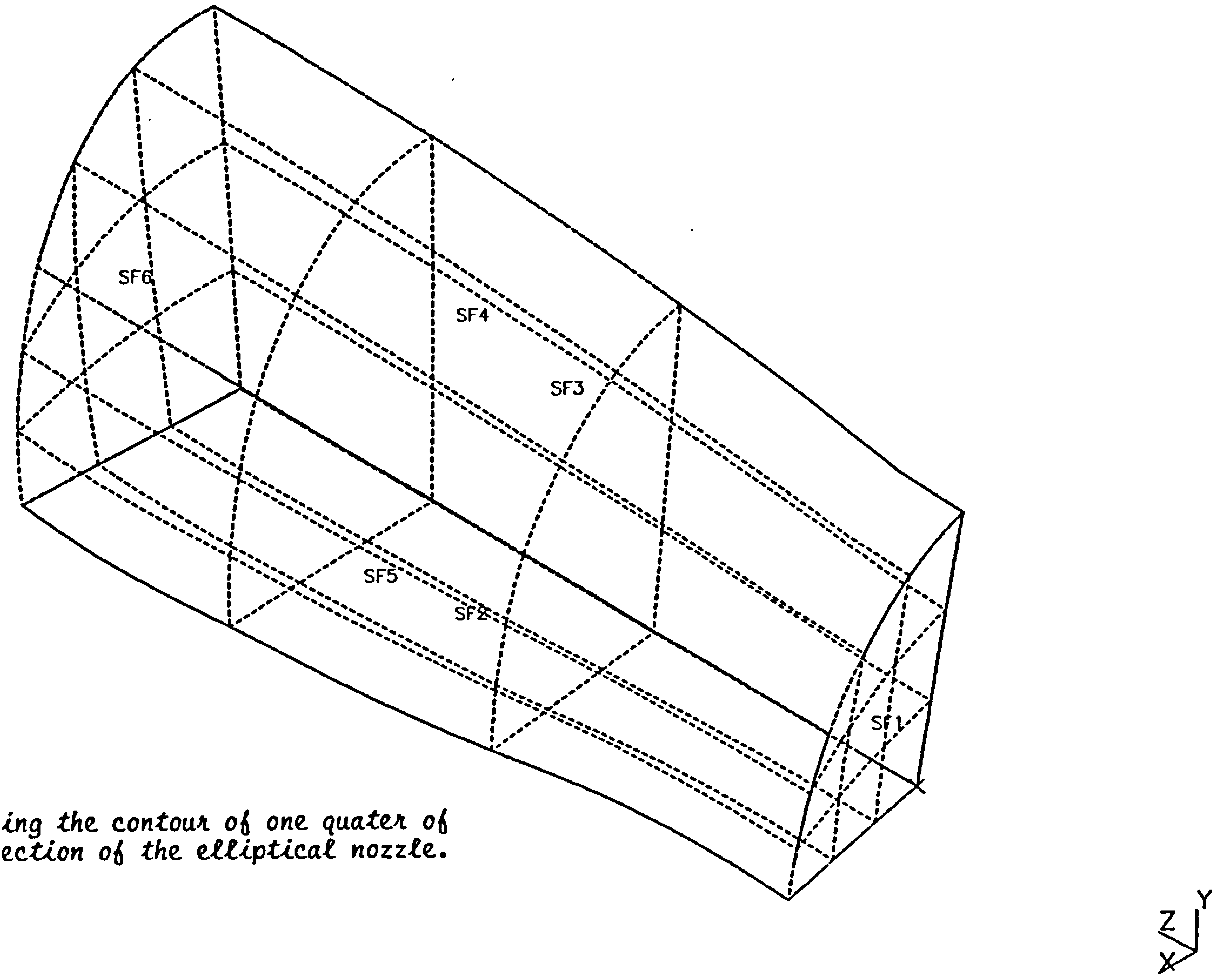

Fig. 7.3: Surfaces enclosing the contour of one quater of the divergent section of the elliptical nozzle.

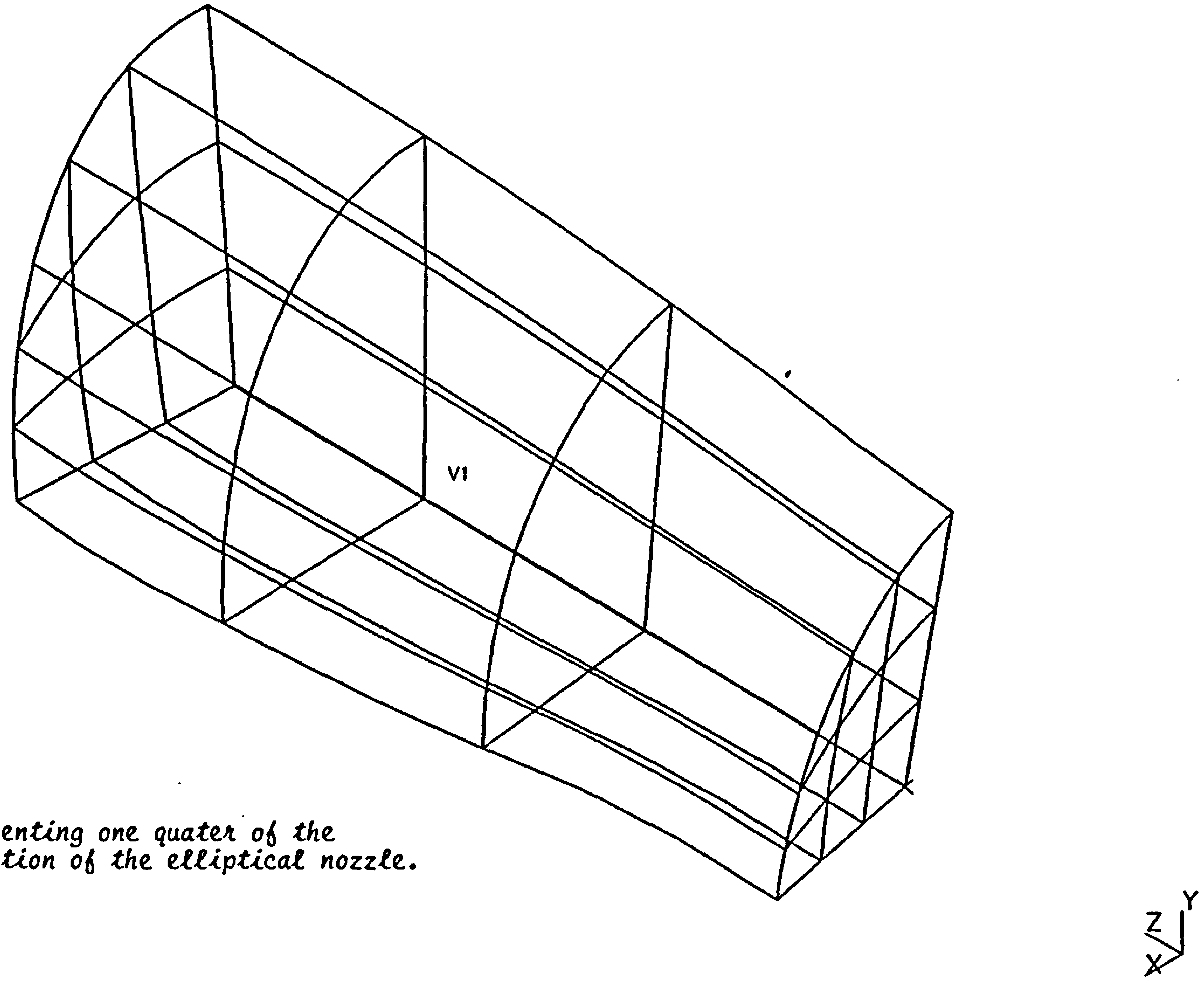

Fig. 7.4: Volume representing one quater of the divergent section of the elliptical nozzle.

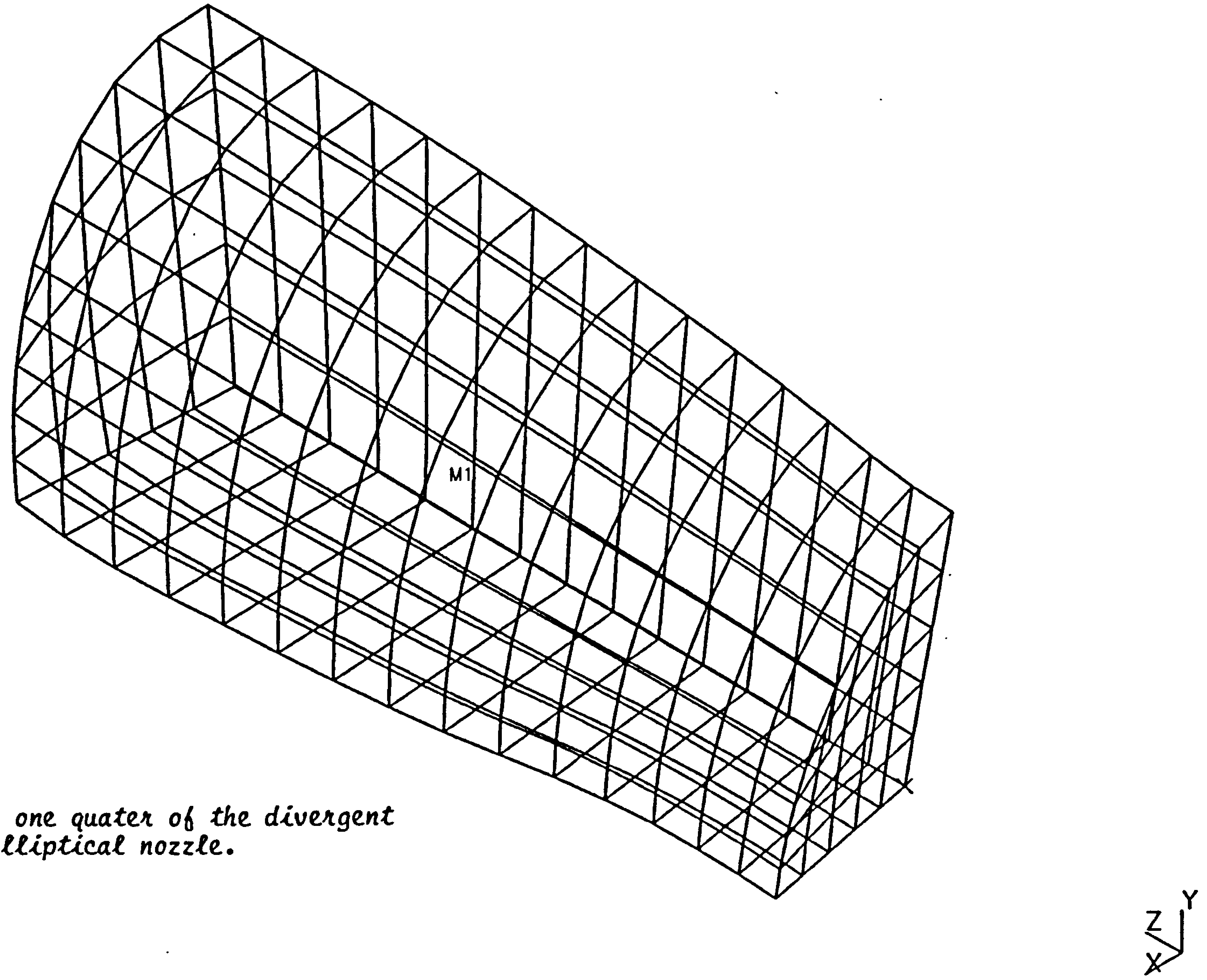

Fig. 7.5: Mesh describing one quater of the divergent section of the elliptical nozzle.

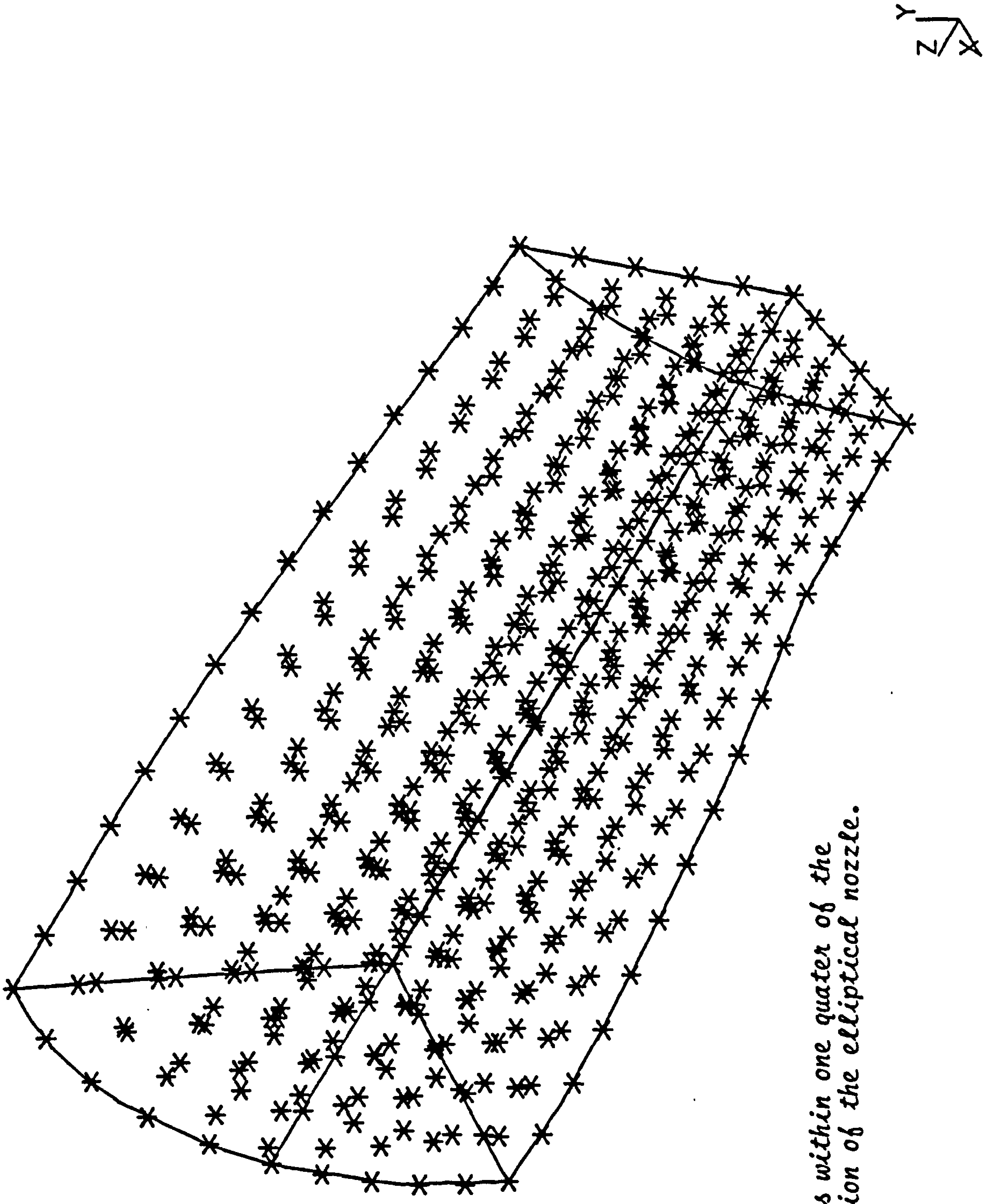

Fig. 7.6: Generated nodes within one quater of the divergent section of the elliptical nozzle.

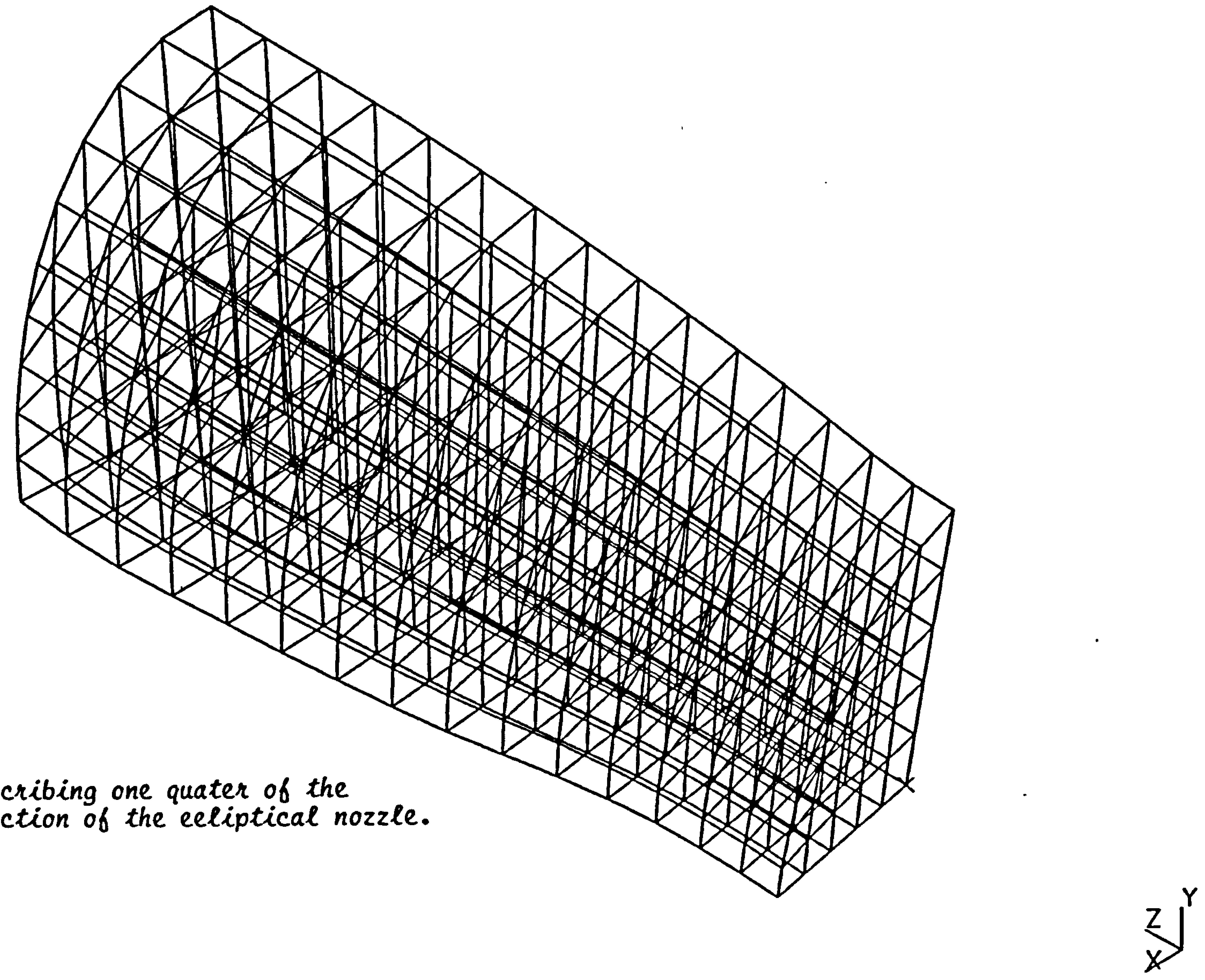

Fig. 7.7: Elements describing one quater of the divergent section of the eeliptical nozzle.

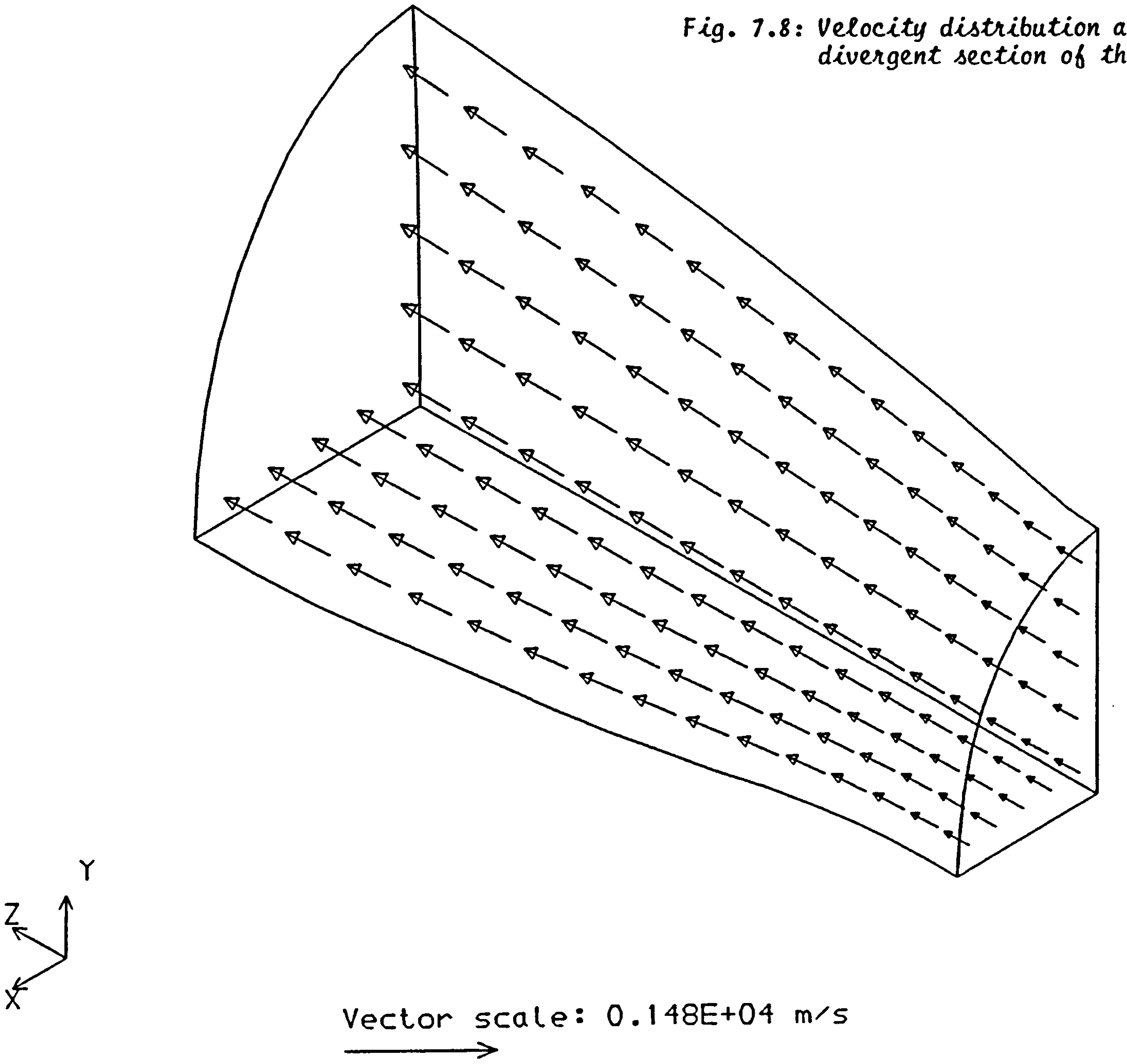

Fig. 7.8: Velocity distribution along the walls of the divergent section of the elliptical nozzle.

Fig. 7.9: Velocity distribution at specific cross-sections (z = 1.319mm; 13.54mm; 32.95mm & 57.31mm) of the divergent section of the elliptical nozzle.

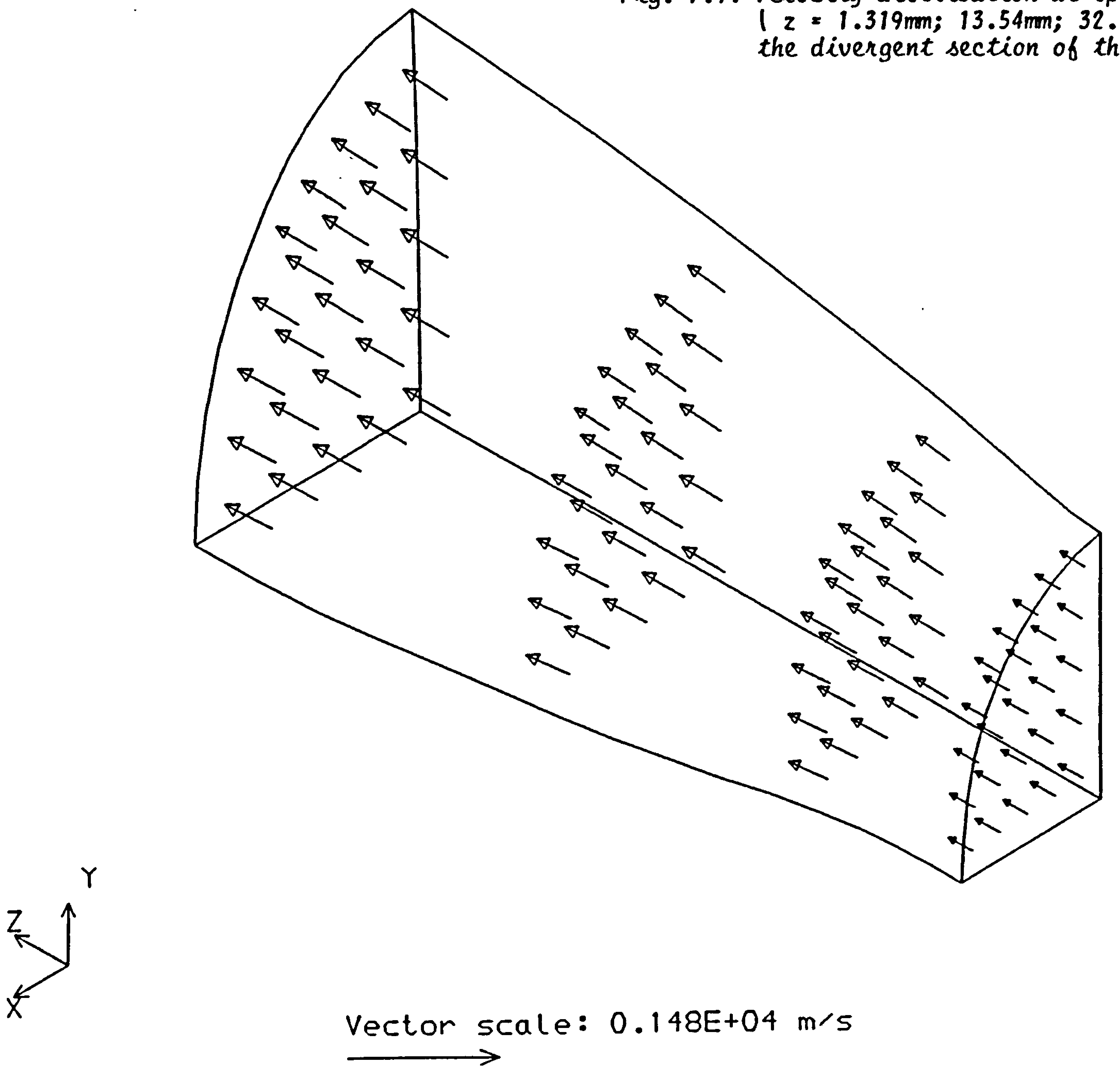

Fig. 7.10: Mesh describing one quater of the divergent section of the two-dimensional wedge nozzle.

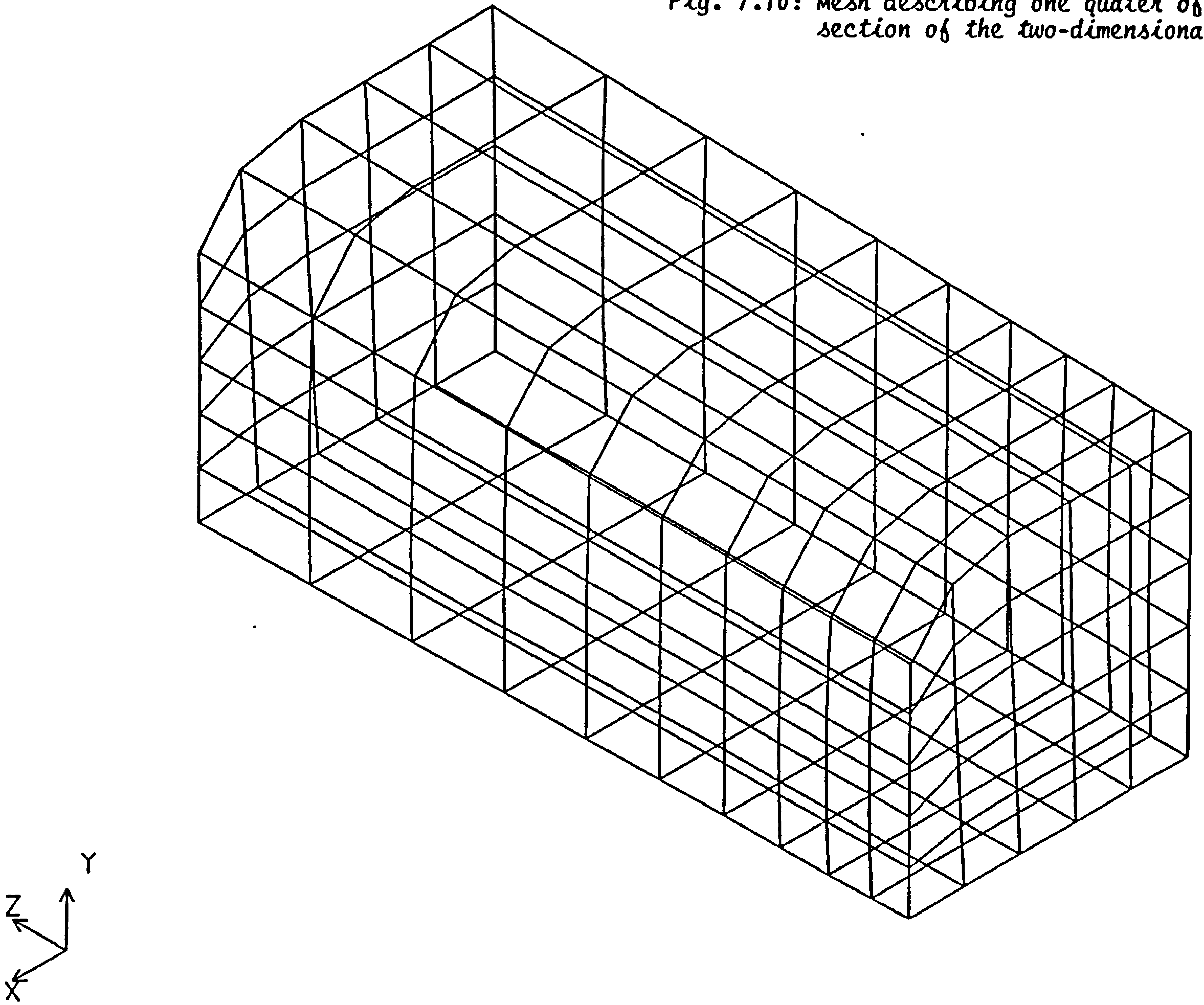

Fig. 7.11: Velocity distribution along the walls of the divergent section of the two-dimensional wedge nozzle.

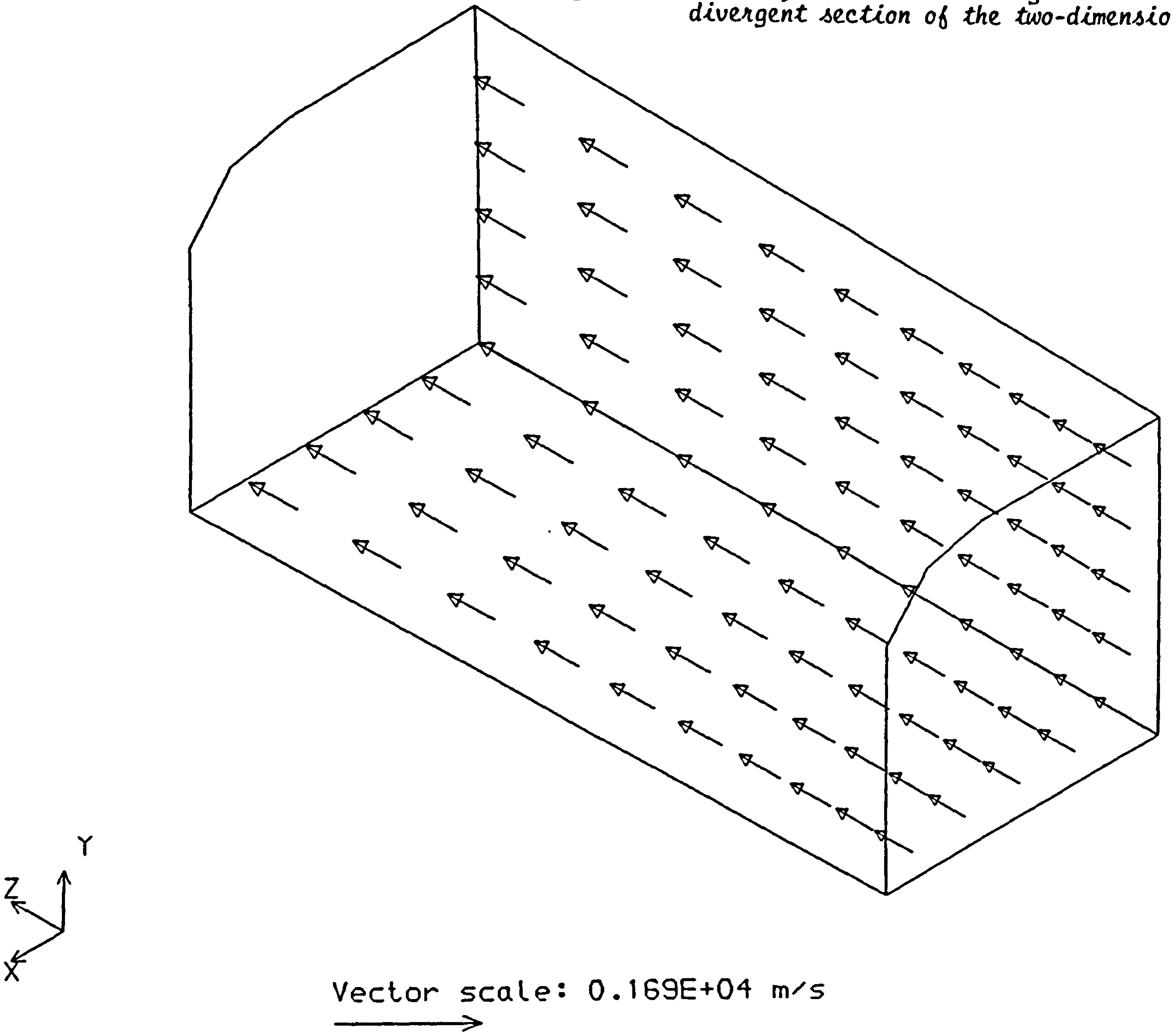

Fig. 7.12: Velocity distribution at specified cross-sections (z = 14.89mm; 174.76mm; 363.17mm & 527.51mm) of the divergent section of the two-dimensional wedge nozzle.

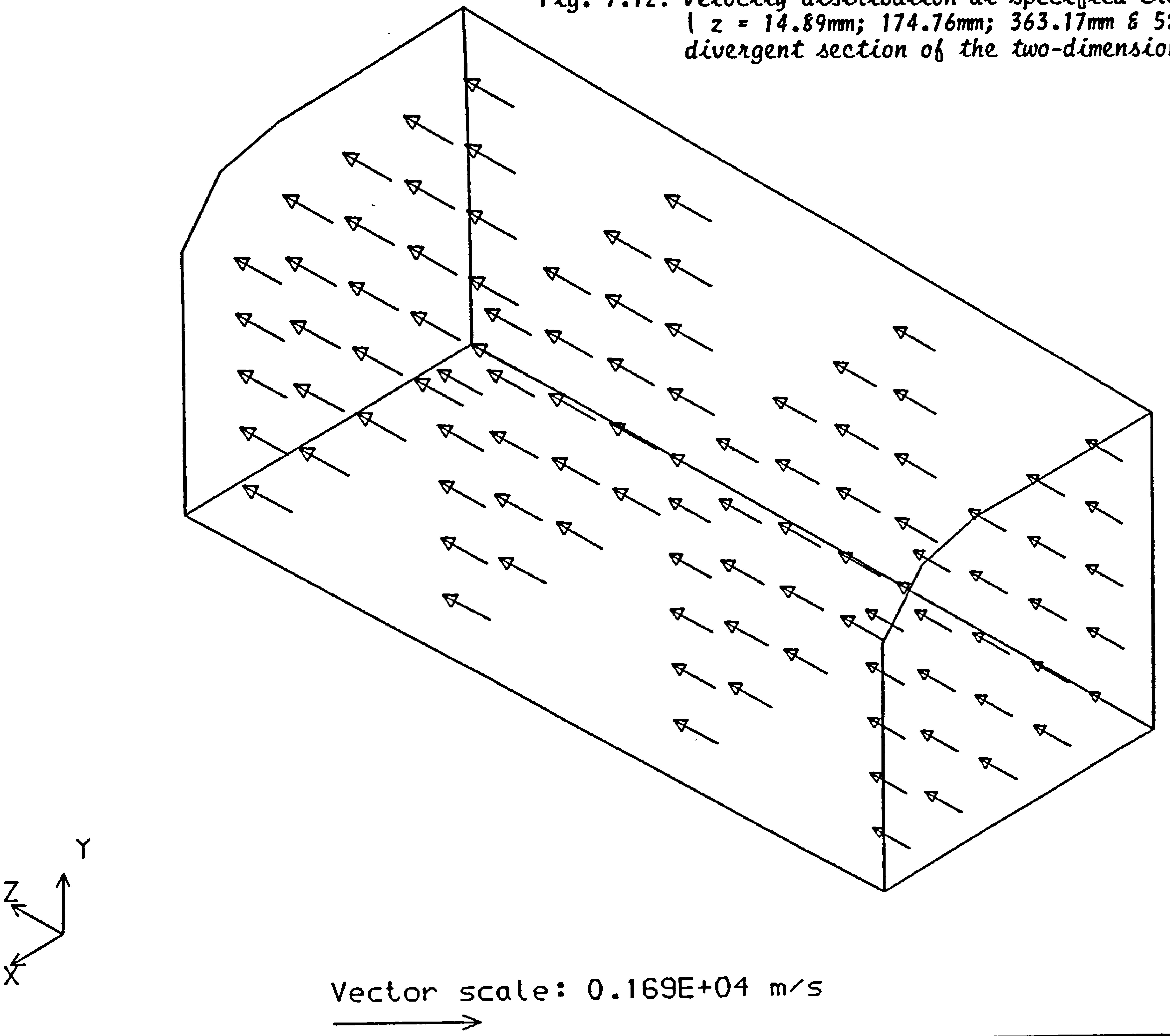

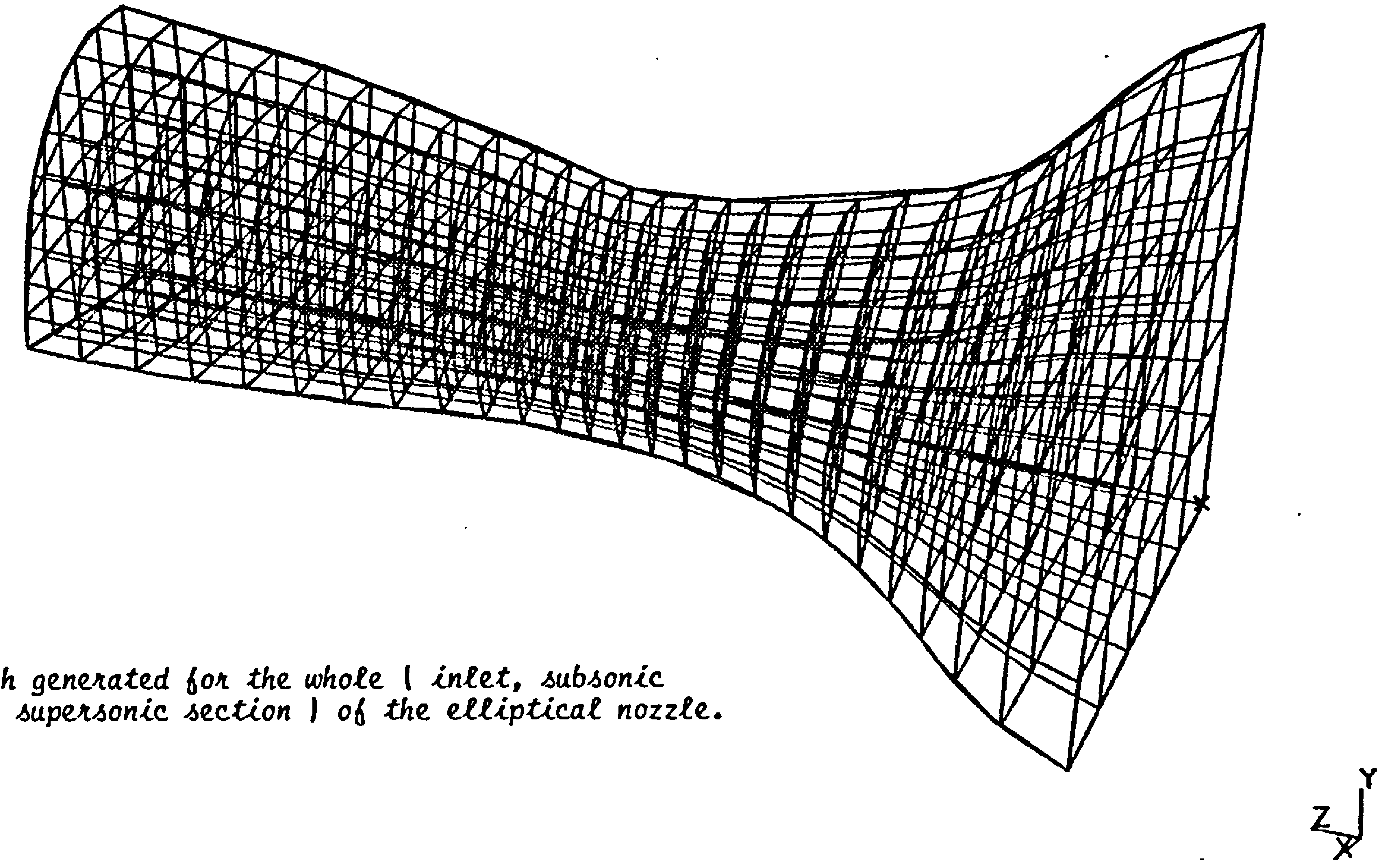

Fig. 7.13: Mesh generated for the whole (inlet, subsonic and supersonic section) of the elliptical nozzle.

supersonic) may require the intervention of the user to 'help' the code achieve the required invariable convergence (CHAM report TR/100).

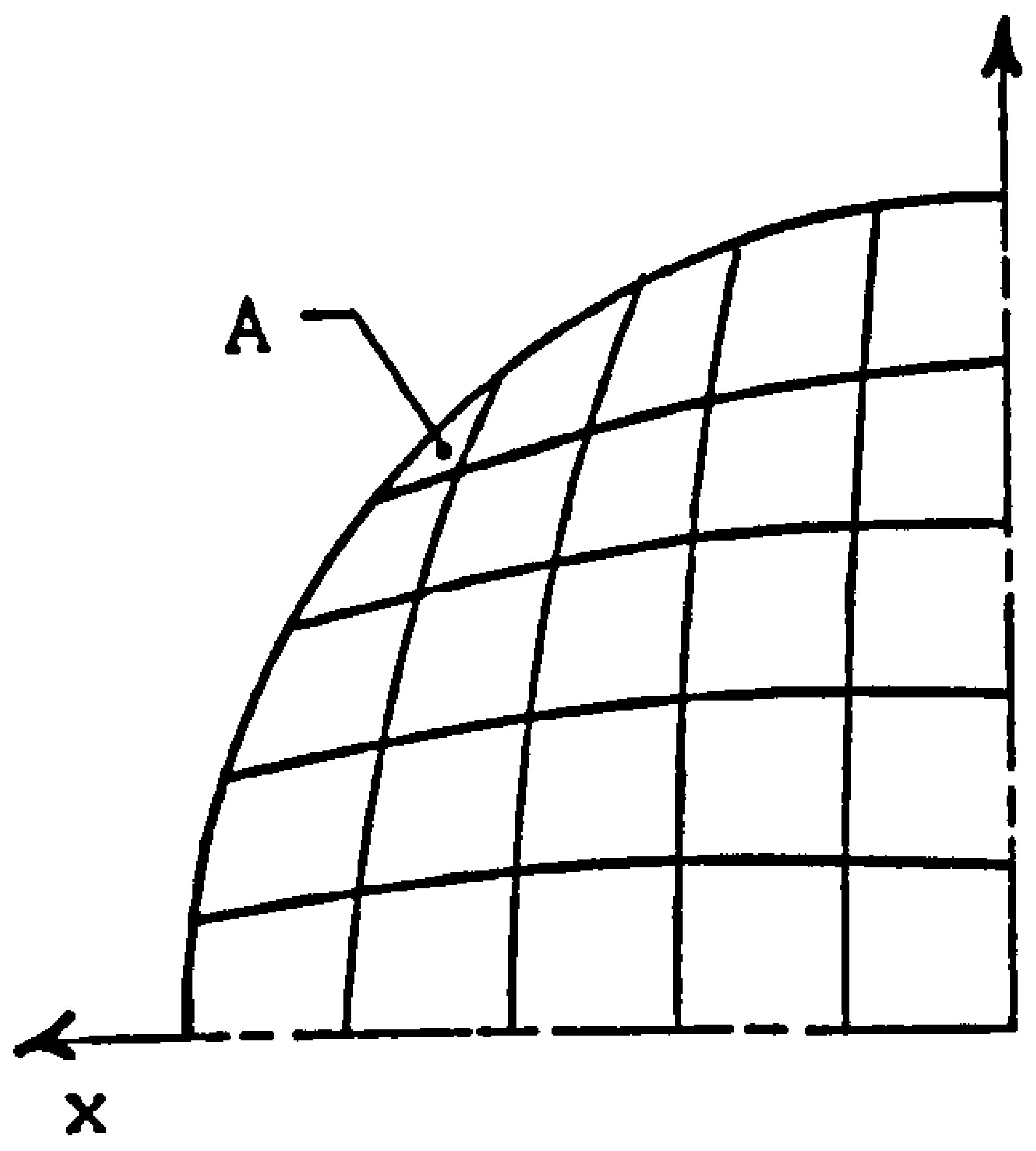

Fig. 7.14: Grid used to describe the elliptical nozzle.

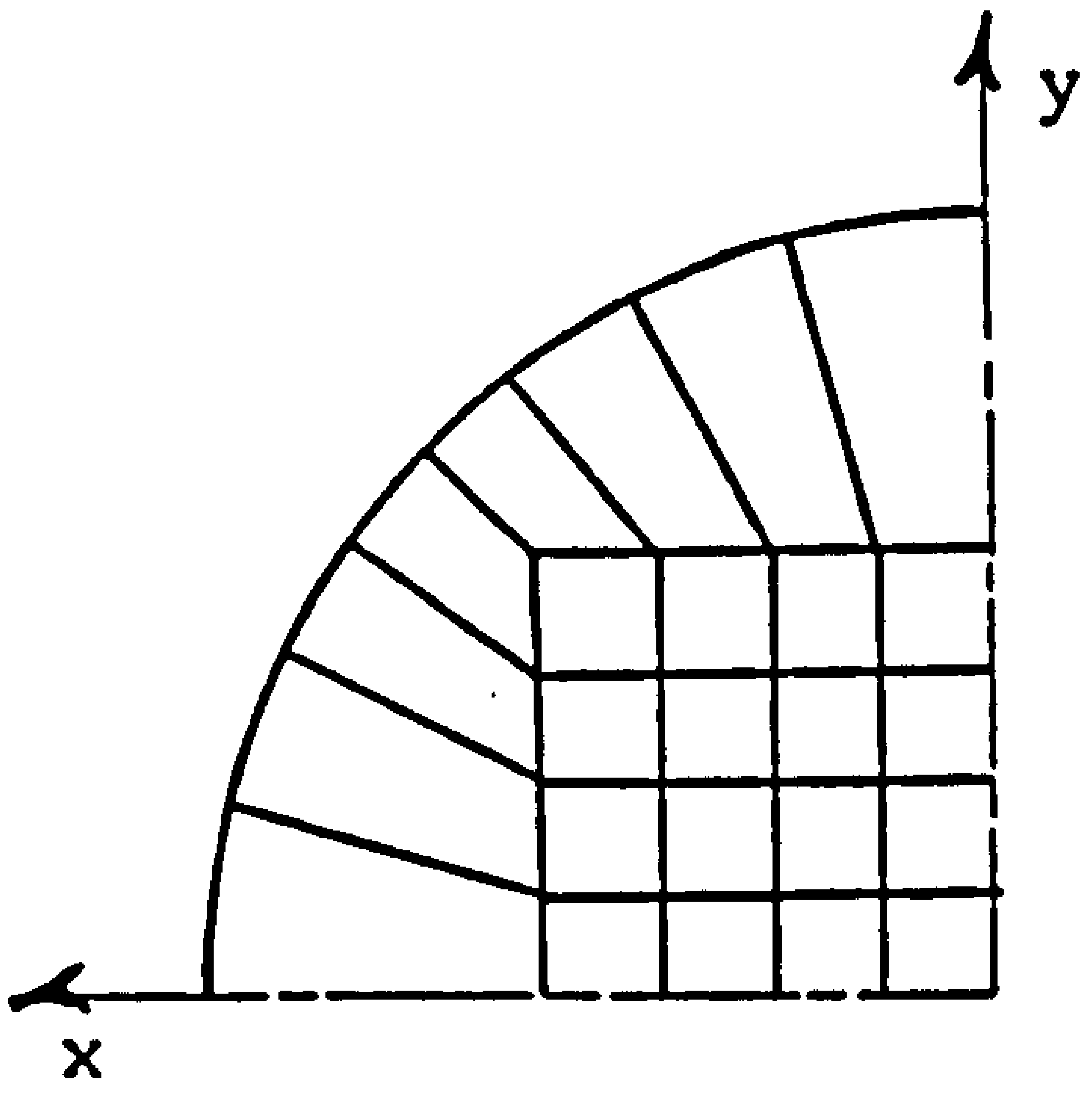

Fig. 7.15: Proposed grid designed to eliminate the loss of orthogonality.

3. In most cases, the boundary layer which develops along the wall of supersonic nozzles is very thin. For the present simulation to achieve computations inside the boundary layer, the grid must be greatly refined allowing nodes (at which the computation are carried out) to be situated inside the boundary layer.

In the case of the axisymmetric nozzle from which the elliptical nozzle was designed using the method investigated in this thesis, the boundary layer thickness was found to be of the order of 1/10 mm. For the three-dimensional simulation to achieve computation inside the boundary layer, a grid comprising an excess of one million cells must then be used. With a view towards the high computer time and large storage required to achieve a similar design, such a simulation could not be realistically considered.

SECTION 8 : Results and discussion

8.1 General

At the present time no exact solution for fully three-dimensional supersonic internal flows exist. Consequently, it is not possible to make detailed comparisons with existing results. However, to illustrate the general capabilities of the preliminary design technique described earlier, three-dimensional simulation of the flowfield inside the two nonaxisymmetric configurations has been performed using a general purpose CFD code. Furthermore, the validity of the method has been demonstrated, at least in part, experimentally. A nozzle was constructed to the specifications of the elliptical configuration and tested with air as the fluid medium.

Results obtained from these two aspects of the study will be presented in the following chapters.

8.2 The elliptical nozzle

In the case of the elliptical nozzle, the design is not directed towards any specific application but is intended to be typical of the types of configurations which might perhaps be used as either integrated rocket, ramjet or scramjet nozzles.

The nozzle was submitted to cold flow testing using compressed air (section 6). Typical total pressure and temperature of the flow were 16.3 atm. and 350° K. These values were used as the initial conditions necessary to carry out the three-dimensional computations of the flowfield performed by 'Phoenics' (section 7)..

Static pressure distributions along the axis, derived from the three-dimensional simulation, experimental tests of the elliptical cross-section nozzle and the method of characteristics computations of

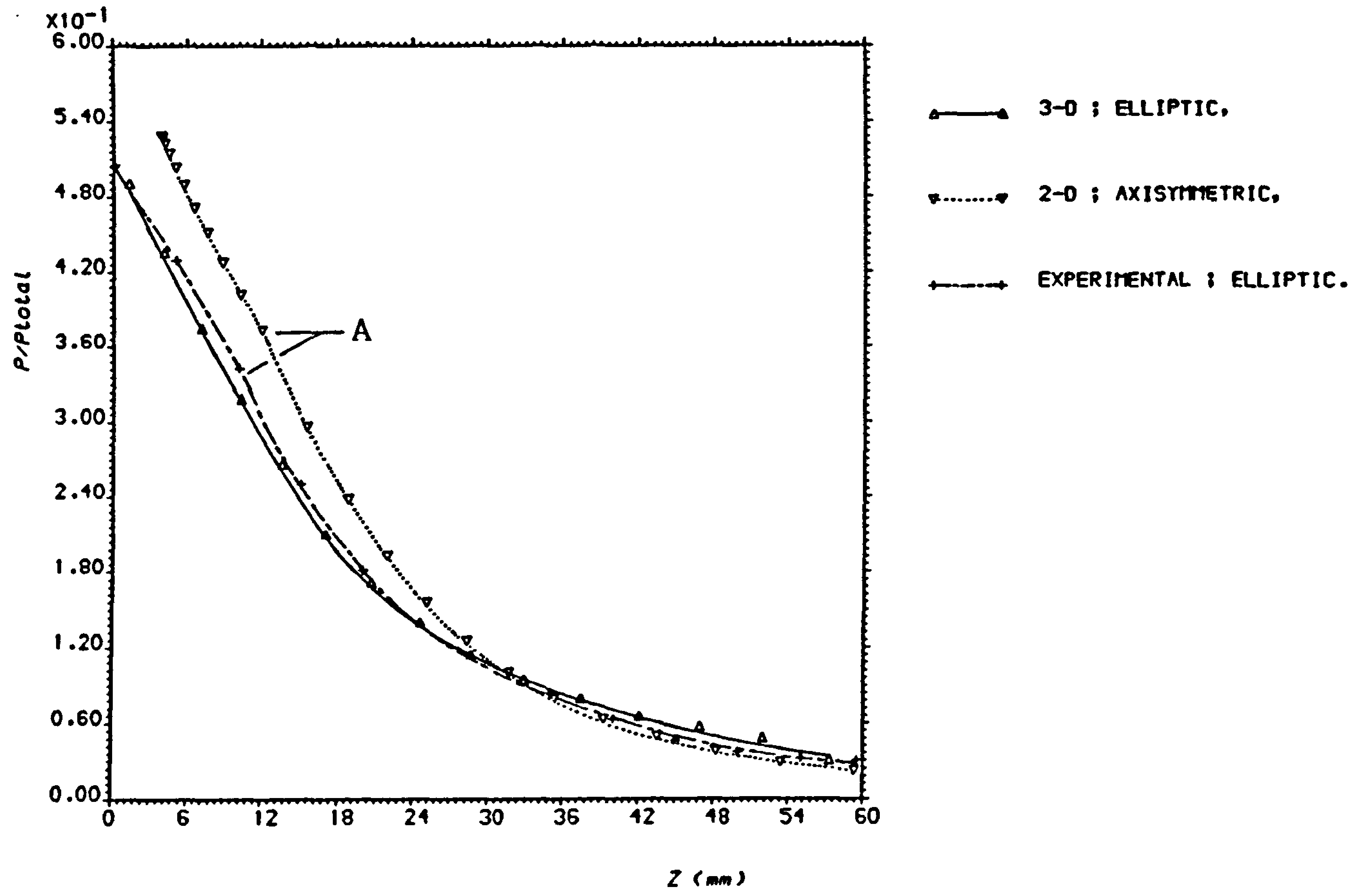

FIG :[8.1] PRESSURE DISTRIBUTIO N ALONG CENTRELINE.

AR(Axisymmetric)=2.3 27 ; AR(Elliptic)=2.465

its axisymmetric counterpart are shown in Figure 8.1. Agreement between the three-dimensional solution and the experimental investigation is good except at points of discontinuous rates of change in flow properties. The point on the nozzle at which the first expansion wave from the wall reaches the axis is such a point and is labelled by 'A' in Figure 8.1. The same change in slope is shown by the method of characteristics computations which are performed along characteristics and thus do not require interpolation, giving the true character of the solution. The three-dimensional calculations smooth out this point. This diffusive characteristic is inherent to any three-dimensional calculation scheme because of the necessity to interpolate and because of the need to satisfy the stability criterion which requires that numerical disturbances be propagated at a velocity greater than the infinitesimal propagation speed i.e. the speed of sound.

In Figure 8.1, the two-dimensional solution of the flowfield performed within the initial axisymmetric nozzle from which the elliptical nozzle was developed subsequently does not originate at the throat (z=0). This is due to the position of the initial-value line from which the method of characteristics computations started. The initial-value line was defined using the method of (Sauer, 1947) and is situated beyond the throat section (Figure 8.2). Sauer's method

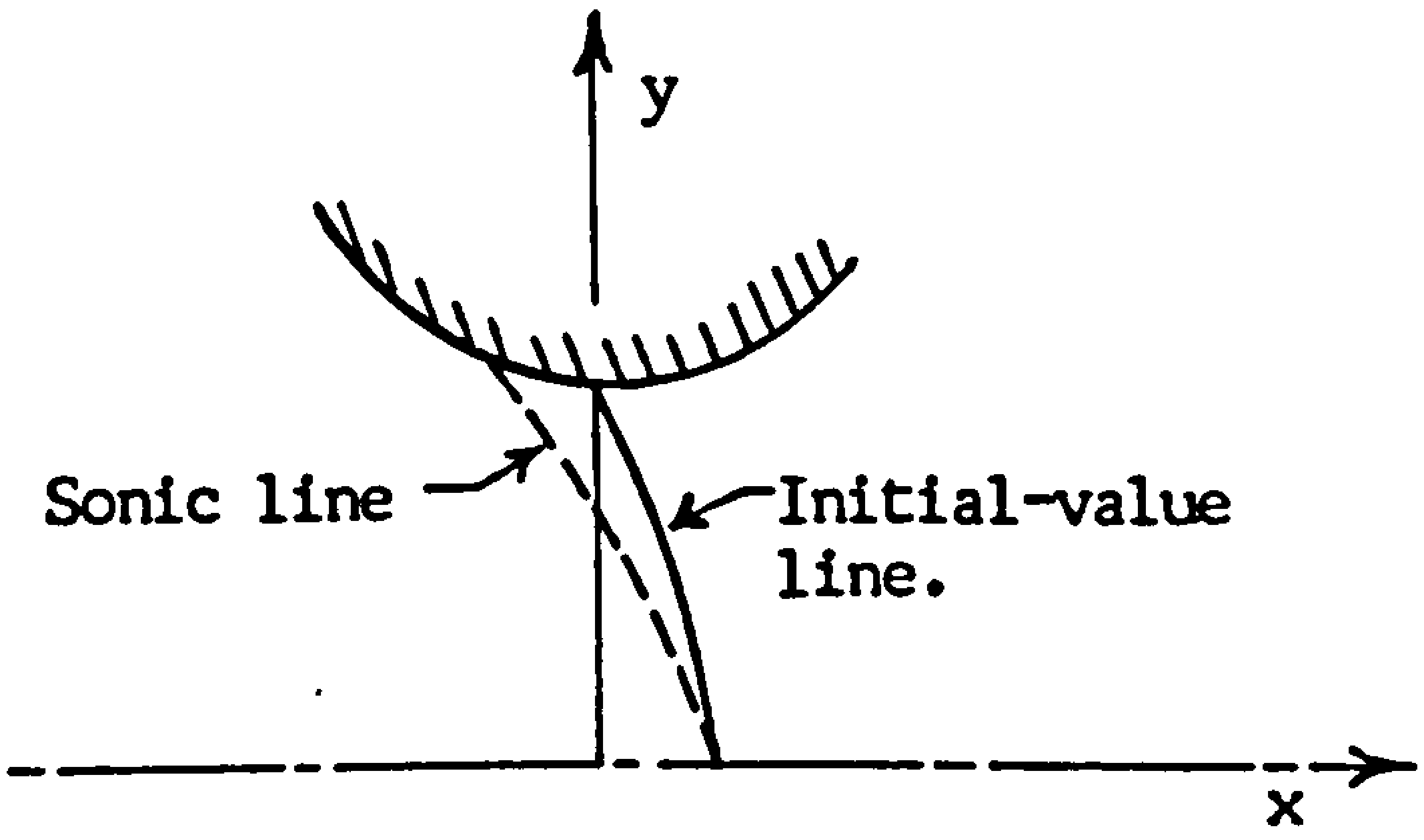

Fig. 8.2: Throat cross-section.

was used to solve the transonic flow along the initial-value line, thus providing the initial boundary conditions necessary for the method of characteristics to carry out the supersonic flowfield

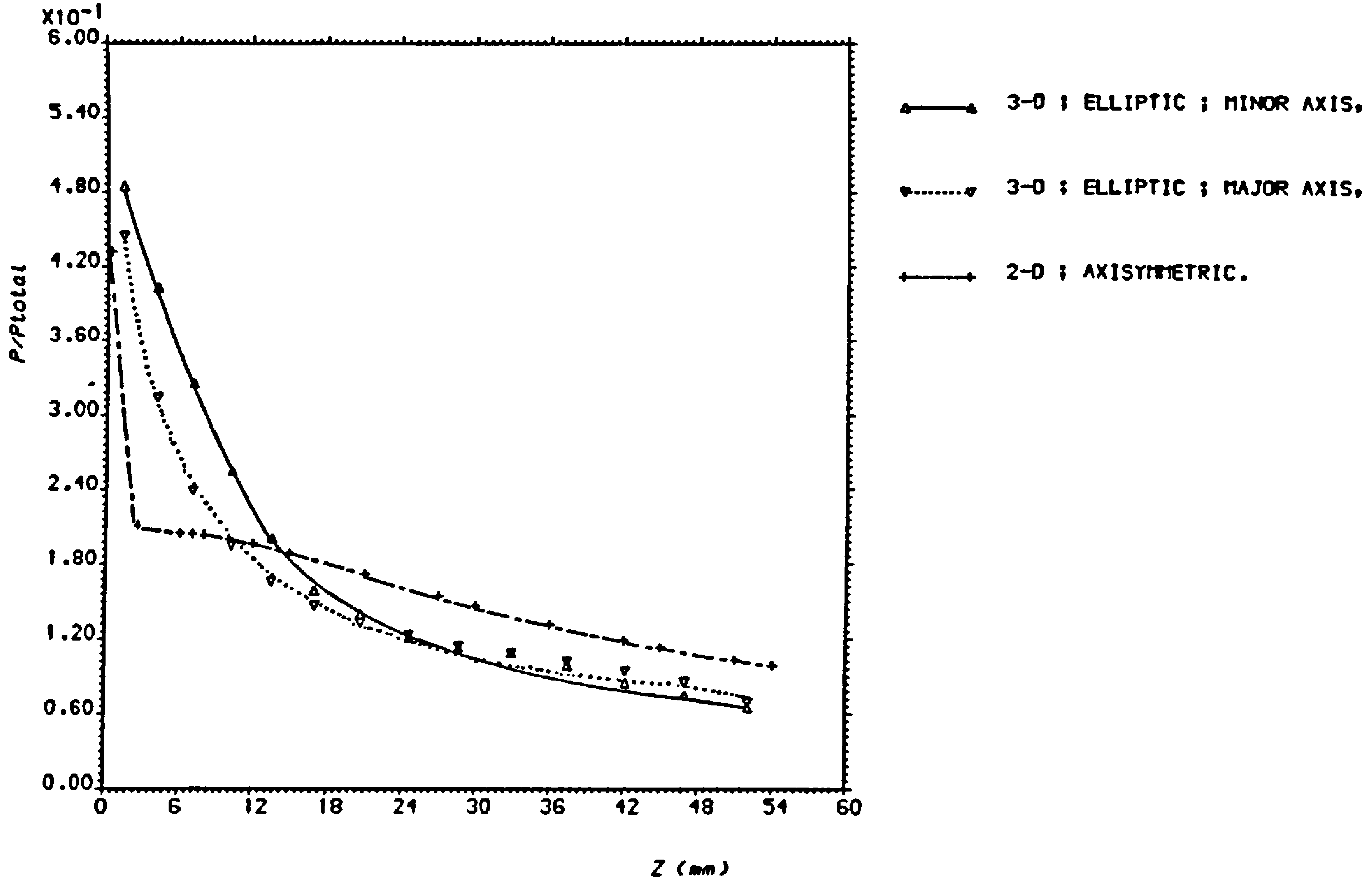

FIG :[8.3] PRESSURE DISTRIBUTION ALONG WALL.

AR(Axisymmetric)=2.3 27 ; AR(Elliptic)=2.465

computation (section 3).

The finite-difference calculations also predict that the expansion along the walls (Figure 8.3) proceeds smoothly along both the minor and major axes of the elliptical nozzle. Within the axisymmetric nozzle, however, the method of characteristics calculations show that the pressure drops sharply in the immediate vicinity of the throat tending to stabilize further downstream. This discrepancy between the two solutions may be attributed to the way the elliptical configuration has been generated by 'I-Deas' (gridding) and its implication on the three-dimensional calculations carried out by 'Phoenics'. The results of the axisymmetric computations carried out by the method of characteristics, which show the true character of the solution, are characteristic of an axisymmetric contoured supersonic nozzle with a relatively large contour angle which allows a large part of the expansion to occur near the throat, the remaining contoured walls straightening the flow. The advantageous result is a substantially shorter nozzle.

In the time available to the study we were unable to add pressure tappings to the elliptical nozzle; the highly curved surfaces and small scale making this an awkward task (section 6.2.4). However, the above results compare well with those of (Ransom et al, 1972), on a similarly contoured nozzle, from which Figure 8.4 is reproduced. It represents the centreline and wall pressure ratios as a function of axial position. The drop in pressure seems to be sharper than the one occurring in our case (Figure 8.1 along centreline and Figure 8.3 along wall) reflecting differences in the maximum contour angle whose value reaches 35° in Ransom's case and 15° in our case.

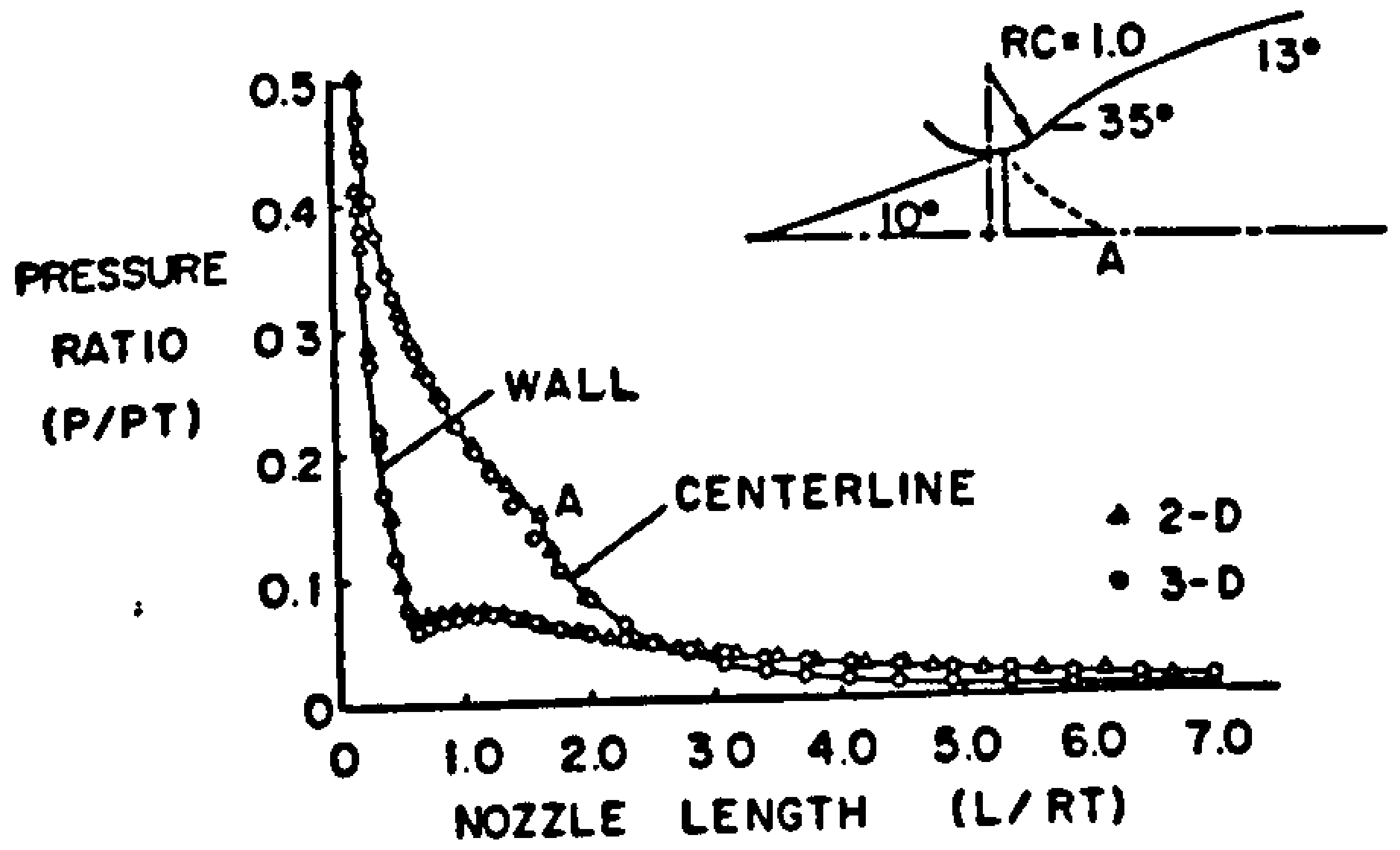

Fig. 8.4: Comparison of the wall and centreline pressure ratios as a function of axial position in a contoured nozzle.
(Ransom et al, 1972)

Figure 8.3 also suggests that the flow expands more rapidly along the minor axis than the major axis. The figure also reflects the azimutal pressure gradient round the contour (since the data shown represent the predicted pressures at the same cross-sections) which is typical of three-dimensional configurations causing cross flows and adding to the build up of the boundary layer. However, experimental results (illustrated by Figures 8.1 for the pressure distribution along the centreline, Figure 8.8 for the pressure distribution at the exit cross-section and Plate 6 for the schlieren picture of the flow exiting from the elliptical nozzle) show that the flow behaved in a satisfactory manner with no evidence of separation. The results illustrated by Figure 8.3 fall close to the predictions of (Ransom, 1972) performed along the so-called super-elliptic nozzle (Figure 8.5) and illustrated in Figure 8.6.

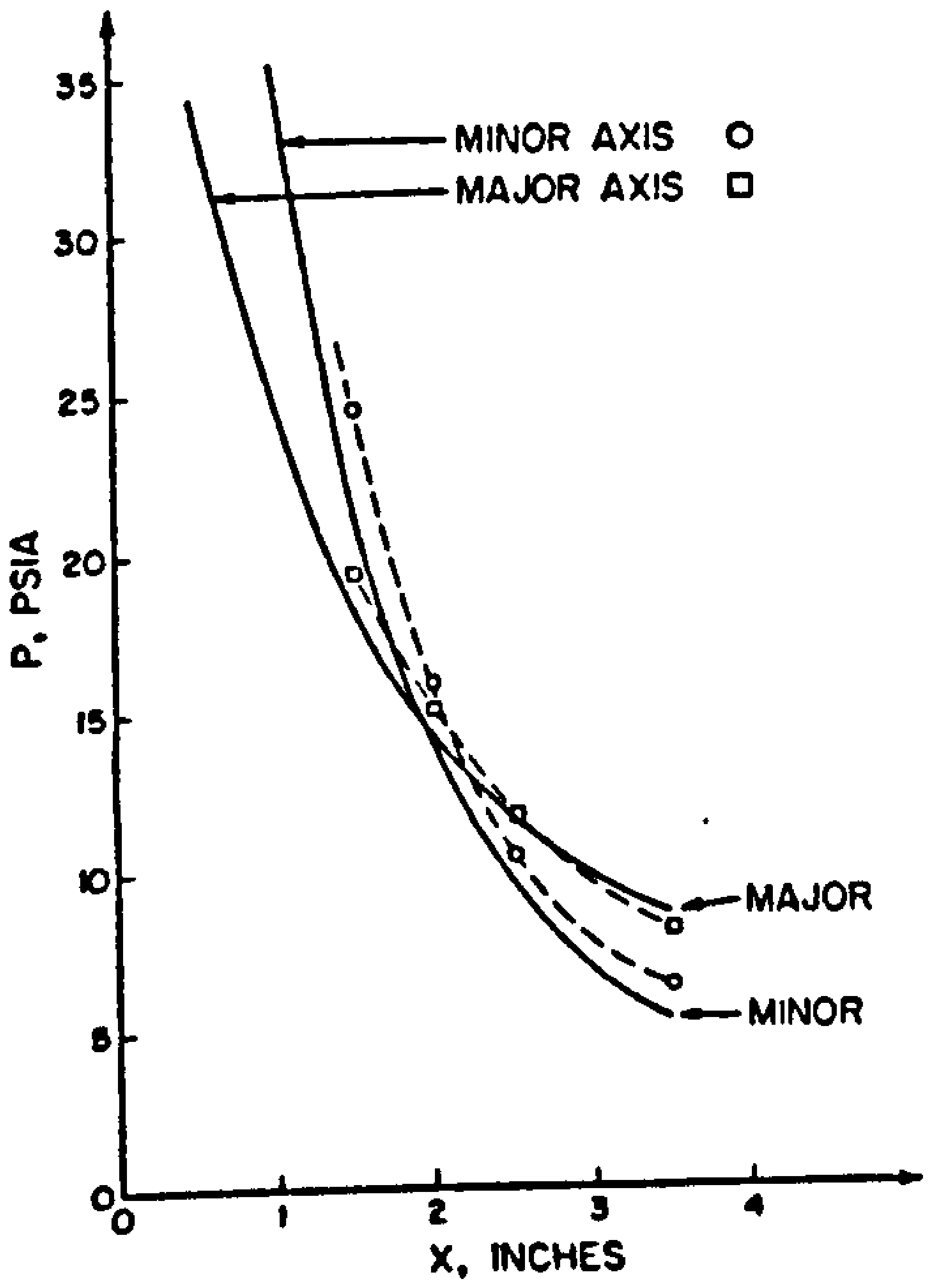

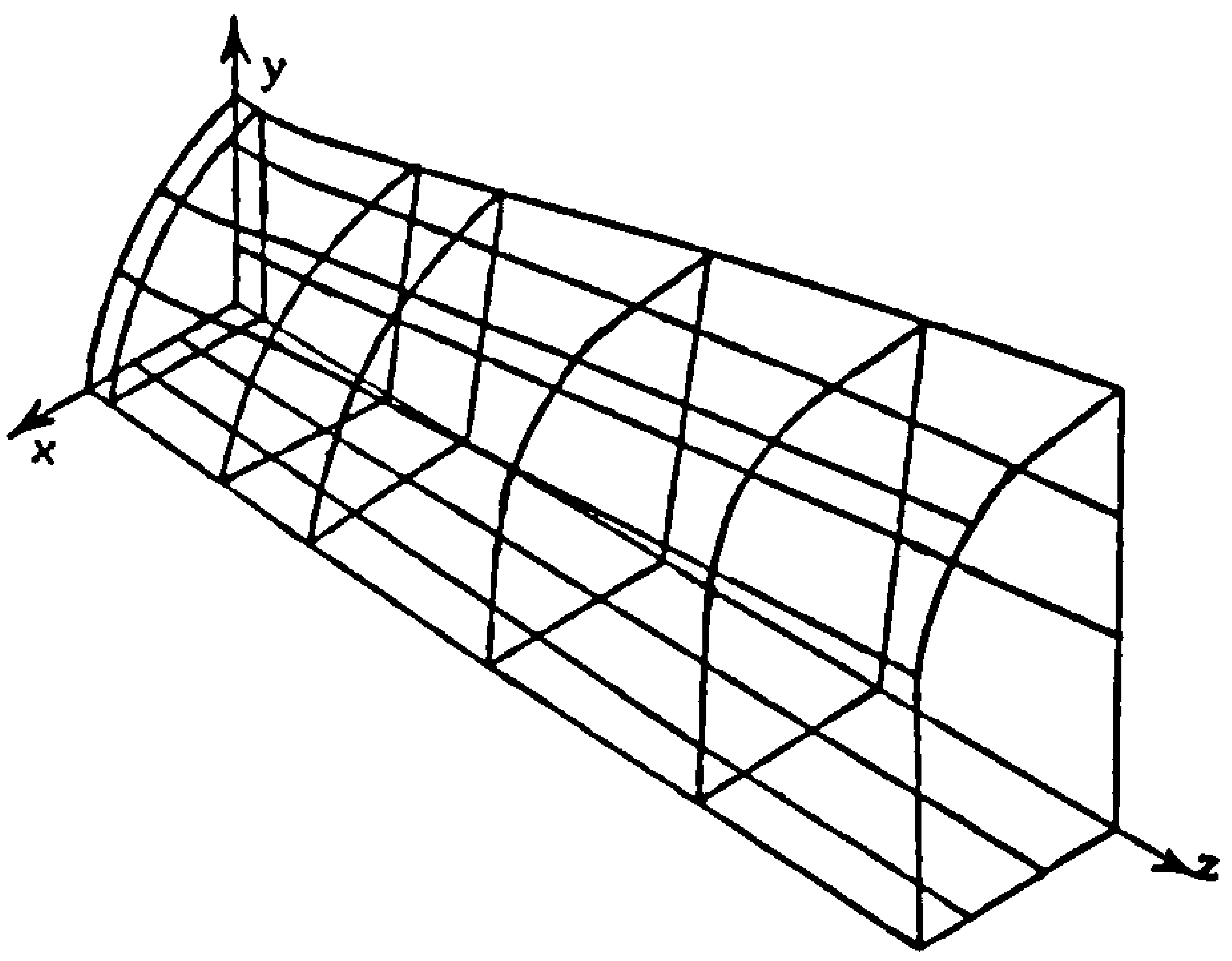

Fig. 8.5 : The super-elliptical nozzle. (ransom et al.,1972)

Fig. 8.6 : A comparison between the theoretical and experimental pressures along the minor and major axes of the super-elliptical nozzle (Ransom et al,1972)

Pressure distributions along cross-sections show a difference of pressure gradient between the axisymmetric and the elliptical nozzles (Figure 8.7). This shows clearly along the nearest cross-section to the throat (z = 4.07 mm in Figure 8.7) where, for the axisymmetric configuration, the static pressure gradient between the centreline and

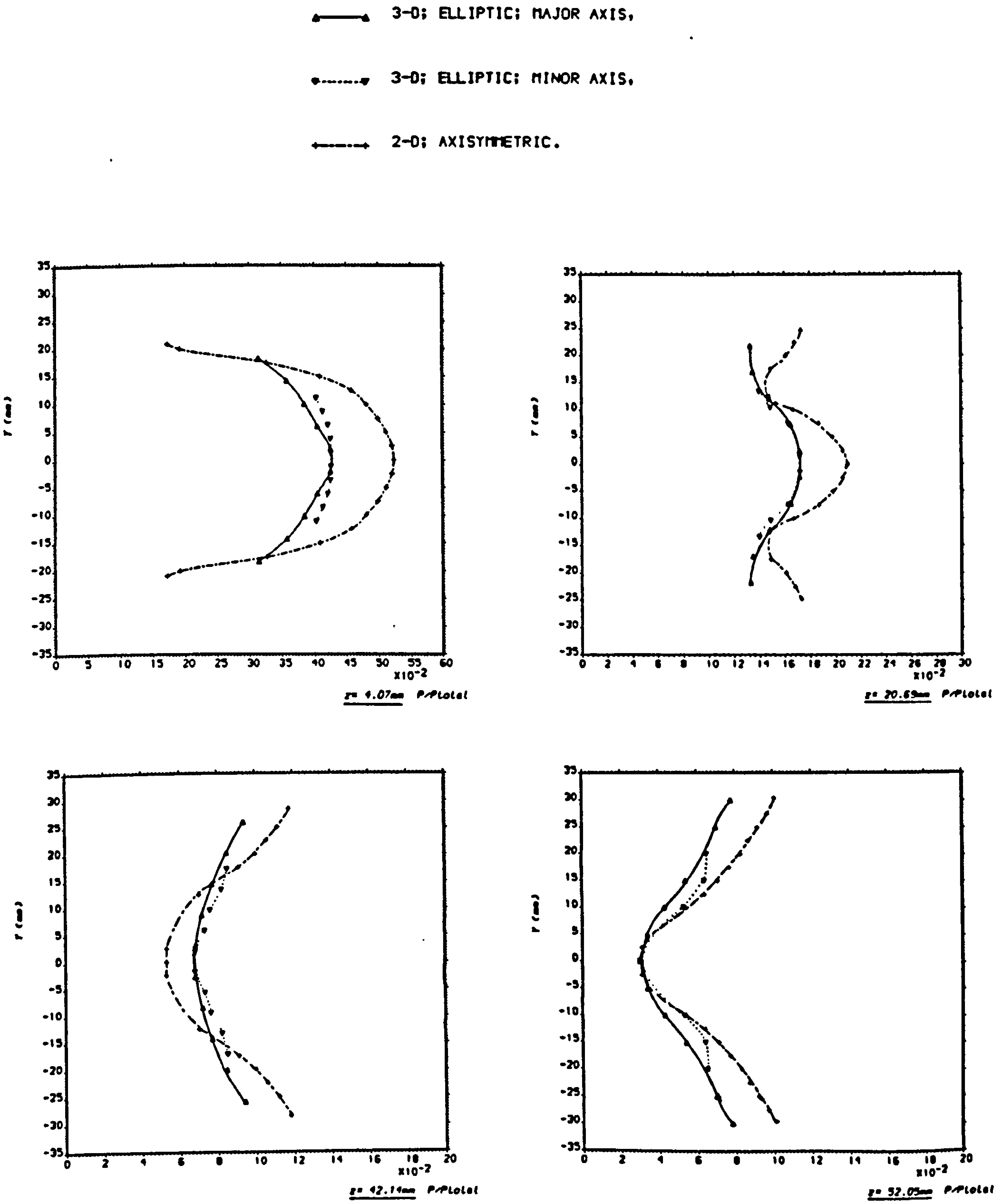

FIG : [8.7] PRESSURE DISTRIBUTION ALONG CROSS-SECTIONS.
AR(Axisymmetric)=2.32 ; AR(Elliptic)=2.46

the wall equals approximatively 35% of the total pressure. When considering the major axis, the pressure gradient along the same cross-section equals 10% of the total pressure while for the minor axis, it decreases to 2% of the same pressure. However, these differences diminish in an appreciable way when we travel further downstream into the supersonic section (z= 20.69mm, 42.14mm & 52.05mm in Figure 8.8) until the exit (illustrated by Figure 8.8) where the two curves are very similar. Differences may be observed between the three-dimensional solution performed by 'Phoenics' for the elliptical nozzle and the method of characteristics solution carried out for its axisymmetric contoured counterpart. These discrepancies may be attributable to the way the flowfield computations were performed by the two methods of solution. While the axisymmetric calculations proceeding along characteristics reflect the true character of the solution, the three-dimensional calculations rely heavily on the grid topology describing the elliptical configuration (c.f. Section 7). Moreover, when performing the three-dimensional computations, the exit static pressure was considered as a boundary condition and the solution had to carry on from the throat to the exit and satisfy the the initial and final boundary conditions represented by the inlet and exit static pressures.

The thrust, thrust coefficient and exit Mach number produced by the elliptical nozzle and its axisymmetric counterpart were determined. Table 8.1 represents a comparison between the elliptical and axisymmetric configurations. These data show that the axisymmetric nozzle exhibits a higher thrust performance than its elliptical counterpart. They also show the difference, with respect to the mass flow required for chocking, between the two configurations.

In order to obscure the influence of the mass flow, comparison is carried out with respect to the specific thrust (defined as the ratio of the calculated thrust to the mass flow). When considering the ratio $T/\dot{m}$, the axisymmetric nozzle exhibits a 20% advantage over its elliptical counterpart demonstrating the high internal performance attainable with axisymmetric nozzles.

When considering the thrust coefficient (defined in Appendix I), the axisymmetric configuration again shows a 5% advantage over the

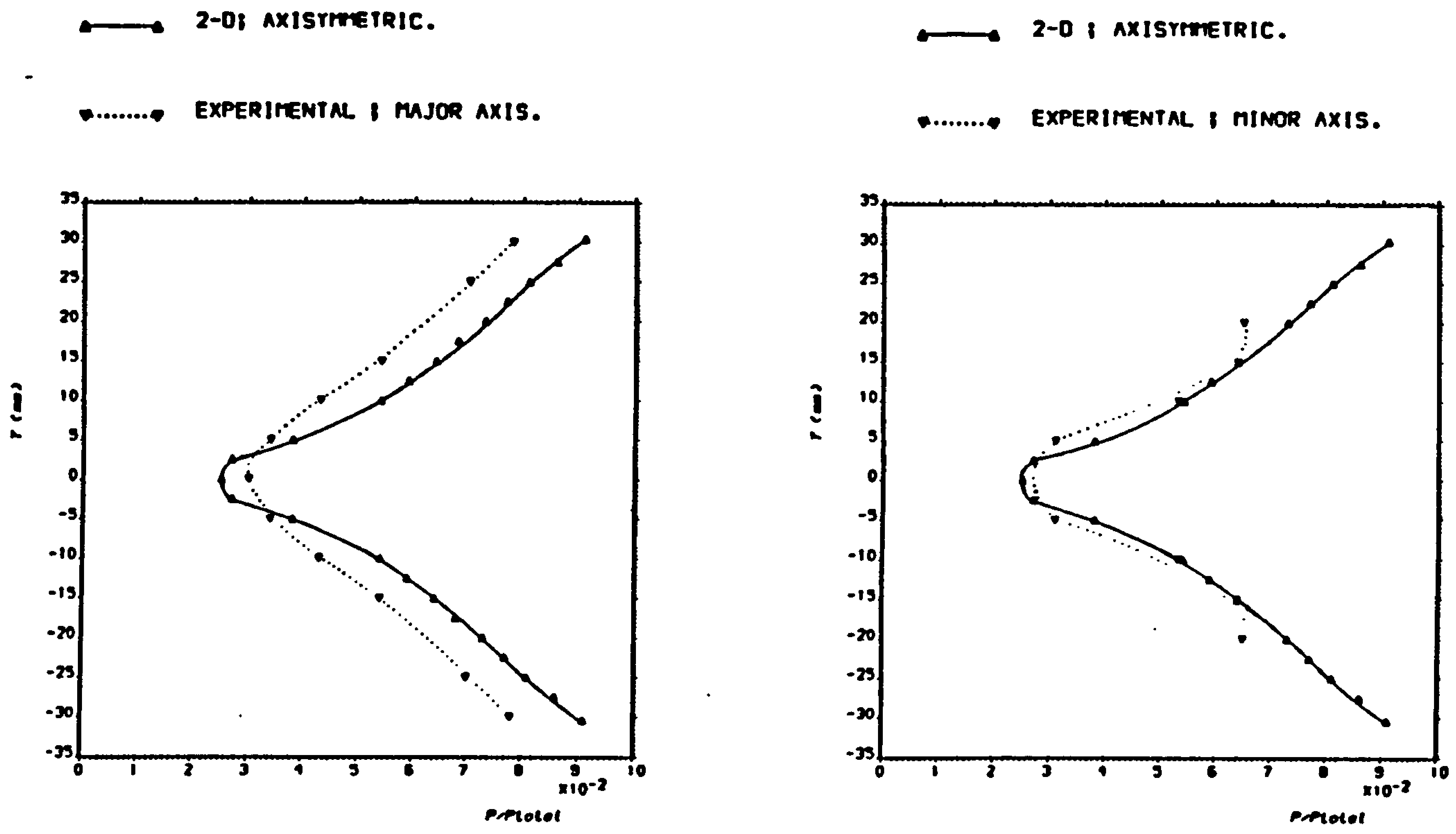

FIG : [8.8] PRESSURE DISTRIBUTION ALONG THE EXIT CROSS-SECTION.
AR(Axisymmetric)=2.32 ; AR(Elliptic)=2.46

elliptical design. The thrust coefficient describes the effectiveness of the expansion of the combustion gases. The above results then demonstrate that the axisymmetric configuration lends itself to better control of the expansion process.

The Mach numbers represented in Tables 8.1 and 8.2 represent the average, calculated with respect to the area, of the Mach number distribution along the exit cross-section of the elliptical and two-dimensional wedge nozzles respectively.

8.3 Two-dimensional wedge nozzle

The two-dimensional wedge is typical of the new technology Con-di nozzles which will be integrated into future fighter aircrafts. Its principal advantages and disadvantages have been summarized in section 2.

At low power settings, the overall area ratios of such nozzles are fairly modest and the expansion process along the two-dimensional wedge nozzle and its axisymmetric counterpart takes place gradually. Figure 8.9 represents the solution along the centreline and Figure 8.10 along the wall. This gradual pressure drop is due to the low value of the divergence angle corresponding to cruise conditions at which the nozzle has been designed.

Table 8.2 presents a comparison between the two-dimensional wedge and axisymmetric nozzles. When considering the thrust coefficient, the axisymmetric nozzle exhibits a 5% advantage over its two-dimensional counterpart. It also develops a greater specific thrust.

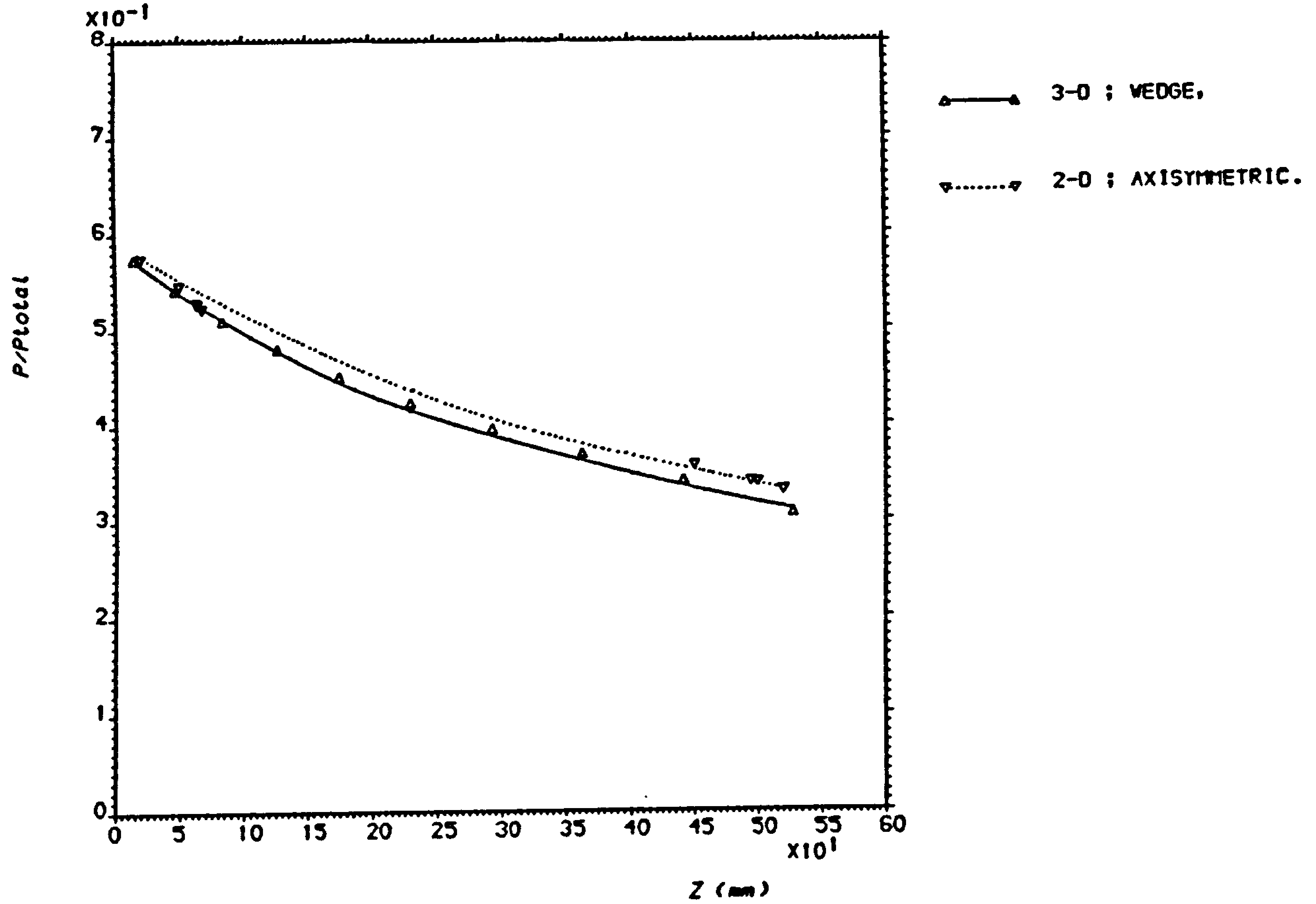

FIG : [8.9] PRESSURE DISTRIBUTI ON ALONG CENTRELINE.

AR(Axisymmetric)=1. 125 ; AR(Wedge)=1.132

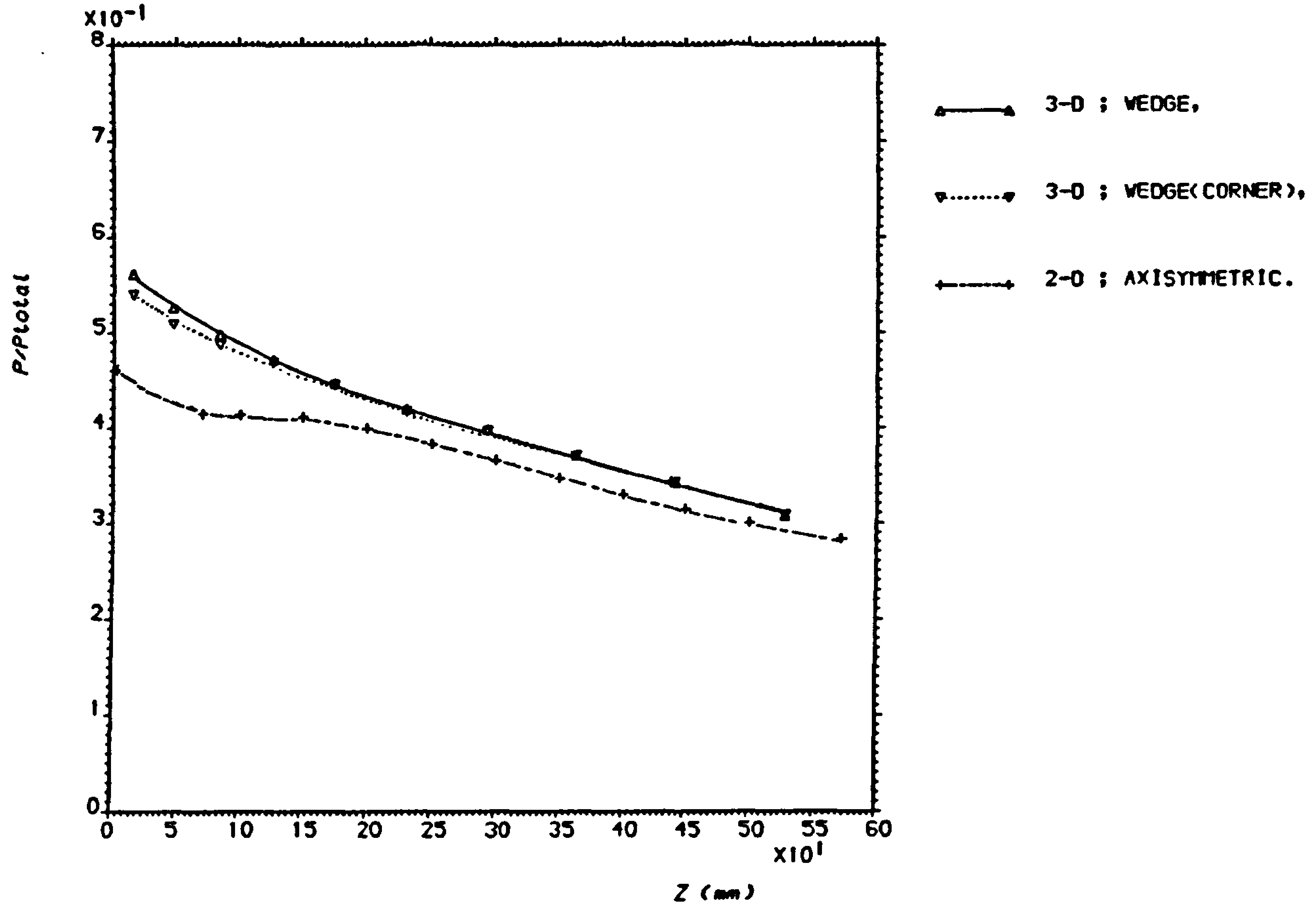

FIG : [8.10] PRESSURE DISTRIBUTION ALONG WALL.

AR(Axisymmetric)=1 .125 ; AR(Wedge)=1.132

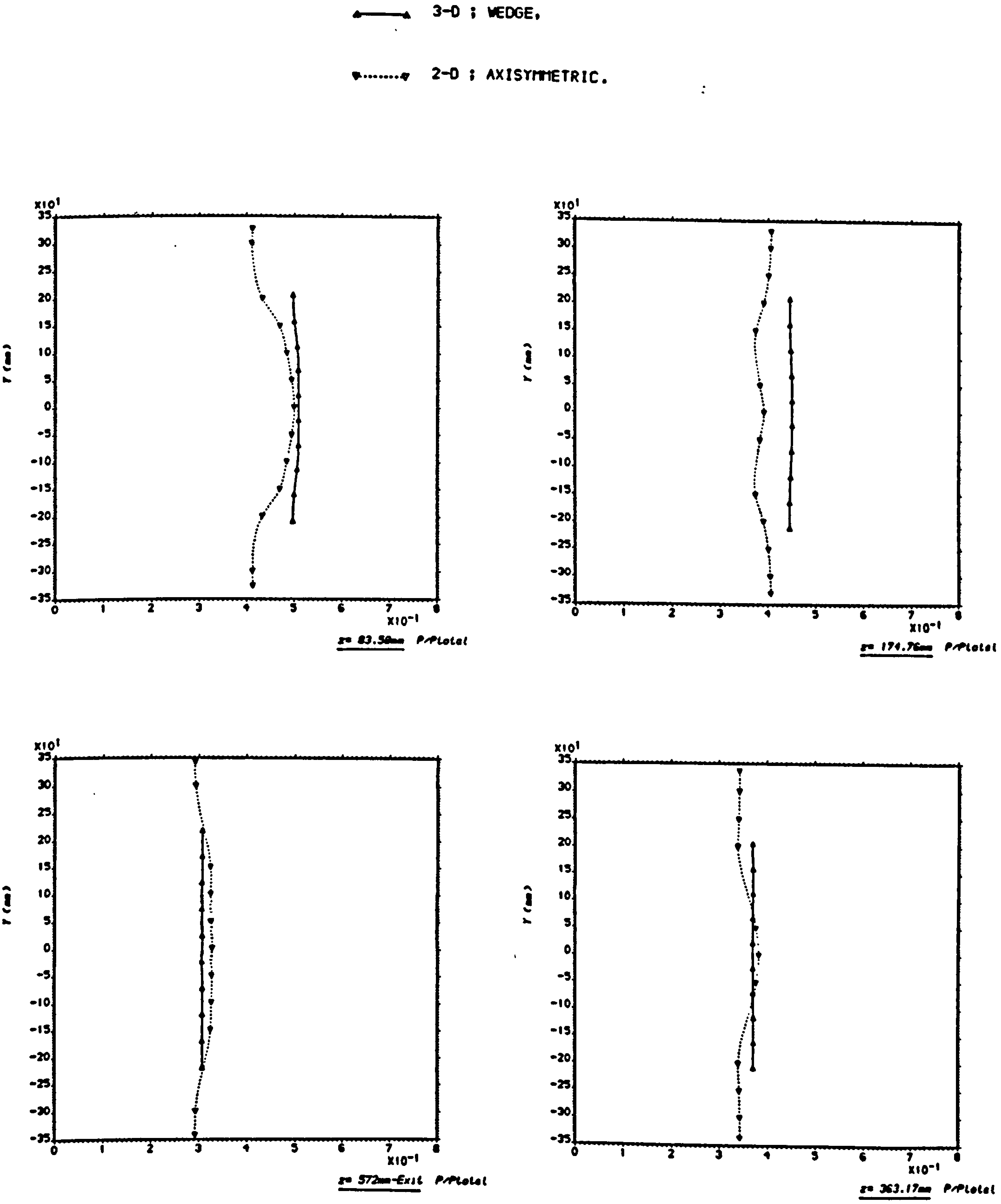

z= 83.50mm P/Ptotal

z= 174.76mm P/Ptotal

z= 572mm-Exit P/Ptotal

z= 363.17mm P/Ptotal

FIG : [8.11] PRESSURE DISTRIBUTION ALONG CROSS-SECTIONS.
AR(Axisymmetric)=1 .125 ; AR(Wedge)=1.132

TABLE 8.1

	Thrust (N)	m (Kg/s)	C_D	T/m (m/s)	M_e
Elliptical nozzle	1578	2.25	1.24	701	2.47
Axisymmetric nozzle	2470	2.80	1.31	882	2.36

TABLE 8.2

	Thrust (N)	m (Kg/s)	C_D	T/m (m/s)	M_e
2-D wedge nozzle	62, 275	90	0.93	692	1.41
Axisymmetric nozzle	105, 868	130	0.98	814	1.44

SECTION 9 : Conclusion

9.1 concluding remarks

A simple and practical method for determining theoretical wall contours of three-dimensional supersonic nozzles from known axisymmetric flows has been developed. Two three-dimensional nozzles have been designed: an elliptical cross-section nozzle and a two-dimensional wedge. Detailed flowfields within these configurations were also computed using a general purpose CFD code. Furthermore, a nozzle was constructed to the specifications of the elliptical nozzle and submitted to cold flow testing. Results from the experimental tests and three-dimensional numerical simulation were obtained. Comparison between the several components of the study leads to the following conclusions :

1. A generalised CFD code 'Phoenics' (Appendic H) using finite difference techniques was used to calculate the flowfield within the three-dimensional configurations (elliptical and two-dimensional wedge). Within the limited time available for this aspect of the simulation and with a view towards computer time and storage, a simple grid describing the elliptical nozzle was generated and used (section 7). When comparing the theoretical predictions for the pressure distribution performed by the method of characteristics to the three-dimensional flow results (figures 8.1, 8.3 and 8.7), discrepancies between the two solutions may be observed. These differences may be attributable to the way the flowfield computations were performed by the two approaches. While the method of characteristics calculations proceed along the characteristics (Mach lines) and thus show the true character of the solution, the three-dimensional calculations rely on the gridding designed to

describe the configuration under consideration. By using a more refined grid, the gap between the two solutions could have been diminished. Moreover, the three-dimensional scheme has to interpolate in order to satisfy the stability criterion while the method of characteristics, as stated above, proceed along characteristics.

2. With a view towards a simple 'proof of concept', a nozzle was constructed to the specifications of the elliptical nozzle and submitted to cold flow testing using compressed air. The static pressures along its centreline were measured and their distribution along with the three-dimensional results are illustrated in Figure 8.1. Agreement between the two solutions is good and shows the ability of the three-dimensional scheme to predict accurately the flowfield expansion along the nozzle centreline.

3. The method investigated herein is based on three important features of axisymmetric inviscid flows (c.f. Introduction) and on the relative similarity between these flowfields and the nonaxisymmetric ones which are developed subsequently. This similarity is demonstrated in Figures 8.1 and 8.8 where the axisymmetric solution is compared to the experimental investigation, the latter having been performed on the elliptical nozzle designed using the approach developed in this thesis (Section 6).

4. When considering the thrust and thrust coefficient, both the axisymmetric nozzles performed better than their three-dimensional counterparts. They demonstrated the higher internal performance and the better control of the expansion process which can be achieved with axisymmetric configurations. However, uninstalled performances alone cannot be the final determinant when selecting a nozzle design. Considerations have to be turned towards other requirements such as the degree of integration, the total weight and cooling requirements. The latter considerations may, in some cases, outweight the former ones (section 2.5 shows how the two-dimensional wedge nozzle performed better than the axisymmetric when installed).

5. The computation of the boundary layer was performed along the divergent section of the two axisymmetric nozzles from which the elliptical and two-dimensional wedge nozzles were subsequently developed (Section 4). In both cases, the results obtained reflected the assumptions generally followed that the corrections required in order to include the viscosity effects for a supersonic flow within an axisymmetric nozzle are negligible.

6. The axisymmetric flowfield has been determined using a computer program based on the method of characteristics and developed following the scheme proposed by (Zucrow & Hoffman, 1976). Although the method can describe the flowfield within a nozzle of any shape, the one implemented into the program was bell shaped. However, enough flexibility is provided for implementing other shapes and thus enhancing the capabilities of the program (section 3).

9.2 Recommendations for further work

1. Two aspects of the theoretical simulation may be investigated further : 1) the first one deals with the study of the response of the boundary layer in such three dimensional flows. In order to achieve that using 'Phoenics', the configurations must be described by a very refined grid allowing the calculations to be carried out inside the boundary layer which develops along the wall (see the closing remarks of section 7). Loss of orthogonality of the cells may constitute a problem. Grid nonorthogonality may be reduced by either increasing the number of grid points or by redesigning the complete grid altogether. The second approach is favoured (see proposed grid in section 5).

2. The experimental investigation can also be carried out further. Static pressure tappings along the major and minor axes of the divergent section of the nozzle built to the specifications of the elliptical nozzle may be provided. Static pressure measurements would then be performed along these axes allowing a more detailed analysis of the influence of the azimutal pressure gradient and its effects on

cross-flows and the build up of the boundary layer.

9.3 Overall conclusion

A simple method for determining three-dimensional contours from axisymmetric or two-dimensional flows has been developed and shown to produce good results. The technique has been applied to the design of two nonaxisymmetric propulsion nozzles and has produced satisfactory configurations.

The culmination of this research is the production of a computer program suitable for the initial design of supersonic nozzles and inlets of quite complex shapes from known or calculated axisymmetric flowfields. Furthermore, that part of the program which calculates the initial axisymmetric flowfield may be used independently to compute compressible, viscous flows with heat transfer.

The success of the method in this application indicates that, even though it does not include the complications involved in generalised three-dimensional methods, it may still be profitably applied for preliminary design work. Indeed, any propulsion contractor would be ill-advised in not making use of a sophisticated program available to him. On the other hand, it is questionable whether the accuracy obtained with sophisticated programs is sufficient to justify their adoption for the bulk of preliminary design work.

LIST OF REFERENCES :

ALBERS, J. A. & GREGG, J. L.
'Computer program for calculating laminar, transitional, and turbulent boundary layers for a compressible axisymmetric flow'
NASA TN D-7521, 1974

ALLMAN, J. G. & HOFFMAN, J. D.
'Design of maximum thrust nozzle contours by direct optimization methods' ; AIAA journal, Vol. 9, Nb 4, pp. 750-751, 1981

BARRERE, M. ; JAUMOTTE, A. ; FRAEIJIS DE VENBEKE, B. & VANDENKERCKHOVE, J.
'Rocket propulsion'
Elsevier Pub. Co., 1960

BAXTER, D. C. & FLUGGE-LOTZ, J.
'The solution of compressible laminar boundary layer problem by a finite difference method, Part II'
TR 110, Division of Engineering Mechanics, Stanford University, Stanford, California, 1957

BERGMAN, D. ; MACE, J. L. & THAYER, E. B.
'Non-axisymmetric nozzle concepts for an F-111 test bed'
AIAA paper Nb 77-841, 1977

BERMAN, K.
'The plug nozzle. A new approach to engine design'
Astronautics, Vol. 5, Nb 4, 1960

BOLDMAN, D. R. ; SHMIDT, J. F. & EHLERS, J. F.
'Experimental and theoretical turbulent boundary layer development in a Mach 4.4 water cooled conical nozzle'
NASA TN D-5377, 1969

BOUSSINESQ, J.
'Theorie de l'ecoulement tourbillonant'
mem. Pre. par. div. Sav. 23, Paris (France)

BUSEMAN, A.
'handbush der experimental- physik'
Wien-Harnus, Vol. 4, pp. 407-422, 1931
(translated as ARC 8224, F.M. 757)

CEBECI, T. & BRADSHAW, P.
'Momentum transfer in boundary layers'
Hemisphere, Washington, 1977

CHAM report TR/100
by: Rosten, H. I. & Spalding, D. B.
'Phoenics beginner's guide and user's manual', 1986

CHAM report TR/140
by: Rosten, H. I. ; Templeman, J. A. & Spalding, D. B.
'The Photon user guide', 1986

COOKSON, R. A.
'Supersonic combustion studies- Part I: Construction and
peformance of a high-enthalpy facility'
CoA report 200, Cranfield Inst. of Tech., 1967

CHUDOV, L. A. & BRAILOVSKAYA, I. Y.
'Reshenie uravenii progranichnozo sloya metodom setok'
(solution of the boundary layer equations by difference methods)
Rept. VTs, Moscow State Univ., 1960

ECKERT, E. R. G
'Engineering relations for friction and heat transfer to
surfaces in high velocity flow'
J. Aeronaut. Sci., Vol. 22, Nb 8, pp. 585-587, 1955

FLAHERTY, R. J.
'A method for estimating turbulent boundary layer and heat
transfer in an arbitrary pressure gradient'
Rep. UAR-G51, United Aircraft Corp., 1968

FLUGGE-LOTZ, I. & BLOTTNER, F. G.
'Computation of the compressible laminar boundary layer flow
including displacement thickness interaction using finite
difference methods'
Journal de mecanique, Vol. II, Nb 4, Dec. 1963

GAL-OR, B.
'New fighter engines, a review', Part I
International journal of Turbo and jet Engines, Vol. I, Nb 3,
pp. 183-194, 1984

GLIDEWELL, R. J. & WARBURTON, R. E.
'Advanced exhaust nozzle technology'
AGARD CP-301, Sept. 1981

GOETZ, G. F. ; YOUNG, J. H. & PALCZA, J. L.
'A two-dimensional airframe integrated nozzle design with
inflight thrust vectoring and reversing capabilities for advanced
fighter aircraft'
AIAA paper Nb 76-626, July 1976

GREEN, J. E. ; WEEKS, D. J. & BROOMAN, J. W. F.
'Prediction of turbulent boundary layer and wakes in
compressible flow by a long-entrainment method'
Tech. Rep. 72231, British RAE, 1973

GUDERLEY, G. & HANTSH, E.
'Beste formen fur achtensymmetrische uberschallshldrisen'
Zeits fur flugwissenschaften, Vol. III, 1955

HAMA, F. R.
'Boundary layer characteristics for smooth and rough surfaces'
Trans. Soc. Nav. Architects and Mar. Eng., Vol 62,
pp. 333-358, 1954

HALL, I. M.
'Transonic flow in two-dimensional and axially-symmetric nozzles'
Quat. journal of Mech. & Applied Math., Vol. 15, Part 4,
pp. 487-508, 1962

HERRING, H. J. & MELLOR, G. L.
'A method for calculating compressible turbulent boundary layers'
NASA CR-1144, 1968

HERRING, H. J. & MELLOR, G. L.
'Computer program for calculating laminar and turbulent
boundary layer developments in compressible flow'
NASA CR-2068, 1972

HOFFMAN, J. D.
'Accuracies studies of the numerical method of characteristics
for axisymmetric, steady supersonic flows'
Journal of computational physics, Vol. II, Nb 2, pp. 210-239, 1973

I-Deas user guide
published by Structural Dynamics Research Corporation, 1986

I-Deas Supetarb
Engineering analysis, Pre and post-processing
Published by Structural Dynamics Research Corporation, 1986

JOHN, J. E. A.
'Gas Dynamics', Second Edition
Allyn & Bacon Inc., 1984

KEENAN, J. H. & KAYE, J.
'Gas tables'
Jonh Wiley & Sons Inc., 1948

KELLER, H. B. & CEBECI, T.
'Accurate numerical methods for boundary layer flows. Part II:
Two-dimensional turbulent flows'
AIAA Jour., Vol. 10, Nb 9, pp. 1193-1199, Sept. 1972

KHALIL, R. A.
'Aerodynamic studies of rocket motors and nozzles'
MSc. thesis, School of Mech. Eng., Cranfield Inst. of Tech., 1987

KLIEGEL, J. R. & LEVINE, J. N.
'Transonic flow in small throat radius of curvature nozzles'
AIAA Journal, Vol. 7, Nb 7, pp. 1375-1378, 1969

KLIEGEL, J. R. & NICKERSON, G. R.
'Flow of gas particle mixtures in axially-symmetric nozzles'
ARS propellants, Combustion and Liquid rocket conference,
Palm Beach, Florida, April 26-28, 1961

KRAMER, R. F. & LIBERSTEIN, H. M.
'Numerical solution of the boundary layer equations
without similarity assumptions'
Journal of Aerospace Sciences, Vol. 26, Nb 8, pp. 508-514,
Aug. 1959

KUHN, G. D.
'Calculation of compressible, nonadiabatic boundary layers in
laminar, transitional, and turbulent flow by the method of integral
relations' ; NASA CR-1797 ,1970
NASA CR-1797, 1970

MAIDEN, D. L. & PETIT, J. E.
'Investigation of two-dimensional wedge exhaust nozzles for
advanced aircraft'
J. Aircraft, Vol. 13, N 10, Oct. 1976

MALINA, F. J.
'Characteristics of the rocket motor based on the theory
of perfect gases'
J. of Franklin Institute, Vol. 230, pp. 433-454, 1940

MASSAU, J.
'Memoire sur l'integration graphique des equations aux derivees
partielles'
F. Meyer-Vaulon, 1899

Mc DONNELL AIRCRAFT Co.
'Experimental evaluation of non axisymmetric exhaust nozzles'
Final report, AFFDL-TR-78-185, Vol. I & II, 1978

Mc KENNY, J. D.
'An investigation of flow separation in an overexpanded
supersonic nozzle'
MSc. Thesis, California Inst. of Tech., Pasadena, California, 1949

MELLOR, G. L.
'Turbulent boundary layers with arbitrary pressure gradients and
divergent or convergent cross-flows'
AIAA journal, Vol. 5, pp. 1570-1579, 1967

MITCHELL, A. R.
'Solution of the Von-Mises boundary layer equations using
a high speed computer'
Math. of Computations, Vol. 15, Nb 75, pp. 238-242, July 1961

PALMER, J. R.
'Course Notes'
School of Mech. Eng, Cranfield Inst. of Tech., 1985

PASKONOV, V. M.
'A standard program for the solution of boundary layers'
Numerical methods in gas dynamics, Moscow, 1963

PATANKAR, S. V. & SPALDING, D. B.
'A finite difference procedure for solving the equations
of the two-dimensional boundary layer'
Int. journal of heat and mass transfer, Vol. 10, pp. 1389-1411, 1967

PATANKAR, S. V. & SPALDING, D. B.
'Heat and mass transfer in boundary layers'
2nd Ed., Int. textbook Co. Ltd., 1970

PETTY, J. S. ; HILL, R. J. ; Col. PICCIRILLO, A. C. &
Maj. FUNNING, A. E.
'The next hot fighter engine'
Aerospace America, June 1986

PICKNEY, S. Z.
'Method of predicting compressible turbulent boundary layer in
adverse pressure gradients'
NASA TM X-2302, 1971

RAO, G. V. R.
'Exhaust nozzle contour for optimum thrust'
Jet Propulsion, Vol. 28, Nb 6, pp. 377-382, 1958

RAO, G. V. R.
'The E-D nozzle'
Aeronautics, Vol. 5, N 9, 1960

RAO, G. V. R.
'Recent developments in rocket nozzle configurations'
ARS journal, Vol. 31, pp. 1488-1494, 1961

RANSOM, V. H. ; HOFFMAN, J. D. & THOMPSON, H. D.
'A second-order bicharacteristics method for three-dimensional,
steady supersonic flow'
AIAA journal, Vol. 10, Nb 12, pp. 1573-1581, 1972

RESHOTKO, E. & TUCKER, M.
'Approximate calculation of the compressible turbulent boundary
layer with heat transfer and arbitrary pressure gradients'
NACA TN 4154, 1957

ROSENHEAD, L.
'Laminar boundary layers'
Clarendon Press, Oxford, 1963

SAUER, R.
'General characteristics of the flow through nozzles at near
critical speeds'
NACA TM-1147

SOMMER, S. C. & SHORT, B. J.
'Free flight measurements of turbulent boundary layer skin friction in the presence of severe aerodynamic heating at Mach numbers from 2.8 to 7.0'
NACA TN-3391, 1955

SPALDING, D. B. & CHI, S. W.
'The drag of a compressible turbulent boundary layer on a smooth flat plate with and without heat transfer'
J. Fluid Mech., Vol. 18, pt. 1, pp. 117-143, 1964

STEWARTSON, K.
'Correlated incompressible and compressible boundary layers'
Proc. Royal Society, Ser. A, Vol. 200, Nb A-1060, pp. 84-100, 1949

STROUD, J. F. & MILLER, L. D.
'An experimental and analytical investigation of hypersonic inlet boundary layers'
Vol. I, AFFDL-TR-65-123, U.S. Air Force, 1965

SUMMERFIELD, M. ; FOSTER, C. R. & SWAN, W. C.
'Flow separation in overexpanded supersonic exhaust nozzles'
Jet Propulsion, Vol. 24, Nb 5, pp. 319-321, 1954

SUN, C. C. & CHILDS, M. E.
'A modified wall wake velocity profile for turbulent compressible boundary layers'
J. Aircr., Vol. 10, Nb 6, pp. 381-383, 1973

TOWNEND, L. H.
'Private communication', 1985

VAN DRIEST, E. R.
'Turbulent boundary layer in compressible fluids'
J. Aeronaut. Sci., Vol. 18, N 3, pp. 145-160, 1951

VAN DRIEST, E. R.
'The problem of aerodynamic heating'
Aeronaut. Eng. Review, Vol. 15, Nb 10, pp. 26-41, 1956

WINPRESS, R. N.
'Internal ballistics of solid fuel rockets'
Mc Graw Hill Book Co. Inc., New York, 1950

ZUCROW, M. J. & HOFFMAN, J. D.
'Gas dynamics'
Jonh Wiley & Sons, 1976

APPENDIX A : Application of the method of characteristics to steady, two-dimensional, irrotational supersonic flow.

A.1 Governing equations

The equations governing a steady, axisymmetric, irrotational supersonic flow are presented in detail in section 3. They are the gas dynamic equation and the irrotationality condition :

$$(u^2-a^2) \frac{\partial u}{\partial x} + (v^2-a^2) \frac{\partial v}{\partial y} + 2 uv \frac{\partial u}{\partial y} - \delta \frac{a^2 v}{y} = 0 \qquad \ldots (A.1)$$

$$\frac{\partial u}{\partial y} - \frac{\partial v}{\partial x} = 0 \qquad \ldots (A.2)$$

The above system comprises a set of two coupled partial differential equations involving the two velocity components u and v. This system may be replaced by an equivalent one of a characteristic and compatibility equations which are total differential equations and thus allow the use of a simple numerical method of solution.

A.2 Characteristic equation

The characteristic and compatibility equations are derived by multiplying equations A.1 and A.2 by the unknowns σ_1 and σ_2 and summing as follows :

$$\sigma_1 (A.1) + \sigma_2 (A.2) = 0 \qquad \ldots (A.3)$$

Substituting and arranging leads to :

$$\sigma_1 (u^2-a^2) [\frac{\partial u}{\partial x} + \frac{\sigma_1 (2uv) + \sigma_2}{\sigma_1 (u^2-a^2)} \frac{\partial u}{\partial y}] + (-\sigma_2) [\frac{\partial v}{\partial x} + \frac{\sigma_1 (v^2-a^2)}{-\sigma_2} \frac{v}{y}] - \frac{\sigma_1 \delta a^2 v}{y} = 0 \quad \ldots (A.4)$$

Assuming u(x,y) and v(x,y) to be continuous functions :

$$\frac{du}{dx} = \frac{\partial u}{\partial x} + \lambda \frac{\partial u}{\partial y}$$

$$\frac{dv}{dy} = \frac{\partial v}{\partial x} + \lambda \frac{\partial v}{\partial y} \quad \ldots (A.5)$$

where the λs represent the slopes of the characteristics and are equal to the coefficient of ($\partial u/\partial y$) and ($\partial v/\partial y$) in equation A.4. Consequently :

$$\lambda = \frac{\sigma_1 (2uv) + \sigma_2}{\sigma_1 (u^2-a^2)}$$

$$\lambda = \frac{\sigma_1 (v^2-a^2)}{-\sigma_2} \quad \ldots (A.6)$$

By considering the σs as the unknowns, equations A.6 are transformed :

$$\sigma_1 [(u^2-a^2)\lambda - 2 uv] + \sigma_2 (-1) = 0$$

$$\sigma_1 (v^2-a^2) + \sigma_2 (\lambda) = 0 \quad \ldots (A.7)$$

For this system to have any solution other than the trivial one of zero, the determinant of the coefficient matrix must vanish, leading to :

$$\lambda_{(+,-)} = \left(\frac{dy}{dx} \right)_{(+,-)} = \frac{uv \pm a^2 \, (M^2-1)^{\frac{1}{2}}}{u^2-a^2} \qquad \dots \text{ (A.8)}$$

The two expressions for λ, denoted by the subscripts (+) and (-), define two curves in the (x,y) plane : the so-called left-hand and right-hand characteristics (Figure A.3) and are real only if the flow is supersonic.

An alternate and simpler form of equation A.8 may be obtained by introducing the flow direction and expressing the Mach number in terms of Mach angle. By considering Figures A.1 and A.2, one can write :

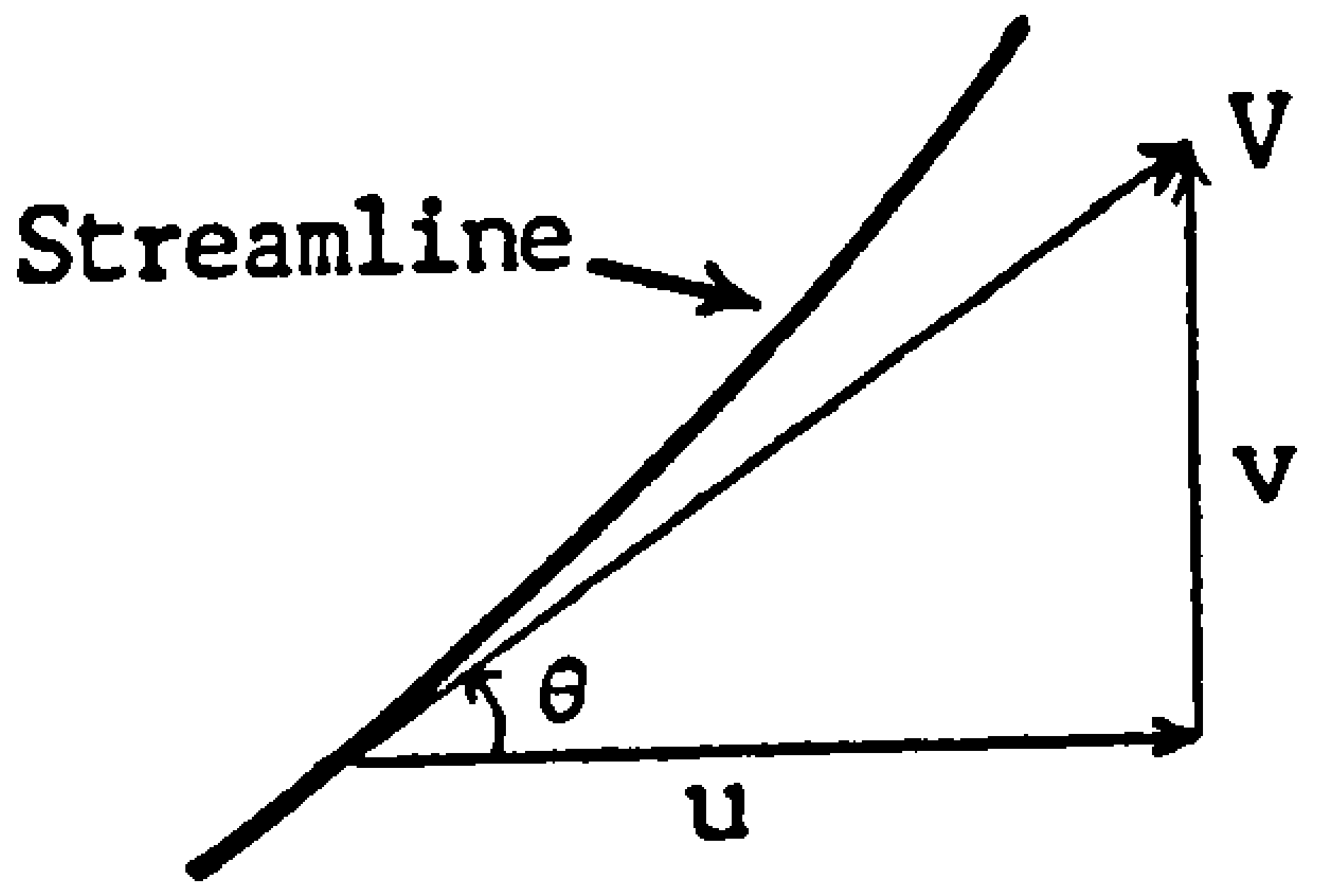

Fig. A.1

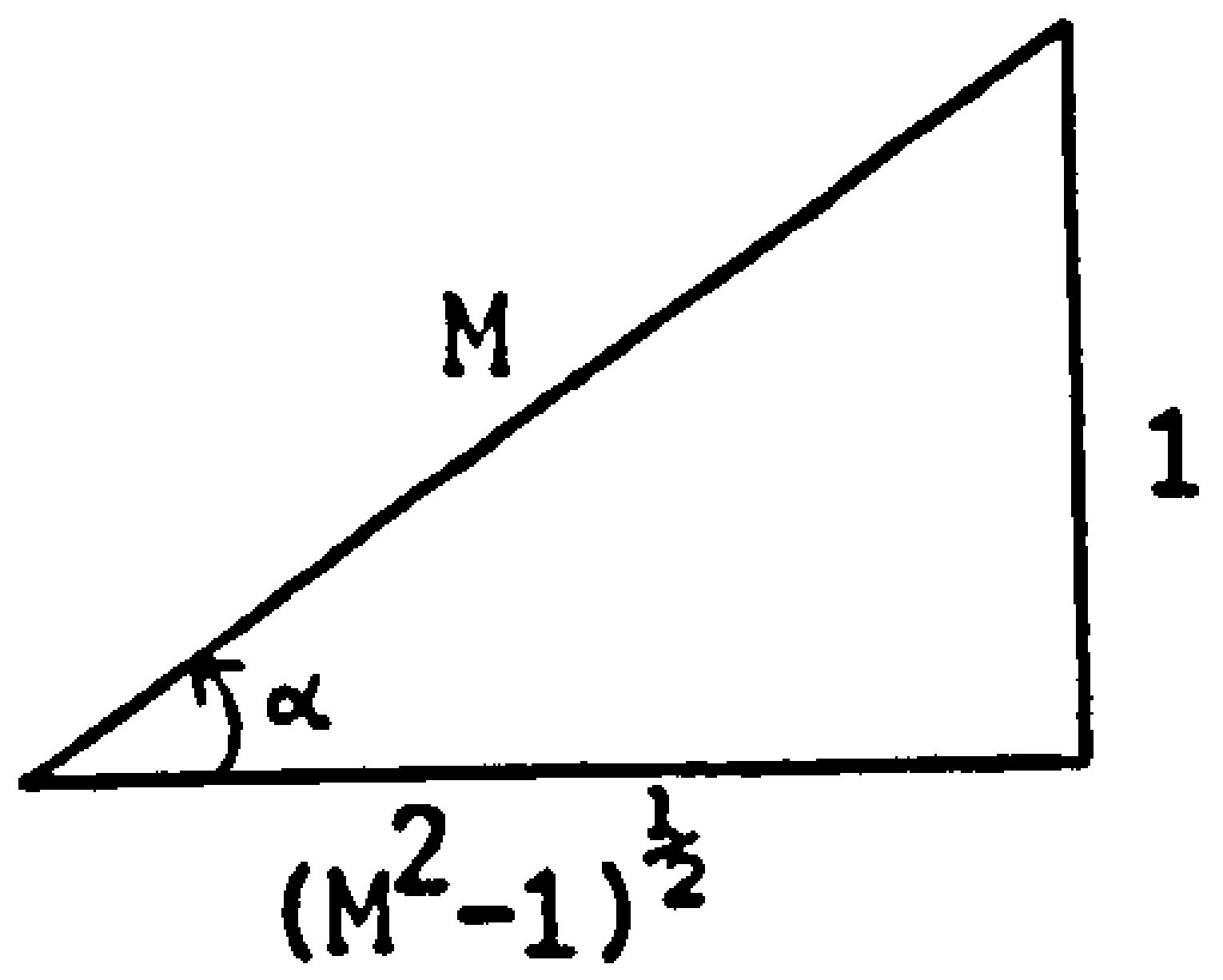

Fig. A.2

$$u = V \cos \theta$$

$$v = V \sin \theta \qquad \dots \text{ (A.9)}$$

$$\theta = tg^{-1} \left(\frac{v}{u} \right)$$

$$\alpha = \sin^{-1} \left(\frac{1}{M} \right)$$

$$M = \frac{1}{\sin \alpha} \qquad \dots \text{ (A.10)}$$

$$(M^2-1) = \text{cotg}\, \alpha$$

Substituting A.9 and A.10 into A.8, rearranging and applying the standard trigonometric identities yields :

$$\lambda_{(+,-)} = \left(\frac{dy}{dx} \right)_{(+,-)} = tg \, (\theta \pm \alpha) \qquad \dots \text{ (A.11)}$$

Equation A.11 is illustrated by Figure A.3, where $C_{(+)}$ and $C_{(-)}$ denote the left-running and right-running characteristics respectively.

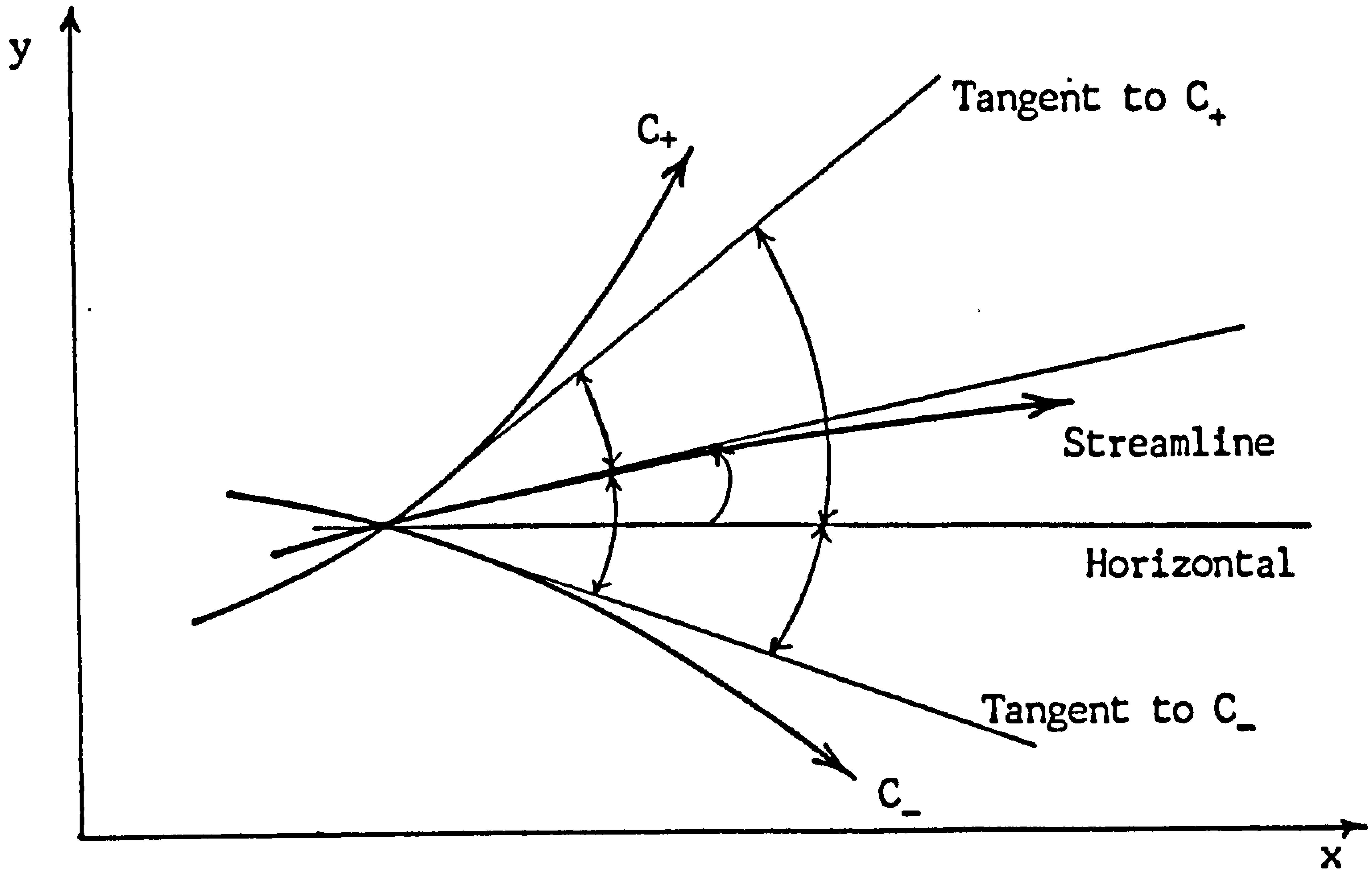

Fig. A.3 : Characteristics (Mach lines) in a steady, 2-D irrotational flow.

A.3 Compatibility equation

The compatibility equation, valid on each characteristic, is obtained from equation A.4 by replacing the λs by their respective expressions (A.5 and A.6) and eliminating the unknowns σs. The result is :

$$(u^2-a^2)\ du_{(+,-)} + [\ 2\ uv + (u^2-a^2)\ \lambda_{(+,-)}\ ]\ dv_{(+,-)} - \left(\frac{\delta\ a^2\ v}{y} \right) dx_{(+,-)} = 0 \qquad \dots\ (\ A.12\ )$$

A.4 Finite-difference equations

The finite difference equations corresponding to the characteristic and compatibility equations are obtained by replacing the differentials dx, dy, du and dv by their differences. This leads to :

$$\Delta y_{(+,-)} = \lambda_{(+,-)} \, \Delta x_{(+,-)} \qquad \ldots (\text{A.13})$$

$$\left(u^2_{(+,-)} - a^2_{(+,-)} \right) \Delta x_{(+,-)} + \left[2\, u_{(+,-)}\, v_{(+,-)} - \left(u^2_{(+,-)} - a^2_{(+,-)} \right) \lambda_{(+,-)} \right] \Delta v_{(+,-)} - \frac{\delta\, a^2_{(+,-)}\, v_{(+,-)}}{y_{(+,-)}} \Delta x_{(+,-)} = 0 \qquad \ldots (\text{A.14})$$

$$\lambda_{(+,-)} = \mathrm{tg}\, (\theta \pm \alpha) \qquad \ldots (\text{A.15})$$

A.5 Implementation of the method of characteristics

A.5.1 Interior point procedure

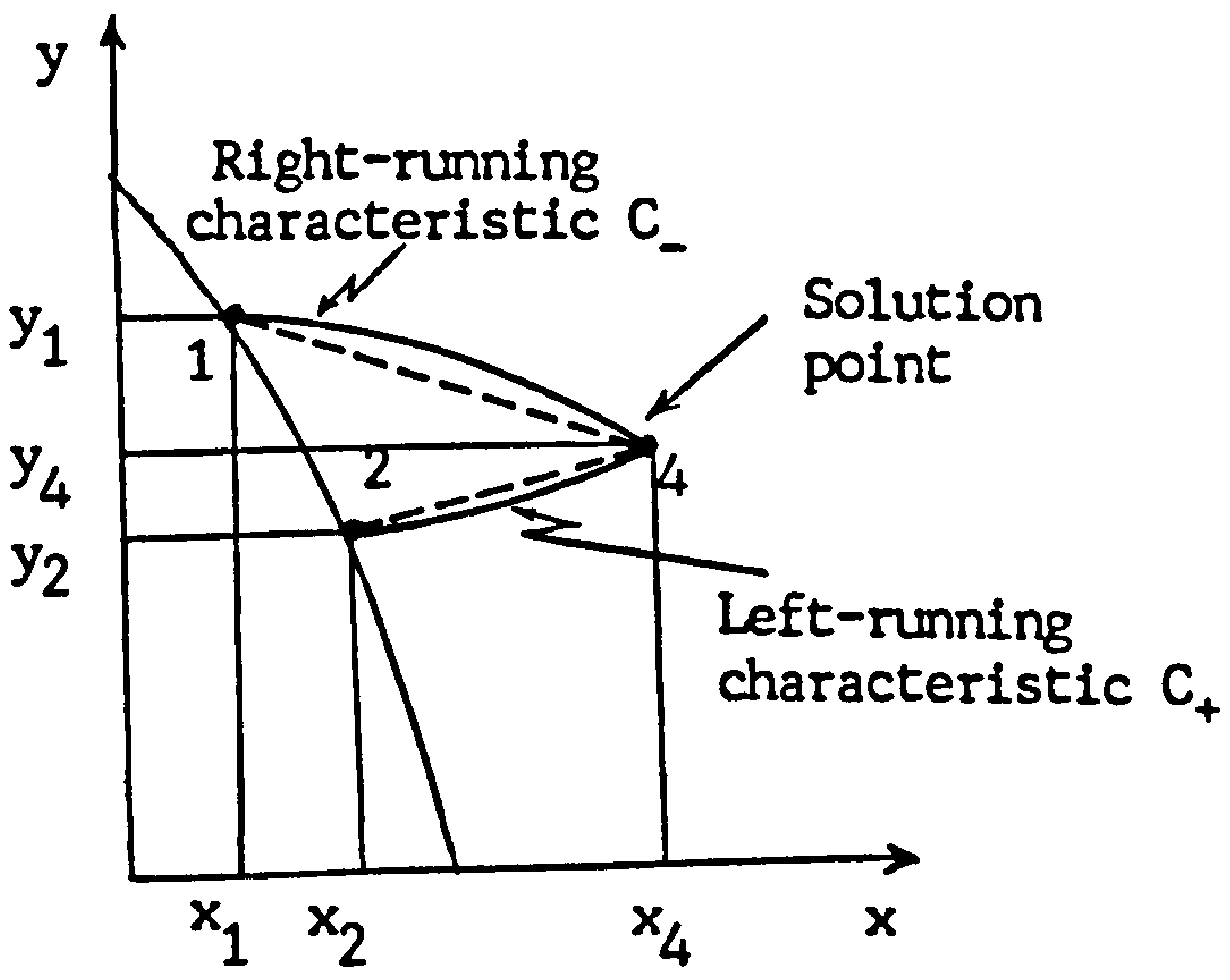

Fig. A.4 : Interior point.

An interior point is represented by point 4 in Figure A.4. Its location is determined by solving, for x_4 and y_4, equation A.13 which may be written as :

$$y_4 - \lambda_{(+)} x_4 = y_2 - \lambda_{(+)} x_2 \qquad \text{... (A.16)}$$

$$y_4 - \lambda_{(-)} x_4 = y_1 - \lambda_{(-)} x_1 \qquad \text{... (A.17)}$$

The values of $\lambda_{(+,-)}$ are function of both $\Theta_{(+,-)}$ and $\alpha_{(+,-)}$ which, in their turn, depend on the velocity components $u_{(+,-)}$ and $v_{(+,-)}$. The velocity components at the solution point are determined by solving the compatibility equation A.14 which may be written as :

$$\begin{aligned}(u^2_{(+)} - a^2_{(+)})\, u_4 + [\, 2\, u_{(+)} v_{(+)} - \\ (u^2_{(+)} - a^2_{(+)})\, \lambda_{(+)} \,]\, v_4 = T_{(+)}\end{aligned} \qquad \text{... (A.18)}$$

$$\begin{aligned}(u^2_{(-)} - a^2_{(-)})\, u_4 + [\, 2\, u_{(-)} v_{(-)} - \\ (u^2_{(-)} - a^2_{(-)})\, \lambda_{(-)} \,]\, v_4 = T_{(-)}\end{aligned} \qquad \text{... (A.19)}$$

where :

$$\begin{aligned}T_{(+)} = \delta \frac{a^2_{(+)} v_{(+)}}{y_{(+)}} (x_4 - x_2) + (u^2_{(+)} - a^2_{(+)})\, u_2 + \\ [\, 2\, u_{(+)} v_{(+)} - (u^2_{(+)} - a^2_{(+)})\, \lambda_{(+)} \,]\, v_2\end{aligned} \qquad \text{... (A.20)}$$

$$\begin{aligned}T_{(-)} = \delta \frac{a^2_{(-)} v_{(-)}}{y_{(-)}} (x_4 - x_1) + (u^2_{(-)} - a^2_{(-)})\, u_1 + \\ [\, 2\, u_{(-)} v_{(-)} - (u^2_{(-)} - a^2_{(-)})\, \lambda_{(-)} \,]\, v_1\end{aligned} \qquad \text{... (A.21)}$$

It is possible at this stage to determine all the parameters if the velocity components $u_{(+,-)}$, $v_{(+,-)}$ and the station coordinates $y_{(+,-)}$ are known. They are calculated by applying the modified Euler predictor-corrector algorithm (Appendix B) to the points 1,2 and 4 of Figure A.4. The predictor is applied first and the values of $u_{(+,-)}$, $v_{(+,-)}$ and $y_{(+,-)}$ are taken as :

$$\begin{array}{lll} u_{(+)} = u_2 & v_{(+)} = v_2 & y_{(+)} = y_2 \\ u_{(-)} = u_1 & v_{(-)} = v_1 & y_{(-)} = y_1 \end{array} \qquad \ldots \text{ (A.22)}$$

The substitution of equation A.22 into A.16, A.17, A.31 and A.32 and their simultaneous solution would lead to the predicted values x_4' , y_4' , u_4' , and v_4' .

The next step would be to apply the corrector algorithm to the same stations, taking :

$$\begin{array}{lll} u_{(+)} = \dfrac{u_2 + u_4'}{2} & v_{(+)} = \dfrac{v_2 + v_4'}{2} & y_{(+)} = \dfrac{y_2 + y_4'}{2} \\ u_{(-)} = \dfrac{u_1 + u_4'}{2} & v_{(-)} = \dfrac{v_1 + v_4'}{2} & y_{(-)} = \dfrac{y_1 + y_4'}{2} \end{array} \qquad \ldots \text{ (A.23)}$$

Substituting again and solving would lead to the corrector values x_4'' , y_4'' , u_4'' and v_4'' . The last step is to apply iteration to the corrector algorithm. The iteration may be applied as many times as required until the desired degree of convergence is reached. The procedure, for an interior point, is incorporated in subroutine 'Intpoint' (section 3).

A.5.2 Axis of symmetry point procedure

Any point located on the axis of symmetry (i.e. point 4 in Figure A.5) is called an axis of symmetry point. In this case, a point 2 below the axis of symmetry, which is the image of point 1, may be defined. As a result, the solution point becomes analogous to an interior point.

Because of the particular position of point 4 ($y_4 = v_4 = \theta_4 = 0$), the procedure is simplified and only the right-running characteristic 14 is employed. The solutions x_4 and u_4 are respectively obtained by solving the finite difference equations A.17 and A.19. The procedure, for an axis of symmetry point, is incorporated in subroutine 'Axipoint' (section 3).

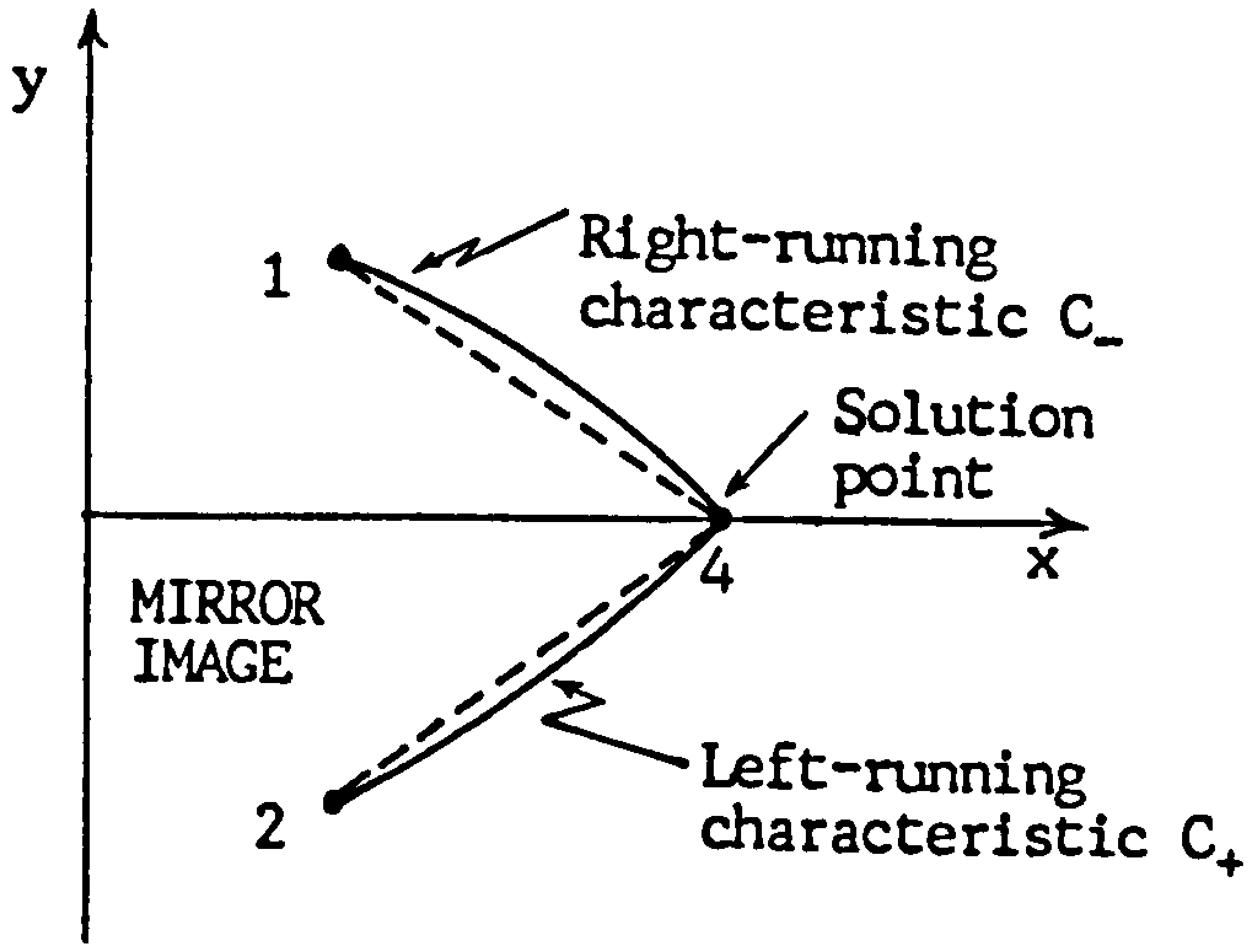

Fig. A.5 : Axis of symmetry point.

A.5.3 Direct wall point procedure

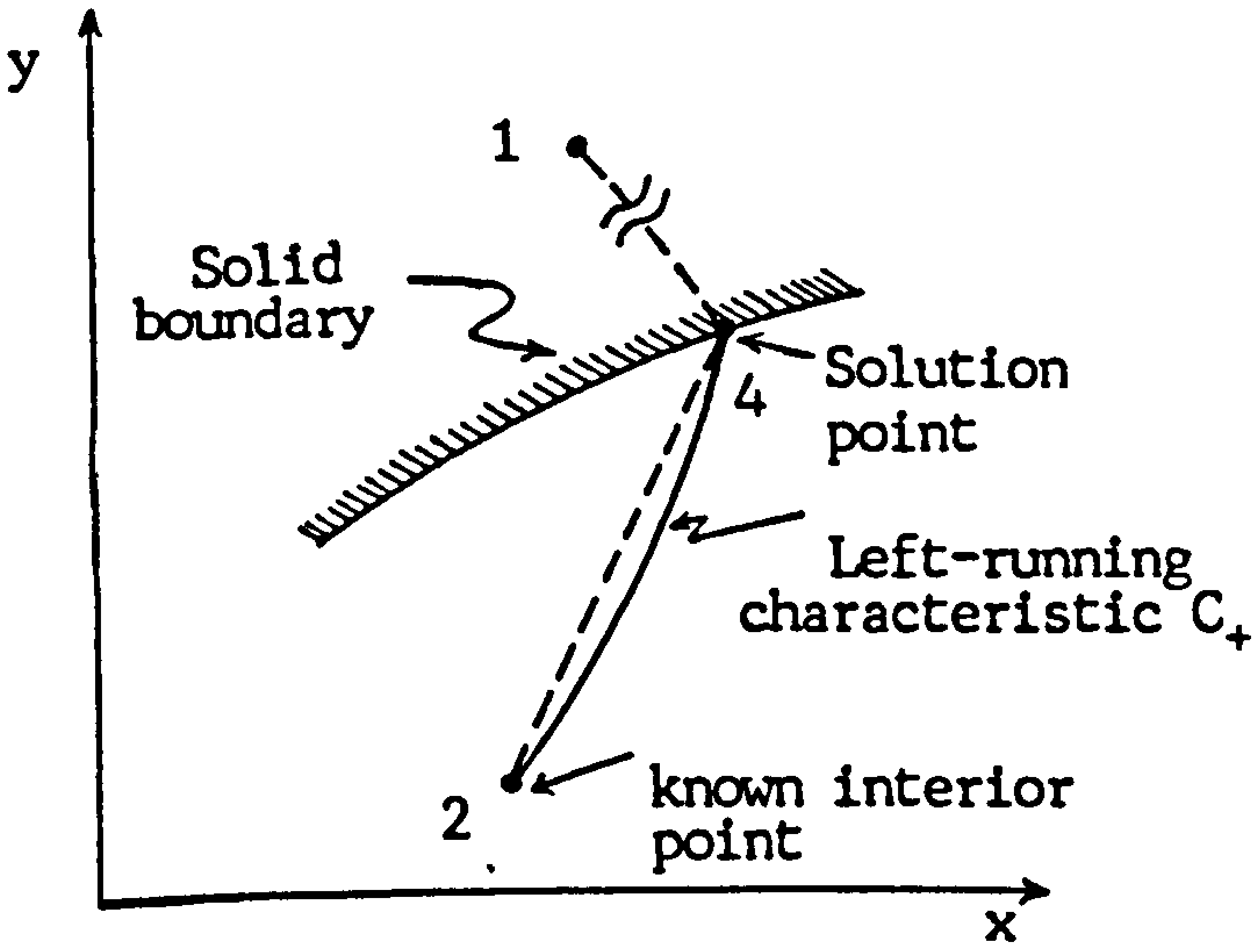

Fig. A.6 : Direct wall point.

A point is termed as a direct wall point if it is located at a solid boundary such as point 4 in Figure A.6. In that figure, point 1 does not exist physically, consequently only one characteristic and one compatibility equations are available. Two additional equations are thus needed for determining the location of the direct wall point and the flow properties at that point.

At the wall, the direction of the flow velocity vector must be identical to the slope of the wall, thus :

$$y = y(\ x\ ) \qquad \text{... (A.24)}$$

$$\frac{dy}{dx} = tg\ \Theta = \frac{v}{u} \qquad \text{... (A.25)}$$

The above equations constitute the two additional equations which, along with the solutions of equations A.16 and A.18, would determine the location and properties at the solution point. The procedure, for a direct wall point, is incorporated in subroutine 'Dirpoint' (section 3).

A.5.4 Inverse wall point procedure

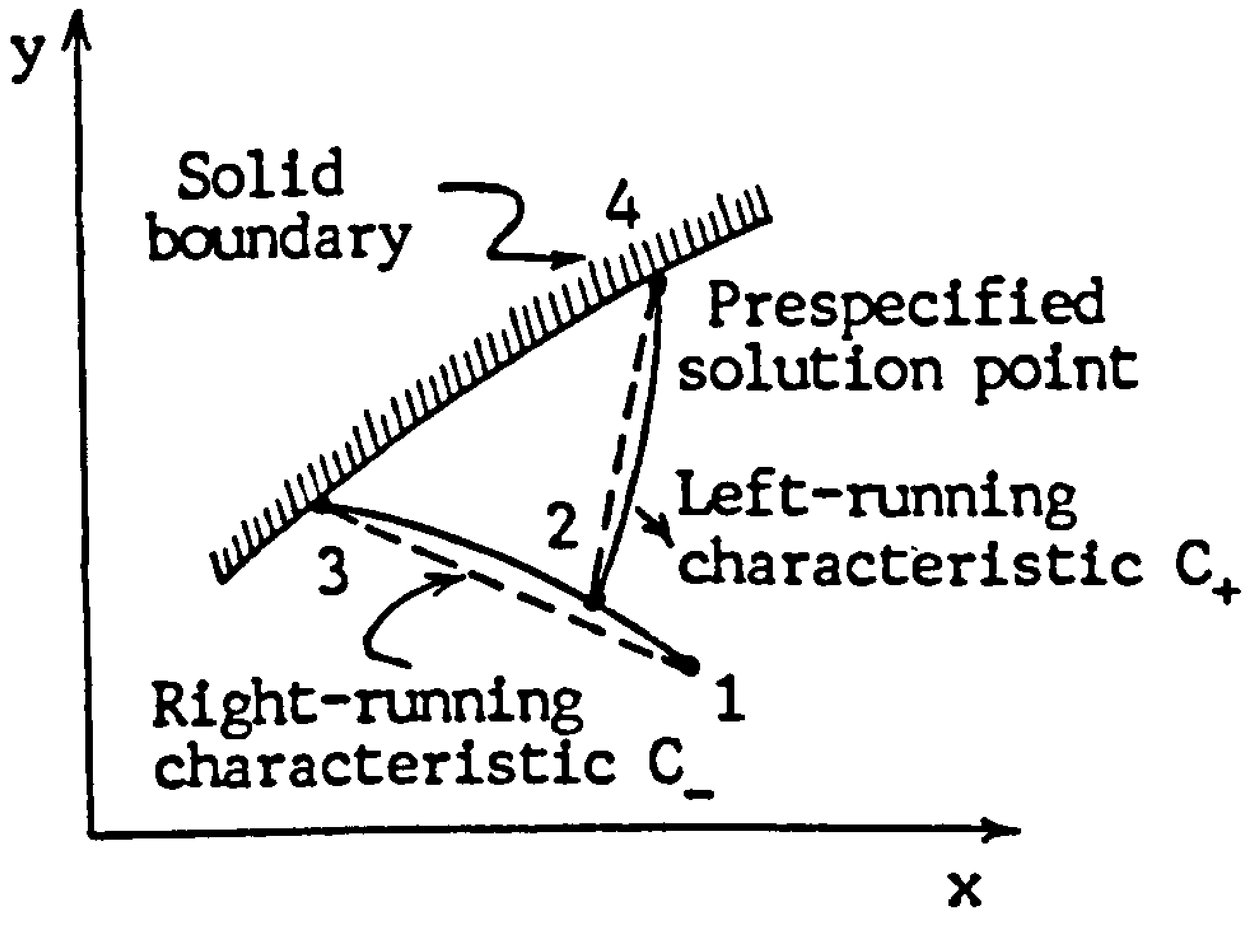

Fig. A.7 : Inverse wall point.

In regions of the flowfield where the property gradients are extremely large (transonic region for example), the direct method may result in too large spacing of the solution points along the wall. In that case, the inverse method may be employed. It involves prespecifying the position of the solution point and using the method of characteristics to determine the flow properties at these points. Figure A.7 illustrates schematically the situation where point 4 is the prespecified point, point 2 being the intersection of the rearward left-running characteristic $C_{(+)}$ through the solution point 4 and the right-running characteristic $C_{(-)}$. Because the solution point is prespecified, x_4 and y_4 are known and only the flow properties at point 4 have to be determined, involving the calculation of the location and properties at point 2. The location is established by determining the intersection of the rearward left-running characteristic 24 (Equation A.16) with the right-running characteristic 13 (Equation A.17). Flow properties at this point are determined by linear interpolation between points 1 and 3. The solution of equations A.16 and A.25 will determine the properties at point 4. The procedure, for an inverse wall point, is incorporated in subroutine 'Invpoint' (section 3).

A.6 Particular cases for an interior point

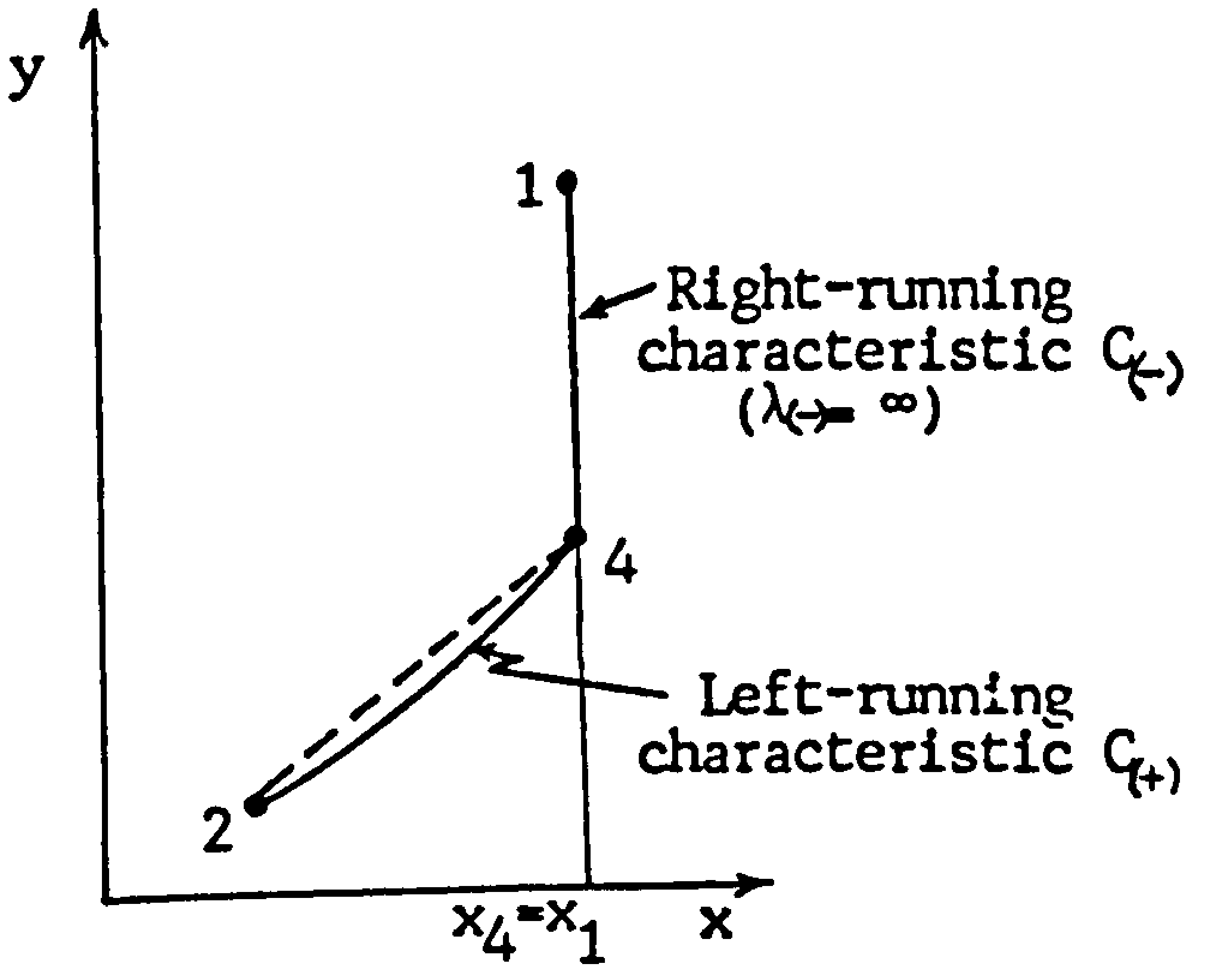

Fig. A.8 : Case where $\lambda_{(-)} = \infty$ for an interior point.

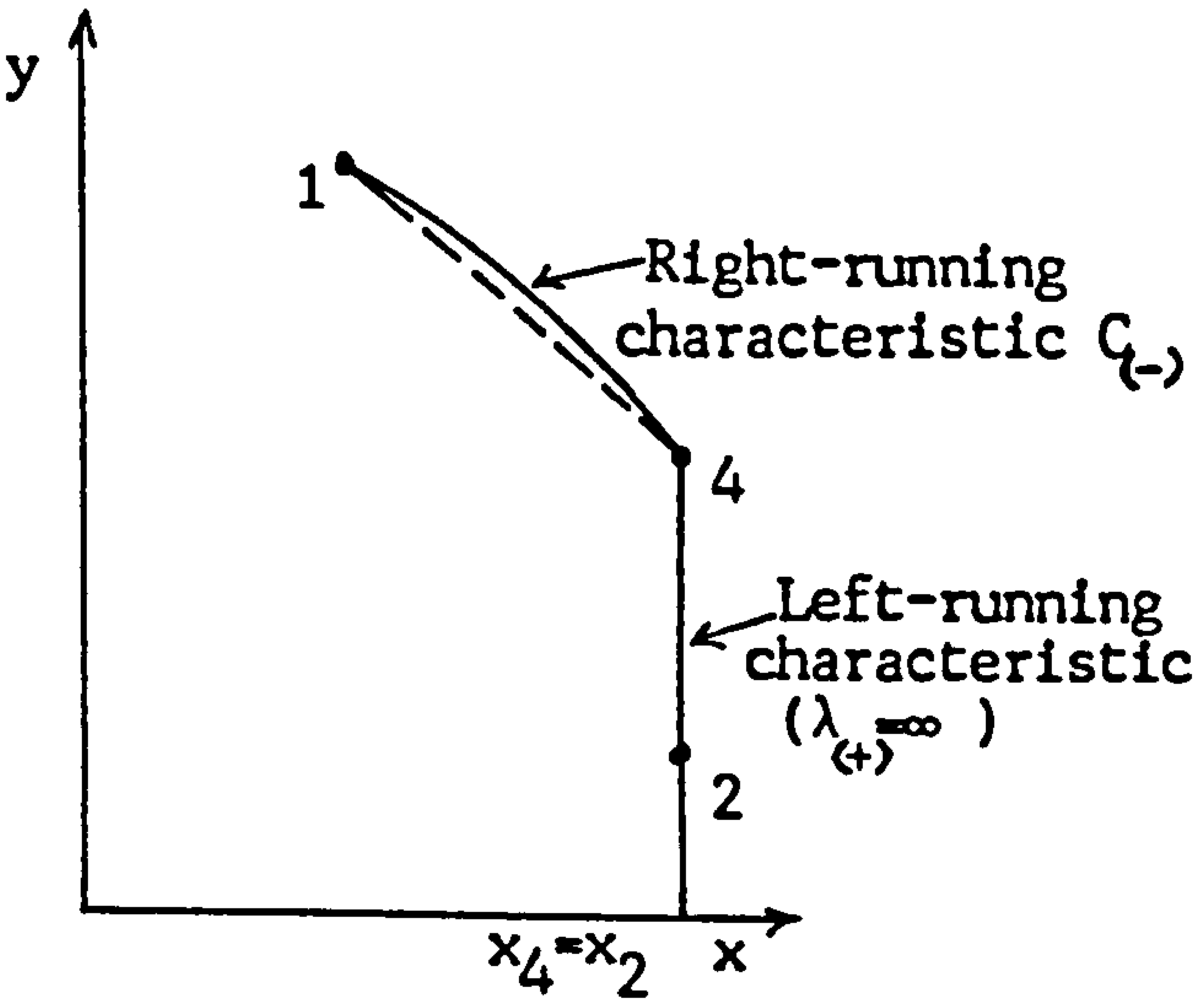

Fig. A.9 : Case where $\lambda_{(+)} = \infty$ for an interior point.

Two special cases may occur in the calculation of the flow properties at an interior point. The first one occurs when the slope of the right-running characteristic $C_{(-)}$ is infinity (Figure A.8). In that case, x_4 is taken equal to x_1 and y_4 obtained from equation A.13 when applied to the right-running characteristic $C_{(+)}$.

The second case occurs when the slope of the left-running characteristic $C_{(+)}$ is infinity (Figure A.9). In that case, x_4 is taken equal to x_2 and y_4 obtained from equation A.13 when applied to the right-running characteristic $C_{(-)}$.

The two possibilities have been taken into account and the solutions included into the computer program (subroutine 'Intpoint').

A.7 Particular case for a direct point

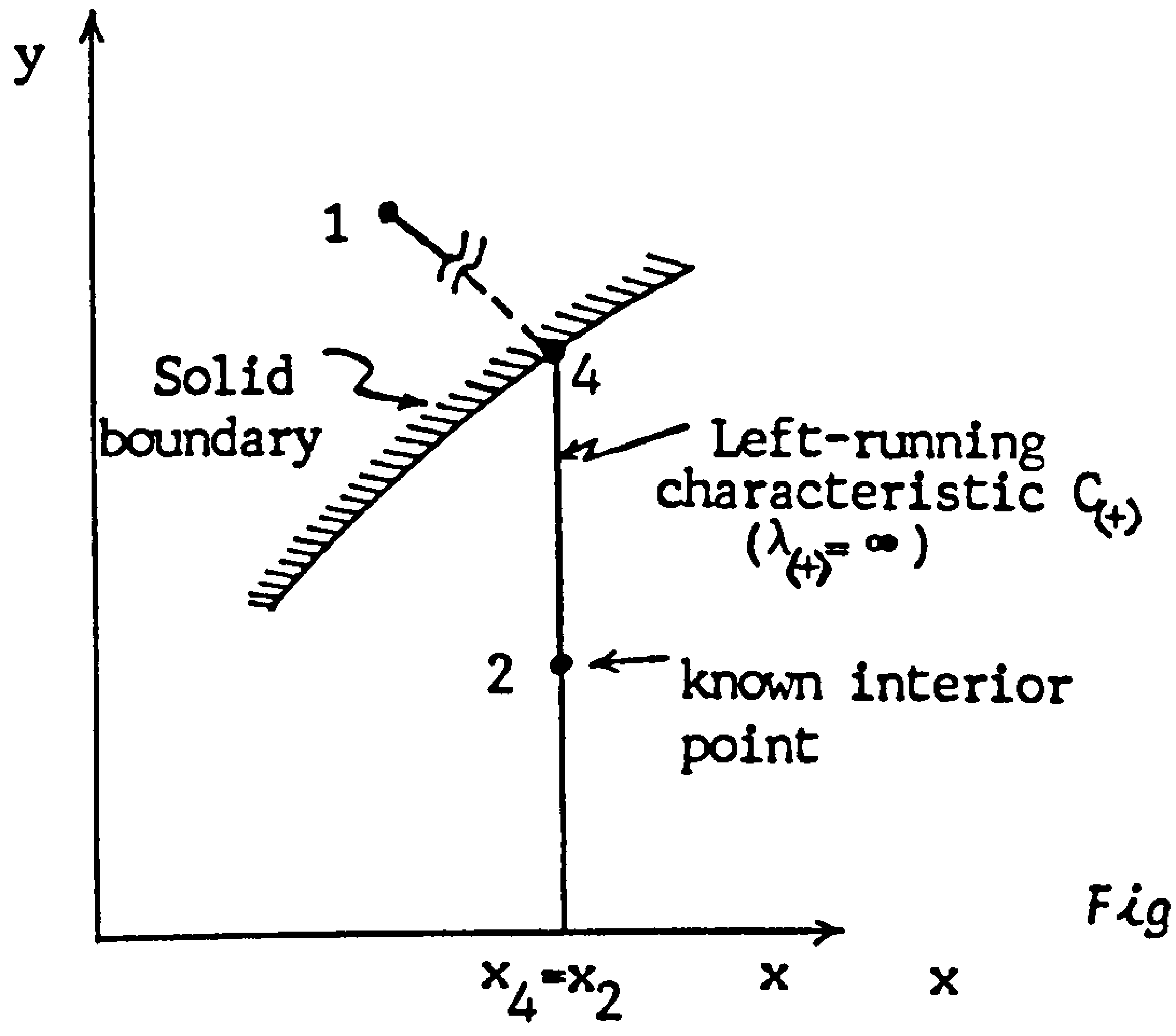

Fig. A.10 : Case where $\lambda_{(+)} = \infty$ for a direct wall point.

As in the internal point procedure, a technique has been incorporated within the computations of a direct wall point to handle the case of $\lambda_{(+)} = \infty$ (Figure A.10). In that case, x_4 is taken equal to x_2 and y_4 determined from the equation of the wall contour.

APPENDIX B : Modified Euler predictor-corrector algorithm based on the average property method.

B.1 Euler's method

The most straighforward approach for approximating the solution $y(x)$ of an ordinary differential equation is to express the unknown function in the form of a Taylor serie expansion about the initial point (x_o,y_o). Therefore :

$$y(x_o+h) = y(x_o) + h\,y'\,[\,x_o,y(x_o)\,] + \ldots + \frac{h^n}{n!}\,y^{(n)}\,[\,x_o,y(x_o)\,] \qquad \ldots\ (\text{B.1})$$

The Euler's method takes n equal to 1 for the above Taylor's expansion, leading to :

$$y(x_o+h) = y(x_o) + h\,y'\,[\,x_o,y(x_o)\,] \qquad \ldots\ (\text{B.2})$$

B.2 Basic features of the modified Euler predictor-corrector algorithm based on the average property method.

The modified Euler predictor-corrector method is a second-order procedure for integrating total differential equations. For the predictor step, Euler's method is employed :

$$y_{n+1} = y_n + h\,f\,(\,x_n,y_n\,) \qquad \ldots\ (\text{B.3})$$

For the corrector step, (Hoffman, 1973) showed that more accurate results are obtained by employing a corrector algorithm that is based on average properties. Within this algorithm, the numerical values of the coefficients of the differential equations are determined on the basis of the average values of the properties at the initial and solution points. Therefore, if we consider an ordinary differential equation :

$$dy = f(x,y)\,dx \qquad \text{... (B.4)}$$

The problem is to integrate it from a known starting point i(x_i, y_i) where $y_i = y(x_i)$. If Δx is the step size of the finite-difference equation, a predicted value of the solution at $x_{i+1} = x_i + \Delta x$ is obtained from the Euler predictor algorithm (equation B.3) :

$$y^o(x_i + \Delta x) = y^o_{i+1} = y_i + f(x_i, y_i)\,\Delta x \qquad \text{... (B.5)}$$

The accuracy of the solution obtained by the predictor may be improved by employing y_i and y^o_{i+1} for estimating the value of :

$$y_{(\frac{i+1}{2})} = y\left(x_i + \frac{\Delta x}{2}\right) \qquad \text{... (B.6)}$$

and replacing f(x_i, y_i) in equation B.5 by the value of f(x,y) determined at the mid-point of the interval. Thus :

$$y'_{i+1} = y_i + f\left(x_i + \frac{\Delta x}{2}, \frac{y_i + y^o_{i+1}}{2}\right)\Delta x \qquad \text{... (B.7)}$$

where y'_{i+1} is the corrected value of the solution at x_{i+1}. Equation B.7 represents the corrector algorithm.

The continued application of this procedure leads to the modified

Euler predictor-corrector method with iteration :

$$y^{n}_{i+1} = y_i + f\left(x_i + \frac{\Delta x}{2} , y_i + \frac{y^{n-1}_{i+1}}{2} \right) \Delta x \qquad \text{... (B.8)}$$

where y^{n}_{i+1} is the value of y after n applications of the corrector.

APPENDIX C : Subroutine WALCON

C.1 General

Given the throat radius y_t, the downstream radius of curvature R_{td}, the divergence angle A_a and the exit radius y_e, WALCON determines the equation of the wall and consequently the coordinates of the stations from which the characteristics are issued. The cases, investigated in this thesis, involve boundaries constituted by a circular-arc throat contour and a divergent wall simulated as a second-order polynomial. The two parts are linked together at the attachment point.

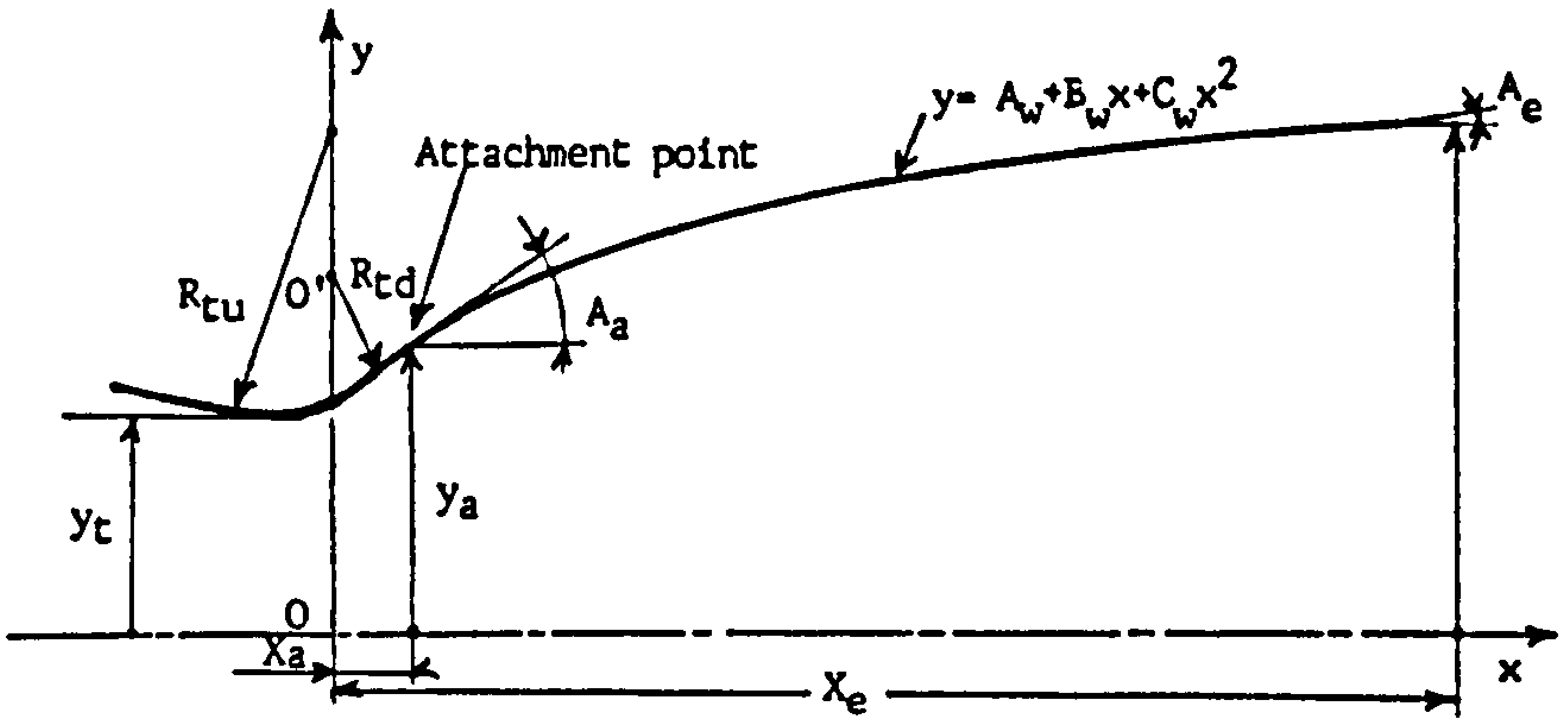

Divergent section of a contoured nozzle.

C.2 Circular-arc throat contour

The equation describing the circular-arc throat contour permits the determination of the radial coordinate of the prespecified points computed by the inverse wall point procedure (Appendix A). It is expressed as :

$$/O'xy \quad x^2 + y^2 = R_{td}^2 \qquad \ldots (\text{ C.1 })$$

$$/Oxy \quad x^2 + (y - R_{td} - y_t)^2 = R_{td}^2 \qquad \ldots (\text{ C.2 })$$

C.3 Attachment point

The coordinates of the attachment point are determined as :

$$x_a = R_{td} \sin (A_a) \qquad \ldots (\text{ C.3 })$$

$$y_a = y_t + R_{td} [1 - \cos (A_a)] \qquad \ldots (\text{ C.4 })$$

C.4 Second-order polynomial wall

Depending on whether the nozzle length or the exit radius are specified, two methods may be used to determine the equation of the second-order polynomial wall.

The first procedure lies on a prespecified value for the nozzle length which is used as an input data in order to carry out the computation of the flowfield. The final design is obtained by cutting the nozzle at the particular cross-section producing the exit pressure needed. This method is widely used in industry.

Assuming the polynomial to be of the form (Section 2.4) :

$$y = A_w + B_w x + C_w x^2 \qquad \ldots (\text{ C.5 })$$

The equations to be solved in order to use the above method are :

$$\begin{array}{ll} y (x=x_a) = y_a & A_w + B_w x_a + C_w x_a^2 = y_a \\ \left.\dfrac{dy}{dx}\right|_{x=x_a} = tg (A_a) & B_w + 2 C_w x_a = tg (A_a) \end{array} \qquad \ldots (\text{ C.6 })$$

$$\left.\frac{dy}{dx}\right|_{x=x_e} = tg\ (\ A_e\ ) \qquad B_w + 2\ C_w\ x_e = tg\ (\ A_e\ )$$

where the unknowns are the coefficients of the wall polynomial A_w, B_w and C_w.

The second method involves the use of the supersonic tables. Having specified the expected exit Mach number, the tables are used to determine the corresponding area ratio permitting a complete expansion. In this case, the equations involved are :

$$\begin{aligned} & y\ (\ x=x_a\ ) = y_a && A_w + B_w\ x_a + C_w\ x_a^{\ 2} = y_a \\ & \left.\frac{dy}{dx}\right|_{x=x_a} = tg\ (\ A_a\ ) && B_w + 2\ C_w\ x_a = tg\ (\ A_a\ ) \\ & \left.\frac{dy}{dx}\right|_{x=x_e} = tg\ (\ A_e\ ) && B_w + 2\ C_w\ x_e = tg\ (\ A_e\ ) \\ & y\ (\ x=x_e\ ) = y_e && A_w + B_w\ x_e + C_w\ x_e^{\ 2} = y_e \end{aligned} \qquad \ldots\ (\ C.7\ )$$

where the unknowns are the coefficients of the polynomial wall A_w, B_w, and C_w and the nozzle length x_e.

APPENDIX D : Boundary layer computation

D.1 Governing equations

The equations governing the boundary layer are presented in section 4 (Equations 4.11 to 4.13). In order to close the system, The boundary conditions were derived :

$$u(x,0) = 0 \qquad \ldots (D.1)$$

$$v(x,0) = v_w(x) \qquad \ldots (D.2)$$

$$\lim_{\rightarrow\infty} \int_0^y [\, u_e(x) - u(x,y) \,]\, dy \quad \text{is bounded} \qquad \ldots (D.3)$$

$$h_t(x,0) = h_{t,w}(x) \qquad \ldots (D.4)$$

$$\lim_{\rightarrow\infty} \int_0^y u\, [\, h_{t,e} - h_t(x,y) \,]\, dy \quad \text{is bounded} \qquad \ldots (D.5)$$

Because the calculation method was oriented towards turbulent flow, it was convenient to define a new set of variables in which the velocity and enthalpy profiles are expressed in defect form :

$$\eta = \frac{y}{\delta^*(x)} \qquad \ldots (D.6)$$

$$f' = \frac{\rho_e u_e(x) - \rho\, u(x,y)}{\rho_e u_e(x)} \qquad \ldots (D.7)$$

$$g' = \frac{h_{t,e} - h_t(x,y)}{h_{t,e} - h_r} \qquad \text{... (D.8)}$$

$$d = \frac{\rho_e(x)}{\rho(x,y)} \qquad \text{... (D.9)}$$

$$T = \frac{\nu_e}{u_e\ \delta^*} \qquad \text{... (D.10)}$$

$$T_g = \frac{K_e}{u_e\ \delta^*} \qquad \text{... (D.11)}$$

In terms of these variables, the governing equations became :

$$- [\ (1+ C_a\eta)\frac{T}{d}\,[d(1-f')]'\ ]' + [\ (Q+R)\ (\eta-f) - \frac{\rho_w v_w}{\rho_e u_e} - \delta^*\frac{\partial f}{\partial x}\ ]\ df'' +$$

$$[\ [\ (Q+R)\ (\eta-f) - \frac{\rho_w v_w}{\rho_e u_e} - \delta^*\frac{\partial f}{\partial x}\ ]\ d' - (\ P\ d + \delta^*\frac{\partial d}{\partial x}\ )\ (2-f')\ ]\ f' -$$

$$[\ (Q+R)\ (\eta-f) - \frac{\rho_w v_w}{\rho_e u_e} - \delta^*\frac{\partial f}{\partial x}\ ]\ d' + P\ (d-1) + \delta^*\frac{\partial d}{\partial x} = (1-f')\ \delta^*\ d\,\frac{\partial f'}{\partial x}$$

$$\text{... (D.12)}$$

$$[\ (1+C_a\eta)\ \frac{T_g}{d}\ [\ g'' - \frac{\frac{\gamma-1}{2}M_e^{\,2}}{H\ (\ 1+\frac{\gamma-1}{2}M_e^{\,2})}\ (\ \frac{\nu_e}{K_e} - 1\ )\ [\ d^2\ (1-f')^2\ ]'\ ]\ ]' +$$

$$[\ (Q+R)\ (\eta-f)\ - \delta^*\frac{\partial f}{\partial x} - \frac{\rho_w v_w}{\rho_e u_e}\ ]\ g'' = (1-f')\ \delta^*\frac{\partial g'}{\partial x} \qquad \text{... (D.13)}$$

where :

$$P = \frac{1}{u_e} \frac{\partial u_e}{\partial x} \qquad \text{... (D.14)}$$

$$Q = \frac{1}{\rho_e u_e} \frac{\partial(\delta^* \rho_e u_e)}{\partial x} \qquad \text{... (D.15)}$$

$$R = \frac{\delta^*}{r_w} \frac{\partial(r_w)}{\partial x} \qquad \text{... (D.16)}$$

$$C_a = 2 \left(\frac{\delta^*}{r_w} \right) \cos \alpha \qquad \text{... (D.17)}$$

and where the functions T and T_g have the form (Herring & Mellor, 1968) :

$$T = \frac{\delta^*_K}{\delta^*} \left[\frac{\varphi (X R_{\delta^*_K})}{R_{\delta^*_K}} + \Phi (X) - X \right] \qquad \text{... (D.18)}$$

$$T_g = \frac{\nu}{\nu_e} \frac{1}{R_{\delta^*_K} P_r} + \frac{1}{P_{rt}} \left[T - \frac{\nu}{\nu_e} \frac{1}{R_{\delta^*}} \right] \qquad \text{... (D.19)}$$

The above set of equations along with the boundary conditions are sufficient to calculate the development of the boundary layer. However, small inaccuracies in the numerical solution which are negligible after one step in x, are frequently cumulative. Greater accuracy can be achieved by correcting the integral parameters obtained from the numerical solution of equation D.11 by comparing them to those obtained from the Von-Karman integral momentum equation which can be obtained by integrating equation 4.15 of section 4 accross the layer. The result is :

$$\frac{d}{dx} (r_w \rho_e u_e^2 \theta) + r_w \delta^* \rho_e u_e \frac{du_e}{dx} = r_w (\tau_w + \rho_w v_w u_e)$$

... (D.20)

where : $$\Theta = \int_0^\infty \frac{\rho u}{\rho_e u_e} \left(1 - \frac{u}{u_e} \right) dy \qquad \ldots (D.21)$$

D.2 Numerical method

The procedure of obtaining a solution to the governing partial differential equations comprises two main phases : 1) conversion of the governing equations to ordinary differential equations using finite-differences for the x-derivatives and 2) solution of the resulting system of equations.

In the first phase, the x-derivatives were represented by finite differences according to an adaptation of the scheme of (Crank & Nicholson, 1947). The method is of implicit type and its error is of second order. The resulting equations were solved by applying a Gaussian elimination procedure to their characteristic matrices.

D.3 Effective viscosity and diffusivity hypotheses

In the boundary layer equations, the influence of turbulence appears through the expression of the shear stress and heat transfer. Therefore, in order to complete the governing equations (Equations 4.12 and 4.13 of section 4), these quantities must be related to the mean flow variables.

D.3.1 Effective viscosity hypothesis

The hypothesis for the form of the effective viscosity represented in equation 4.9 of section 4 and first proposed by Boussinesq, is based on three assumptions supposed to be universally valid :

1. In the defect layer, the effective viscosity depends on only three quantities : ($\delta_K^* u_e$), y and ($\partial u/\partial y$). From this assumption, ν_e must be of the form :

$$\frac{\nu_e}{\delta_K^* u_e} = \left(\frac{K^2 y^2}{\delta_K^* u_e} \frac{\partial u}{\partial y} \right) \qquad \ldots (D.22)$$

2. In the inner or wall layer, ν_e again depends on only three quantities : ν, y and $(\partial u/\partial y)$. From this assumption, ν_e must be of the form :

$$\frac{\nu_e}{\nu} = \left(\frac{K^2\, y^2}{\nu} \frac{\partial u}{\partial y} \right) \qquad \ldots\ (\text{ D.23 })$$

3. Both the above expressions apply simultaneously in the region where the layers overlap. Consequently, the form of the effective viscosity in the overlap region must be :

$$\nu_e = \nu\varphi = \delta_K^*\ u_e\ \Phi = K^2\, y^2 \frac{\partial u}{\partial y} \qquad \ldots\ (\text{ D.24 })$$

Equivalent to the above formulation but offering some computational advantage is the functional form suggested by (Mellor, 1967) which may be expressed as :

1. In the defect layer:

$$\frac{\nu_e}{\delta_K^*\, u_e} = \Phi\,(\,X\,) \quad \text{with} \quad X = \frac{K\,y}{\delta_K^*\, u_e}\,(\,\tau/\rho\,)^{\frac{1}{2}} \qquad \ldots\ (\text{ D.25 })$$

2. In the wall layer :

$$\frac{\nu_e}{\nu} = \varphi\,(\,X\,) \qquad \text{with} \qquad = \frac{K\,y}{\nu}\,(\,\tau/\rho\,)^{\frac{1}{2}} \qquad \ldots\ (\text{ D.26 })$$

The functions φ and Φ were determined by comparison of calculated profiles with constant pressure data and are shown in Figure D.1.

D.3.2 Effective diffusivity hypothesis

By analogy to the molecular Prandtl number defined as $P_r = \nu/\alpha$, and since $(\nu_e - \nu)$ and $(\alpha_e - \alpha)$ are the turbulent viscosity and diffusivity respectively, a turbulent Prandt number may be defined :

$$P_{rt} = \frac{\nu_e - \nu}{\alpha_e - \alpha} \qquad \text{... (D.27)}$$

The effective diffusivity can, thus, be written as :

$$\alpha_e = \frac{1}{K_e} = \frac{\nu}{P_r} + \frac{\nu_e - \nu}{P_{rt}} \qquad \text{... (D.28)}$$

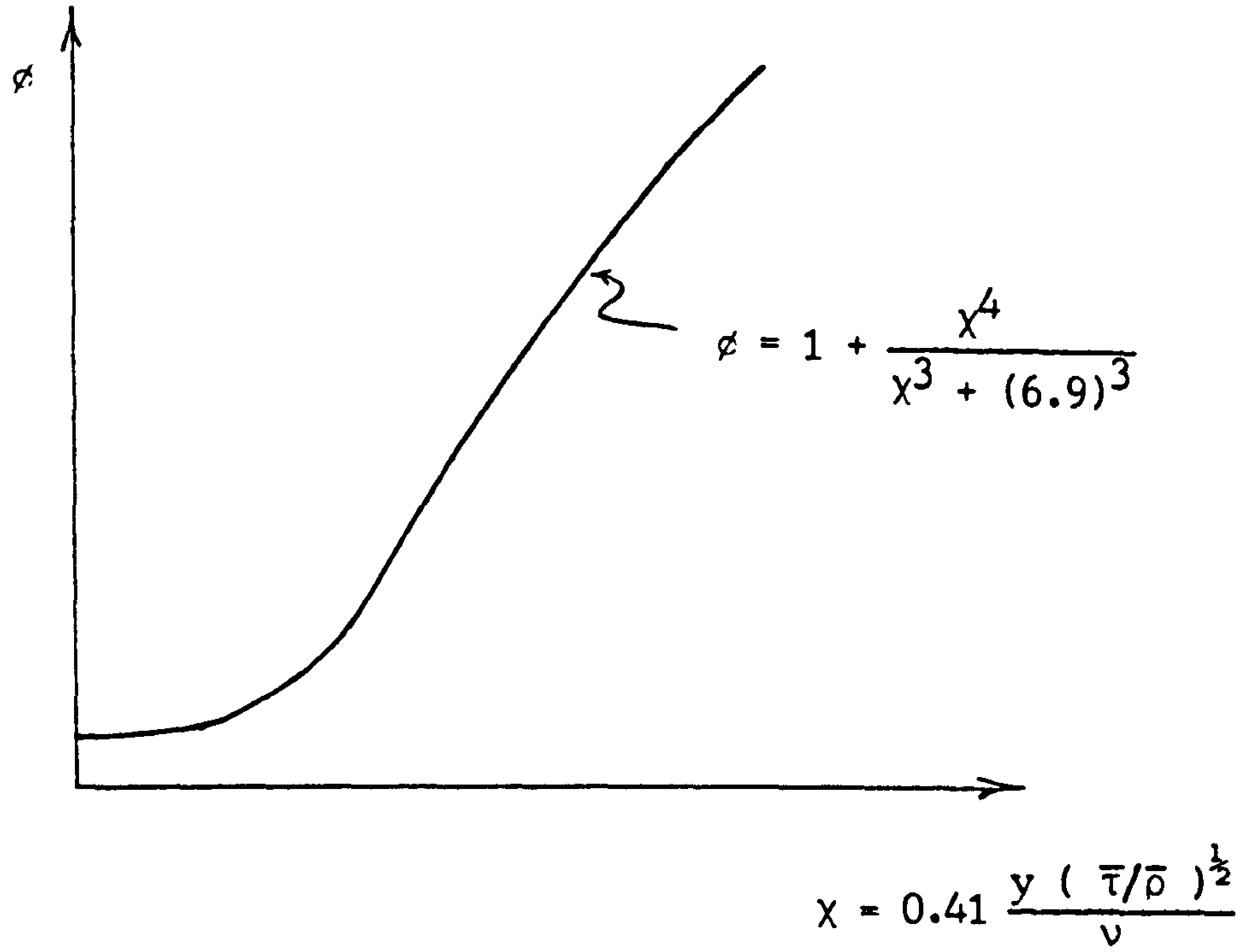

$$\phi = 1 + \frac{\chi^4}{\chi^3 + (6.9)^3}$$

$$\chi = 0.41\,\frac{y\,(\,\bar{\tau}/\bar{\rho}\,)^{\frac{1}{2}}}{\nu}$$

Fig. D.1.a: Inner function $\phi = \phi(\chi)$

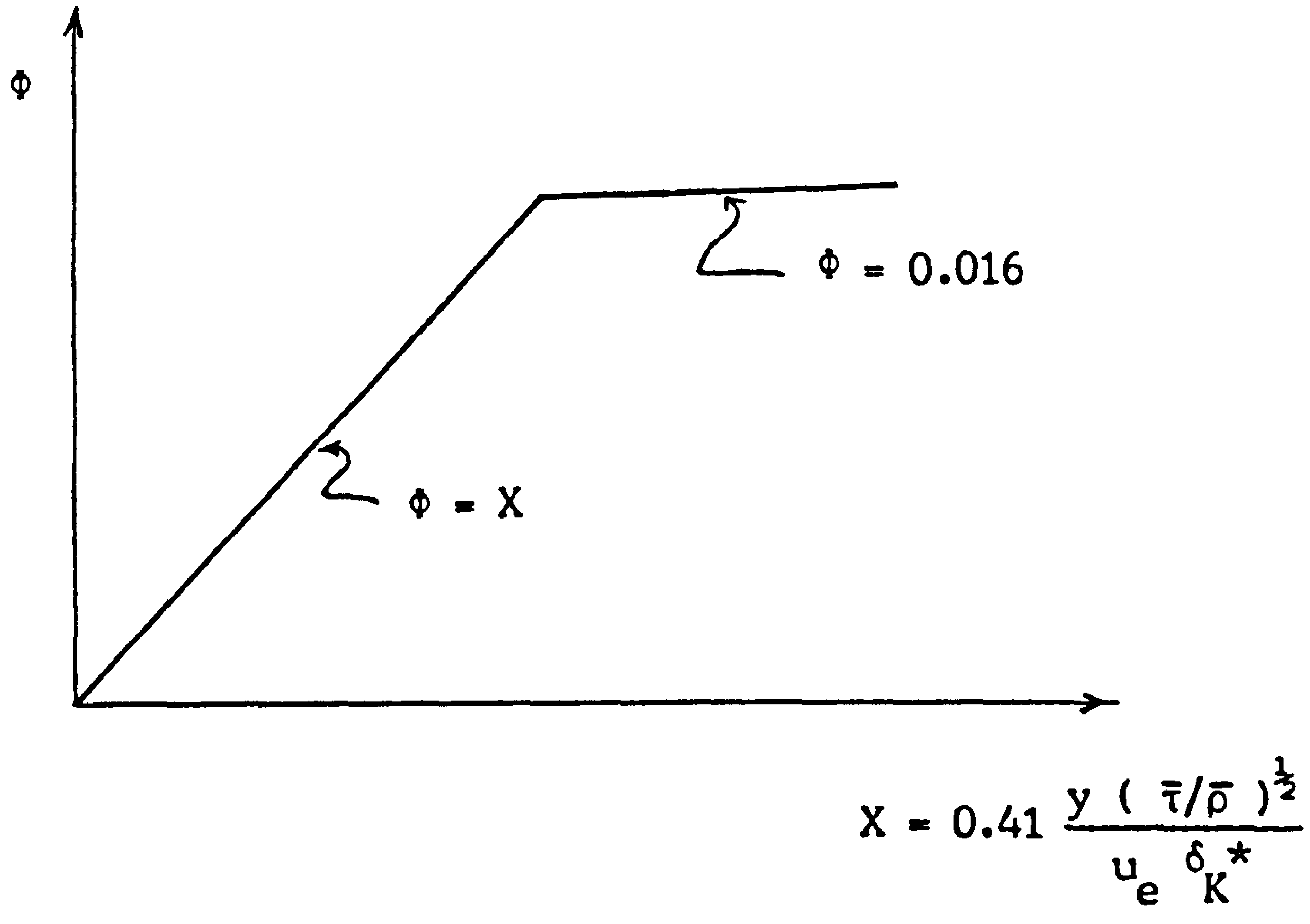

$$\Phi = 0.016$$

$$\Phi = X$$

$$X = 0.41\,\frac{y\,(\,\bar{\tau}/\bar{\rho}\,)^{\frac{1}{2}}}{u_e\,\delta_K^*}$$

Fig. D.1.b : Outer function $\Phi = \Phi(\,X\,)$.

Fig. D.1: Inner and outer functions used in the turbulent effective viscosity hypothesis (Mellor, 1967).

APPENDIX E : Starting velocity profile, starting enthalpy profile and initial pressure gradient.

E.1 Starting velocity and enthalpy profiles

The initial velocity and temperature profiles are assumed to be described by the 1/7 and 1/4 laws respectively i.e. between $y=0$ and $y=\delta$, the profiles are described by the relations :

$$\frac{u}{u_e} = \left(\frac{y}{\delta} \right)^{1/7} \qquad \dots \text{(E.1)}$$

$$\frac{T_t - T_w}{T_{t,e} - T_w} = \left(\frac{y}{\Delta} \right)^{1/4} \qquad \dots \text{(E.2)}$$

E.1.1 Expression for the velocity defect profile

Using equation E.1, the velocity defect profile may be expressed as :

$$\frac{\rho_e u_e - \rho u}{\rho_e u_e} = 1 - \frac{\rho}{\rho_e} \left(\frac{y}{\delta} \right)^{1/7} \qquad \dots \text{(E.3)}$$

Assuming the pressure to be constant along a cross-section ($\partial p/\partial y=0$), the equation of state for a perfect gas is :

$$\frac{\rho}{\rho_e} = \frac{T_e}{T} = \frac{T_{t,e} - \frac{u_e^2}{2 C_p}}{T_t - \frac{u^2}{2 C_p}} \qquad \dots \text{(E.4)}$$

From equations E.1 and E.2 :

$$\frac{u^2}{2\,C_p} = \frac{u_e^{\,2}}{2\,C_p}\left(\frac{y}{\delta}\right)^{2/7} \qquad \ldots\ (\text{ E.5 })$$

$$T_t = \left(\frac{y}{\Delta}\right)^{1/4}\left(T_{t,e} - T_w\right) + T_w \qquad \ldots\ (\text{ E.6 })$$

Substituting equations E.5 and E.6 into E.4 gives the expression of (ρ/ρ_e) which, when replaced into equation E.3, leads to the initial velocity defect profile used to start the computations :

$$\frac{\rho_e\,u_e - \rho\,u}{\rho_e\,u_e} =$$

$$1 - \left(\frac{y}{\delta}\right)^{1/7}\frac{T_{t,e} - \dfrac{u_e^{\,2}}{2\,C_p}}{\left(\dfrac{y}{\Delta}\right)^{1/4}\left(T_{t,e} - T_w\right) + T_w - \dfrac{u_e^{\,2}}{2\,C_p}\left(\dfrac{y}{\delta}\right)^{2/7}} \qquad \ldots\ (\text{ E.7 })$$

E.1.2 Expression for the enthalpy defect profile

$$\frac{h_{t,e} - h_t}{h_{t,e}} = 1 - \frac{h_t}{h_{t,e}} = 1 - \frac{T_t}{T_{t,e}} \qquad \ldots\ (\text{ E.8 })$$

Dividing the left-hand side of equation E.2 by $T_{t,e}$:

$$\frac{\dfrac{T_w}{T_{t,e}} - \dfrac{T_w}{T_{t,e}}}{1 - \dfrac{T_w}{T_{t,e}}} = \left(\frac{y}{\Delta}\right)^{1/4} \qquad \ldots\ (\text{ E.9 })$$

Simplification leads to :

$$\frac{T_t}{T_{t,e}} = \left(\frac{y}{\Delta} \right)^{1/4} \left(1 - \frac{T_w}{T_{t,e}} \right) + \frac{T_w}{T_{t,e}} \qquad \ldots \ (\text{E.10})$$

Substituting into equation E.8 leads to the expression of the initial enthalpy profile used to start the flow computations :

$$\frac{h_{t,e} - h_t}{h_{t,e}} = 1 - \left[\left(\frac{y}{\Delta} \right)^{1/4} \left(1 - \frac{T_w}{T_{t,e}} \right) + \frac{T_w}{T_{t,e}} \right] \qquad \ldots \ (\text{E.11})$$

E.2 Expression for the initial pressure gradient

For a frictionless adiabatic flow of a perfect gas :

$$\frac{\dot{m} \, (T_t)^{\frac{1}{2}}}{A \, P} = \left(\frac{1}{R} \right) \left(\frac{u}{(T_t)^{\frac{1}{2}}} \right) \left(\frac{T_t}{T} \right) \qquad \ldots \ (\text{E.12})$$

$$P = \frac{1}{A} \frac{\dot{m} \, R \, T}{u} \qquad \ldots \ (\text{E.13})$$

The velocity may be expressed as :

$$u = M \, (T_t)^{1/2} \left(\frac{\gamma R}{\frac{T_t}{T}} \right) \qquad \ldots \ (\text{E.14})$$

Substituting E.14 into E.13 leads to :

$$P = \frac{1}{A} \left[\frac{\dot{m} \left(\gamma R \, \frac{T_t}{1 + \frac{\gamma - 1}{2} M^2} \right)^{\frac{1}{2}}}{M \, \gamma} \right] \qquad \ldots \ (\text{E.15})$$

For an isentropic flow, the total pressure is assumed constant and the pressure would depend on only the area and Mach number :

$P = P\ (A, M)$

Therefore :

$$\frac{dP}{dx} = \frac{\partial P}{\partial A}\frac{dA}{dx} + \frac{\partial P}{\partial M}\frac{dM}{dx} \qquad \ldots\ (\text{E.16})$$

E.2.1 Expression of (∂P/∂A)

From equation E.13 :

$$\frac{\partial P}{\partial A} = -\frac{1}{A^2}\left[\frac{\dot{m}\left(\gamma R\,\dfrac{T_t}{1+\dfrac{\gamma-1}{2}M^2}\right)^{\frac{1}{2}}}{\gamma M}\right] \qquad \ldots\ (\text{E.17})$$

E.2.2 Expression of (∂P/∂M)

Using equation E.13 again :

$$\frac{\partial P}{\partial M} = -\frac{1}{A}\left[\frac{\dfrac{\dot{m}\,M}{2}\left[\dfrac{\gamma\,(\gamma-1)\,R\,T_t\,M}{\left(1+\dfrac{\gamma-1}{2}M^2\right)^2}\right]^{-\frac{1}{2}} + \dot{m}\left(\dfrac{\gamma\ R\,T_t}{1+\dfrac{\gamma-1}{2}M^2}\right)}{\gamma M^2}\right]$$

$$\ldots\ (\text{E.18})$$

E.2.3 Expression of (dA/dx)

This relation depends on the form of the equation describing the area of a cross-section which depends on the nozzle shape.

E.2.4 Expression of (dM/dx)

$$\frac{dM}{dx} = \frac{dM}{dA}\frac{dA}{dx} \qquad \ldots\ (\text{E.19})$$

(dM/dA) may be written as :

$$\frac{dM}{dA} = \frac{d\left(\frac{M}{A^*}\right)}{d\left(\frac{A}{A^*}\right)} = \frac{1}{\frac{d(A/A^*)}{d(M/A^*}} \qquad \ldots \text{(E.20)}$$

Thus :

$$\frac{dM}{dx} = \frac{\frac{dA}{dx}}{\frac{d(A/A^*)}{d(M/A^*)}} \qquad \ldots \text{(E.21)}$$

For an isentropic flow with area change :

$$\frac{A}{A^*} = \frac{1}{\frac{\dot{m}\ (\ T_t\ )^{\frac{1}{2}}}{A\ P}} [\ (\ \frac{2}{\gamma+1}\ )^{\frac{\gamma+1}{\gamma-1}}\ \frac{\gamma}{R}\ ]^{\frac{1}{2}} \qquad \ldots \text{(E.22)}$$

Using equation E.13 and E.14, the above expression becomes :

$$\frac{A}{A^*} = \frac{R\ [\ (\frac{2}{\gamma+1})^{\frac{\gamma+1}{\gamma-1}}\ \frac{\gamma}{R}\ ]^{\frac{1}{2}}}{A^*\ (\frac{M}{A^*})\ [\ \frac{\gamma R}{1 + \frac{\gamma-1}{2}\ (\frac{M}{A^*})^2\ A^{*2}}\ ]^{\frac{1}{2}}\ [\ \frac{1}{1 + \frac{\gamma-1}{2}\ (\frac{M}{A^*})^2\ A^{*2}}\ ]^{\frac{1}{\gamma-1}}}$$

$$\ldots \text{(E.23)}$$

Deriving equation E.23 with respect to (M/A^*) and substituting the result into equation E.21 gives :

$$\frac{dM}{dx} = [\ -\frac{dA}{dx}\ [\ M\ (\ \frac{\gamma\ R}{1 + \frac{\gamma-1}{2} M^2}\ )^{\frac{1}{2}}\ (\ \frac{1}{1 + \frac{\gamma-1}{2} M^2}\ )^{\frac{1}{\gamma-1}}\ ]^2$$

$$[\ \frac{1}{R\ [\ (\frac{2}{\gamma+1})^{\frac{\gamma+1}{\gamma-1}}\ \frac{\gamma}{R}\ ]^{\frac{1}{2}}\ [\ [\ A^*\ (\ \frac{\gamma\ R}{1 + \frac{\gamma-1}{2} M^2}\ )^{\frac{1}{2}} - \frac{M}{2} [\ \frac{\gamma R\ (\gamma-1)\ A^*\ M}{(1 + \frac{\gamma-1}{2} M^2\ )^2}\ ]^{-\frac{1}{2}}]}\ ]$$

$$\left[\frac{1}{\left[\left(\frac{1}{1 + \frac{\gamma-1}{2} M^2} \right)^{\frac{1}{\gamma-1}} - \left[\frac{1}{\gamma-1} \left[\frac{(\gamma-1)\, A^* \, M}{(1+\frac{\gamma-1}{2} M^2)^2} \right]^{\frac{2-\gamma}{\gamma-1}} \right] \left[M \left(\frac{\gamma R}{1+\frac{\gamma-1}{2} M^2} \right) \right] \right]} \right.$$

... (E.24)

$$\frac{dP}{dx} = \left(- \frac{1}{A^2} \right) \left[\frac{\dot{m} \left(\gamma R \frac{T_t}{1 + \frac{\gamma-1}{2} M^2} \right)^{\frac{1}{2}}}{\gamma M} \right] \left(\frac{dA}{dx} \right) +$$

$$\left(\frac{1}{A} \right) \left[\frac{\frac{\dot{m}\, M}{2} \left[\frac{\gamma\, (\gamma-1)\, R\, T_t\, M}{(1+\frac{\gamma-1}{2} M^2)^2} \right]^{-\frac{1}{2}} + \dot{m} \, \frac{\gamma R T_t}{1+\frac{\gamma-1}{2} M^2}}{\gamma M^2} \right] \left(\frac{dM}{dx} \right)$$

... (E.25)

where the expresssion of (dM/dx) is given by equation E.23.

APPENDIX F : Mass flow calculation methods

The mass flow can be calculated from measured data in two ways. Method I uses an orifice flow meter and is based on the pressure drop across the orifice. Method II uses the stagnation pressure and temperature along with isentropic flow theory to expand the gas within the nozzle.

F.1 Method I: orifice flow meter

The basic mass flow equation, derived from the principle of continuity, can be written as :

$$\dot{m} = \frac{\pi}{4} d^2 K \left[2 \rho (\Delta P) \right]^{\frac{1}{2}}$$

The equation of state gives :

$$\rho = \frac{P}{R T z}$$

As the pressure drop is read in height of mercury, it may be expressed in the form :

$$\Delta P = \rho_{Hg} \, g \, \Delta H$$

where :

d = orifice diameter
P = pressure prior to orifice
z = compressibility factor (0.99 for P = 10-25 atm)

The three above equations, when mixed together, would lead to :

$$\dot{m} = \frac{\pi}{4} d^2 K \left(\frac{2g}{R} \right)^{\frac{1}{2}} \left(\frac{P \rho_{Hg} \Delta H}{T} \right)^{\frac{1}{2}} \qquad \ldots \text{(F.1)}$$

F.2 Method II : isentropic flow

At the throat, the principle of continuity gives :

$$\dot{m} = \rho_{th} A_{th} W_{th} \qquad \text{... (F.2)}$$

where :

$$\rho_{th} = \frac{P_{th}}{R\ T_{th}}$$

$$W_{th} = M_{th}\ a_{th} = a_{th} = (\ \gamma\ R\ T_{th}\ )^{\frac{1}{2}}$$

Substituting leads to :

$$\dot{m} = \frac{P_{th}}{R\ T_{th}} (\ \gamma\ R\ T_{th}\ )^{\frac{1}{2}}\ Ath$$

At the sonic Mach number and for a specific heat ratio of 1.4, the isentropic flow tables (Keenan & Kaye,1948) give :

$P_{th} = 0.52828\ P_t$
$T_{th} = 0.83333\ T_t$

Finally :

$$\dot{m} = \frac{0.52828\ P_t}{R\ 0.83333\ T_t} (\ \gamma\ R\ 0.83333\ T_t\ )^{\frac{1}{2}}\ A_{th} \qquad \text{... (F.3)}$$

APPENDIX G : I-Deas

I-DEAS (Internal Design Engineering Analysis Software) is a comprehensive package for mechanical design engineers. Developed by SDRC (Structural Dynamics Research Corporation), it provides capabilities for (I-Deas user guide, 1986) :

> Solid modelling
> System assembly
> Kinematics
> Finite element pre/post processing
> Finite element solution
> System dynamics
> Drafting
> Test data analysis
> Preject relational data base

These capabilities are packaged as families of software :

> Solid modelling family or GEOMOD
> Engineering analysis family or SUPERTAB
> System dynamics family or SYSTAN
> Drafting family or GEODRAW
> Test data analysis family or TDAS

I-Deas Supertab (I-Deas Supertab, 1986) is the machanical tool that provides the ability to model and analyse the statics, dynamics, heat transfer and potential flow behaviour of mechanical components and structures. I-Deas Supertab module has been used to build the models describing the Con-di elliptical and the two-dimensional wedge nozzles. The finite element pre/post processing facility allowed the production of the appropriate grids describing the two configurations. These grids were subsequently injected into 'Phoenics' (see section 7). The following pre/post processing tasks were used :

> Geometry definition: Allows the description of the model's geometry by inserting the coordinates of the stations defining the model. These points are subsequently joined, where necessary, by either arcs, lines or splines.

> Model preparation and checking: This task enables the generation of the necessary nodes, elements and physical and material tables. It also checks the validity of the model before analysis.

> Mesh generation: When the geometry is defined and the model checked, the mesh can then be generated using the Triquamesh algorithm (I-Deas Supertab, 1986).

> File translator: In order to translate the information generated by Supertab and store it into the appropriate file for later use by 'phoenics', the task 'File translator' is used. It enables the reading and writing of the I-Deas universal file for analysis.

The detailed procedure followed in order to generate the models describing the two configurations investigated in this study is presented in section 7.

APPENDIX H : Phoenics

H.1 General

PHOENICS (Parabolic, Hyperbolic or Elliptic Numerical Integration Code Series) is a comprehensive computer code which can simulate fluid flow, heat transfer, chemical reaction and related phenomena. Developed at the Imperial College of Technology, it mainly consists of a pre-processor (SATLIT), a main processor (EARTH) and two utility post-processors (Photon and Guide).

H.1.1 The pre-processor: 'Satlit'

Satlit turns the instructions provided by the user into a data file which can be understood by the main processor, enabling it to proceed with the integration of the appropriate equations governing the simulated flowfield. It also has the ability to transmit the information concerning the geometrical data to the processor.

For the configurations investigated in this thesis, two instruction files were prepared (one for the elliptical nozzle and the other for the two-dimensional wedge). The required geometrical data were stored in two files prepared by I-Deas (section 7 and Appendix G) and retrieved by Satlit to be used in the main processor computations.

H.1.2 The processor: 'Earth'

Earth is the main processor. It contains the main flow simulating software representing the relevant laws of physics. It reads and execute the instructions contained into the data file provided by Satlit and then produces an output file representing the results which the user have instructed it to provide.

Inserted into Earth are a collection of subroutines called: GROUND. They contain a variety of useful data-settings which may help the user to supply the processor with the appropriate boundary conditions, sources, fluid properties and output control features. In modelling the flow as compressible, the subroutine GRND3 which is contained into Ground was used to provide the appropriate relations describing the density variation within the flowfield.

H.1.3 The post-processor: 'Photon'

Photon is an interactive plotting code which picks up results from the result files produced by Earth. Responding to the instructions entered by the user through the VDU keyboard, it represents the computed grid and flow pattern graphically on the screen (see CHAM TR/140).

H.1.4 The post-processor: 'Guide'

Guide is a help-file available to the user to help him while using Phoenics.

H.2 Geometry definition

Phoenics can employ grids of three distinct kinds, namely:

> Cartesian,
> Cylindrical polar,
> Curvilinear.

The shapes of the configurations investigated in this thesis are very much curved (especially the elliptical nozzle) and thus the curvilinear grid option (often called boundary fitted coordinates) had to be used. The grid and the nodes at which the equations are solved was produced by the I-Deas supertab software module (Appendix G).

H.3 The equations solved by Phoenics

The equations solved by Phoenics may be presented in the general discretized form (see CHAM TR/100):

$$\frac{\partial}{\partial x_i}(r_i \, \rho_i \, \varphi_i) + \mathrm{div} (r_i \, \rho_i \, \vec{v} \, \varphi_i - r_i \, \Gamma_{\varphi i} \, \mathrm{grad} \, \varphi_i) = r_i \, S_i \qquad \ldots (H.1)$$

where: t = time ; S = source rate
r = volume fraction ; i = phase
ρ = density
φ = any conserved property
v = velocity vector
Γ_φ = exchange coefficient for the entity φ

The algebraic equations included into Phoenics are numerous and strongly coupled. Phoenics solve them in an iterative 'guess-and-correct' manner, the object of which is to reduce the imbalance between the left and right sides of every equation to a magnitude which is small enough to be negligible. The most effective solution for potential fluid flow is the so-called 'whole-field solution'. It uses more computer storage but reduces the number of sweeps (a sweep is represented by the total steps conducted to describe the whole domain) required in order to eliminate the imbalances in the equations and thus reach the solution more rapidly. The whole-field solution was used to solve the cases investigated.

Phoenics describes a phenomenon in terms of distribution in space and time of the so-called 'dependent variables'. These distributions involve prescribing numerical values to the variables of each array of locations. The main processor Earth is equiped to solve up to 50 dependent variables. Solution of our cases have been operated with four dependent variables, namely the static pressure and the three components of the velocity.

The 'independent variables' for which phoenics is able to simulate a phenomenon are represented by the time and the coordinate directions. The flowfields investigated in this study are assumed to be steady and thus the independent variable 'time' does not appear and we were limited to a three-dimensional problem.

The 'auxiliary variables' are those derived from the algebraic equations involving the dependent and independent variables calculated before by solving the appropriate differential equations. An auxiliary relation used to derive the density is the perfect gas law:

$$\rho = \frac{P}{R\,T}$$

where:

ρ = density

P = pressure

R = gas constant

T = temperature

Another auxiliary variable, the static temperature, is computed using the isentropic flow relationship:

$$T = \frac{T_t}{\left(\frac{P_t}{P}\right)^{\frac{\gamma-1}{\gamma}}}$$

where P_{total} and T_{total} are the total pressure and temperature whose values are prescribed as initial conditions.

APPENDIX I : Thrust and thrust coefficient

I.1 Thrust

Once the mass flow is calculated (Appendix F), the following basic equation can be used to calculate the thrust :

$$T_c = \dot{m} V_e + (P_e - P_a) A_e \qquad \ldots (I.1)$$

I.2 Thrust coefficient

The thrust coefficient is used to determine the quality of a nozzle. It is defined as :

$$C_D = \frac{T_c}{P_{cc} A_{th}} \qquad \ldots (I.2)$$

As the pressure in the combustion chamber increases, it should be possible to obtain greater thrust. Similarly, as the throat area is increased, greater mass rate of the flow and hence greater thrust should result. Dividing the calculated thrust by the combustion chamber pressure and the nozzle throat area gives a measure of the effectiveness of the expansion of the combustion gases. The quality of the nozzle controls the expansion process and hence is indicated by the thrust coefficient (Barrere et al, 1960).

APPENDIX J : Subsonic section design of the elliptical nozzle and supersonic section design of the two-dimensional wedge nozzle.

J.1 Subsonic section design of the elliptical nozzle

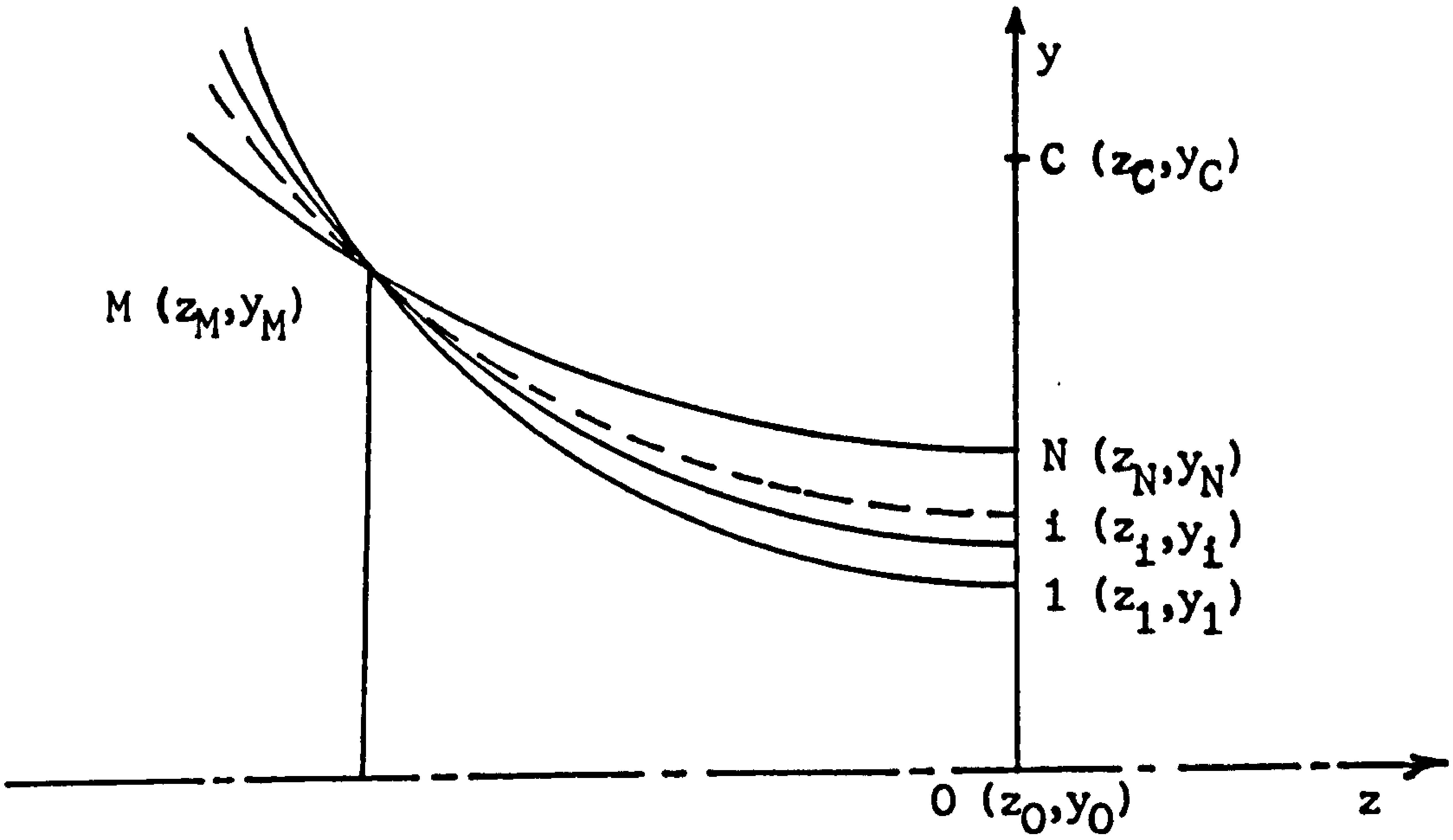

Fig. J.1: Subsonic section design.

The equations of the different circles to which the arcs defining the subsonic section of the elliptical nozzle belong are defined as follows:

Point i (z_i,y_i) lies on the circle of centre C and radius R_i, thus:

$$(z_i - z_{oc})^2 + (y_i - y_{oc})^2 = R_i^2 \qquad \text{... (J.1)}$$

Point M (z_M,y_M) also lies on the same circle:

$$(z_M - z_{oc})^2 + (y_M - y_{oc})^2 = R_i^2 \qquad \text{... (J.2)}$$

where:

$z_{oc} = 0$ is the axial distance between the centre of the circle and the origin of the coordinate system,

$z_i = 0$

z_M, y_M are prescribed by the inlet section which must match the exit of the supplying pipe.

Solution of the equations J.1 and J.2 leads to:

$$y_{oc} = \frac{y_M^2 + z_M^2 - y_i^2}{2\,(\,y_M - y_i)} \qquad \text{... (J.3)}$$

$$R_i = |\, y_i - y_{oc} \,| \qquad \text{... (J.4)}$$

The general equation of a circle, when expressed relatively to the coordinate system (0,z,y) is:

$$(\, z - z_{oc}\,)^2 + (\, y - y_{oc}\,)^2 = R_i^2$$

where:

$z_{oc} = 0$

y_{oc} and R_i are defined by equations J.3 and J.4.

Replacing leads to:

$$z^2 + \left[\, y - \frac{y_M^2 + z_M^2 - y_i^2}{2\,(\,y_M - y_i\,)}\,\right]^2 = (\, y_i - y_{oc}\,)^2 \quad ; \quad i = 1,N \qquad \text{... (J.5)}$$

Equation J.5 defines the circles to which the arcs drawn on Figure J.1 belong. The arcs define the subsonic section of the elliptical nozzle. the characteristics of the circles (radius and centre position) are presented in table 5.3 of section 5.

J.2 Coordinates of the stations defining the 2-D wedge nozzle

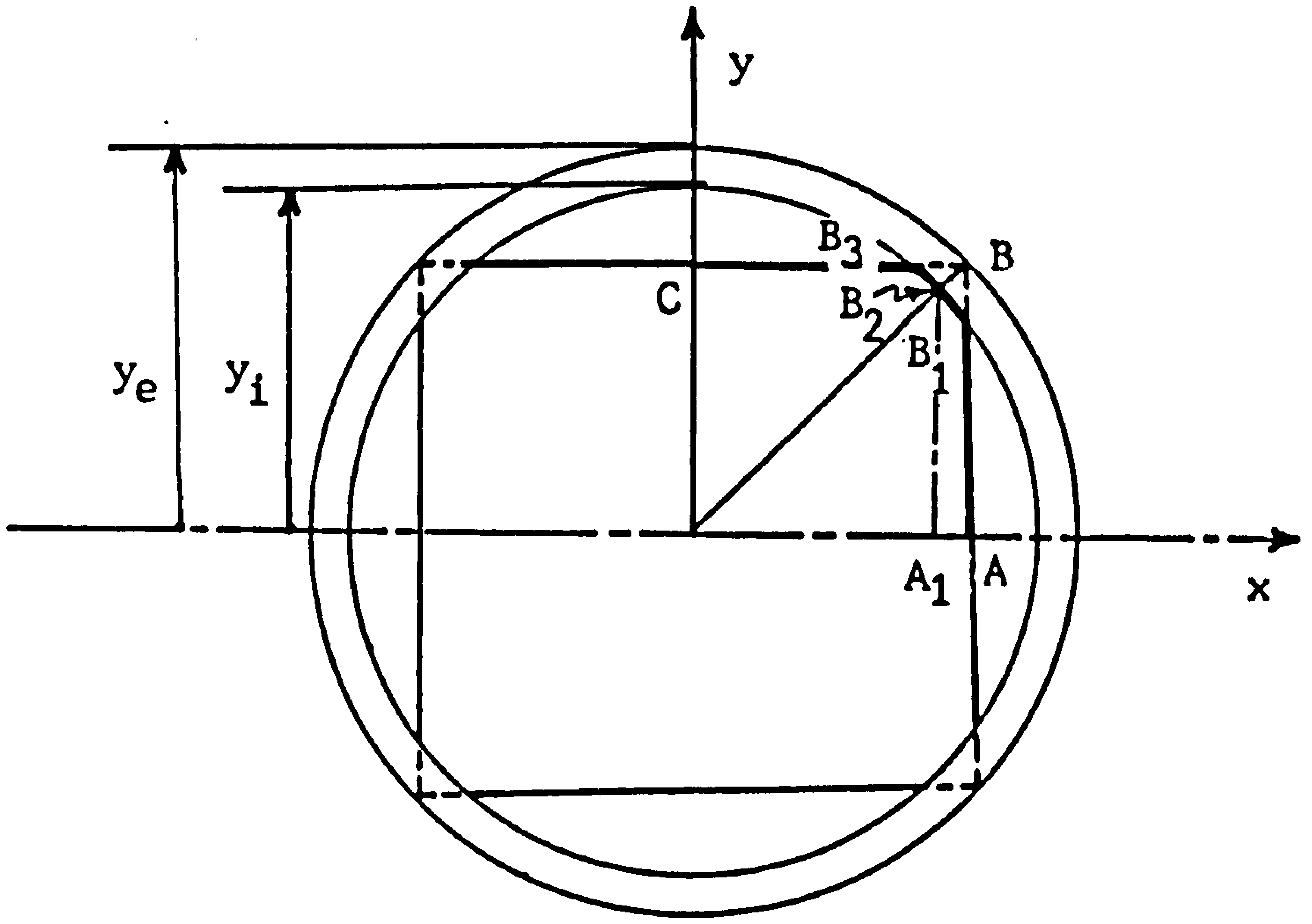

Fig. J.2: Axisymmetric and 2-D wedge exit cross-sections.

The ratio of the internal radius y_i to the external one y_e was selected equal to 9/10 (section 5).

Considering the triangles OBA, OB_1A and OB_2A_1, it is found:

$$x_A = \frac{y_e}{(2)^{\frac{1}{2}}} \quad \text{and} \quad y_A = 0$$

$$x_{B1} = \frac{y_e}{(2)^{\frac{1}{2}}} \quad \text{and} \quad y_{B1} = y_e \ (0.31)^{\frac{1}{2}} \qquad \ldots \ (\ J.6\ )$$

$$x_{B2} = \frac{9/10\ y_e}{(2)^{\frac{1}{2}}} \quad \text{and} \quad y_{B2} = \frac{9/10\ y_e}{(2)^{\frac{1}{2}}}$$

Symmetry about the axis OB leads to:

$$x_{B3} = y_e \ (0.31)^{\frac{1}{2}} \quad \text{and} \quad y_{B3} = \frac{y_e}{(2)^{\frac{1}{2}}}$$

$$x_C = 0 \quad \text{and} \quad y_C = \frac{y_e}{(2)^{\frac{1}{2}}} \qquad \ldots \ (\ J.7\ )$$

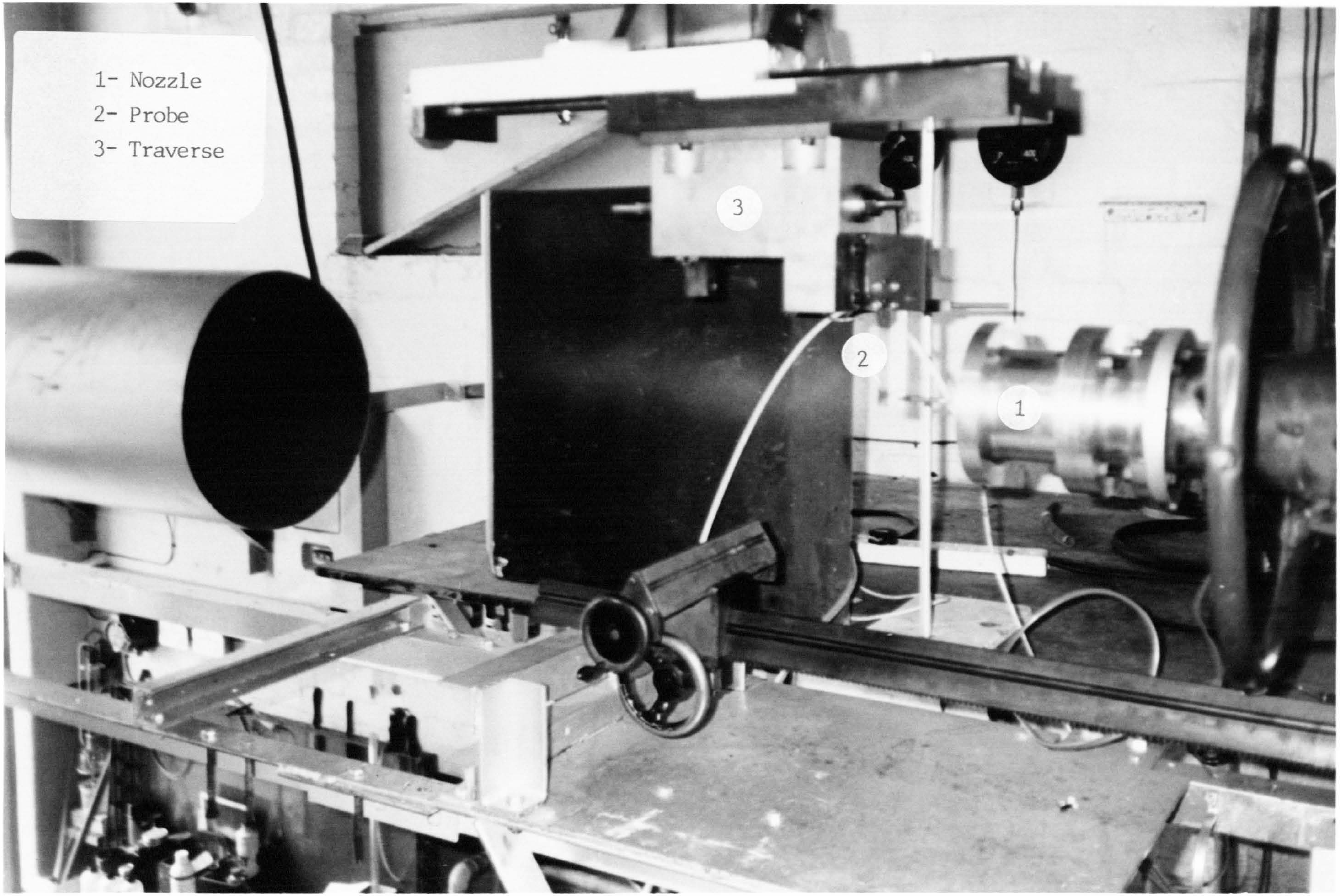

PLATE 1 : Layout of test rig

1- Connection to transducer or manometer.
2- Connection to traverse.
3- Losenge cross-section bar.
4- Hypodermic tube.

PLATE 2 : Internal probe.

1- Flange.
2- Probe holder.
3- 120° positioned legs.

PLATE 3 : Internal probe holder.

1- Connection to transducer or manometer.
2- Connection to traverse.
3- Losenge cross-section bar.
4- Hypodermic tube.

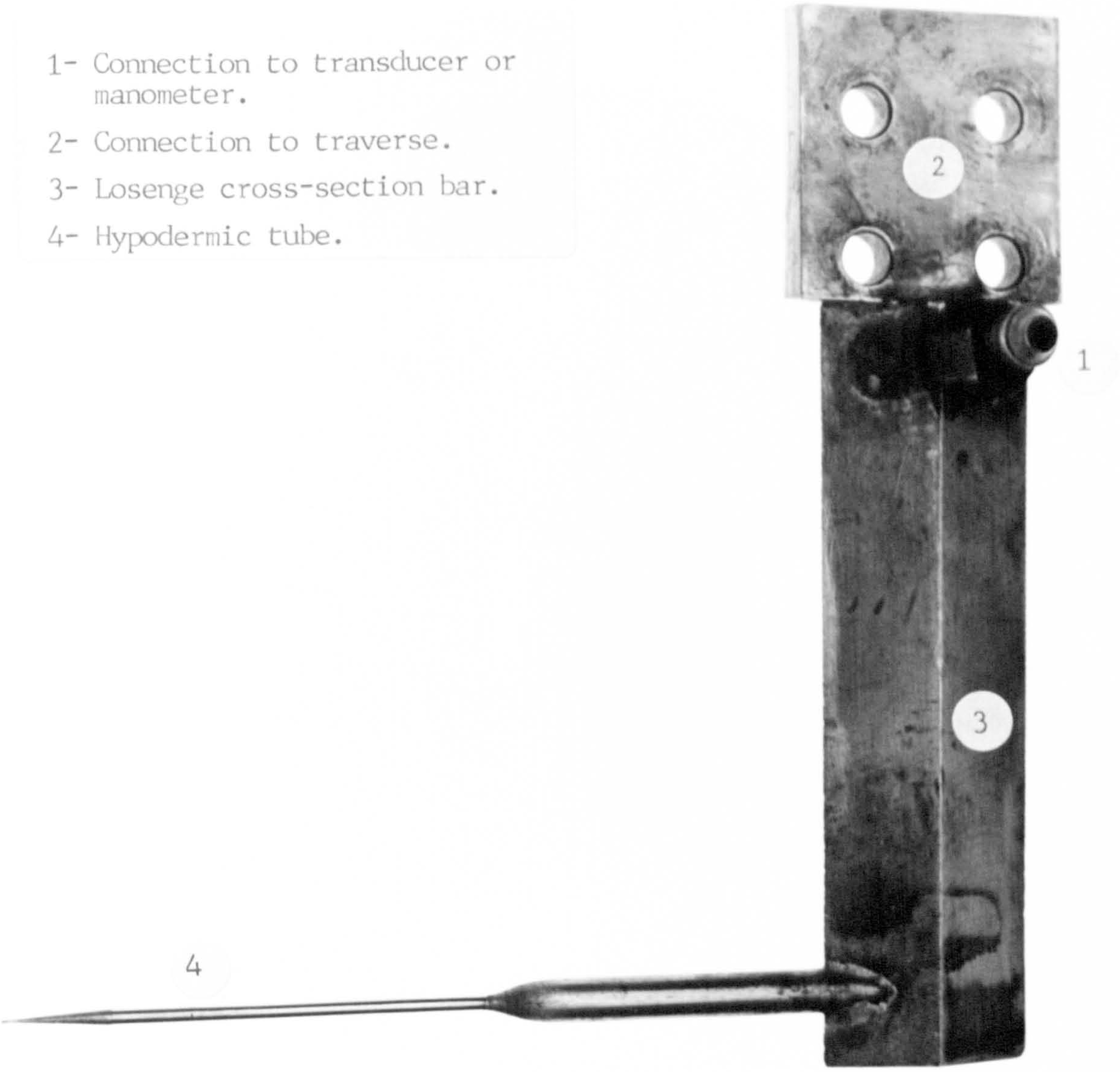

<u>PLATE 4 :</u> External probe.

1- Exit section.

PLATE 5 : Elliptical nozzle.

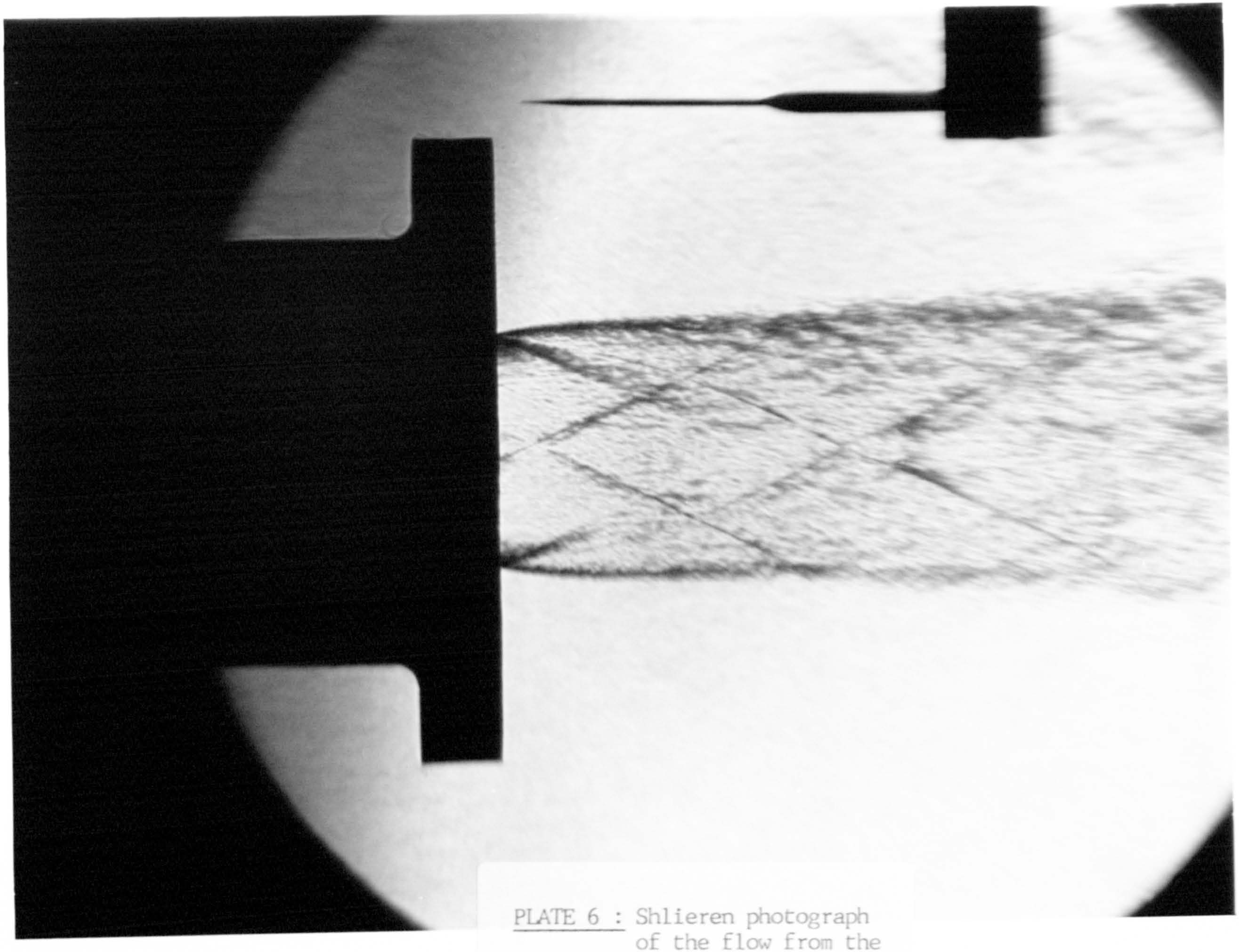

PLATE 6 : Shlieren photograph of the flow from the elliptical cross-section nozzle.